T2R2 東京科学大学 リサーチリポジトリ Science Tokyo Research Repository

論文 / 著書情報 Article / Book Information

題目(和文)	化学蓄熱に用いる金属水酸化物の材料複合化の効果に関する研究
Title(English)	Studies on modification effect on metal hydroxides for thermochemical energy storage
著者(和文)	石飛宏和
Author(English)	Hirokazu Ishitobi
出典(和文)	学位:博士(工学), 学位授与機関:東京工業大学, 報告番号:甲第9120号, 授与年月日:2013年3月26日, 学位の種別:課程博士, 審査員:加藤 之貴
Citation(English)	Degree:Doctor (Engineering), Conferring organization: Tokyo Institute of Technology, Report number:甲第9120号, Conferred date:2013/3/26, Degree Type:Course doctor, Examiner:
Type(English)	Doctoral Thesis

Studies on modification effect on metal hydroxides for thermochemical energy storage

化学蓄熱に用いる金属水酸化物の材料複合化の 効果に関する研究



Hirokazu ISHITOBI

石飛 宏和

Department of Nuclear Engineering
Graduate school of Science and Engineering
Tokyo Institute of Technology

Supervisor: Assoc. Prof., Dr. Yukitaka KATO

A thesis is submitted for the degree of *Doctor of Engineering*. February 22, 2013

Chapter 1	General introduction	1
1.1 Backgro	ound of research	1
1.1.1 Deple	etion of primary energy source	1
1.1.2 Mism	natches of supply and demand of energy	1
1.1.3 Utiliz	ration of un-used thermal energy	2
1.1.3.1	Exhaust and surplus heats from industrial plants, cogeneration systems, and	l small
nuclear i	reactors	2
1.1.3.2	Heat supply for district heating or drying processes	3
1.2 Previous	s researches for thermal energy storages	3
1.2.1 Sensi	ble and latent heat storages	3
1.2.1.1	Principle	3
1.2.1.2	Materials for sensible heat storage and latent heat storage	3
1.2.2 Therr	nochemical energy storages	4
1.2.2.1	Principle	4
1.2.2.2	Materials for thermochemical energy storage.	7
1.3 Develop	oment of materials for thermochemical energy storages	8
1.3.1 Motiv	vation of development of materials for thermochemical energy storage	8
1.3.2 Modi	fication of surface state	8
1.3.3 Modi	fication of bulk composition	11
1.4 Objectiv	/e	13
1.4.1 Lithiu	um chloride-modified magnesium hydroxide	13
1.4.1.1	Dehydration/hydration kinetics	13
1.4.1.2	Relation between reaction conditions and heat output capacity	13
1.4.1.3	Durability properties	14
1.4.2 Rare	earth mixed hydroxides	14
1.4.2.1	Dehydration reactivity	14
1.4.2.2	Hydration reactivity at low vapor pressure	14
1.4.3 Com	abination of thermochemical energy storages based on lithium chloride-m	odified
magnesium	n hydroxide and small nuclear reactors	15
1.4.3.1	District heating system with thermochemical energy storage	15
1.4.3.2	Emergency core cooling system with TCM	15
1.5 Structur	e of thesis	15
1.6 Referen	ces	16
Chapter 2	Dehydration of lithium chloride-modified magnesium hydroxide	22
•	etion	
2.2 Experim	nental	23
2.2.1 Samp	ole preparation	23

2.2.2 Char	acterization techniques	23
2.2.2.1	Scanning electron microscopy	23
2.2.2.2	Powder X-ray diffraction analysis	23
2.2.2.3	Measurements of specific surface area	23
2.2.3 Dehy	dration measurement with thermogravimetry	23
2.3 Results		24
2.3.1 Char	acterization of the samples	24
2.3.1.1	Surface morphology of lithium chloride-modified magnesium hydroxide	24
2.3.1.2	Crystal structure of lithium chloride-modified magnesium hydroxide	25
2.3.1.3	Specific surface area of lithium chloride-modified magnesium hydroxide	27
2.3.2 Dehy	dration measurement with thermogravimetry	28
2.3.2.1	The relationship between temperature and dehydration rate	28
2.3.2.2	The relationship between lithium chloride mixing ratio and dehydration rate	31
2.4 Discuss	ion	32
2.4.1 Dehy	/dration model	32
2.4.1.1	Authentic magnesium hydroxide and lithium chloride-modified magnesium h	ydroxide
$(\alpha = 0.0$	2)	32
2.4.1.2	Lithium chloride modified magnesium hydroxide ($\alpha = 0.10, 0.30$)	36
2.4.2 Arrh	enius parameters for dehydration rate	38
2.4.3 Effec	et of lithium chloride modification on dehydration	43
2.4.4 Abso	lute reaction rate	44
2.5 Summa	ry	48
2.6 Referen	ices	49
Chapter 3	Hydration reactivity of lithium chloride-modified magnesium oxi	de 50
-	ction	
3.2 Experin	nental	50
3.2.1 Samp	ole preparation	50
3.2.2 Char	acterization techniques	51
3.2.2.1	Scanning electron microscopy	51
3.2.2.2	Powder X-ray diffraction analysis	51
3.2.3 Hydr	ration measurement with thermogravimetry	51
3.3 Results		53
	acterization of samples	
3.3.1.1	Surface morphology of lithium chloride-modified magnesium oxide	53
3.3.1.2	Crystal structure of lithium chloride-modified magnesium oxide	54
3.3.2 Hydi	ration measurement with thermogravimetry	
3.3.2.1	Relationship between composition and hydration behavior	

3.3.2.2	Relationship between hydration temperature and hydration behavior	58
3.3.2.3	Relationship between vapor pressure and hydration behavior	60
3.3.2.4	Relationship between time for vapor supply and hydration behavior	61
3.4 Discuss	ion	63
3.4.1 Heat	output capacity	63
3.4.1.1	Relationship between composition and heat output capacity	63
3.4.1.2	Relationship between hydration temperature and heat output capacity	65
3.4.1.3	Relationship between vapor pressure and heat output capacity	66
3.4.1.4	Relationship between time for vapor supply and heat output capacity	67
3.4.2 Kinet	tic analysis of hydration for lithium chloride-modified magnesium oxide	71
3.4.2.1	Shrinking core model	71
3.4.2.2	Hydration rate equations and kinetic parameters	74
3.4.2.3	Effect of lithium chloride modification on hydration	82
3.4.3 Heat	output rate	83
3.5 Summa	ry	84
3.6 Referen	ces	85
Chapter 4	Near infrared spectroscopy for hydration observation	of lithium
	chloride-modified magnesium oxide	86
4.1 Introduc	ction	86
4.2 Experin	nental	86
4.2.1 Samp	ple preparation	86
4.2.2 Obse	rvation of hydration by near infrared spectroscopy	86
4.3 Results		89
4.3.1 Speci	trum measurement to identify peak position	89
4.3.1.1	Spectra of authentic magnesium hydroxide	89
4.3.1.2	Water adsorption on authentic magnesium hydroxide	90
4.3.1.3	Water sorption at lithium chloride-modified magnesium hydroxide	91
4.3.2 Speci	trum measurement for analysis of hydration	93
4.3.2.1	Hydration of authentic magnesium oxide	93
4.3.2.2	Hydration of lithium chloride-modified magnesium oxide	94
4.4 Discuss	ion	96
4.4.1 Spect	trum decomvolution for analysis of hydration process	96
4.4.1.1	Peak positions of each component	96
4.4.1.2	Spectrum deconvolution of the samples under hydration process	100
4.4.2 Hydr	ation mechanism	104
4.4.2.1	Authentic magnesium oxide	104
4.4.2.1 I	Lithium chloride-modified magnesium oxide	106

4.5 Summa	ry	112
	ices	
Chapter 5	Durability of lithium chloride-modified magnesium hydro	xide on
	repetitive reactions	114
5.1 Introduc	ction	114
5.2 Experin	nental	114
5.2.1 Samp	ple preparation	114
5.2.2 Repe	etitive dehydration-hydration measurement with thermogravimetry	114
5.2.3 Char	acterization techniques	116
5.2.3.1	Scanning electron microscopy	116
5.2.3.2	Powder X-ray diffraction analysis	116
5.2.3.3	Measurements of specific surface area	116
5.3 Results		116
5.3.1 Repe	etitive dehydration-hydration measurement with thermogravimetry	116
5.3.2 Char	acterization of samples	122
5.3.2.1	Surface morphology of the material before and after cyclic operation	122
5.3.2.2	Crystal structure of the material before and after cyclic operation	123
5.3.2.3	Specific surface area of the material before and after cyclic operation	124
5.4 Discuss	ion	124
5.4.1 Com	parison with authentic magnesium hydroxide	124
5.4.2 Chan	ge of heat output capacity	125
5.4.3 Chan	nge of surface state	125
5.5 Summa	ry	126
5.6 Referen	ices	126
Chapter 6	Rare earth mixed hydroxide for thermochemical energy storage	128
6.1 Introduc	ction	128
6.2 Experin	nental	131
6.2.1 Samp	ple preparation	131
6.2.2 Char	acterization	133
6.2.2.1	Scanning electron microscopy	133
6.2.2.2	Powder X-ray diffraction analysis	133
6.2.2.3	Infrared spectroscopy	133
6.2.3 Ther	mal decomposition measurement with thermogravimetry	133
6.2.4 Dehy	dration-hydration measurement with thermogravimetry	134
6.2.5 Meas	surement of reaction heat with differential scanning calorimetry	135
6 3 Results		135

(210)	125
6.3.1 Characterization	
6.3.1.1 Surface morphology of rare earth mixed hydroxide	
6.3.1.2 Crystal structure of rare earth mixed hydroxide	
6.3.1.3 Infrared spectroscopy	142
6.3.2 Thermal decomposition measurement with thermogravimetry	143
6.3.3 Dehydration-hydration measurement with thermogravimetry	145
6.3.4 Measurement of reaction heat with differential scanning calorimetry	
6.4 Discussion	154
6.4.1 Relationship between composition and thermal decomposition temperature	2154
6.4.2 Relationship between composition and conversion of hydration	156
6.4.3 Relationship between composition and reaction heat	158
6.4.4 Heat output capacity	159
6.4.5 Rare earth elements from spent nuclear fuels	161
6.5 Summary	162
6.6 References	162
Chapter 7 Combination of thermochemical energy storage ba chloride-modified magnesium hydroxide and small nuclear reactors	164
7.1 Introduction	
7.2 Small nuclear reactor for district heating	
7.2.1 District heating system with thermochemical energy storage	164
7.2.2 Emergency core cooling system with thermochemical energy storage	169
7.2.3 Future prospects of thermochemical energy storage	172
7.3 Summary	172
7.4 References	173
Chapter 8 Conclusion	174
Nomenclature	177
Research achievements	178
Acknowledgements/謝辞	180

Chapter 1 General introduction

1.1 Background of research

1.1.1 Depletion of primary energy source

Our civilized life was supported by energy consumption. For example, air conditioning, automobile, light, and television require energy. Energy consumption in the world for each primary energy source is shown in **Figure 1.1-1**. Consumptions of fossil fuels (oil, coal, and natural gas) shows upward trend. Demand of oil and natural gas would be increased for next 25 years because of economic growth of developing countries.

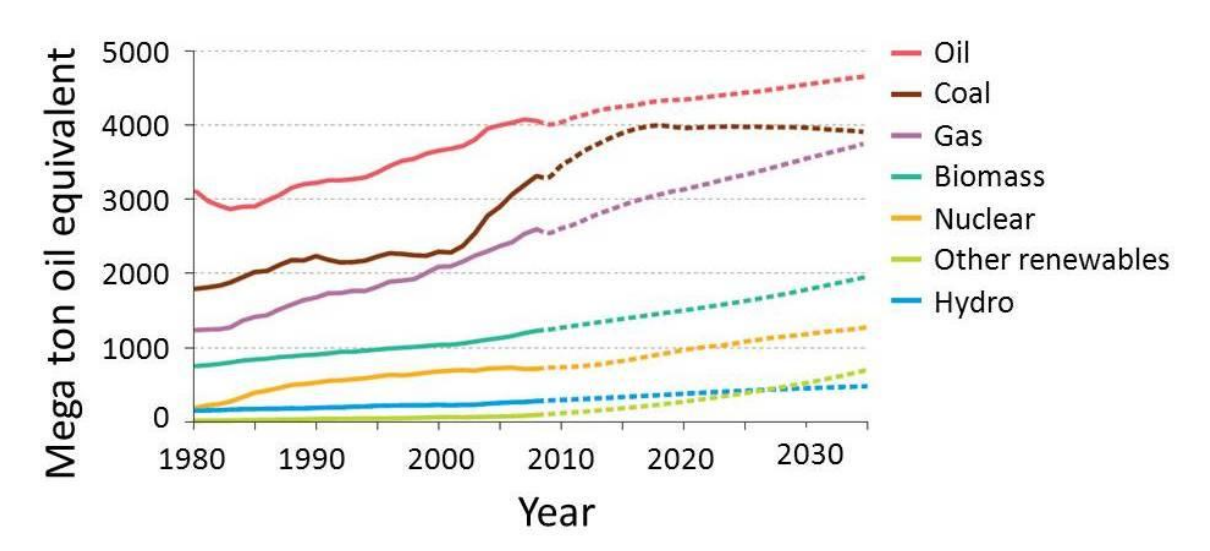


Figure 1.1-1 Energy consumption in the world for each primary energy source. Dashed lines indicate prediction of consumptions [1].

However, oil, coal, and natural gas are exhaustible resource. Depletion of primary energy sources makes severe effects to economic activity in the world. Hence, research and development of energy saving technologies is required.

1.1.2 Mismatches of supply and demand of energy

Mismatches of supply and demand of energy are becoming big social issue. It is recorded that the difference of power load between peak load and bottom load was 85 GW in Japan at August 23, 2010 [2]. Thermal energy for residential area is usually in demand at morning and evening. On the other hand, exhaust heat from industrial area does not match the demand of heat because most of industrial plants are operated at daytime or whole day. Cogeneration (combined heat and power supply) systems have been installed in Japan. The demand of power and that of heat often tend to show different peak time. As a result, research and development of the recovery, storage and

conversion of surplus heat is required.

1.1.3 Utilization of un-used thermal energy

1.1.3.1 Exhaust and surplus heats from industrial plants, cogeneration systems, and small nuclear reactors

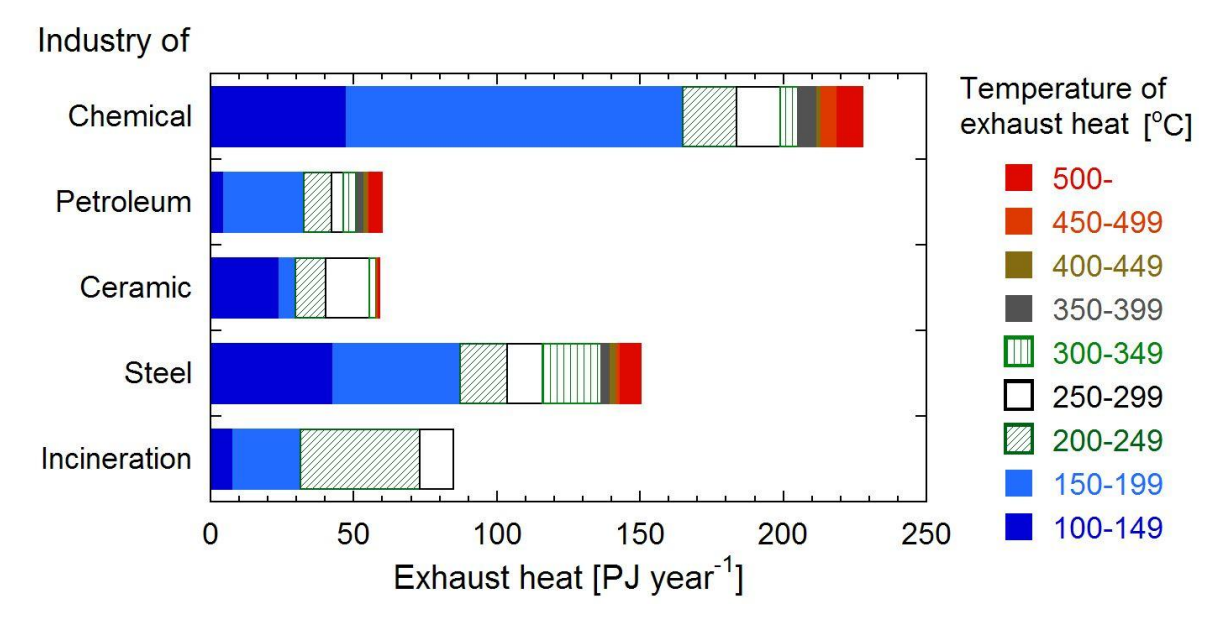


Figure 1.1-2 Amount of exhaust heat for each industry in Japan [3]. Heat in exhaust gas is shown in these data.

Heat storages from industrial plants, cogeneration systems, or small nuclear reactors are important to utilize surplus thermal energy. Amount of exhaust heat for each industry in Japan is shown in **Figure 1.1-2** [3]. Exhaust heat at 250–299°C is released from industrial plants. Especially, it is released from chemical industry (15.4 PJ year⁻¹), ceramic industry (15.2 PJ year⁻¹), and steel industry (12.5 PJ year⁻¹). Also exhaust heat at 300–349°C is released from steel industry (20.4 PJ year⁻¹), chemical industry (6.00 PJ year⁻¹), and petroleum industry (4.84 PJ year⁻¹), and exhaust heat at 200–249°C is released from incineration industry (41.7 PJ year⁻¹), chemical industry (18.8 PJ year⁻¹), and steel industry (16.3 PJ year⁻¹) The exhaust at 100-200°C can be recovered by using adsorption-type thermochemical energy storages [4]. Thus, recovery of exhaust heat at 200-300°C is important. The exhaust gas from cogeneration systems is generally at around 450°C. Steam and/or hot water are produced by using the exhaust heat from internal combustion engine or micro gas turbine. After these thermal processes, heat at around 300°C can be stored. The primary outlet temperature of pressurized water reactor (PWR) is around 350°C, and that of boiling water reactor (BWR) is around 300°C. In past decades, small nuclear reactors were studied for district heating [5,6]. However, usually nuclear plants are operated at steady state. On the other hand, the demand of heat is not steady. Hence, thermal energy at 200–350°C from above mentioned sources should be stored until periods of the demand.

1.1.3.2 Heat supply for district heating or drying processes

District heating systems have been designed for cold area [7-9]. Supplied heat is used for space heating, supply of hot-water, and road heating, for example. Generally, hot-water or steam at 80–150°C are supplied to district area. Drying processes in industrial processes (paper drying process, for example) also require heat [10]. Heat supply by using fossil fuels is not good in the viewpoint of depletion of primary energy source (**Section 1.1.1**). Thus, stored heat from other processes should be used for district heating or drying processes. Hence, research and development of thermal energy storages (TES) is important.

1.2 Previous researches for thermal energy storages

1.2.1 Sensible and latent heat storages

1.2.1.1 Principle

Sensible heat storages can store thermal energy by heat capacity of the materials [11].

$$Q = \int_{T_{\rm p}}^{T_{\rm f}} C_{\rm p} \ dt \tag{1-1}$$

Here, Q [kJ kg⁻¹]: heat output capacity, C_p [kJ K⁻¹ kg⁻¹]: Specific heat capacity of the material, T_i [°C]: initial temperature, T_f [°C]: final temperature, respectively. Advantages of sensible heat storages are reasonable cost and safety. On the other hand, disadvantages of them are relatively low heat output capacity (several tens kJ kg⁻¹), heat loss to environment, and change of heat output temperature.

Latent heat storages can store thermal energy by enthalpy change by fusion [11].

$$Q = \Delta H_{\rm fsn} / M_{\rm mtr} \tag{1-2}$$

Here, $M_{\rm mtr}$ [kg mol⁻¹]: a molecular weight of the material, $\Delta H_{\rm fsn}$ [kJ mol⁻¹]: enthalpy change of fusion, respectively. Advantages of sensible heat storages are constant value of heat output temperature and higher heat output capacity (around 100–500 kJ kg⁻¹ [11–13]) than sensible heat storages. On the other hand, disadvantage of them is heat loss to environment.

1.2.1.2 Materials for sensible heat storage and latent heat storage

For sensible heat storages, water, brick, steel slab, and aluminum are proposed as materials [11,14], for example. For latent heat storages, ice, erithritol, polyethylene, LiNO₃, NaNO₃, K₂CO₃ are proposed as materials [11–14], for example. The materials should be selected to match target temperature and to avoid thermal decomposition.

1.2.2 Thermochemical energy storages

1.2.2.1 Principle

Thermodynamic cycles are used for thermochemical energy storages (TcES). The cycles are based on Clausius-Clapeyron equation [15].

$$\ln K = \ln \left(\frac{P}{P_0}\right) = -\frac{\Delta H}{RT} + \frac{\Delta S}{R} \tag{1-3}$$

Here, K: equilibrium constant, P: equilibrium pressure, P_0 : standard pressure, ΔH : enthalpy change by evaporation, adsorption, or reaction, ΔS : entropy change by evaporation, adsorption, absorption, or reaction, R: gas constant, T: absolute temperature, respectively.

Adsorption cycle

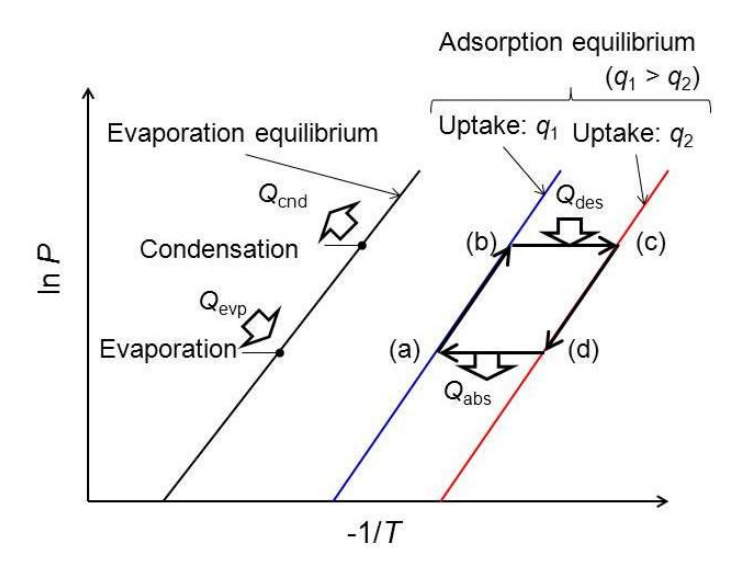


Figure 1.2-1 Clapeyron-diagram of thermochemical energy storage by using adsorption refrigeration cycle (adsorption isostere).

Commonly, TcES by using adsorption are used for refrigeration. It consists of evaporator/condenser and adsorption bed. Clapeyron-diagram of thermochemical energy storage by using adsorption refrigeration cycle is shown in **Figure 1.2-1.** The adsorption cycle consists of four processes as follows; (a \rightarrow b): isosteric heating, (b \rightarrow c): isobaric desorption, (c \rightarrow d): isosteric cooling, (d \rightarrow a): isobaric adsorption. Here, Q_{evp} : evaporation heat, Q_{end} : condensation heat, Q_{des} : desorption heat, Q_{ads} : adsorption heat, respectively. Generally, the heat input and output in the process (a \rightarrow b) and (c \rightarrow d) are negligible. Evaporation equilibrium (K_1), adsorption equilibrium of lean adsorbed bed (K_2), and adsorption equilibrium of rich adsorbed bed (K_3) is expressed as below.

$$\ln K_1 = \ln \left(\frac{P_1}{P_0}\right) = -\frac{\Delta H_{\text{evp}}}{RT} + \frac{\Delta S_{\text{evp}}}{R}$$
(1-4)

$$\ln K_2 = \ln \left(\frac{P_2}{P_0} \right) = -\frac{\Delta H_{\text{ads-1}}}{RT} + \frac{\Delta S_{\text{ads-1}}}{R}$$
 (1-5)

$$\ln K_3 = \ln \left(\frac{P_3}{P_0} \right) = -\frac{\Delta H_{\text{ads-2}}}{RT} + \frac{\Delta S_{\text{ads-2}}}{R}$$
 (1-6)

Here, P_1 : equilibrium pressure of evaporation, P_2 : equilibrium pressure of adsorption bed for uptake of q_1 , P_3 : equilibrium pressure of adsorption bed for uptake of q_2 ($q_1 > q_2$), ΔH_{evp} : enthalpy change by evaporation, $\Delta H_{\text{ads-1}}$: enthalpy change by adsorption for adsorption bed for uptake of q_1 , $\Delta H_{\text{ads-2}}$: enthalpy change by adsorption for adsorption bed for uptake of q_2 , ΔS_{evp} : entropy change by evaporation, $\Delta S_{\text{ads-1}}$: entropy change by adsorption for adsorption bed for uptake of q_1 , $\Delta S_{\text{ads-2}}$: entropy change by adsorption for adsorption bed for uptake of q_2 , respectively. Thermochemical energy storages by using adsorption can store heat at the process of isobaric desorption (Q_{des}), and evaporation heat (Q_{evp}) is used for refrigeration.

Absorption cycle

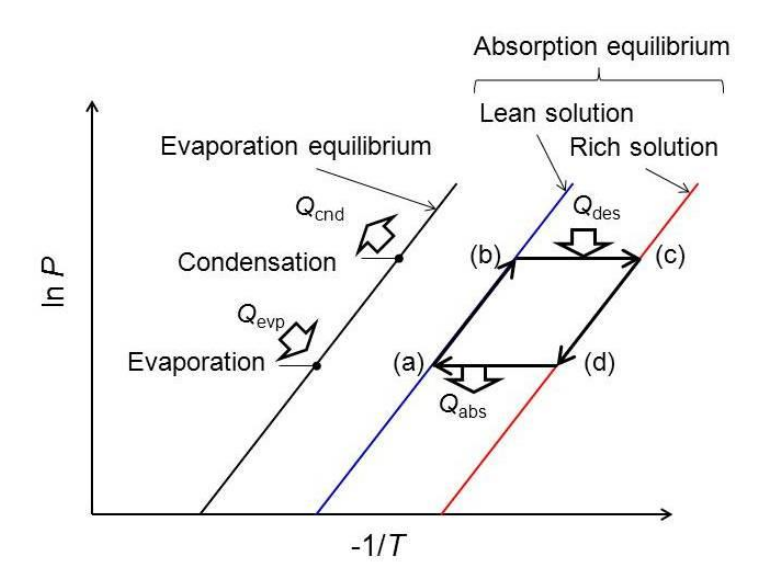


Figure 1.2-2 Clapeyron-diagram of thermochemical energy storage by using absorption cycle.

Generally, TcES by using absorption are also used for refrigeration. It consists of evaporator, absorber, generator (for desorption), and condenser. Clapeyron-diagram of thermochemical energy storage by using absorption refrigeration cycle is shown in **Figure 1.2-2.** The absorption cycle consists of four processes as follows; $(a \rightarrow b)$: isosteric heating, $(b \rightarrow c)$: isobaric desorption, $(c \rightarrow d)$: isosteric cooling, $(d \rightarrow a)$: isobaric absorption. Here, Q_{abs} : absorption heat. The heat input and output in the process $(a \rightarrow b)$ and $(c \rightarrow d)$ are negligible because usually absorption chillers include a heat exchanger between $(a \rightarrow b)$ and $(c \rightarrow d)$. Evaporation equilibrium (K_1) , absorption equilibrium of lean solution (K_4) , and absorption equilibrium of rich solution (K_5) is expressed as below.

$$\ln K_1 = \ln \left(\frac{P_1}{P_0}\right) = -\frac{\Delta H_{\text{evp}}}{RT} + \frac{\Delta S_{\text{evp}}}{R}$$
(1-4)

$$\ln K_4 = \ln \left(\frac{P_4}{P_0} \right) = -\frac{\Delta H_{\text{abs-l}}}{RT} + \frac{\Delta S_{\text{abs-l}}}{R}$$
 (1-7)

$$\ln K_5 = \ln \left(\frac{P_5}{P_0}\right) = -\frac{\Delta H_{\text{abs-r}}}{RT} + \frac{\Delta S_{\text{abs-r}}}{R}$$
(1-8)

Here, P_4 : equilibrium pressure of absorption for lean solution, P_5 : equilibrium pressure of absorption for rich solution, $\Delta H_{\text{abs-l}}$: enthalpy change by absorption for lean solution, $\Delta H_{\text{abs-r}}$: enthalpy change by adsorption for rich adsorbed bed, $\Delta S_{\text{abs-l}}$: entropy change by absorption for lean solution, $\Delta S_{\text{abs-r}}$: entropy change by absorption for rich solution, respectively. Thermochemical energy storages by using absorption can store heat at the process of isobaric desorption (Q_{des}), and evaporation heat (Q_{evp}) is used for refrigeration.

Chemical reaction cycle

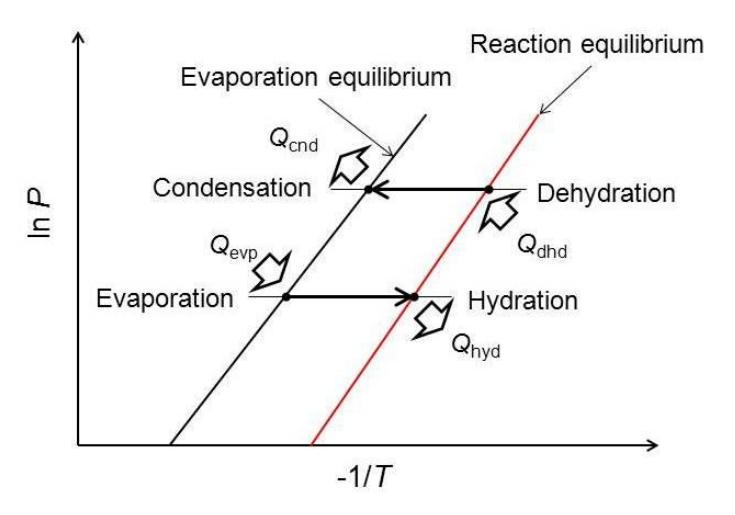


Figure 1.2-3 Clapeyron-diagram of heat enhancement mode of thermochemical energy storage by using chemical reaction. Dehydration/hydration was considered as the reactions in this case.

TcES by using chemical reaction can operate heat enhancement mode, heat storage mode, temperature upgrading mode, and refrigeration mode [16,17]. The heat enhancement mode is important for applications for heat supply (district heating and drying processes). Clapeyron-diagram of heat enhancement mode of TcES by using chemical reaction is shown in **Figure 1.2-3.** Dehydration/hydration was considered as reversible reactions in this case. Here, Q_{dhd} : dehydration heat, Q_{hyd} : hydration heat, respectively. Evaporation equilibrium (K_1), reaction equilibrium (K_6) is expressed as below.

$$\ln K_1 = \ln \left(\frac{P_1}{P_0}\right) = -\frac{\Delta H_{\text{evp}}}{RT} + \frac{\Delta S_{\text{evp}}}{R}$$
(1-4)

$$\ln K_6 = \ln \left(\frac{P_6}{P_0} \right) = -\frac{\Delta H_r}{RT} + \frac{\Delta S_r}{R}$$
 (1-9)

Here, P_6 : equilibrium pressure of the reaction, ΔH_r : enthalpy change by reaction, ΔS_r : entropy change by reaction, respectively. Thermochemical energy storages by using chemical reaction can store heat by endothermic reaction (dehydration, decarbonation...), and output heat by exothermic reaction (hydration, carbonation...).

1.2.2.2 Materials for thermochemical energy storage

Adsorption-type TcES

Zeolite-H₂O [4,18–25], silica gel-H₂O [26], and active carbon-CH₃OH [27–29] were proposed as adsorbent-adsorbate pairs, for example. Heat storage capacities of the materials are around 180–640 MJ m⁻³ [11], and heat at around 60–200°C can be stored [4]. In recent years, silicoaluminophosphate zeolites (SAPO) [23,24] and ferroaluminophosphate zeolites (FAPO) [25] are studied because of their adsorption isotherm shows S-shape, large uptake of water, and preferable regeneration temperature.

Absorption-type TcES

LiBr-water [30–33], LiNO₃-NH₃ [33,34], NaOH-H₂O [35], and KOH-H₂O-NH₃ [36] are proposed as working pairs, for example. Heat storage capacities of the materials are around 430–910 MJ m⁻³ [11], and heat at around 40–150°C can be stored [11]. Because absorption-typeTcES can be used as liquid-gas two phase flow, the heat transformation system is useful continuous heat pump operation. The technical problems of absorption-type TcES are that the reactor design needs high-vacuum chamber because the operation pressure is relatively low, and they require periodical maintenance because the solutions are corrosive.

Chemical-type TcES

TcES by using reversible chemical reactions has been studied in the past decades. For example, metal hydroxides [16,37–43], metal carbonates [44–48], metal salt hydrates [49–59], metal salt·*n*CH₃OH [56,57,60–62], and metal salt·*n*NH₃ [63–66] have been reported as thermochemical energy storage materials (TCMs). The advantage of TCMs is their high heat storage capacities (more than 1000 MJ m⁻³ for metal hydroxides and metal carbonates). Thus, TCMs by using chemical reactions are studied in this work. A TCM on Mg(OH)₂ has been examined earlier [37–39].

$$MgO(s)+H_2O(g) \iff Mg(OH)_2(s) \quad \Delta H_r^{\circ} = -81.0 \text{ kJ mol}^{-1}$$
 (1-10)

$$H_2O(g) \rightleftharpoons H_2O(l) \Delta H_{cnd}^{\circ} = -40.7 \text{ kJ mol}^{-1}$$
 (1-11)

The dehydration (endothermic reaction) in Eq. (1-10) corresponds to the heat storage operation, while the hydration (exothermic reaction) corresponds to the heat output operation.

The technical problem of TCM based on metal hydroxides and metal carbonates is that they cannot store thermal energy at 200–300°C. Generally, heat storage temperature for metal hydroxides and metal carbonates are equal to or higher than 350°C. On the other hand, the target temperatures of thermal energy storage for metal salt hydrates, metal salt $\cdot n$ CH₃OH, and metal salt $\cdot n$ NH₃ are around 100°C.

1.3 Development of materials for thermochemical energy storages

1.3.1 Motivation of development of materials for thermochemical energy storage

As mentioned at **Section 1.1.3.1**, exhaust heat at around 200–350°C is needed to be stored. Thus, TCMs which can dehydrate at 200–350°C are required. A technical problem of Mg(OH)₂ and Ca(OH)₂ (conventional TCMs) is that these materials dehydrate at 350°C or higher temperature within 30 min. Thus, reactivity enhancement for dehydration is required. Developments of TCMs which can dehydrate at lower temperature were performed by following procedures.

1.3.2 Modification of surface state

The dehydration reactivity could be enhanced by surface modification by hygroscopic compounds. TCMs which were modified by metal salt or metal hydroxide were proposed by Hirao [67] and Ryu et al. [68]. A schematic model of the surface modification by hygroscopic compounds is shown in Figure 1.3-1. The surface of Mg(OH)₂ was covered with hygroscopic compounds (lithium chloride (LiCl) or sodium hydroxide (NaOH), for example). **Figure 1.3-2** shows thermal decomposition curves for metal salt- or metal hydroxide-modified Mg(OH)₂ [67]. The mixing molar ratio of additive to Mg(OH)₂ was one to ten in **Figure 1.3-2**. Metal salt- or metal hydroxide-modified Mg(OH)₂ is abbreviated as "name of additive/Mg(OH)₂" (For example, LiCl-modified Mg(OH)₂ is abbreviated as LiCl/Mg(OH)₂). The dehydration of surface-modified Mg(OH)₂ started at lower temperature than that of authentic Mg(OH)₂.

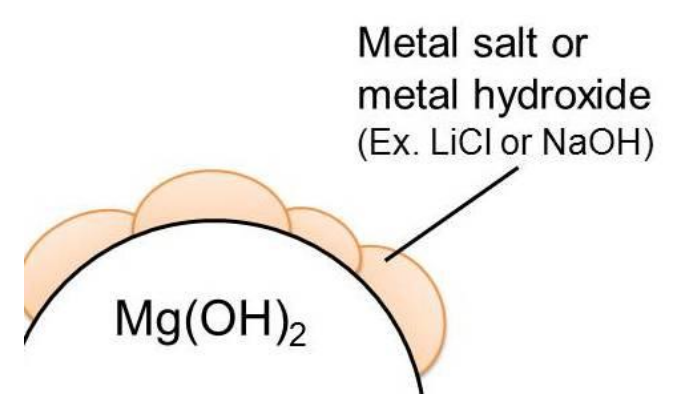


Figure 1.3-1 Schematic model of surface modification by hygroscopic compounds.

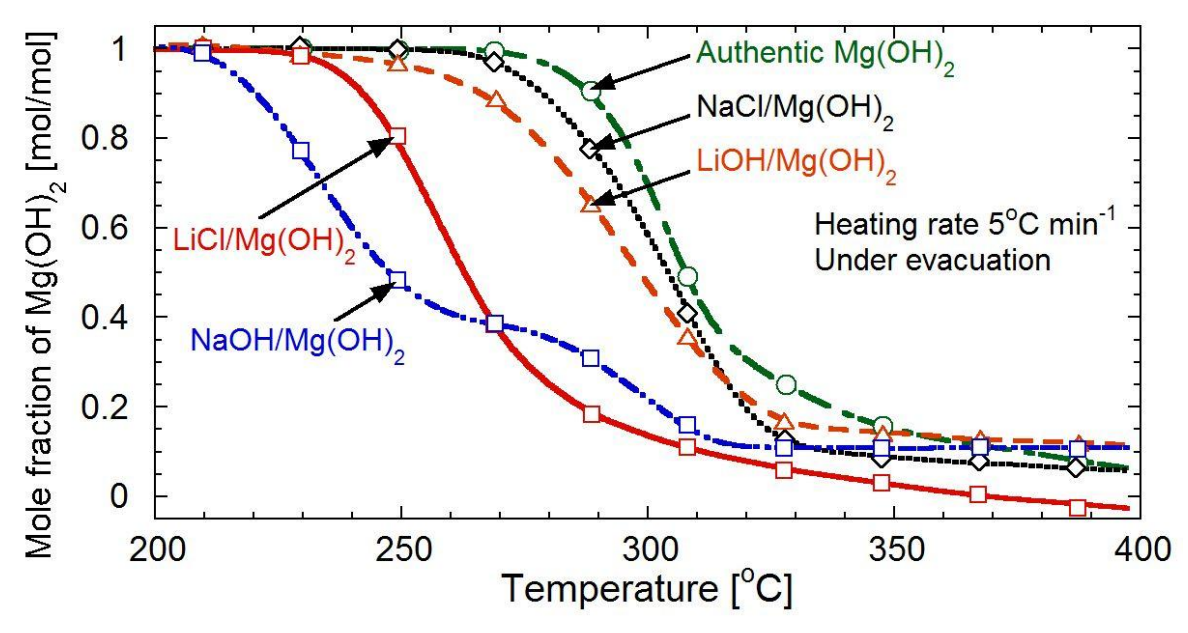


Figure 1.3-2 Thermal decomposition curves for metal salt- or metal hydroxide-modified Mg(OH)₂ [67].

Dehydration temperatures of authentic and surface modified $Mg(OH)_2$ is shown **Table 1.3-1** [67]. An order of dehydration temperature was as follows; $NaOH/Mg(OH)_2 < LiCl/Mg(OH)_2 < LiOH/Mg(OH)_2 < NaCl/Mg(OH)_2 < Authentic <math>Mg(OH)_2$.

Table 1.3-1 Dehydration temperatures of authentic and surface modified Mg(OH)₂ [67].

Material	Dehydration temperature [°C]
Authentic Mg(OH) ₂	277
$NaCl/Mg(OH)_2$	267
$LiOH/Mg(OH)_2$	255
LiCl/Mg(OH) ₂	232
NaOH/Mg(OH) ₂	205

The hygroscopic property of the metal salts or metal hydroxides could be known by the enthalpy change by dissolution. Values of enthalpy change by dissolution ($\Delta H_{\rm sol}^{\circ}$) for each metal salt or metal hydroxide are shown in **Table 1.3-2**. An order of $\Delta H_{\rm sol}^{\circ}$ for these four compounds is as follows; NaOH < LiCl < LiOH < NaCl. It can be concluded a compound which has large negative value of $\Delta H_{\rm sol}^{\circ}$ is a candidate for an additive. Metal hydroxides show negative value of $\Delta H_{\rm sol}^{\circ}$. However, these materials are not recommended as additives because of their strong basic property.

Table 1.3-2 Values of enthalpy change by dissolution for each metal salt or metal hydroxide [69]. *Values of enthalpy change by dissolution for CsF was obtained from [70].

Cation	Anion	$\Delta H_{\rm sol}^{\circ} [\text{kJ mol}^{-1}]$		Cation	Anion	$\Delta H_{\rm sol}^{\circ} [\text{kJ mol}^{-1}]$
Cs ⁺	Ī_	33.3		Na ⁺	Br ⁻	-0.60
Cs^+	Br^{-}	26.0		Na^{+}	I^-	-7.531
Rb^+	I^-	25.1		K^{+}	F^{-}	-17.7
Rb^+	Br^{-}	21.9		Li^{+}	OH^-	-23.56
K^{+}	I^-	20.33		Cs^+	F^{-}	-29.03*
K^{+}	Br^{-}	19.9		Li^{+}	Cl	-37.03
Cs^+	Cl^{-}	17.8		Na^{+}	OH^-	-44.52
Rb^+	Cl^{-}	17.28		Li ⁺	Br^{-}	-48.83
K^{+}	Cl^{-}	17.217		K^{+}	OH^-	-57.61
Li ⁺	F^{-}	4.73		Rb^{+}	OH^-	-62.3
Na ⁺	Cl^-	3.883		Li ⁺	Γ	-63.26
Na ⁺	F^{-}	0.91	_	Cs^+	OH^-	-71.0

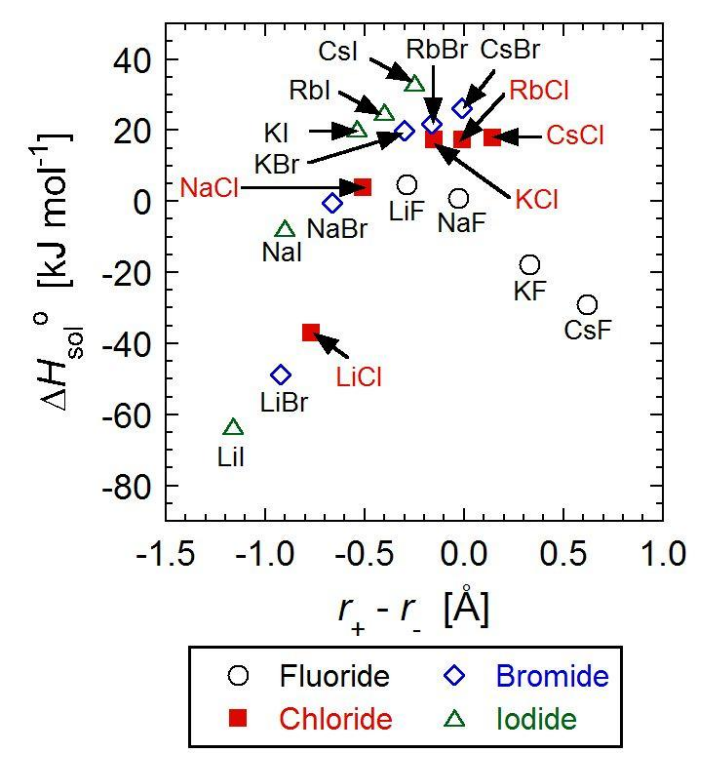


Figure 1.3-3 Relationship between difference of ionic radius $(r_+ - r_-)$ and enthalpy change by dissolution (ΔH_{sol}) for each metal salt.

It is known that the value of $\Delta H_{\rm sol}^{\circ}$ becomes large when the difference of ionic radius of metal salt is large [71]. Relationship between difference of ionic radius $(r_+ - r_-)$ and enthalpy change by

dissolution for each metal salt is plotted in **Figure 1.3-3**. The metal salt with big cation (Cs⁺) and small anion (F⁻), or small cation (Li⁺) and big anion (Cl⁻, Br⁻, I⁻) shows large negative value of ΔH_{sol}° . LiI, LiBr, LiCl are candidates for additives. However, metal iodides are easy to oxidize in the atmospheric condition. Thus LiI was removed from candidates of additives. The melting points of the additives should be high to avoid melting at any accidents. The melting point of LiCl (605°C [69]) is higher than LiBr (550°C [69]), thus LiCl/Mg(OH)₂ was studied further.

Hydration (exothermic reaction) of LiCl/MgO was studied in the previous study [67]. Conversion of the hydration of the material was greater than 0.5 at 110–180°C, water vapor pressure of 57.8 kPa, and 80 min for supply of water vapor. The dehydration and hydration of the material are reversible. Hence, LiCl/Mg(OH)₂ has a potential for TCMs.

1.3.3 Modification of bulk composition

The other procedure for reactivity enhancement is modification of bulk composition. The dehydration reactivity of mixed hydroxides could be enhanced by adjusting metal ion composition. Magnesium-cobalt mixed hydroxides $(Mg_xCo_{1-x}(OH)_2)$ and magnesium-nickel mixed hydroxides $(Mg_xNi_{1-x}(OH)_2)$ are proposed as TCMs by Takahashi [72] and Ryu et al. [73]. The dehydration proceeded at lower temperature when the concentration of Co or Ni in the hydroxide was increased.

The change of Gibbs energy by reaction under the standard condition is expressed as follows.

$$\Delta G_{\rm r}^{\rm o} = \Delta H_{\rm r}^{\rm o} - T \Delta S_{\rm r}^{\rm o} \tag{1-12}$$

Here, ΔG_r° [kJ mol⁻¹]: change of Gibbs free energy by reaction, ΔH_r° [kJ mol⁻¹]; change of enthalpy by reaction, T [K]; absolute temperature, ΔS_r° [J mol⁻¹ K⁻¹]; change of entropy by reaction. ΔG_r° is zero at equilibrium state. Thereby, a temperature at equilibrium state (turnover temperature, T_{turn}) is expressed as below.

$$T_{\text{turn}} = \frac{\Delta H_{\text{r}}^{\circ}}{\Delta S_{\text{r}}^{\circ}} \tag{1-13}$$

The values of ΔH_r° and ΔS_r° for reaction from oxide (rock salt structure) to hydroxide (brucite structure) are shown in **Table 1.3-3**. The values of ΔS_r° is almost constant ($\approx 150 \text{ J mol}^{-1} \text{ K}^{-1}$) for these reactions because major contribution of entropy change is dissipation of H_2O (g) by the reaction. Hence, T_{turn} depends on the value of ΔH_r° (**Figure 1.3-4**).

Table 1.3-3 The values of ΔH_r° and ΔS_r° for reaction from oxide (rock salt structure) to hydroxide (brucite structure).

	$\Delta H_{ m r}^{\circ}$	$\Delta S_{ m r}^{\circ}$
Reaction	$[kJ mol^{-1}]$	$[\mathrm{J} \; \mathrm{mol}^{-1} \mathrm{K}^{-1}]$
$Ca(OH)_2 \rightleftharpoons CaO + H_2O(g)$	109	145
$Mg(OH)_2 \rightleftharpoons MgO + H_2O(g)$	81.0	152
$Cd(OH)_2 \rightleftharpoons CdO + H_2O(g)$	60.7	148
$Fe(OH)_2 \Rightarrow FeO + H_2O(g)$	60.2	162
$Co(OH)_2 \rightleftharpoons CoO + H_2O(g)$	60.0	163
$Ni(OH)_2 \rightleftharpoons NiO + H_2O(g)$	48.2	139

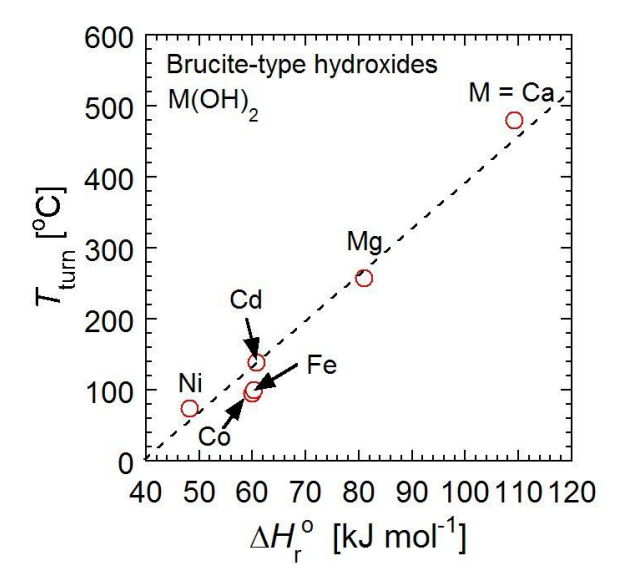


Figure 1.3-4 Relationship between $\Delta H_{\rm r}^{\circ}$ and $T_{\rm turn}$.

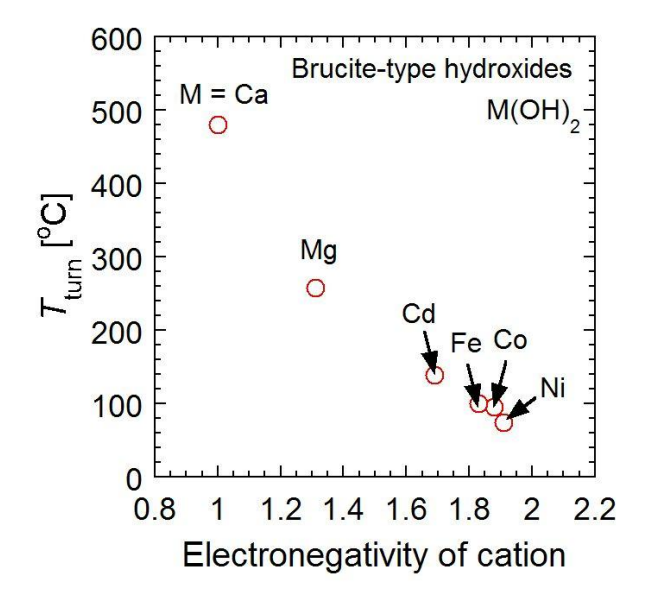


Figure 1.3-5 Relationship between electronegativity of cation and T_{turn} .

It is known electronegativity of cation and basicity of solid catalyst has a relationship for metal oxides or hydroxides [74,75]. Metal hydroxides whose cation has a small value of electronegativity show basicity in the aqueous solution because hydroxyl groups are easy to remove in the solution. Thus, electronegativity of cation and ΔH_r° for metal hydroxides should have a correlation. Therefore, electronegativity of cation and T_{turn} should have a relation. Figure 1.3-5 shows a relationship between electronegativity of cation and T_{turn} . Metal hydroxides whose cation has a large value of electronegativity show lower turning temperature.

The mixed hydroxide can be prepared when two hydroxides have a same crystal structure and similar ionic radiuses. The dehydration reactivity of mixed hydroxides can be enhanced by adjusting metal ion composition in the mixed hydroxide. Magnesium-cobalt mixed hydroxides $(Mg_xCo_{1-x}(OH)_2)$ and magnesium-nickel mixed hydroxides $(Mg_xNi_{1-x}(OH)_2)$, which have brucite structure, were proposed as a TCM [72,73]. Some of these mixed hydroxides could dehydrate at 280° C and hydrated at 110° C with water vapor pressure of 57.8 kPa.

It is known that rare earth hydroxides have a same structure (Y(OH)₃-type structure). Thus, rare earth mixed hydroxides can be prepared as candidates for TCMs. Nagao et al. reported that some of rare earth oxides showed high hydration reactivity at 25°C with saturated water vapor [76]. Batsanov et al. [77] and Yamamoto et al. [78] reported that the temperatures of first dehydration for rare earth hydroxides proceed at 250–410°C. Thus, rare earth hydroxides would store thermal energy from chemical plants, steel plants, and light-water reactors.

1.4 Objective

1.4.1 Lithium chloride-modified magnesium hydroxide

1.4.1.1 Dehydration/hydration kinetics

Some technical issues have been remained for practical application of TcES by using LiCl/Mg(OH)₂. Although kinetic equations and parameters for dehydration of LiCl/Mg(OH)₂ and kinetic equations and parameters for hydration of LiCl/MgO are important to design reactors of TcES, there are no kinetic study on dehydration of LiCl/Mg(OH)₂ and hydration of LiCl/MgO. Kinetic equations and parameters for dehydration of LiCl/Mg(OH)₂ and hydration of LiCl/MgO have been unclear. In this work, dehydration profiles and hydration profiles of materials at various temperatures are measured, and kinetic analysis is performed. The effect of LiCl-modification on enhancement of hydration reactivity has been also unexplained. The understanding about hydration mechanism of LiCl/MgO is important to design new TCM. In this work, hydration of LiCl/MgO is observed by near infrared spectroscopy, and measured spectrum is deconvoluted into components (spectrum of Mg(OH)₂ and that of sorbed water). The hydration mechanism is discussed by profile of peak area for each component with time.

1.4.1.2 Relation between reaction conditions and heat output capacity

A TcES should be corresponded a temperature of exhaust heat and that of demand of heat. Thus, operation conditions of TcES should be designed to satisfy the objective. The relation between reaction conditions and hydration reactivity affects heat output capacity. The relation between reaction conditions and conversion of the hydration of LiCl/MgO with LiCl mixing molar ratio of 0.01, 0.02, and 0.10 were studied previously [67]. However, detailed study on the effect of lithium chloride mixing ratio, hydration temperature, and water vapor pressure were not performed. Heat output capacities of the TCM were not evaluated in the previous study. In this work, hydration of LiCl/MgO at various lithium chloride mixing ratio, hydration temperature, and water vapor pressure are examined, and heat output capacities for each condition are evaluated.

1.4.1.3 Durability properties

The durability properties of TCMs are important for practical application. The reactivity change affects heat output capacity of TCMs. A relationship between reactivity and number of operation should be known to decide a period of replacement. The period of replacement affects economic potential of TCMs. Twelve runs of dehydration-hydration operation for LiCl/Mg(OH)₂ was performed in previous study [67]. However, the reactivity change has been expected to be occurred at more than twelve runs. The reactivity change would cause by change of surface state. In this work, 105 runs of repetitive reactions are examined to evaluate durability properties for practical application. The characterization of the samples is carried out to confirm any changes at surface state during 105 runs of repetitive reactions.

1.4.2 Rare earth mixed hydroxides

1.4.2.1 Dehydration reactivity

As mentioned at **Section 1.1.3.1**, surplus/exhaust heat at around 250–300°C is needed to be stored. Rare earth mixed hydroxides is proposed as TCMs in this work. The dehydration reactivity of rare earth mixed hydroxides could be enhanced by adjusting metal ion composition. However, there are no studies on the dehydration reactivity of rare earth mixed hydroxides. In this work, dehydration of rare earth mixed hydroxides is measured by thermogravimetry. The relationship between composition of rare earth mixed hydroxides and dehydration temperature is studied.

1.4.2.2 Hydration reactivity at low vapor pressure

Mg_xCo_{1-x}(OH)₂ and Mg_xNi_{1-x}(OH)₂ can store thermal energy at 250–300°C, but these materials require water vapor pressure of 57.8 kPa for hydration. It means these materials need heat at 85°C for evaporation of water for the hydration, and extra heat sources such as exhaust heat from cooling media of internal combustion engines, polymer electrolyte fuel cells, or industrial plants are needed for the water evaporation. However, it is hard to use these heat sources following with the requirement for hydration, that is, heat output operation. Hence, it is necessary to develop new materials that can be used at a lower water vapor pressure (lower heat source temperature) during the heat output operation. Rare earth mixed hydroxides are candidate for TCMs. However, there is no information about hydration reactivity of these TCMs under low water vapor pressure. Thus, hydration behaviors of these materials under low water vapor pressure are studied.

1.4.3 Combination of thermochemical energy storages based on lithium chloride-modified magnesium hydroxide and small nuclear reactors

1.4.3.1 District heating system with thermochemical energy storage

As mentioned at **Section 1.1.3.1**, small nuclear reactors were designed for district heating. Generally, nuclear plants are operated steady. However, heat load is not steady. Load leveling by using TcES is considered as one of the methods to overcome the problem [79,80]. LiCl/Mg(OH)₂ is expected as a material for load leveling because theoretical heat output capacity of Mg(OH)₂ is enough large (1.4 MJ kg⁻¹). It is needed to estimate a required amount of LiCl/Mg(OH)₂ to evaluate a possibility for load leveling. In this work, the required amount of LiCl/Mg(OH)₂ is estimated by the modeled district heating system with a small nuclear reactor.

1.4.3.2 Emergency core cooling system with TCM

At the accident at nuclear power plant, it is needed to remove decay heat from the reactor. Thus, emergency core cooling systems (ECCS) are installed in the nuclear power plants. However, severe accidents would occur with blackout. Hence, ECCS which can work without power is needed. LiCl/Mg(OH)₂ is a candidate as a heat absorber because it dehydrate (endothermic reaction) at around 300°C, which is suitable for temperature of light water reactors (LWRs), and it's high heat storage capacity. It is needed to calculate required amount of LiCl/Mg(OH)₂ for ECCS to evaluate a potential of the material. In this work, the decay heat from a small nuclear reactor after shutdown is calculated, and then required amount of LiCl/Mg(OH)₂ for ECCS was estimated.

1.5 Structure of thesis

A structure of the thesis is described as below.

In **Chapter 1**, the background of research was explained. Previous researches for thermal energy storages were reviewed and technical issues were clarified. The motivation of development of TCMs was shown. The potential of LiCl/Mg(OH)₂ and rare earth mixed hydroxides for TCMs were discussed. The problems of LiCl/Mg(OH)₂ and rare earth mixed hydroxides for practical application were shown. Then, the objectives of research were explained.

In **Chapter 2**, $LiCl/Mg(OH)_2$ with a series of LiCl mixing molar ratios are prepared. The dehydration of authentic $Mg(OH)_2$ (conventional material) and $LiCl/Mg(OH)_2$ are performed. Kinetic analysis of dehydration is performed.

In **Chapter 3**, the hydration of LiCl/MgO at various LiCl mixing molar ratio, hydration temperature, and water vapor pressure are examined. Heat output capacities of the materials for each condition are evaluated. Kinetic analysis of hydration is performed by using shrinking core model.

In **Chapter 4**, observation of hydration by near infrared spectroscopy is performed to understand the contribution of LiCl-modification. The obtained spectra are decrivoluted into components (Mg(OH)₂, and adsorbed water or sorbed water). The hydration mechanism was discussed by profile of peak area for each component with time.

In Chapter 5, 105 runs of dehydration-hydration cyclic operations are performed. The

samples are dehydrated at 250°C and hydrated at 110°C with water vapor pressure of 57.8 kPa. The change of heat output capacity is evaluated. The change of surface state is examined to understand a reason of reactivity change of the material.

In **Chapter 6**, rare earth mixed hydroxides are proposed as candidates for TCMs. Thermal decomposition profiles of the rare earth pure/mixed hydroxides are measured to evaluate the dehydration reactivity of each hydroxide. Dehydration-hydration behaviors of the rare earth pure/mixed hydroxides are examined. The samples are dehydrated at 300°C and hydrated at 110°C with water vapor pressure of 7.4 kPa (relatively low water vapor pressure). Reaction heats of the samples are measured. Then heat output capacities of the samples are evaluated.

In Chapter 7, combination of a small nuclear reactor for district heating and a TcES based on LiCl/Mg(OH)₂ (α = 0.10) is studied. A district heating system by using a small nuclear reactor is modeled, and then amount of LiCl/Mg(OH)₂ for load leveling is estimated. LiCl/Mg(OH)₂ (α = 0.10) is also expected to use as a heat absorber for emergency core cooling system (ECCS). Required amount of LiCl/Mg(OH)₂ for ECCS of the small nuclear reactor is estimated.

In Chapter 8, the results of research are summarized, and conclusion of thesis is stated.

1.6 References

- [1] International energy agency ed.; World energy outlook 2010, IEA publications, Paris, France (2010)
- [2] The federation of electric power companies of Japan ed.; Graphical flip-chart of nuclear & energy related topics 2012 (*in Japanese*), the federation of electric power companies of Japan, Tokyo, Japan (2012)
- [3] The energy conservation center, Japan ed., Report of exhaust heat from industrial plants in Japan, The energy conservation center, Japan, Tokyo, Japan (2001)
- [4] H. Demir, M. Mobedi, S. Ülkü; A review on adsorption heat pump: problems and solutions, *Renew. Sustainable Energy Rev.*, **12**, 2381–2403 (2008)
- [5] E. O. Adamov, Yu. M. Cherkashov, A. A. Romenkov, V.I. Mikhan, V.I. Semenikhin; Inherently safe pool-type reactor as a generator of low-grade heat for district heating, air conditioning and salt water desalination, Nucl. Eng. Des., 173, 167–174 (1997)
- [6] O. Sambuu, T. Obara; Conceptual design for a small modular district heating reactor for Mongoliam Ann. Nucl. Energy, 47, 210–215 (2012)
- [7] E. Dotzauer; Simple model for prediction of loads in district-heating systems, *Appl. Energy*, **73**, 277–284 (2002)
- [8] I. Gabrielaitiene, B. Bøhm, B. Sunden; Modelling temperature dynamics of a district heating system in Naestved, Denmark—A case study, *Energy Convers. Manage.*, **48**, 78–86 (2006)
- [9] Y. Wang, Y. Zhang; Analysis of the dilatancy technology of district heating system with high-temperature heat pump, *Energy and Buildings*, **47**, 230–236 (2012)
- [10] K. Abrahamsson, S. Stenström, G. Aly, Å. Jernqvist, Application of heat pump system for energy conservation in paper drying, Int. J. Energy Res., 21, 631–642 (1997)

- [11] P. Tatsidjodoung, N. L.Pierrès, L. Luo; A review of potential materials for thermal energy storage in building applications, *Renew. Sustainable Energy Rev.*, **18**, 327–349 (2013)
- [12] M. Liu, W. Saman, F. Bruno; Review on storage materials and thermal performance enhancement techniques for high temperature phase change thermal storage systems, *Renew. Sustainable Energy Rev.*, **16**, 2118–2132 (2012)
- [13] H. Michels, R. Pitz-Paal; Cascaded latent heat storage for parabolic trough solar power plants, *Sol. Energy*, **81**, 829–837 (2007)
- [14] Society of chemical engineers, Japan ed.; Sustainable energy systems (*in Japanese*), Maki-shoten, Tokyo, Japan (2002)
- [15] Y. I-ida, M. Kamimoto, H. Kameyama ed., Thermal energy storages –Theory and applications—Part II "Latent heat storages and thermochemical energy storages" (*in Japanese*), Shinzansha-Sci-tech, Tokyo, Japan (2001)
- [16] H. Ogura, T. Yamamoto, H. Kage; Efficiencies of CaO/H₂O/Ca(OH)₂ chemical heat pump for heat storing and heating/cooling, *Energy*, **28**, 1479–1493 (2003)
- [17] Y. Kato ed., Large-boned energy loadmap, Kagaku Kogyo Sha, Kawasaki, Japan, 178–187 (2005)
- [18] L. Bonaccorsi, E. Proverbio; Synthesis of thick zeolite 4A coatings on stainless steel, *Microporous Mesoporous Mater.*, **74**, 221–229 (2004)
- [19] L. Bonaccorsi, A. Freni, E. Proverbio, G. Restuccia, F. Russo; Zeolite coated copper foams for heat pumping applications, *Microporous Mesoporous Mater.*, **91**, 7–14 (2006)
- [20] L. Bonaccorsi, E. Proverbio, Angelo Freni, G. Restuccia; In situ growth of zeolites on metal foamed supports for adsorption heat pumps, *J. Chem. Eng. Jpn.*, **40**, 1307–1312 (2007)
- [21] M. Tatlier, A. Erdem-Şenatalar; Polymeric heat exchangers to increase the COP values of adsorption heat pumps utilizing zeolite coatings, *Appl. Therm. Eng.*, **24**, 69–78 (2004)
- [22] J. Jänchen, D. Ackermann, H. Stach, W. Brösicke, Studies of the water adsorption on Zeolites and modified mesoporous materials for seasonal storage of solar heat, *Sol. Energy*, **76**, 339–344 (2004)
- [23] L. Bonaccorsi, L. Calabrese, A. Freni, E. Proverbio, Hydrothermal and microwave synthesis of SAPO (CHA) zeolites on aluminium foams for heat pumping applications, *Microporous Mesoporous Mater.*, available online (2012)
- [24] H. Kakiuchi, S. Shimooka, M. Iwade, K. Oshima, M. Yamazaki, S. Terada, H. Watanabe, T. Takewaki, Water vapor adsorbent FAM-Z02 and its applicapibility to adsorption heat pump, *Kagaku Kogaku Ronbunshu* (*in Japanese with English abstract*), **31**, 273–277 (2005)
- [25] H. Kakiuchi, S. Shimooka, M. Iwade, K. Oshima, M. Yamazaki, S. Terada, H. Watanabe, T. Takewaki, Novel water vapor adsorbent FAM–Z01 and its applicability to an adsorption heat pump, *Kagaku Kogaku Ronbunshu (in Japanese with English abstract)*, **31**, 361–364 (2005)
- [26] Y. Hamamoto, K. C. A. Alam, A. Akisawa, T. Kashiwagi; Performance evaluation of a two-stage adsorption refrigeration cycle with different mass ratio, *Int. J. Refrig.*, **28**, 344–352 (2005)
- [27] Y. Hamamotoa, K. C.A. Alam, B. B. Saha, S. Koyama, A. Akisawa, T. Kashiwagi; Study on adsorption refrigeration cycle utilizing activated carbon fibers. part 1. adsorption characteristics, *Int. J.*

- Refrig., 29, 305–314 (2006)
- [28] J. Y. Wu, R. Z. Wang, Y. X. Xu; Influence of adsorption and desorption capacity on operating process for adsorption heat pump, *Appl. Therm. Eng.*, **22**, 471–476 (2002)
- [29] Y. B. Gui, R. Z. Wang, W. Wang, J. Y. Wu, Y. X. Xu; Performance modeling and testing on a heat-regenerative adsorptive reversible heat pump, *Appl. Therm. Eng.*, **22**, 309–320 (2002)
- [30] K. E. N'Tsoukpoe, N. Le Pierrès, L.. Luo; Numerical dynamic simulation and analysis of a lithium bromide/water long-term solar heat storage system, *Energy*, **37**, 346–358 (2012)
- [31] B. Bakhtiari, L. Fradette, R. Legros, J. Paris; A model for analysis and design of H₂O-LiBr absorption heat pumps, *Energy Convers. Manage.*, **52**, 1439–1448 (2011)
- [32] K. Wang, O. Abdelaziz, P. Kisari, E. A. Vineyard; State-of-the-art review on crystallization control technologies for water/LiBr absorption heat pumps, *Int. J. Refrig.*, **34**, 1325–1337 (2011)
- [33] X. Li, W. Wu, X. Zhang, W. Shi, B. Wang; Energy saving potential of low temperature hot water system based on air source absorption heat pump, *Appl. Therm. Eng.*, **48**, 317–324 (2012)
- [34] W. Wu, X. Zhang, X. Li, W. Shi, B. Wang; Comparisons of different working pairs and cycles on the performance, *Appl. Therm. Eng.*, **48**, 349–358 (2012)
- [35] R. Weber, V. Dorer, Long-term heat storage with NaOH, Vacuum, 82, 708–716 (2008)
- [36] G. Cacciola, G. Restuccia, G. Rizzo, Theoretical performance of an absorption heat pump using ammonia-water-potassium hydroxide solution, *Heat Recovery Systems and CHP*, **10**, 177–185 (1990)
- [37] Y. Kato, F. Takahashi, A. Watanabe, Y. Yoshizawa; Thermal analysis of a magnesium oxide/water chemical heat pump for cogeneration, *Appl. Therm. Eng.*, **21**, 1067–1081 (2001)
- [38] Y. Kato, Y. Sasaki, Y. Yoshizawa; Thermal performance measurement of packed bed reactor of a magnesium oxide/water chemical heat pump, *J. Chem. Eng. Jpn.*, **36**, 833–839 (2003)
- [39] Y. Kato, Y. Sasaki, Y. Yoshizawa; Magnesium oxide/water chemical heat pump to enhance energy utilization of a cogeneration system, *Energy*, 30, 2144–2155 (2005)
- [40] H. Matsuda, T. Ishizu, S.K. Lee, M. Hasatani; Kinetic study of Ca(OH)₂/CaO reversible thermochemical reaction for thermal energy storage by means of chemical reaction, *Kagaku Kogaku Ronbunshu* (in Japanese with English abstract), **11**, 542–548 (1985)
- [41] H. Ogura, T. Yamamoto, H. Kage, Y. Matsuno, A. S. Mujumdar; Effects of heat exchange condition on hot air production by a chemical heat pump dryer using CaO/H₂O/Ca(OH)₂ reaction, *Chem. Eng. J.*, **86**, 3–10 (2002)
- [42] H. Ogura, T. Yamamoto, H. Kage; Efficiencies of CaO/H₂O/Ca(OH)₂ chemical heat pump for heat storing and heating/cooling, *Energy*, **28**, 1479–1493 (2003)
- [43] S. Abliz, O. Fujioka, H. Ogura, H. Kage; Reaction activity of CaO particles prepared by calcination of some CaCO₃ materials, *J. Chem. Eng. Jpn.*, **37**, 815–821 (2004)
- [44] K. Kyaw, M. Kanamori, H. Matsuda, M. Hasatani; Study of carbonation reactions of Ca-Mg oxides for high temperature energy storage and heat transportation, *J. Chem. Eng. Jpn.*, **29**, 112–118 (1996)
- [45] K. Kyaw, H. Matsuda, M. Hasatani; Applicability of carbonation/decarbonation reactions to high temperature thermal energy storage and temperature upgrading, *J. Chem. Eng. Jpn.*, **29**, 119–125 (1996)

- [46] M. Kubota, K. Kyaw, F. Watanabe, H. Matsuda, M. Hasatani; Study of decarbonation of CaCO₃ for high temperature thermal energy storage, *J. Chem. Eng. Jpn.*, **33**, 797–800 (2000)
- [47] M. Aihara, T. Nagai, J. Matsushita, Y. Negishi, H. Ohya; Development of the porous solid reactant for thermal-energy storage and temperature upgrade using carbonation/decarbonation reaction, *Appl. Energy*, **69**, 225–238 (2001)
- [48] M. Aihara, T. Yoshii, Y. Shimazaki, T. Takeuchi, H. Habuka; Dacarbonation and pore structural change of Ca-solid reactant for CaO/CO₂ chemical heat pump, *J. Chem. Eng. Jpn.*, **41**, 513–518 (2008)
- [49] S. K. Lee, H. Matsuda, M. Hasatani; Fundamental studies of CaSO₄•(1/2)H₂O/CaSO₄ thermochemical reaction cycle for thermal energy storage by means of chemical reaction, *Kagaku Kogaku Ronbunshu* (in Japanese with English abstract), **12**, 75–82 (1986)
- [50] H. Ogura, M. Haguro, Y. Shibata, Y. Otsubo; Reaction characteristics of CaSO₄/CaSO₄ 1/2H₂O reversible reaction for chemical heat pump, *J. Chem. Eng. Japan*, **40**, 1252–1256 (2007)
- [51] H. Lahmidi, S. Mauran, V. Goetz; Definition, test and simulation of a thermochemical storage process adapted to solar thermal systems, *Sol. Energy*, **80**, 883–893 (2006)
- [52] S. Mauran, H. Lahmidi, V. Goetz; Solar heating and cooling by a thermochemical process. First experiments of a prototype storing 60 kWh by a solid/gas reaction, *Sol. Energy*, **82**, 623–636 (2008)
- [53] K. Fujioka, H. Suzuki; Thermophysical properties and reaction rate of composite reactant of calcium chloride and expanded graphite, *Appl. Therm. Eng.*, available online (2011)
- [54] A. Freni, M. M. Tokarev, G. Restuccia, A.G. Okunev, Yu. I. Aristov; Thermal conductivity of selective water sorbents under the working conditions of a sorption chiller, *Appl. Therm. Eng.*, **22**, 1631–1642 (2002)
- [55] A. Freni, F. Russo, S. Vasta, M. Tokarev, Yu. I. Aristov, G. Restuccia; An advanced solid sorption chiller using SWS-1L, *Appl. Therm. Eng.*, **27**, 2200–2204 (2007)
- [56] L. G. Gordeeva, A. D. Grekova, T. A. Krieger, Yu. I. Aristov; Adsorption properties of composite materials (LiCl + LiBr)/silica, *Microporous Mesoporous Mater.*, **126**, 262–267 (2009)
- [57] L. G. Gordeeva, A. Freni, T. A. Krieger, G. Restuccia, Yu. I. Aristov; Composites "lithium halides in silica gel pores": Methanol sorption equilibrium, *Microporous Mesoporous Mater.*, **112**, 254–261 (2008)
- [58] K. Posern, C. Kaps; Calorimetric studies of thermochemical heat storage materials based on mixtures of MgSO₄ and MgCl₂, *Thermochim. Acta*, **502**, 73–76 (2010)
- [59] S. Hongois, F. Kuznik, P. Stevens, J. Roux; Development and characterisation of a new MgSO₄ zeolite composite for long-term thermalenergystorage, *Sol. Energy Mater. Sol. Cells*, **95**, 1831–1837 (2011)
- [60] L. G. Gordeeva, Y. I. Aristov; Composite sorbent of methanol "LiCl in mesoporous silica gel" for adsorption cooling: dynamic optimization, *Energy*, **36**, 1273–1279 (2011)
- [61] L. G. Gordeeva, A. Freni, G. Restuccia, Yu. I. Aristov; Influence of characteristics of methanol sorbents "salts in mesoporous silica" on the performance of adsorptive air conditioning cycle, *Ind. Eng. Chem. Res*, **46**, 2747–2752 (2007)

- [62] L. G. Gordeeva, A. Freni, Yu. I. Aristov, G. Restuccia; composite sorbent of methanol "lithium chloride in mesoporous silica gel" for adsorption cooling machines: performance and stability evaluation, *Ind. Eng. Chem. Res.*, **48**, 6197–6202 (2009)
- [63] B. Zajaczkowski, Z. Królicki, A. Jezowski; New type of sorption composite for chemical heat pump and refrigeration systems, *Appl. Therm. Eng.*, **30**, 1455–1460 (2010)
- [64] K. Fujioka, S. Kato, Y. Hirata; Measurement of effective thermal conductivity of CaCl₂ reactor beds used for driving chemical heat pumps, *J. Chem. Eng. Jpn.*, **31**, 266–272 (1998)
- [65] E. R. T. Bevers, P. J. van Ekeren, W. G. Haije, H. A. J. Oonk; Thermodynamic properties of lithium chloride ammonia complexes for application in a high-lift high temperature chemical heat pump, *J. Therm. Anal. Calorim.*, **86**, 825–832 (2006)
- [66] E. R. T. Bevers, H. A. J. Oonk, W. G. Haije, P. J. van Ekeren; Investigation of thermodynamic properties of magnesium chloride amines by HPDSC and TG for application in a high-lift high-temperature chemical heat pump, *J. Therm. Anal. Calorim.*, **90**, 923–929 (2007)
- [67] N. Hirao; Study on thermochemical energy storages by using metal salt-modified metal oxides, Tokyo Institute of Technology, Master's thesis (2008)
- [68] J. Ryu, N. Hirao, R. Takahashi, Y. Kato; Dehydration behavior of metal-salt-added magnesium hydroxide as chemical heat storage media, *Chem. Lett.*, **37**, 1140–1141 (2008)
- [69] The Chemical Society of Japan ed., Handbook of chemistry (*in Japanese*), fifth ed., Maruzen Publishing, Tokyo, Japan (2004)
- [70] E. H. P. Cordfunke, W. Ouweltjes, P. van Vlaanderen; The standard molar enthalpy of formation of Cs₂ZrO₃, *J. Chem. Thermodyn.*, **19**, 1117–1120 (1987)
- [71] D. F. Shriver, P. W. Atkins; Inorganic chemistry, third ed., Oxford university press, Oxford, U.K. (1999)
- [72] R. Takahashi; Development of materials for thermochemical energy storages which can store exhaust heat at medium temperature, Tokyo Institute of Technology, Master's thesis (2007)
- [73] J. Ryu, R. Takahashi, N. Hirao, Y. Kato; Effect of transition metal mixing on reactivities of magnesium oxide for chemical heat pump, *J. Chem. Eng. Jpn.*, **40**, 1281–1286 (2007)
- [74] K. Tanaka, A. Ozaki; Acid-base properties and catalytic activity of solid surfaces, *J. Catal.*, **8**, 1–7 (1967)
- [75] K. Shibata, T. Kiyoura, J. Kitagawa, T. Sumiyoshi, K. Tanabe; Acidic properties of binary metal oxides, *Bull. Chem. Soc. Jpn.*, **46**, 2985–2988 (1973)
- [76] M. Nagao, H. Hamano, K. Hirata, R. Kumashiro, Y. Kuroda; Hydration process of rare-earth sesquioxides having different crystal structures, *Langmuir*, **19**, 9201–9209 (2003)
- [77] S. S. Batsanov, A. A. Deribas, G. N. Kustovq; Reaction of rare-earth metal oxides with water, *Russ. J. Inorg. Chem.*, **12**, 1206–1207 (1967)
- [78] O. Yamamoto, Y. Takeda, R. Kanno, M. Fushimi; Thermal decomposition and electrical conductivity of M(OH)₃ and MOOH (M = Y, Lamthanide), *Solid State Ionics*, **17**, 107–114 (1985)
- [79] Y. Kato, N. Harada, Y. Yoshizawa; Kinetic feasibility of a chemical heat pump for heat utilization

Chapter 1 General introduction

of high-temperature processes, Appl. Therm. Eng., 19, 239–254 (1999)

[80] Y. Kato, M. Yamada, T. Kanie, Y. Yoshizawa; Calcium oxide/carbon dioxide reactivity in a packed bed reactor of a chemical heat pump for high-temperature gas reactors, *Nucl. Eng. Des.*, **210**, 1–8 (2001)

Chapter 2 Dehydration of lithium chloride-modified magnesium hydroxide

2.1 Introduction

Magnesium hydroxide (Mg(OH)₂) is expected as a thermochemical energy storage material (TCM). Studies on a thermochemical energy storage by using Mg(OH)₂ were performed previously [1–4]. However its technical problem is that the dehydration temperature of Mg(OH)₂ for heat storage operation is at 350–400°C. The dehydration of Mg(OH)₂ corresponds to heat storage operation. As mentioned at **Chapter 1**, the utilization of waste heat at 200–300°C has an impact on thermal energy saving (i.e. recovery of exhaust/surplus heat from steel plants, chemical plants, and light water reactors). Hence, a new material, lithium chloride-modified magnesium hydroxide (LiCl/Mg(OH)₂), was proposed to reduce dehydration temperature [5]. LiCl was expected to accelerate dehydration of Mg(OH)₂ because of its higher hygroscopic property.

Although to obtain rate equations and dehydration kinetic parameters of LiCl/Mg(OH) $_2$ are important to design reactors of thermochemical energy storages (TcES), and decide operation conditions of TcES. There are no kinetic study on dehydration of LiCl/Mg(OH) $_2$. Many theories for the dehydration of Mg(OH) $_2$ have been proposed; one of them is the interface reaction model, which can be expressed as follows:

$$(1-X)^n = 1 - (k't/R)$$
 (2-1)

where X is the conversion of dehydration, k' is the reaction rate constant, t is the reaction time, and R is the initial crystal radius. Eq. (2-1) with n=1/2 (two-dimensional reaction interface model) was proposed by Anderson and Horlock [6], while Gregg and Razouk proposed the same equation with n=1/3 (spherical reaction interface model) [7]. On the other hand, Gordon and Kingery reported that the dehydration of $Mg(OH)_2$ is a first-order reaction [8]. As previously stated, rate equations and kinetic parameters of dehydration of $LiCl/Mg(OH)_2$ are unclear. Thus, the dehydration of $LiCl/Mg(OH)_2$ is studied empirically in this chapter.

In this chapter, $LiCl/Mg(OH)_2$ at various LiCl mixing ratios were prepared. The characterization of $LiCl/Mg(OH)_2$ was performed by scanning electron microscopy, powder X-ray diffraction analysis, and measurement of specific surface area. Then the dehydration rate parameters of authentic $Mg(OH)_2$ (conventional material) and $LiCl/Mg(OH)_2$ were analyzed by thermogravimetry.

2.2 Experimental

2.2.1 Sample preparation

LiCl/Mg(OH)₂ was prepared using an impregnation method. A LiCl aqueous solution was prepared from LiCl·H₂O (99.9%, Wako Pure Chemical Industries, Ltd.) and pure water. Mg(OH)₂ (0.07- μ m diameter, 99.9%, Wako Pure Chemical Industries, Ltd.) was impregnated with the LiCl aqueous solution, evaporated at 40°C using a rotary evaporator, and then dried at 120°C overnight. Dried powder was mixed at agate mortar. The LiCl mixing ratio (α) is defined as follows:

$$\alpha = \frac{\text{amount of LiCl [mol]}}{\text{amount of Mg(OH)}_2 \text{ (or MgO)[mol]}}$$
(2-2)

here, $\alpha = 0$ indicates authentic Mg(OH)₂. A series of LiCl/Mg(OH)₂ with $\alpha = 0.02$, 0.10, 0.30 was prepared.

2.2.2 Characterization techniques

2.2.2.1 Scanning electron microscopy

Scanning electron microscopy (SEM) was performed to identify the microstructures and surface morphologies of the samples. A scanning electron microscope (SM-200, TOPCON Corp.) was used. An acceleration voltage was 8 kV. The samples were pretreated at 120°C for 30 min (or more).

2.2.2.2 Powder X-ray diffraction analysis

Powder X-ray diffraction (XRD) measurements were carried out under atmospheric conditions at room temperature using an X-ray diffractometer (Ultima IV, Rigaku Corp.) through a 2θ range 10° – 90° at a scan speed of 1.0° min⁻¹ using monochromatic CuK α radiation, 40-kV generator voltage, and 40-mA current.

2.2.2.3 Measurements of specific surface area

The nitrogen adsorption isotherm at 77.4 K was measured (Omnisorp 100CX, Beckman Coulter Inc., or Autosorb 1MP, Quantachrome instruments). The specific surface area of the samples was calculated using the BET method. Prior to nitrogen adsorption, the samples were evacuated at 120°C for 30 min (or more) as a pretreatment.

The specific surface area of authentic $Mg(OH)_2$ and $LiCl/Mg(OH)_2$ ($\alpha = 0.10$) were measured by Omnisorp 100CX, and that of $LiCl/Mg(OH)_2$ ($\alpha = 0.02$, 0.30) were measured by Autosorb 1MP.

2.2.3 Dehydration measurement with thermogravimetry

The dehydration profiles of the samples at several temperatures were measured by isothermal method by using a thermobalance (TGD9600, Ulvac-Riko Inc.). The samples were charged in the Pt cell of the balance in a hydroxide form. In this study, the dehydration rate constants were examined with an isothermal method. The dehydration temperatures (T_d) for the samples were analyzed at 5 temperatures: 270, 280, 290, 300 and 320°C for authentic Mg(OH)₂, 250, 270, 280, 290 and 300°C for

LiCl/Mg(OH)₂ ($\alpha = 0.02$), 230, 250, 270, 280 and 300°C for LiCl/Mg(OH)₂ ($\alpha = 0.10$), and 230, 250, 270, 280 and 300°C for LiCl/Mg(OH)₂ ($\alpha = 0.30$). The dehydration was carried out with a heating rate of 20°C min⁻¹ under a 100 mL min⁻¹ of Ar gas flow. Before dehydration, the samples were dried at 120°C for 30 min to remove sorbed water. The mole fraction of Mg(OH)₂ in the MgO and Mg(OH)₂ particles (x) was evaluated from the weight change of the samples as follows:

$$x [mol/mol] = 1 + \frac{\Delta w / M_{H_2O}}{w_{hydroxide} / M_{hydroxide}}$$
 (2-3)

where Δw [kg] is the weight change of the sample, $M_{\rm H2O}$ [kg mol⁻¹] is the molecular weight of water, $w_{\rm hydroxide}$ [kg] is the initial sample weight, and $M_{\rm hydroxide}$ [kg mol⁻¹] is the molecular weight of magnesium hydroxide (Mg(OH)₂). To remove the influence of dehydration during the heating operation until $T_{\rm d}$, a region at $x \le 0.90$ was studied.

2.3 Results

2.3.1 Characterization of the samples

2.3.1.1 Surface morphology of lithium chloride-modified magnesium hydroxide

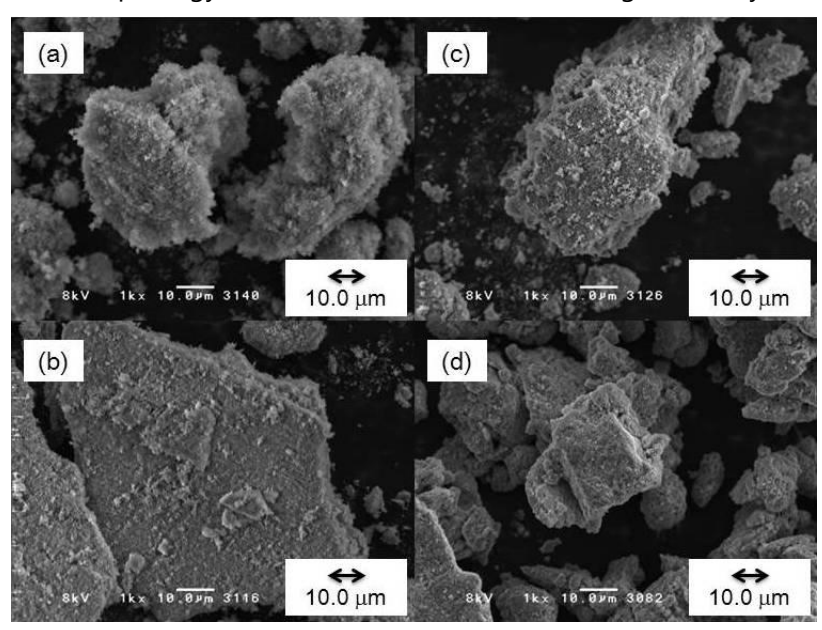


Figure 2.3-1 SEM micrographs of authentic Mg(OH)₂, and LiCl/Mg(OH)₂ (α = 0.02, 0.10, 0.30). The graph is magnified a 1000 times. (a) authentic Mg(OH)₂, (b) LiCl/Mg(OH)₂ (α = 0.02), (c) LiCl/Mg(OH)₂ (α = 0.10), and (d) LiCl/Mg(OH)₂ (α = 0.30).

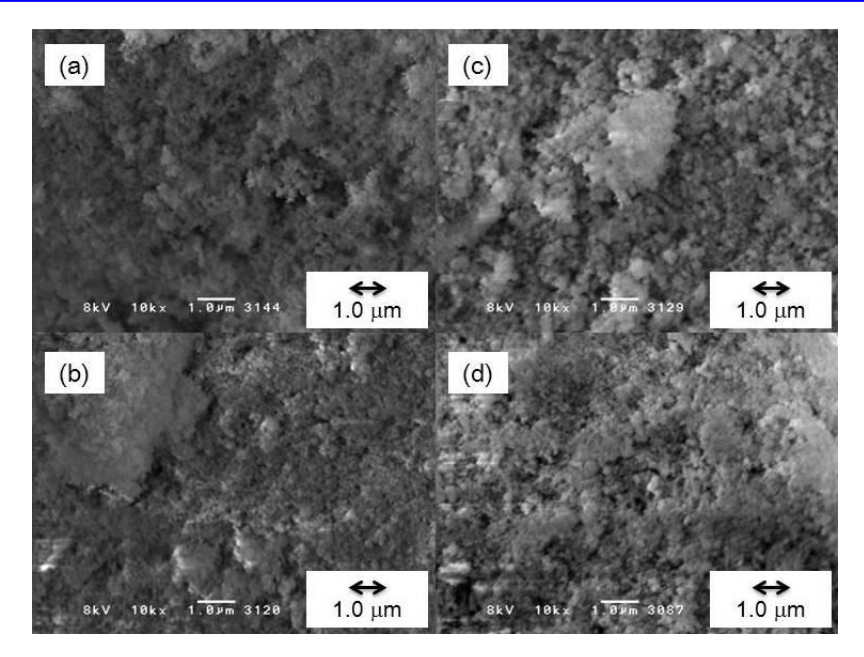


Figure 2.3-2 SEM micrographs of authentic Mg(OH)₂, and LiCl/Mg(OH)₂ (α = 0.02, 0.10, 0.30). The graph is magnified a 10000 times. (a) authentic Mg(OH)₂, (b) LiCl/Mg(OH)₂ (α = 0.02), (c) LiCl/Mg(OH)₂ (α = 0.10), and (d) LiCl/Mg(OH)₂ (α = 0.30).

SEM micrographs of authentic $Mg(OH)_2$, and $LiCl/Mg(OH)_2$ ($\alpha = 0.02, 0.10, 0.30$) are shown in **Figure 2.3-1** and **Figure 2.3-2**. The needle-like crystals of LiCl were not found from these micrographs. This result indicates that the LiCl was highly dispersed on the $Mg(OH)_2$ particle.

2.3.1.2 Crystal structure of lithium chloride-modified magnesium hydroxide

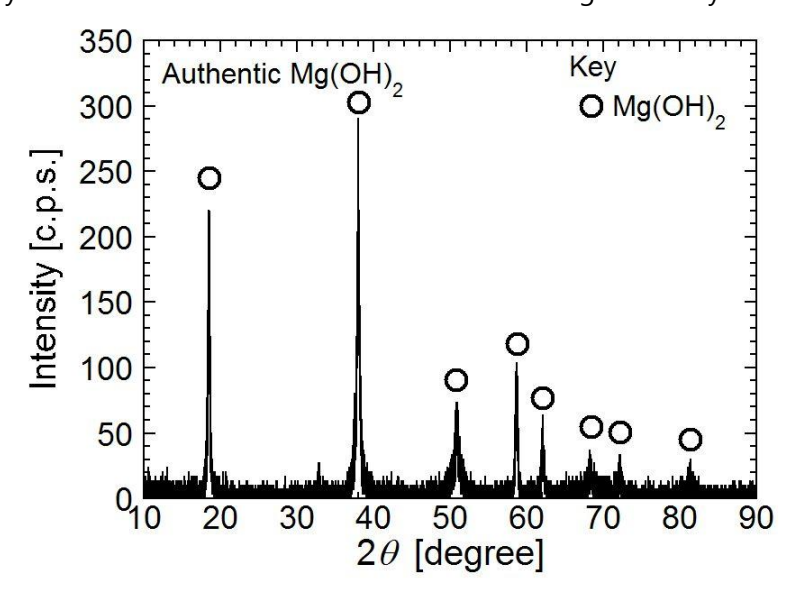


Figure 2.3-3 XRD pattern of authentic Mg(OH)₂. (\circ) indicates reference peak of Mg(OH)₂ (ICDD 10830114).

XRD pattern of authentic $Mg(OH)_2$ are shown in **Figure 2.3-3**. The characteristic peaks of $Mg(OH)_2$ were identified.

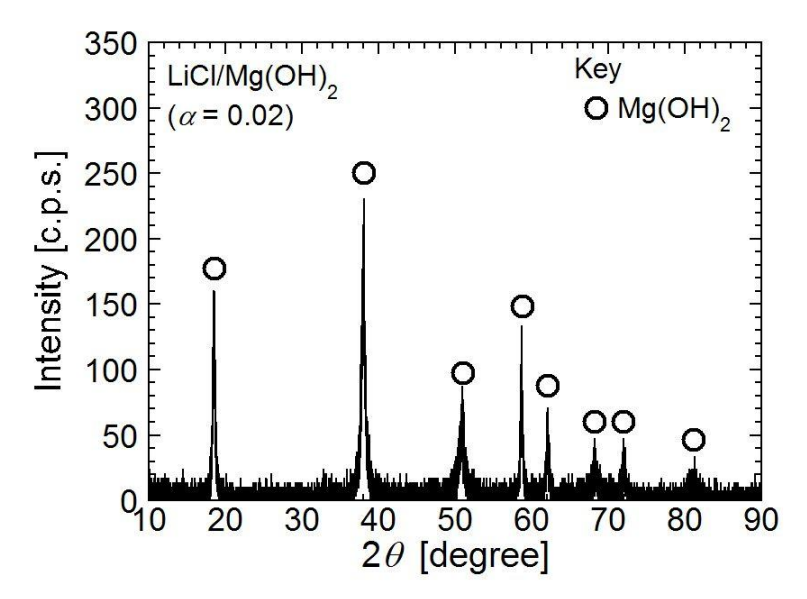


Figure 2.3-4 XRD pattern of LiCl/Mg(OH)₂ ($\alpha = 0.02$). (\circ) indicates reference peak of Mg(OH)₂ (ICDD 10830114).

XRD pattern of LiCl/Mg(OH)₂ ($\alpha = 0.02$) are shown in **Figure 2.3-4**. The characteristic peaks of Mg(OH)₂ were identified.

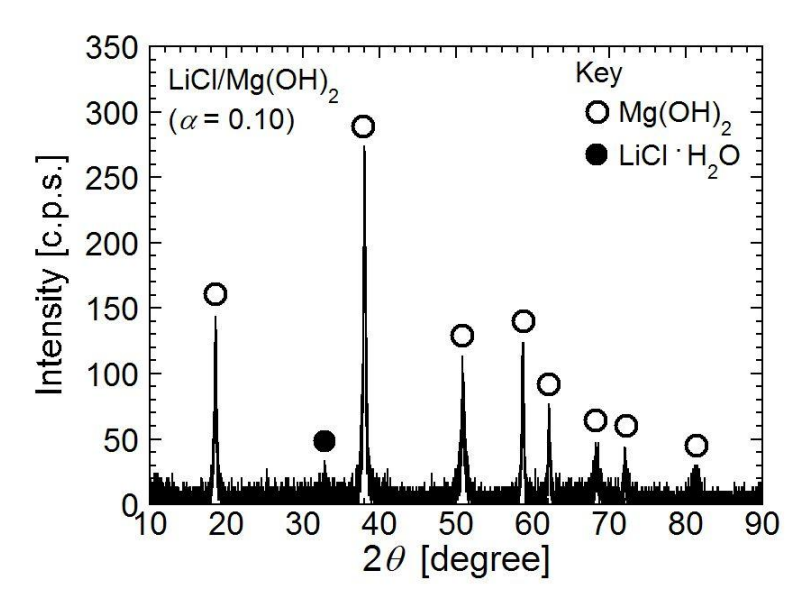


Figure 2.3-5 XRD pattern of LiCl/Mg(OH)₂ (α = 0.10). (\circ) indicates reference peak of Mg(OH)₂ (ICDD 10830114), and (\bullet) indicates reference peak of LiCl·H₂O (ICDD 221142).

XRD pattern of LiCl/Mg(OH)₂ ($\alpha = 0.10$) are shown in **Figure 2.3-5**. The characteristic peaks of Mg(OH)₂ and LiCl·H₂O were identified.

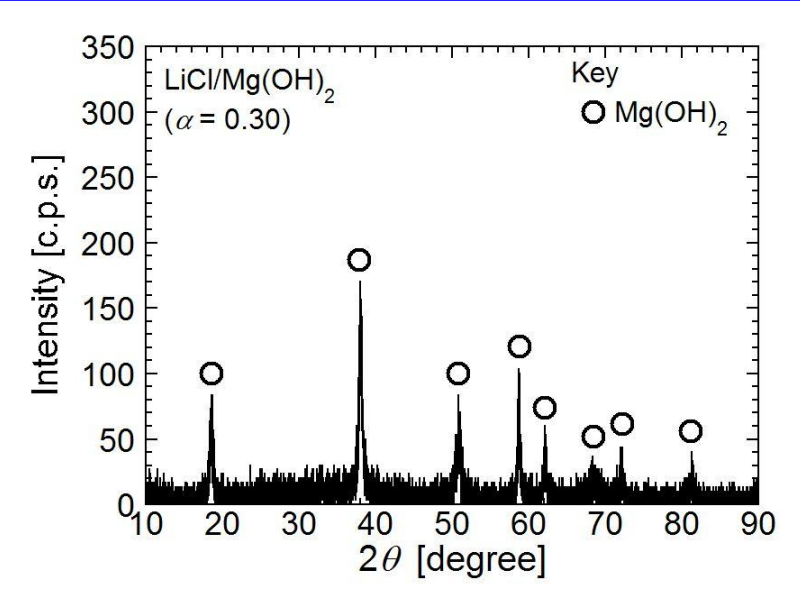


Figure 2.3-6 XRD pattern of LiCl/Mg(OH)₂ ($\alpha = 0.30$). (\circ) indicates reference peak of Mg(OH)₂ (ICDD 10830114).

XRD pattern of LiCl/Mg(OH)₂ ($\alpha = 0.30$) are shown in **Figure 2.3-6**. The characteristic peaks of Mg(OH)₂ were identified.

The brucite structure of Mg(OH)₂ was not affected by the LiCl-modification.

2.3.1.3 Specific surface area of lithium chloride-modified magnesium hydroxide

Table 2.3-1 Specific surface area of the samples at various LiCl mixing molar ratio ($\alpha = 0-0.30$).

LiCl mixing molar ratio (α)	[mol/mol]	0*	0.02	0.10	0.30
Specific surface area	$[m^2 g^{-1}]$	35.4	36.2	24.6	19.7

^{*} α = 0 indicates the authentic Mg(OH)₂.

Specific surface area of the samples at various LiCl mixing molar ratio ($\alpha = 0$ –0.30) are shown in **Table 2.3-1**. For LiCl/Mg(OH)₂ ($\alpha = 0.02$ –0.30) samples, specific surface area decreased from 36.2 m² g⁻¹ to 19.7 m² g⁻¹ with higher α .

2.3.2 Dehydration measurement with thermogravimetry

2.3.2.1 The relationship between temperature and dehydration rate

Dehydration profile for authentic $Mg(OH)_2$ at $T_d = 270-320$ °C are shown in **Figure 2.3-7** with calculated profiles which derived by kinetic analysis at **Section 2.4**.. The dehydration profiles were convex downward curve. The dehydration rate became faster with higher dehydration temperature (T_d) .

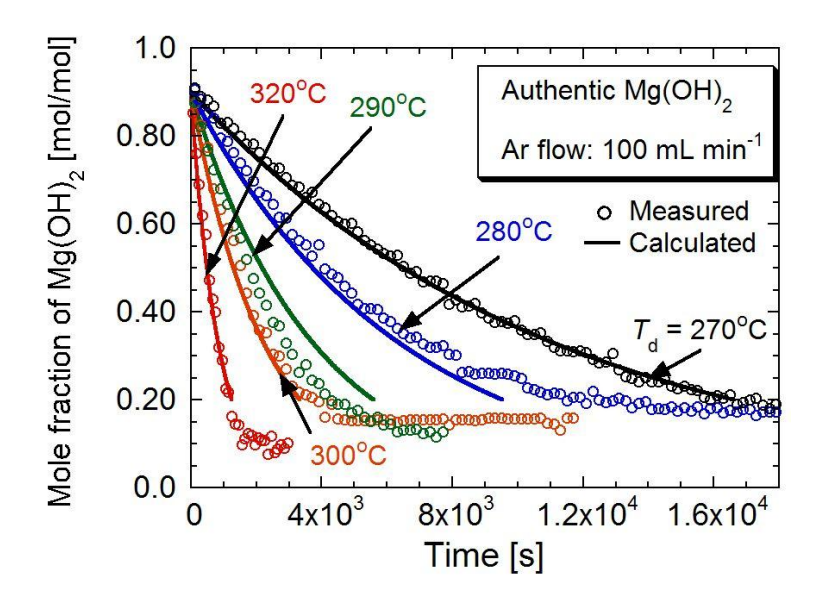


Figure 2.3-7 Dehydration profiles for authentic Mg(OH)₂ at $T_d = 270-320$ °C. Calculated profiles are obtained at **Section 2.4.** Red line: calculated line at 320°C, orange line: calculated line at 300°C, green line: calculated line at 290°C, blue line: calculated line at 280°C, black line: calculated line at 270°C, respectively.

Dehydration profile for LiCl/Mg(OH)₂ ($\alpha = 0.02$) at $T_{\rm d} = 250{\text -}300^{\circ}{\rm C}$ are shown in **Figure 2.3-8** with calculated profiles which derived by kinetic analysis at **Section 2.4**. The dehydration profiles were convex downward curve. The dehydration rate became faster with higher dehydration temperature ($T_{\rm d}$).

Dehydration profile for LiCl/Mg(OH)₂ ($\alpha = 0.10$) at $T_{\rm d} = 230$ –300°C are shown in **Figure 2.3-9** and at high temperatures of $T_{\rm d} = 270$ –300°C are shown in **Figure 2.3-10** with calculated profiles which derived by kinetic analysis at **Section 2.4**. The dehydration profiles were linear at 0.40 mol/mol $\leq x \leq 0.90$ mol/mol, and convex downward curve at $x \leq 0.30$ mol/mol. The dehydration rate became faster with higher dehydration temperature ($T_{\rm d}$). An area at 0.30 mol/mol $\leq x \leq 0.40$ mol/mol would be a transition region of these two processes. LiCl/Mg(OH)₂ ($\alpha = 0.10$) reached x = 0.10 for 8.2×10^3 s (≈ 2.3 h) at 250°C and for 7.2×10^2 s (≈ 0.2 h) at 300°C. LiCl/Mg(OH)₂ ($\alpha = 0.10$) can store thermal energy practically at 250–300°C.

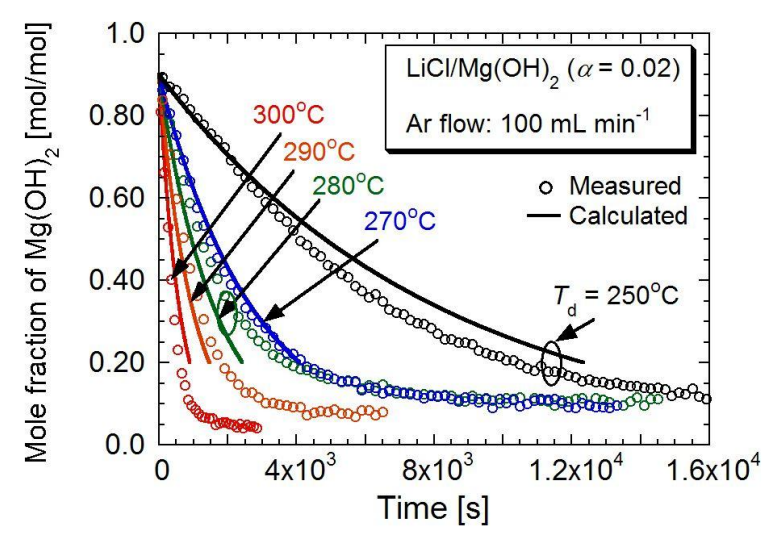


Figure 2.3-8 Dehydration profiles for LiCl/Mg(OH)₂ ($\alpha = 0.02$) at $T_{\rm d} = 250$ –300°C. Calculated profiles are obtained at **Section 2.4.** Red line: calculated line at 300°C, orange line: calculated line at 290°C, green line: calculated line at 280°C, blue line: calculated line at 270°C, black line: calculated line at 250°C, respectively.

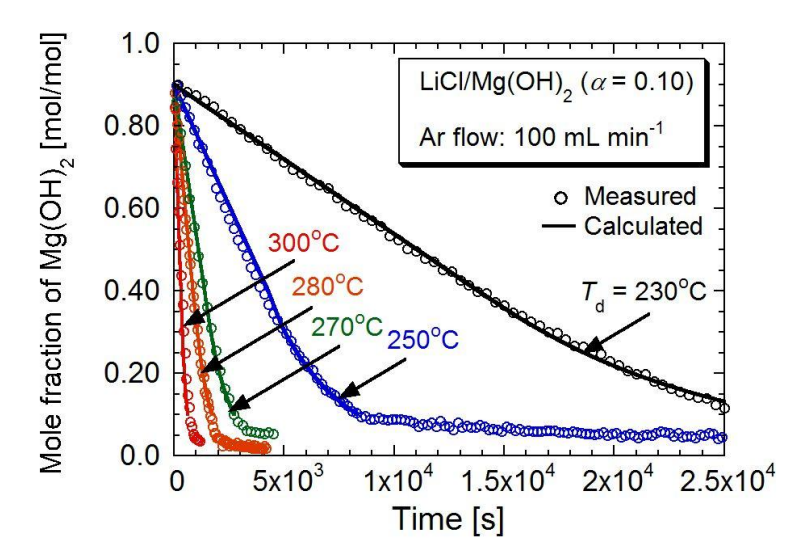


Figure 2.3-9 Dehydration profiles for LiCl/Mg(OH)₂ ($\alpha = 0.10$) at $T_{\rm d} = 230$ –300°C. Calculated profiles are obtained at **Section 2.4.** Red line: calculated line at 300°C, orange line: calculated line at 280°C, green line: calculated line at 270°C, blue line: calculated line at 250°C, black line: calculated line at 230°C, respectively.

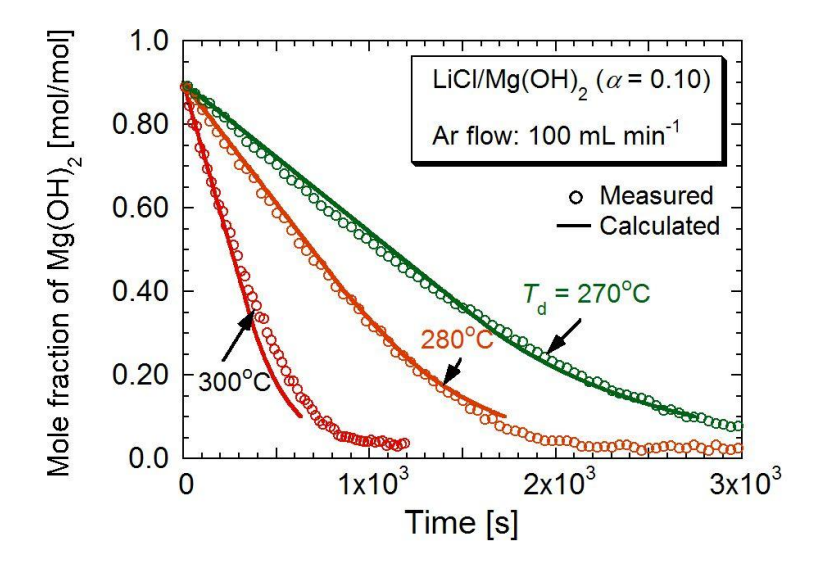


Figure 2.3-10 Dehydration profiles for LiCl/Mg(OH)₂ (α = 0.10) at high temperatures of T_d = 270–300°C. Calculated profiles are obtained at **Section 2.4.** Red line: calculated line at 300°C, orange line: calculated line at 280°C, green line: calculated line at 270°C, respectively.

Dehydration profile for LiCl/Mg(OH)₂ ($\alpha = 0.30$) at $T_{\rm d} = 230{\text -}300^{\circ}{\rm C}$ are shown in **Figure 2.3-11** and at high temperatures of $T_{\rm d} = 270{\text -}300^{\circ}{\rm C}$ are shown in **Figure 2.3-12** with calculated profiles which derived by kinetic analysis at **Section 2.4**. The dehydration profiles were linear at 0.40 mol/mol $\leq x \leq 0.90$ mol/mol, and convex downward curve at $x \leq 0.30$ mol/mol. The dehydration rate became faster with higher dehydration temperature ($T_{\rm d}$). An area at 0.30 mol/mol $\leq x \leq 0.40$ mol/mol would be a transition region of these two processes.

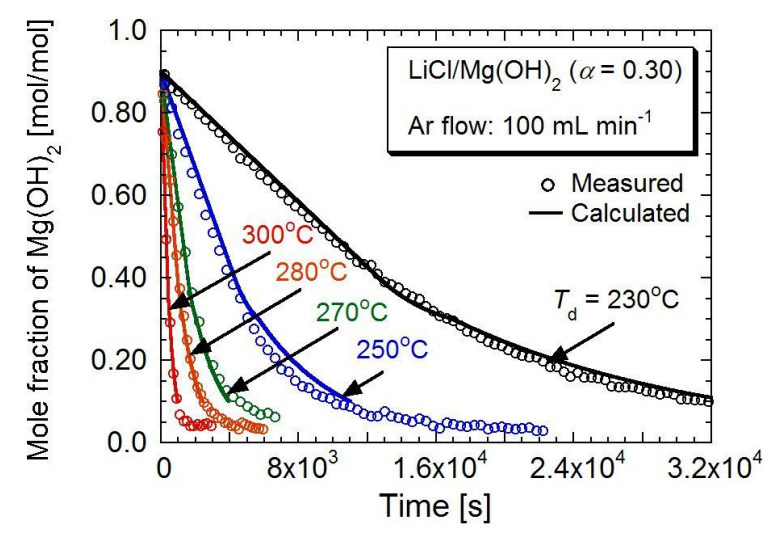


Figure 2.3-11 Dehydration profiles for LiCl/Mg(OH)₂ ($\alpha = 0.30$) at $T_d = 230$ –300°C. Calculated profiles are obtained at **Section 2.4.** Red line: calculated line at 300°C, orange line: calculated line at 280°C, green line: calculated line at 270°C, blue line: calculated line at 250°C, black line: calculated line at 230°C, respectively.

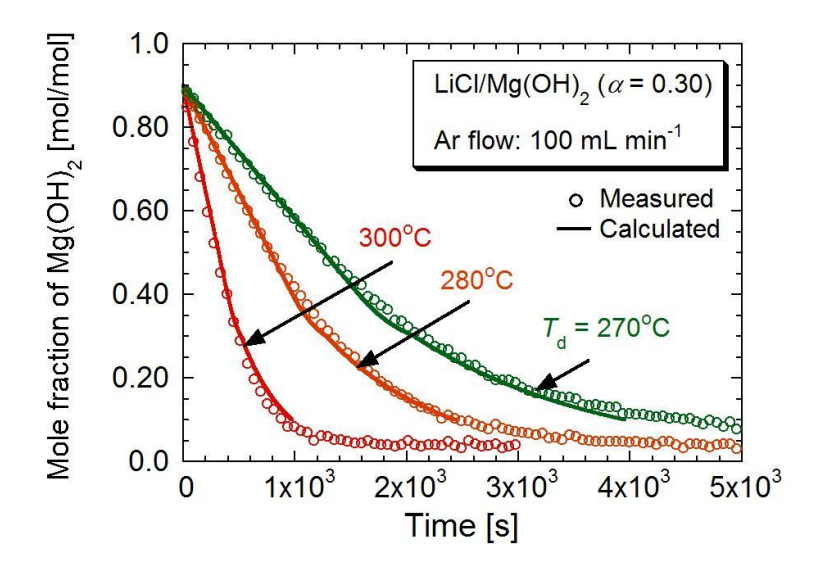


Figure 2.3-12 Dehydration profiles for LiCl/Mg(OH)₂ (α = 0.30) at high temperatures of $T_{\rm d}$ = 270–300°C. Calculated profiles are obtained at **Section 2.4.** Red line: calculated line at 300°C, orange line: calculated line at 280°C, green line: calculated line at 270°C, respectively.

2.3.2.2 The relationship between lithium chloride mixing ratio and dehydration rate

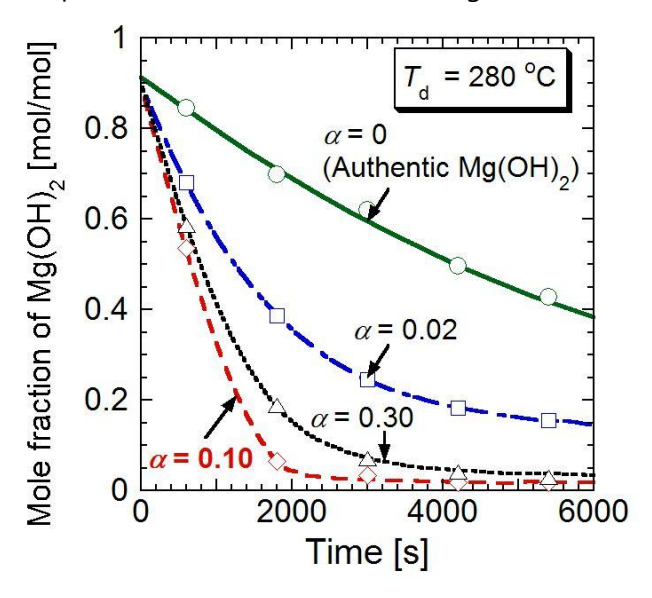


Figure 2.3-13 The dehydration profiles for authentic Mg(OH)₂ and LiCl/Mg(OH)₂ (α = 0.02, 0.10, 0.30) at 280°C.

Figure 2.3-13 describes the dehydration profile for authentic Mg(OH)₂ and LiCl/Mg(OH)₂ (α = 0.02, 0.10, 0.30) at 280°C. LiCl/Mg(OH)₂ (α = 0.10) has the fastest dehydration rate among the four samples. It is concluded that α of 0.10 was the optimum value for dehydration.

2.4 Discussion

2.4.1 Dehydration model

2.4.1.1 Authentic magnesium hydroxide and lithium chloride-modified magnesium hydroxide (α = 0.02)

The mole fraction of $Mg(OH)_2(x)$ showed convex downward curve (decreased in proportion to inverse exponential) with the reaction time (**Figure 2.3-7** and **Figure 2.3-8**). The typical dehydration rate equations (integrated form) which were submitted previously are summarized in **Table 2.4-1** [9].

Table 2.4-1 Typical dehydration rate equations (integrated form) [9].

First-order reaction	Mampel Equation	Jander equation	
(Homogeneous reaction model)	(Interface reaction model)	(Diffusion controlled model)	
$ \ln x = -kt $	$1 - x^{1/n} = \frac{kt}{R}$	$\left(1-x^{1/3}\right)^2 = \frac{kt}{R^2}$	

Here, $k [s^{-1}, m^{-1} s^{-1}, or m^{-2} s^{-1}]$ is a rate constant, and R is a radius of solid reactant. The relationships between time and function of x are shown in Figure 2.4-1. Then, linearity of each plot is evaluated. Squared correlation coefficients (R^2) for each model are shown in **Table 2.4-2**. The plot of first-order reaction shows best linearity ($R^2 = 0.996$). Thus, first-order reaction is thought to be appropriate to analyze the dehydration rate of authentic Mg(OH)₂.

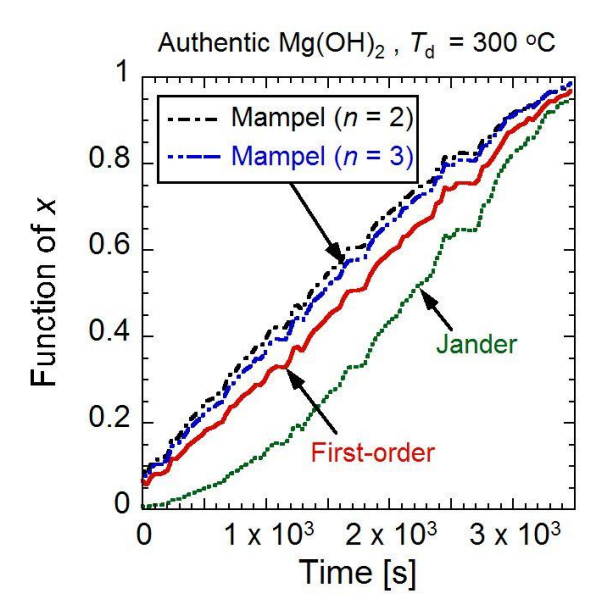


Figure 2.4-1 Relationships between time and function of x (first-order reaction, Mampel equation, and Jander equation) for dehydration of authentic Mg(OH)₂ at 300°C.

Table 2.4-2 Squared correlation coefficients for first-order reaction, Mampel equation, and Jander equation for dehydration of authentic Mg(OH)₂ at 300°C.

	First-order reaction	Mampel Equation Mampel Equation		Jander equation	
	Trist-order reaction	(n = 2)	(n = 3)	Januer equation	
R^2	0.996	0.989	0.993	0.969	

In this work, the dehydration rate constants were evaluated employing an integration method. A rate of the first-order dehydration is written as follows:

$$-\frac{dx}{dt} = k_{\rm f} x \tag{2-4}$$

where t is the reaction time [s], and k_f is the rate constant of first-order reaction [s⁻¹]. Eq. (2-4) can be integrated by the initial condition ($t = t_0$, x = 0.90) to yield Eq. (2-5) as follows:

$$\ln x = -k_{\rm f}t - 0.105\tag{2-5}$$

Because dehydration proceeded partially during the heating process until desired temperature, thus, x = 0.90 was selected as the initial period for kinetic analysis to avoid the effect of dehydration during the heating process. From Eq. (2-5), it is evident that the rate constant, $k_{\rm f}$, corresponds to the slope of the plot of t vs. $\ln x$.

A dehydration profile for authentic Mg(OH)₂ at 300°C is shown in **Figure 2.4-2**. The dehydration profile was convex downward curve. **Figure 2.4-3** describes a dehydration rate analysis plot of authentic Mg(OH)₂ based on Eq. (2-5). The dehydration rate analysis plot showed linearity in the in the region of 0.20 mol/mol $\le x \le 0.90$ mol/mol, that is, $-1.6 \le \ln x \le -0.11$. The assumptions made held in the region of 0.20 mol/mol $\le x \le 0.90$ mol/mol. The dehydration analysis plots did not show linearity in the region of x < 0.20 mol/mol ($\ln x < -1.6$) because dehydration was saturated at around x = 0.15 ($\ln x = -1.9$) (**Figure 2.4-2**). The authentic Mg(OH)₂ showed similar behaviors in the temperatures of 270–320°C. From **Figure 2.4-3**, the dehydration rate constant, k_f , at 300°C was calculated to be 4.18×10^{-4} s⁻¹.

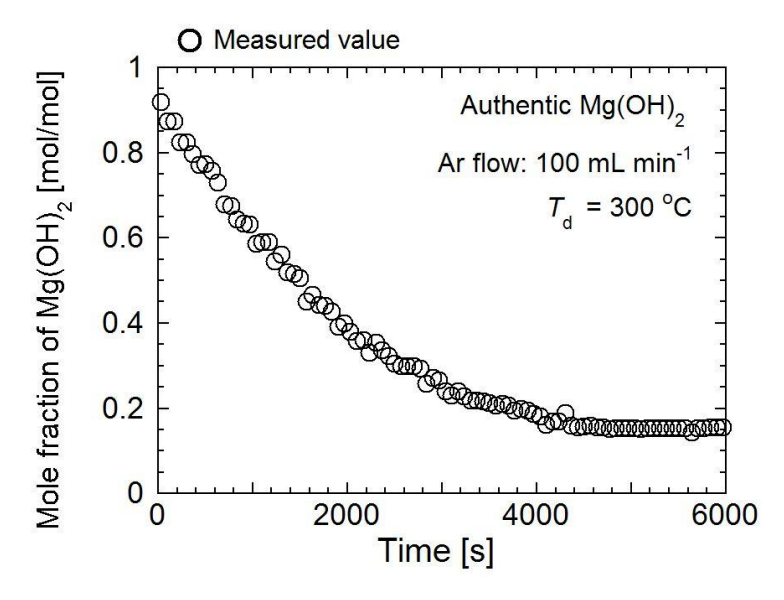


Figure 2.4-2 Dehydration profile for authentic Mg(OH)₂ at 300°C.

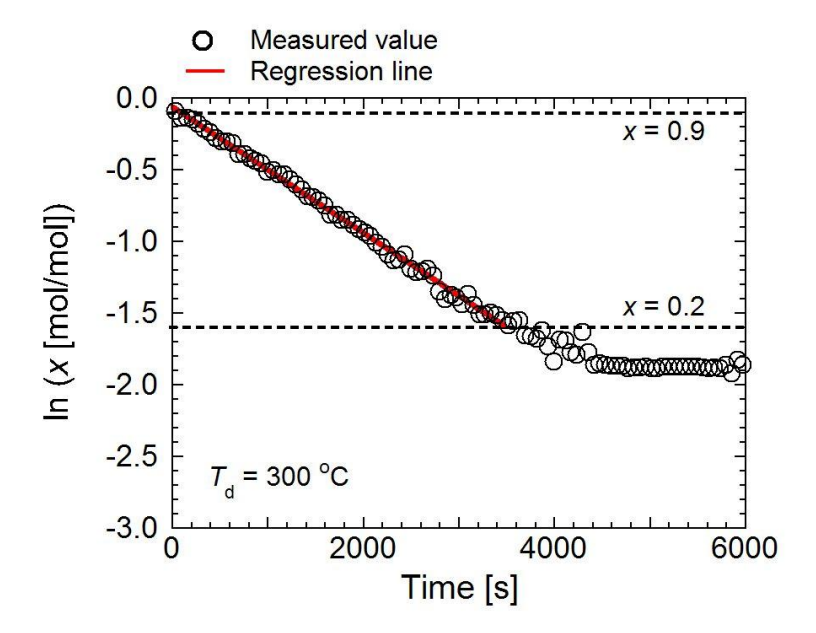


Figure 2.4-3 Dehydration rate analysis plot for authentic Mg(OH)₂ at 300°C.

A dehydration profile for LiCl/Mg(OH)₂ (α = 0.02) at 300°C is shown in **Figure 2.4-4**. The dehydration profile was convex downward curve. **Figure 2.4-5** describes a dehydration rate analysis plot of LiCl/Mg(OH)₂ (α = 0.02) based on Eq. (2-5). The dehydration rate analysis plot showed linearity in the in the region of 0.20 mol/mol $\leq x \leq$ 0.90 mol/mol (-1.6 \leq ln $x \leq$ -0.11). The assumption was applied in the region of 0.20 mol/mol $\leq x \leq$ 0.90 mol/mol. The LiCl/Mg(OH)₂ (α = 0.02) showed similar behaviors in the temperatures of 250–300°C. From **Figure 2.4-5**, the dehydration rate constant, $k_{\rm f}$, at 300°C was calculated to be 2.55 \times 10⁻³ s⁻¹.

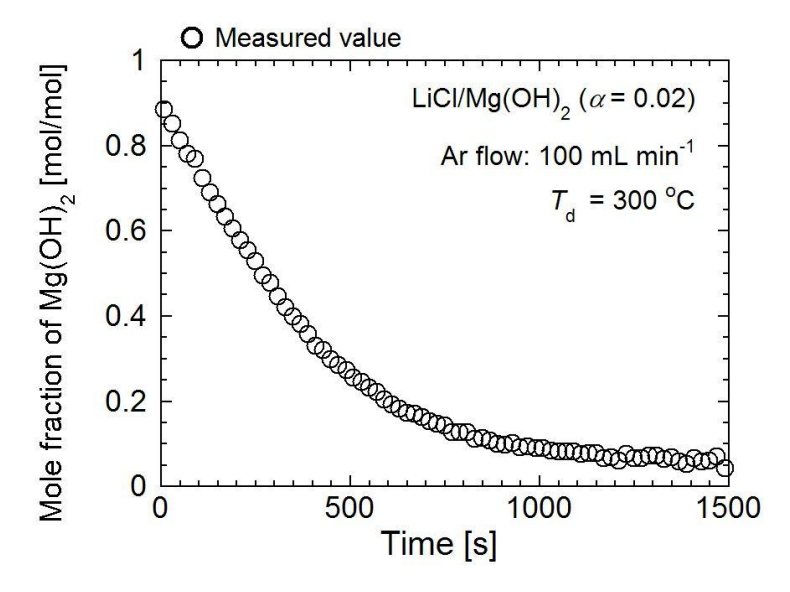


Figure 2.4-4 Dehydration profile for LiCl/Mg(OH)₂ (α = 0.02) at 300°C.

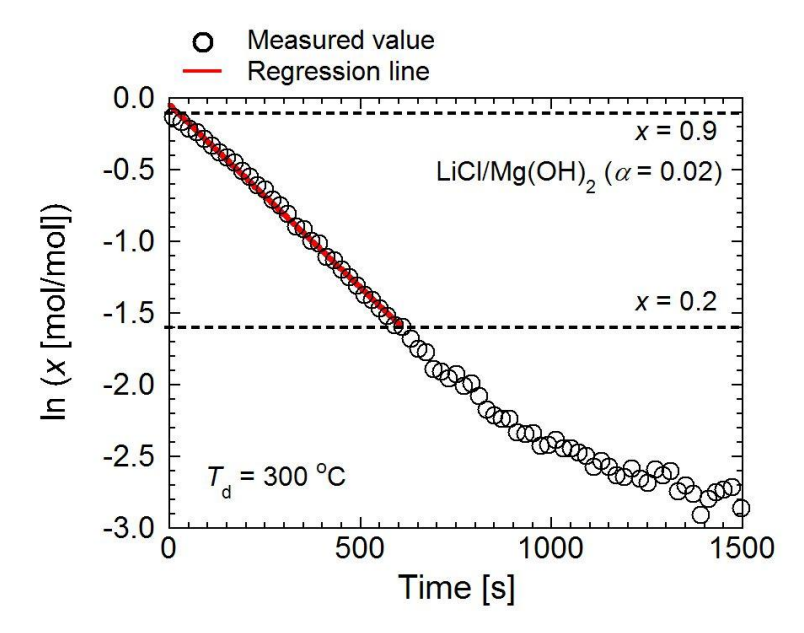


Figure 2.4-5 Dehydration rate analysis plot for LiCl/Mg(OH)₂ (α = 0.02) at 300°C.

2.4.1.2 Lithium chloride modified magnesium hydroxide (α = 0.10, 0.30)

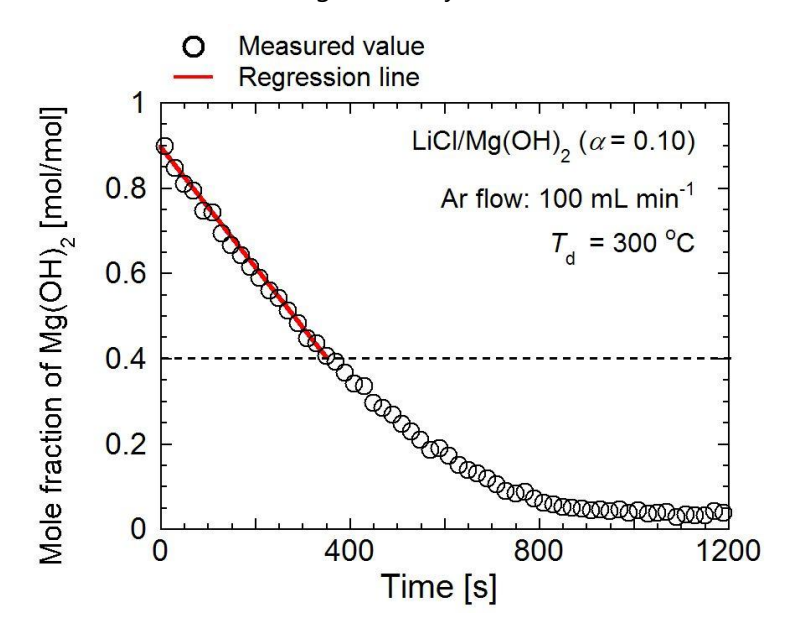


Figure 2.4-6 Dehydration profile for LiCl/Mg(OH)₂ (α = 0.10) at 300°C.

A dehydration profile for LiCl/Mg(OH)₂ ($\alpha = 0.10$) at 300°C is shown in **Figure 2.4-6**. As previously stated, the mole fraction of Mg(OH)₂ decreased linearly in the region of 0.40 mol/mol $\leq x \leq$ 0.90 mol/mol (**Figure 2.4-6**). Therefore, the process in this region was independent of the mole fraction of Mg(OH)₂. In this region, the dehydration rate equation can be written as follows:

$$-\frac{dx}{dt} = k_{z} \tag{2-6}$$

where k_z is the rate constant of the process (zero-order reaction) [s⁻¹]. The dehydration rate constant in the region of 0.40 mol/mol $\le x \le 0.90$ mol/mol at 300°C was calculated to be 1.46 \times 10⁻³ s⁻¹. The formed H₂O was passed at LiCl layer. This process would be related with the H₂O diffusion in LiCl layer.

A dehydration rate analysis plot of LiCl/Mg(OH)₂ (α = 0.10) based on Eq. (2-5) is shown in **Figure 2.4-7**. The rate analysis plot showed inflection points at around $\ln x = -1.2$ (x = 0.3) and at around $\ln x = -2.3$ (x = 1.2). A linear trend was observed in the region of 0.10 mol/mol $\leq x \leq 0.30$ mol/mol ($-2.3 \leq \ln x \leq -1.2$). At the region, first-order dehydration of Mg(OH)₂ was a rate controlling process of the overall dehydration rate. The dehydration behavior of LiCl/Mg(OH)₂ (α = 0.10) at temperatures of 230°C–300°C showed the same tendency. From **Figure 2.4-7**, the dehydration rate constant in the region of 0.10 mol/mol $\leq x \leq 0.30$ mol/mol ($-2.3 \leq \ln x \leq -1.2$) at 300°C was calculated to 4.04×10^{-3} s⁻¹. In this region, the dehydration of Mg(OH)₂ is a first-order reaction.

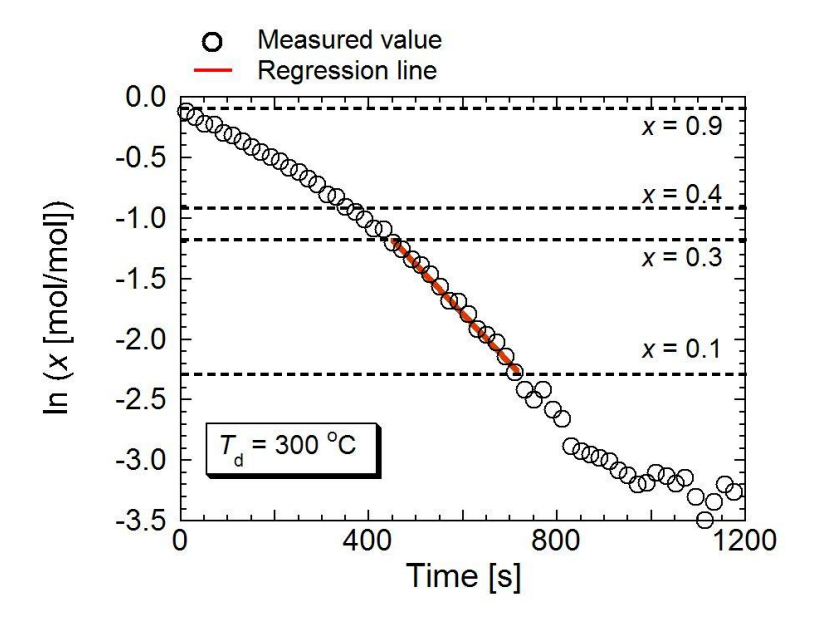


Figure 2.4-7 Dehydration rate analysis plot for LiCl/Mg(OH)₂ (α = 0.10) at 300°C.

According to these results, the dehydration of LiCl/Mg(OH)₂ (α = 0.10) can be separated into two steps: First step (0.40 mol/mol $\leq x \leq$ 0.90 mol/mol) is the zero-order dehydration of Mg(OH)₂ because the mole fraction of Mg(OH)₂ decreased linearly in the region of 0.40 mol/mol $\leq x \leq$ 0.90 mol/mol (**Figure 2.4-6**). Second step (0.10 mol/mol $\leq x \leq$ 0.30 mol/mol) is the first-order dehydration of Mg(OH)₂ (based on Eq. (2-4)) because the rate analysis plot showed linear trend at the region (**Figure 2.4-7**). The region for first-order dehydration of Mg(OH)₂ was different between LiCl/Mg(OH)₂ (α = 0.02) (0.20 mol/mol $\leq x \leq$ 0.90 mol/mol) and LiCl/Mg(OH)₂ (α = 0.10) (0.10 mol/mol $\leq x \leq$ 0.30 mol/mol). It was inferred that the surface modification was not enough significant when α < 0.10 (**Section 2.3.2.2**). Thus, H₂O diffusion resistance in LiCl layer or H₂O desorption from LiCl is not rate controlling step for LiCl/Mg(OH)₂ (α = 0.02). On the other hand, enough LiCl-modification for LiCl/Mg(OH)₂ (α = 0.10) would accelerate first-order dehydration of Mg(OH)₂ , but H₂O diffusion in LiCl layer or H₂O desorption from LiCl would be rate controlling process in the region of 0.40 mol/mol $\leq x \leq$ 0.90 mol/mol.

Similarly, the dehydration of LiCl/Mg(OH)₂ (α = 0.30) can be separated into two steps: step 1 (0.40 mol/mol $\leq x \leq$ 0.90 mol/mol) is the zero-order dehydration of Mg(OH)₂, and step 2 (0.10 mol/mol $\leq x \leq$ 0.30 mol/mol) is the first-order dehydration of Mg(OH)₂. A dehydration profile for LiCl/Mg(OH)₂ (α = 0.30) at 300°C is shown in **Figure 2.4-8**. The dehydration rate constant of zero-order dehydration, k_z , at 300°C was calculated to be 1.30 × 10⁻³ s⁻¹. A dehydration rate analysis plot of LiCl/Mg(OH)₂ (α = 0.30) based on Eq. (2-5) is shown in **Figure 2.4-9**. A linear trend was observed again in the region of 0.10 mol/mol $\leq x \leq$ 0.30 mol/mol (-2.3 \leq ln $x \leq$ -1.2). The dehydration behavior of LiCl/Mg(OH)₂ (α = 0.30) at temperatures of 230°C-300°C showed the same tendency. From **Figure 2.4-9**, the dehydration rate constant of first-order dehydration at 300°C was calculated to 2.77 × 10⁻³ s⁻¹.

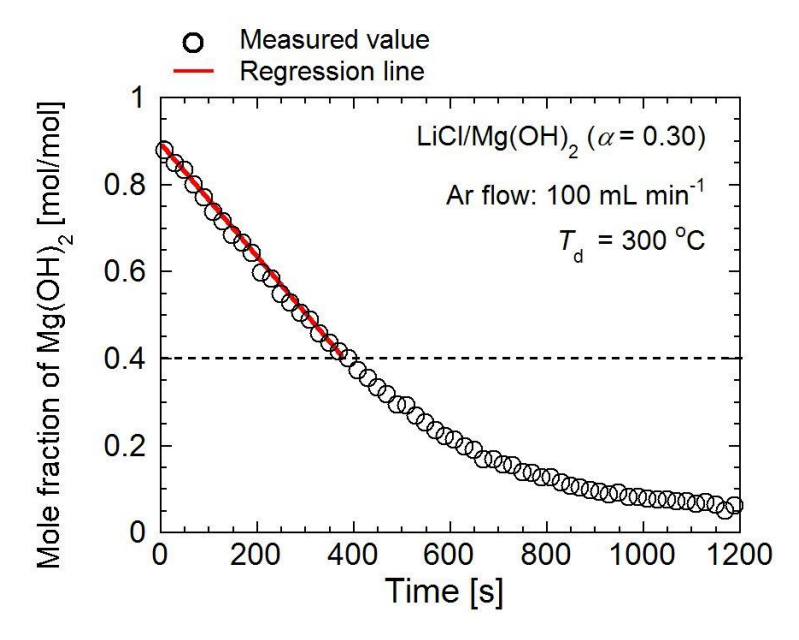


Figure 2.4-8 Dehydration profile for LiCl/Mg(OH)₂ (α = 0.30) at 300°C.

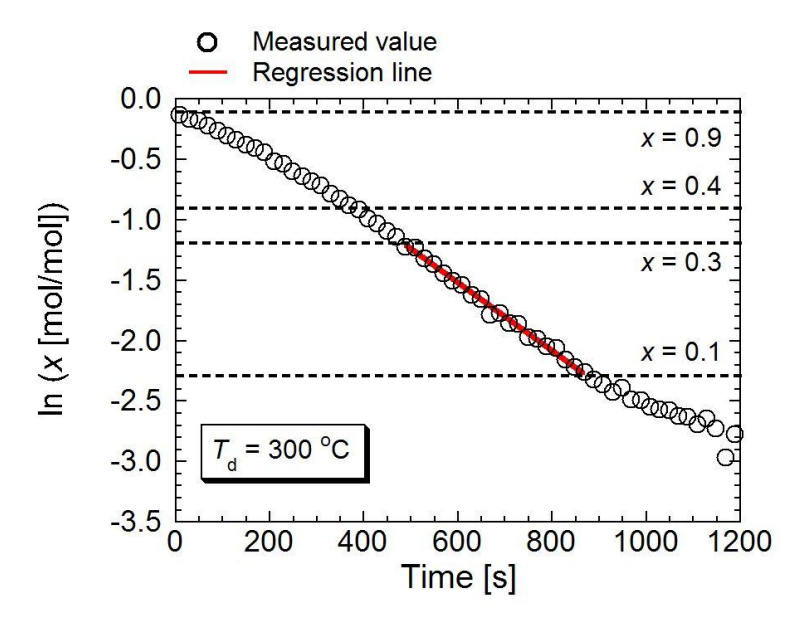


Figure 2.4-9 Dehydration rate analysis plot for LiCl/Mg(OH)₂ ($\alpha = 0.30$) at 300°C.

2.4.2 Arrhenius parameters for dehydration rate

In this work, Arrhenius-type temperature dependence on rate constants is assumed as follows.

$$k_{\rm f} = k_{\rm f0} \, \exp\left(\frac{-E_{\rm af}}{RT}\right) \tag{2-7}$$

$$k_{z} = k_{z0} \exp\left(\frac{-E_{az}}{RT}\right) \tag{2-8}$$

Here, k_{f0} [s⁻¹] and k_{z0} [s⁻¹] are pre-exponential factors, E_{af} [kJ mol⁻¹] and E_{zf} [kJ mol⁻¹] are activation

energies, R [J K⁻¹ mol⁻¹] is a gas constant, and T [K] indicates absolute temperature.

The Arrhenius plot of the rate constants for the dehydration at several temperatures are shown in Figure 2.4-10 and Figure 2.4-11. Table 2.4-3 and

Table 2.4-4 describes pre-exponential factors and activation energies of authentic Mg(OH)₂ and LiCl/Mg(OH)₂ (α = 0.02. 0.10, 0.30) that were derived from **Figure 2.4-10** and **Figure 2.4-11**. Here, the region of x for first-order reaction is 0.2 mol/mol $\leq x \leq$ 0.9 mol/mol for authentic Mg(OH)₂ and LiCl/Mg(OH)₂ (α = 0.02), and 0.1 mol/mol $\leq x \leq$ 0.3 mol/mol for LiCl/Mg(OH)₂ (α = 0.10, 0.30). The region of x for zero-order reaction is 0.4 mol/mol $\leq x \leq$ 0.9 mol/mol for LiCl/Mg(OH)₂ (α = 0.10, 0.30). Gordon and Kingery reported that the activation energy of the dehydration for 325 mesh brucite powder *in vacuo* was 125 kJ mol⁻¹ [8], whereas the activation energy of authentic Mg(OH)₂ in this study was 139 kJ mol⁻¹. Hence, the result in this chapter appears to be reasonable. As shown in **Table 2.4-3**, the activation energies of the first-order dehydration of Mg(OH)₂ were decreased by surface modification on Mg(OH)₂ particles. It can be seen that the activation energy of the first-order dehydration decreased by 8.2% for LiCl/Mg(OH)₂ (α = 0.10) compared with authentic Mg(OH)₂.

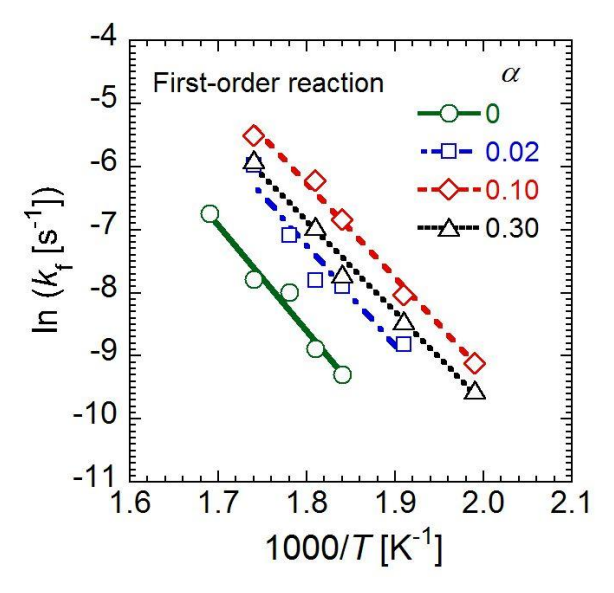


Figure 2.4-10 Arrhenius plots of the dehydration rate constants (first-order reaction). $\alpha = 0$ indicates the authentic Mg(OH)₂.

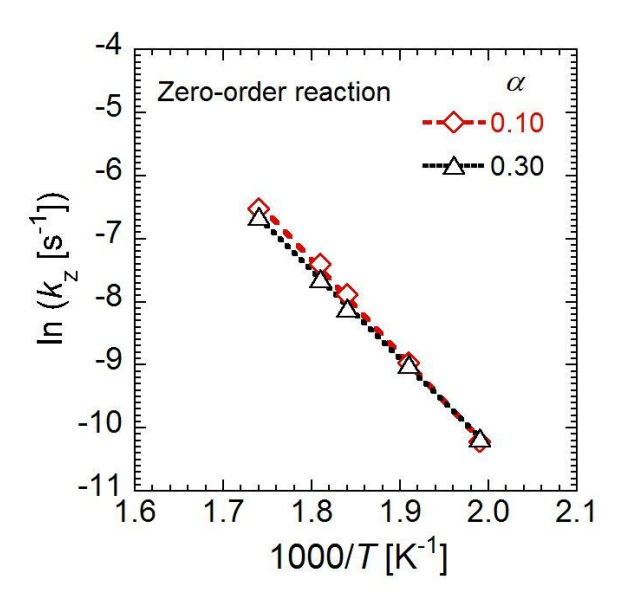


Figure 2.4-11 Arrhenius plots of the dehydration rate constants (zero-order reaction).

Table 2.4-3 Pre-exponential factors (k_{f0}) and activation energies (E_{af}) of first-order reaction for authentic Mg(OH)₂ and LiCl/Mg(OH)₂ ($\alpha = 0.02, 0.10, 0.30$) for dehydration.

	The region of x [mol/mol]	$k_{\mathrm{f0}}[\mathrm{s}^{-1}]$	$E_{\rm af}$ [kJ mol ⁻¹]
Authentic Mg(OH) ₂	0.2 < < 0.0	1.90×10^{9}	139
$LiCl/Mg(OH)_2 (\alpha = 0.02)$	$0.2 \le x \le 0.9$	1.26×10^{9}	130
$LiCl/Mg(OH)_2 (\alpha = 0.10)$	0.1 < < 0.2	1.74×10^{9}	127
$LiCl/Mg(OH)_2 (\alpha = 0.30)$	$0.1 \le x \le 0.3$	3.70×10^{8}	123

Table 2.4-4 Pre-exponential factors (k_{z0}) and activation energies (E_{az}) of zero-order reaction for LiCl/Mg(OH)₂ ($\alpha = 0.10, 0.30$) for dehydration.

	The region of x [mol/mol]	$k_{z0} [s^{-1}]$	$E_{\rm az}$ [kJ mol ⁻¹]
LiCl/Mg(OH) ₂ (α = 0.10)	0.4 < < 0.0	5.23×10^{8}	126
LiCl/Mg(OH) ₂ ($\alpha = 0.30$)	$0.4 \le x \le 0.9$	7.79×10^7	118

The dehydration profiles of authentic Mg(OH)₂ and LiCl/Mg(OH)₂ (α = 0.10) were calculated to confirm a validity of the proposed model. **Figure 2.4-12**, **Figure 2.4-13**, **Figure 2.4-14**, and **Figure 2.4-15** show comparisons of the measured and calculated dehydration profiles for authentic Mg(OH)₂ and LiCl/Mg(OH)₂ (α = 0.10) at 300°C and 270°C. The values calculated for LiCl/Mg(OH)₂ (α = 0.10) in the region of 0.30 mol/mol $\leq x \leq$ 0.40 mol/mol were weighted average values from calculations based on step 1 and step 2 (Eqs. (2-9) and (2-10)).

$$-\frac{dx}{dt} = (1 - b_{t=t}) k_z + b_{t=t} k_f t$$
 (2-9)

$$b_{t=t} = \frac{0.4 - x_{t=t-2}}{0.4 - 0.3} \tag{2-10}$$

Here, $b_{t=t}$ [-]: weighting coefficient at t = t [s], $x_{t=t-2}$ [mol/mol]: mole fraction of Mg(OH)₂ at t = t - 2 [s]. The mole fractions of Mg(OH)₂ calculated using the value of **Table 2.4-3** and **Table 2.4-4** successfully described the dehydration profiles.

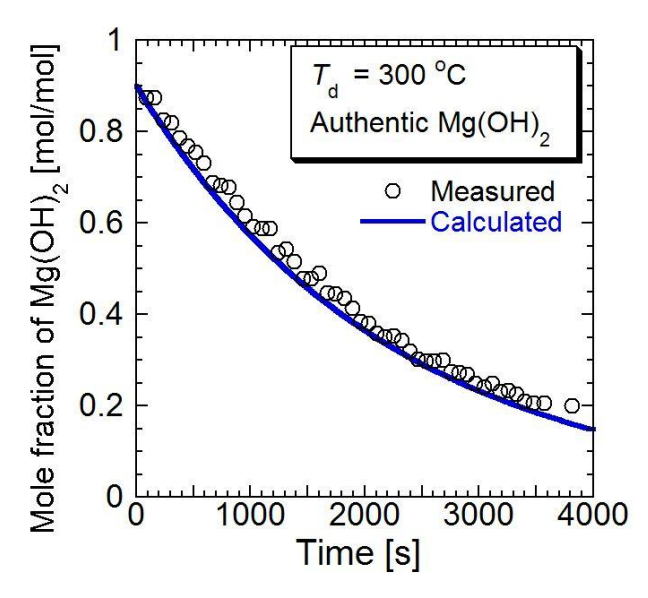


Figure 2.4-12 Comparison of the measured and calculated dehydration profiles for authentic Mg(OH)₂ at 300°C.

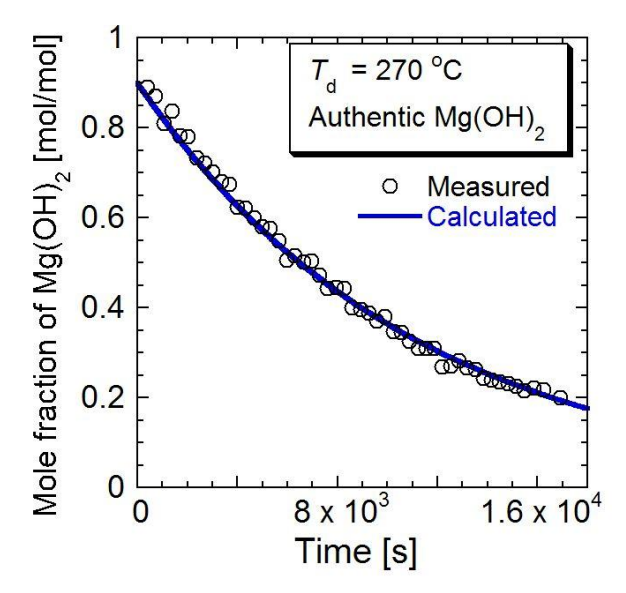


Figure 2.4-13 Comparison of the measured and calculated dehydration profiles for authentic Mg(OH)₂ at 270°C.

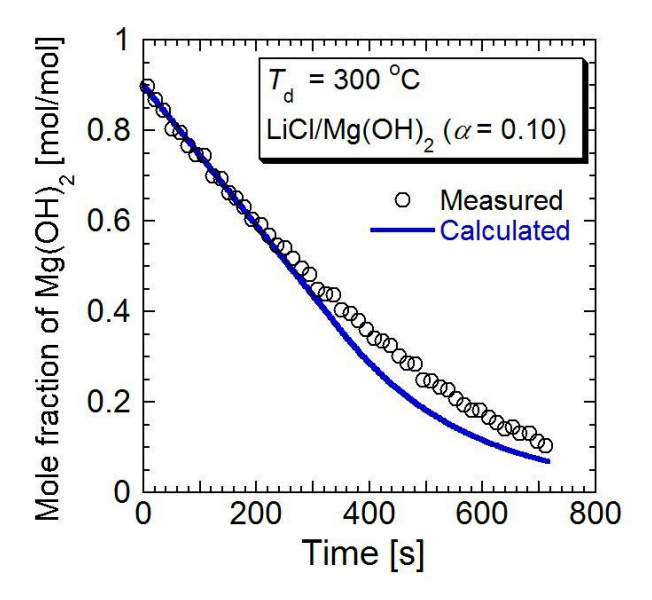


Figure 2.4-14 Comparison of the measured and calculated dehydration profiles for LiCl/Mg(OH)₂ (α = 0.10) at 300°C.

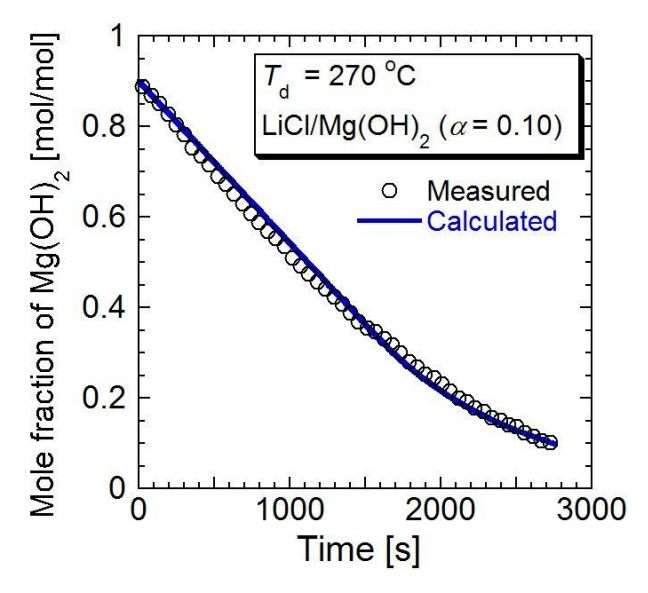


Figure 2.4-15 Comparison of the measured and calculated dehydration profiles for LiCl/Mg(OH)₂ (α = 0.10) at 270°C.

The obtained kinetic equations for dehydration of authentic Mg(OH)₂ and LiCl/Mg(OH)₂ (α = 0.02, 0.10, 0.30) are summarized in **Table 2.4-5**.

Table 2.4-5 Summarized kinetic equations for dehydration of authentic Mg(OH)₂ and LiCl/Mg(OH)₂ ($\alpha = 0.02, 0.10, 0.30$)

Authentic Mg(OH) ₂ , LiCl/Mg(OH) ₂ (α = 0.02)					
Region of x	Kinetic equation	Temperature dependence			
$0.2 \le x \le 0.9$	$-\frac{dx}{dt} = k_{\rm f} x$	$k_{\rm f} = k_{\rm f0} \exp\!\left(\frac{-E_{\rm af}}{RT}\right)$			

LiCl/Mg(OH) ₂ ($\alpha = 0.10, 0.30$)					
Region of x	Kinetic equation	Temperature dependence			
$0.4 \le x \le 0.9$	$-\frac{dx}{dt} = k_{z}$	$k_{z} = k_{z0} \exp\left(\frac{-E_{az}}{RT}\right)$			
0.3 < x < 0.4	$-\frac{dx}{dt} = \left(1 - b_{t=t}\right) k_z + b_{t=t} k_f t$	$k_{z} = k_{z0} \exp\left(\frac{-E_{az}}{RT}\right)$			
	$b_{t=t} = \frac{0.4 - x_{t=t-2}}{0.4 - 0.3}$	$k_{\rm f} = k_{\rm f0} \exp\left(\frac{-E_{\rm af}}{RT}\right)$			
$0.2 \leq x \leq 0.3$	$-\frac{dx}{dt} = k_{\rm f} x$	$k_{\rm f} = k_{\rm f0} \exp\left(\frac{-E_{\rm af}}{RT}\right)$			

2.4.3 Effect of lithium chloride modification on dehydration

The activation energy of the first-order dehydration decreased by 8.2% for LiCl/Mg(OH)₂ (α = 0.10) (**Table 2.4-3**). From SEM micrographs (**Figure 2.3-1** and **Figure 2.3-2**), LiCl was highly dispersed on the Mg(OH)₂ particle. Hence, the surface of Mg(OH)₂ particle was thought to be covered by LiCl (**Figure 2.4-16**) at $\alpha \ge 0.10$. The effect on reduction of the activation energy would be caused by quick removal of H₂O from reaction field, and H₂O was absorbed into LiCl. The lean H₂O atmosphere accelerated the dehydration of Mg(OH)₂ (Eqs. (2-11) and (2-12)).

$$Mg(OH)_2 \longrightarrow MgO + H_2O$$
 (2-11)

$$LiCl + H_2O \longrightarrow LiCl \cdot H_2O$$
 (2-12)

LiCl coverage on Mg(OH)₂ is thought to be not enough for LiCl/Mg(OH)₂ (α = 0.02) (**Figure 2.4-16** (a)) compared with LiCl/Mg(OH)₂ (α = 0.10) (**Figure 2.4-16** (b)). Thus, the dehydration rate of LiCl/Mg(OH)₂ (α = 0.02) was lower than that of LiCl/Mg(OH)₂ (α = 0.10) (**Figure 2.3-13**). On the other hand, LiCl coverage on Mg(OH)₂ is considered to be excess amount for LiCl/Mg(OH)₂ (α = 0.30) (**Figure 2.4-16** (c)) compared with LiCl/Mg(OH)₂ (α = 0.10) (**Figure 2.4-16** (b)). The dehydration rate of LiCl/Mg(OH)₂ (α = 0.30) was lower than that of LiCl/Mg(OH)₂ (α = 0.10) (**Figure 2.3-13**). It is thought that the excess amount of LiCl increased the diffusion resistance of water in LiCl layer, thereby the dehydration rate was reduced.

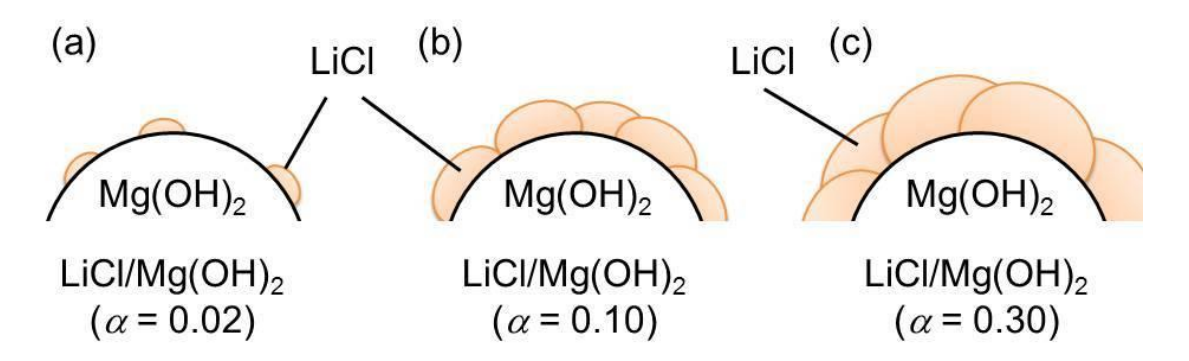


Figure 2.4-16 A schematic model of LiCl-modified Mg(OH)₂. (a) LiCl/Mg(OH)₂ (α = 0.02), (b) LiCl/Mg(OH)₂ (α = 0.10), (c) LiCl/Mg(OH)₂ (α = 0.30).

2.4.4 Absolute reaction rate

To study a mechanism of the dehydration, an analysis of absolute reaction rate is performed. Elementary reactions of the dehydration are expressed as below.

$$Mg(OH)_2 \longleftrightarrow A^* \longrightarrow MgO + H_2O$$
 (2-13)

Here, A^* indicates an activated complex. In the previous studies, two theories for absolute reaction of the dehydration of Mg(OH)₂ were proposed. (1) A transition state is assumed by Martens et al. as a process at which proton is passing through potential barrier [10]. The activated complex was considered as a H_2O -like intermediate (H_2O^*). Potential curve is calculated by Morse equation. In this case, the elementary reactions proceeds uniformly in Mg(OH)₂ particle. Hence, the dehydration rate is expressed by using the equation of first-order reaction. (2) L'vov et al. assumed MgO (g) as an activated complex [11,12]. In this case, the elementary reactions proceed at reaction interface. Hence, the dehydration rate is expressed by using Mampel equation (interface reaction model, Eq. (2-1)). In this work, the dehydration rate is analyzed by the first-order reaction. Thus, the first theory is thought to be appropriate.

The dehydration of $Mg(OH)_2$ is analyzed by the transition state theory [13]. The formation rate of MgO is expressed as follows.

$$\frac{d[MgO]}{dt} = -\frac{d[Mg(OH)_2]}{dt} = k^{\dagger}[A^*]$$
 (2-14)

Here, $k^{\ddagger} [s^{-1}]$ is a rate constant. A pre-equilibrium for $[A^*]$ is assumed.

$$[A^*] = K^{\ddagger}[Mg(OH)_2]$$
 (2-15)

Here, K^{\ddagger} [-] is a pre-equilibrium constant. The rate of passage of the complex through the transition

state is supposed to be proportional to a vibrational frequency along the reaction coordinate.

$$k^{\ddagger} = \kappa v^{\ddagger} \tag{2-16}$$

Here, κ [–] is a transmission coefficient, and v^{\ddagger} [s⁻¹] is the frequency at transition state. In this work, the value of κ is assumed as 1. From results of statistical thermodynamics, a relation between the frequency (v^{\ddagger}) and temperature (T) is expressed as below.

$$v^{\ddagger} = \frac{k_{\rm B}T}{h} \tag{2-17}$$

Here, $k_{\rm B}$ [J K⁻¹] is a Boltzmann's constant, and h [J s] is a Planck's constant. From Eqs. (2-14), (2-15), (2-16), and (2-17), an overall dehydration rate of Mg(OH)₂ is written as follows.

$$-\frac{d[Mg(OH)_2]}{dt} = K^{\ddagger} \frac{k_B T}{h} [Mg(OH)_2]$$
 (2-18)

Here, a Gibbs energy change of activation, ΔG^{\ddagger} [kJ mol⁻¹], an entropy change of activation, ΔS^{\ddagger} [J K⁻¹ mol⁻¹], and an enthalpy change of activation, ΔH^{\ddagger} [kJ mol⁻¹] are introduced. Relationships between pre-equilibrium constant and these state quantities are given as below.

$$K^{\ddagger} = \exp\left(-\frac{\Delta G^{\ddagger}}{RT}\right)$$

$$= \exp\left(\frac{\Delta S^{\ddagger}}{R}\right) \exp\left(-\frac{\Delta H^{\ddagger}}{RT}\right)$$
(2-19)

From Eqs. (2-18) and (2-19), the overall dehydration rate of Mg(OH)₂ is written as follows.

$$-\frac{d[Mg(OH)_2]}{dt} = \frac{k_B T}{h} \exp\left(\frac{\Delta S^{\ddagger}}{R}\right) \exp\left(-\frac{\Delta H^{\ddagger}}{RT}\right) [Mg(OH)_2]$$
 (2-20)

One molecular of H_2O is formed by the dehydration of one molecular of $Mg(OH)_2$. Thus, a stoichiometric coefficient for gas formation, Δn [-], is equal to one. The relationship between the enthalpy change of activation and the activation energy is given as below.

$$\Delta H^{\ddagger} = E_{\text{af}} - (\Delta n - 1)RT$$

$$= E_{\text{af}}$$
(2-21)

Thus, Eq. (2-20) is rewritten by using $E_{\rm af}$.

$$k_{\rm f} = \frac{k_{\rm B}T}{h} \exp\left(\frac{\Delta S^{\dagger}}{R}\right) \exp\left(-\frac{E_{\rm af}}{RT}\right)$$
 (2-22)

From comparison between Eq. (2-7) and (2-22), a following relationship between the pre-exponential factor and temperature, the entropy change of activation is obtained.

$$k_{\text{f0}} = \frac{k_{\text{B}}T}{h} \exp\left(\frac{\Delta S^{\ddagger}}{R}\right) \tag{2-23}$$

The Gibbs energy changes of activation at 300°C are calculated from obtained values at **Table 2.4-3**, and summarized in **Table 2.4-6**. The lowest value of ΔG^{\ddagger} is obtained at $\alpha = 0.10$. The modification of LiCl succeeded to reduce ΔG^{\ddagger} . This result suggests catalytic role of LiCl (**Section 2.4.3**). The negative value of ΔS^{\ddagger} supports the first theory (activated complex: H_2O^*). MgO (g) was assumed by the second theory as the activated complex. A formation of gaseous activated complex results the positive value of ΔS^{\ddagger} . Thus, the second theory is not appropriate for the dehydration of authentic Mg(OH)₂ and LiCl/Mg(OH)₂. A distance between Mg²⁺ and Mg²⁺ is thought to be decreased at the activation state, hence ΔS^{\ddagger} showed negative value.

Table 2.4-6 Activation parameters for first-order dehydration of Mg(OH)₂ at 300°C and various LiCl mixing ratio (α).

α [mol/mol]	0	0.02	0.10	0.30
ΔH^{\ddagger} [kJ mol ⁻¹]	139	130	127	123
$\Delta S^{\ddagger} [J K^{-1} mol^{-1}]$	-72.7	-76.1	-73.4	-86.3
$\Delta G^{\ddagger} [\mathrm{kJ} \; \mathrm{mol}^{-1}]$	181	174	169	173

Distances between Mg^{2+} , O^{2-} , and H^+ were previously studied [14] and are shown in **Figure 2.4-17**. Distances between Mg^{2+} , O^{2-} , and H^+ at a basic state of $Mg(OH)_2$ is shown in **Figure 2.4-17** (a). Here, a motion of H^+ around O^{2-} is needed to be considered. A shortest distance between two protons is 1.228 Å (**Figure 2.4-17 (b)**).

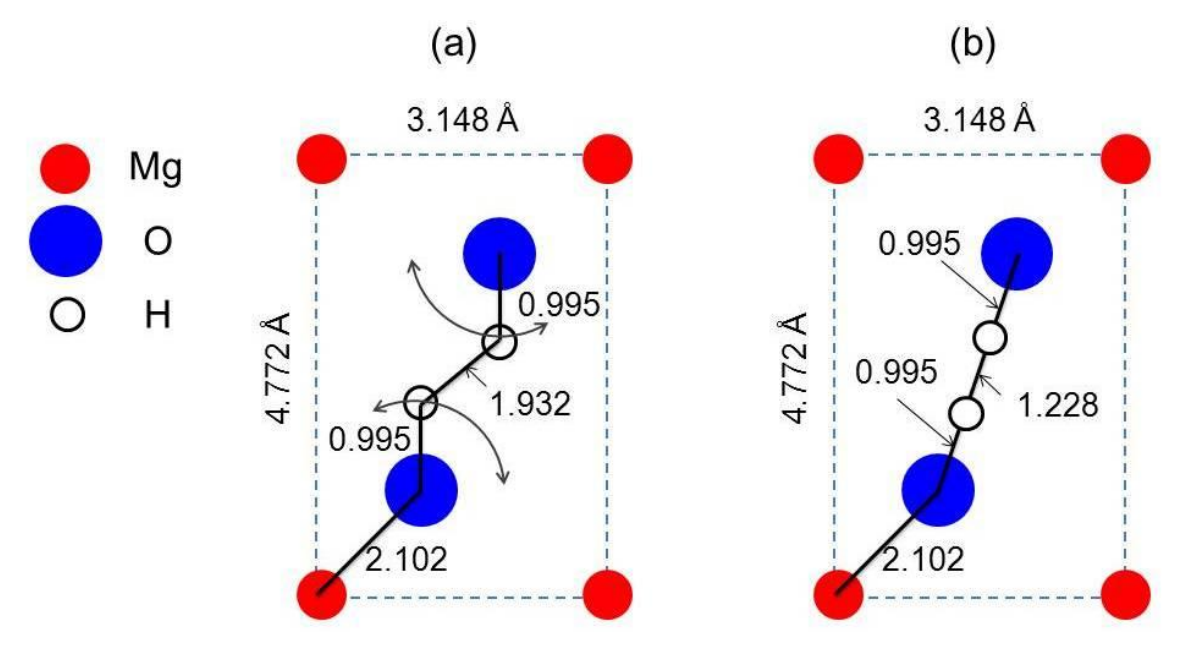


Figure 2.4-17 Distances between Mg^{2+} , O^{2-} , and H^+ in the brucite structure [14]. The numbers indicate distances in Å. (a) Basic state; (b) A state with a shortest distance between two protons. Ionic radiuses are not to real scale.

Morse potential for a proton in the brucite structure was given by Martens et al. [10].

$$V(r) [eV] = 4.70 \left[1 - \exp\left(-2.294 \frac{r - r_0}{r_0}\right) \right]^2$$
 (2-24)

Here, V(r) [eV] is a potential, r [Å] is a coordinate of a proton, and r_0 [Å] is an equilibrium O–H distance. The potential curve of the proton in the brucite structure is overlapped with the other potential curve of a proton. Thus, an overall potential curve is calculated by summation of each potential curve. The overall potential curve is shown in **Figure 2.4-18**. The energy levels for OH vibration of Mg(OH)₂ were given by Martens et al. [10].

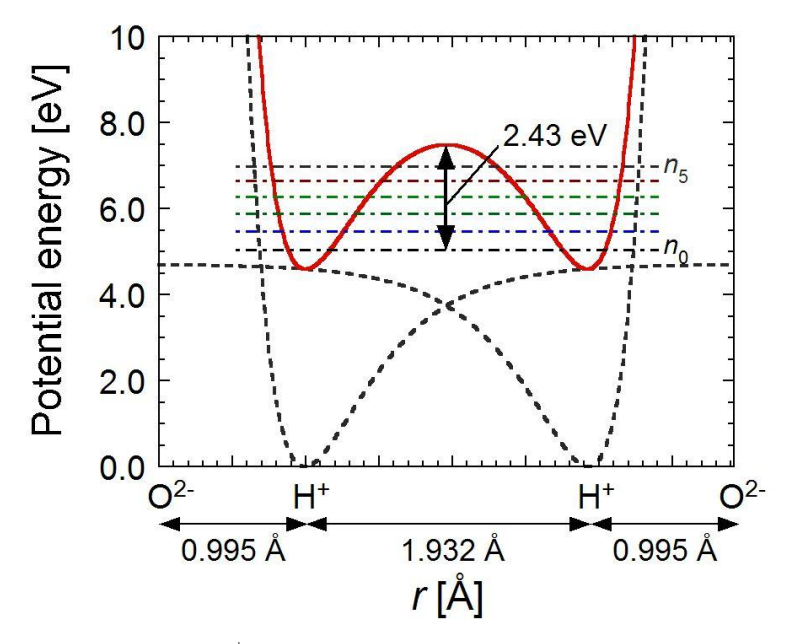


Figure 2.4-18 Potential curve of H⁺ for Mg(OH)₂ [10]. Dashed lines indicate the original potential curve which was calculated by Eq. (2-24). A red solid line shows the overall potential curve. Dashed and single-dotted lines indicate energy levels for O–H vibration of Mg(OH)₂. n_0 shows a ground state of O–H vibrations.

An energy to pass through potential barrier is calculated as 2.43 eV (= 156 kJ mol⁻¹) at basic state, and 0.79 eV (= 50 kJ mol⁻¹) at the state with a shortest distance between two protons. These values (50–156 kJ mol⁻¹) are close to the values of activation energy of first-order reaction (123–139 kJ mol⁻¹) (**Table 2.4-3**). Thus, the transition state of the dehydration is thought to be related with the potential barrier of protons in the brucite structure. The activation energies of LiCl/Mg(OH)₂ was decreased compared with authentic Mg(OH)₂ (**Table 2.4-3**). The activated complex can be backed to the original state. Here, formed H₂O is absorbed into LiCl for LiCl/Mg(OH)₂. Thus, the contribution of reverse process was thought to be decreased. Hence, the activation energies of LiCl/Mg(OH)₂ is thought to be decreased.

2.5 Summary

LiCl/Mg(OH)₂ (α = 0.02, 0.10, 0.30) were prepared as candidates of TCM. LiCl was highly dispersed on the Mg(OH)₂ particle. The dehydration of authentic Mg(OH)₂ and LiCl/Mg(OH)₂ (α = 0.02, 0.10, 0.30) were examined, and kinetic analysis were performed. α of 0.10 was optimum value for thermal energy storage at 250–300°C. The dehydration of LiCl/Mg(OH)₂ (α = 0.10) was understood by a two-step reaction model. The dehydration rate did not depend on the mole fraction of Mg(OH)₂ in the first step (zero-order reaction), but depended on the mole fraction of Mg(OH)₂ as a first-order reaction in the second step. The activation energy of the first-order dehydration of Mg(OH)₂ decreased by 8.2% as a result of LiCl-modification (α = 0.10). The absolute rate for dehydration of authentic Mg(OH)₂ and LiCl/Mg(OH)₂ (α = 0.02, 0.10, 0.30) were studied by using transition state theory. The

transition state of the dehydration is thought to be related with the potential barrier of protons in the brucite structure. The kinetic parameters and equations which submitted at **Chapter 2** would be fruitful for design reactors of TcES, and decide operation conditions of TcES.

2.6 References

- [1] Y. Kato, N. Yamashita, K. Kobayashi, Y. Yoshizawa; Kinetic study of the hydration of magnesium oxide for a chemical heat pump, *Appl. Therm. Eng.*, **16**, 853–862 (1996)
- [2] Y. Kato, F. Takahashi, A. Watanabe, Y. Yoshizawa ; Thermal analysis of a magnesium oxide/water chemical heat pump for cogeneration, *Appl. Therm. Eng.*, **21**, 1067-1081 (2001)
- [3] Y. Kato, Y. Sasaki, Y. Yoshizawa; Thermal performance measurement of packed bed reactor of a magnesium oxide/water chemical heat pump, *J. Chem. Eng. Jpn.*, **36**, 833–839 (2003)
- [4] Y. Kato, Y. Sasaki, Y. Yoshizawa; Magnesium oxide/water chemical heat pump to enhance energy utilization of a cogeneration system, *Energy*, **30**, 2144–2155 (2005)
- [5] J. Ryu, N. Hirao, R. Takahashi, Y. Kato; Dehydration behavior of metal-salt-added magnesium hydroxide as chemical heat storage media, *Chem. Lett.*, **37**, 1140–1141 (2008)
- [6] P. J. Anderson, R. F. Horlock; Thermal decomposition of magnesium hydroxide, *Trans. Faraday Soc.*, **58**, 1993–2004 (1962)
- [7] S. J. Gregg, R. I. Razouk; The kinetics of the thermal decomposition of magnesium hydroxide, *J. Chem. Soc. (London)*, **Suppl. 1**, S36–S44 (1949)
- [8] R. S. Gordon, W. D. Kingery; Thermal decomposition of Brucite: II, Kinetics of decomposition in vacuum, *J. Amer. Ceram. Soc.*, **50**, 8–14 (1967)
- [9] Society of chemical engineers, Japan ed.; Handbook of chemical engineering (*in Japanese*), Revised fifth ed., Maruzen, Tokyo, Japan, 1080–1093 (1988)
- [10] R. Martens, F. Freund; The potential energy curve of the proton and the discussion energy of the OH- ion in Mg(OH)₂, *Phys. Status Solidi A*, **37**, 97–104 (1976)
- [11] B. V. L'vov, A. V. Novichikhin, A. O. Dyakov; Mechanism of thermal decomposition of magnesium hydroxide, *Thermochim. Acta*, **315**, 135–143 (1998)
- [12] B. V. L'vov, V. L. Ugolkov; Kinetics and mechanism of free-surface decomposition of Group IIA and IIB hydroxides analyzed thermogravimetrically by the third-law method, *Thermochim. Acta*, **413**, 7–15 (2004)
- [13] P. Atkins, J. Paula; Atkins' physical chemistry, Oxford university press, New York, U.S., 843–850 (2010)
- [14] F. Zigan, R. Rothbauer; Neues Jahrb. F. Miner., Monatshefte, Stuttgart, Germany, 137 (1967)

Chapter 3 Hydration reactivity of lithium chloride-modified magnesium oxide

3.1 Introduction

Dehydration kinetics LiCl/Mg(OH)₂ was studied at **Chapter 2**. Hydration reaction of LiCl/MgO is used for a heat output operation of thermochemical energy storages (TcES). Although to obtain hydration behaviors of LiCl/MgO are important to design reactors of TcES, there is not enough information on the effects of LiCl mixing ratio, hydration temperature, and water vapor pressure on the hydration behavior of LiCl/MgO.

The hydration rate analysis of the material is also needed to design reactors for TcES and exergy analysis. Understanding about hydration of LiCl/MgO is important to calculate a heat output rate of the material, which is an important performance of TcES. The hydration of MgO was studied by Layden et al. [1] and Kato et al. [2]. Layden et al. reported an interface reaction was rate controlling step for hydration, and the rate depended on the vapor pressure. Kato et al. studied the hydration of MgO, and concluded that the rate controlling process was H₂O diffusion in Mg(OH)₂ layer. Some gas-solid reaction models (i.e. shrinking (unreacted) core model, grain model, and pore model) have been proposed. Matsuda et al. discussed the hydration of calcium oxide (CaO) by using grain model [3]. Aihara et al. studied the carbonation of CaO and decarbonation of calcium carbonate (CaCO₃) by using pore model [4]. Kim et al. examined the hydration of composite material, expanded graphite/calcium chloride (CaCl₂)/MgO, by using shrinking core model [5]. However, there are no studies on a hydration kinetics of LiCl/MgO, thereby it is still unclear.

In this chapter, the hydration of LiCl/MgO was examined by thermogravimetry. The hydration of LiCl/MgO at various lithium chloride mixing ratio, hydration temperature, and water vapor pressure were examined by a thermobalance, and the heat output capacities of the materials were evaluated. Kinetic analysis of hydration was performed, and heat output rate was evaluated.

3.2 Experimental

3.2.1 Sample preparation

LiCl/Mg(OH)₂ was prepared as a precursor of LiCl/MgO. A detail of the procedure was shown in **Section 2.2.1**. In this chapter, a series of LiCl/Mg(OH)₂ with $\alpha = 0.02$, 0.05, 0.10, 0.30 was prepared, and authentic Mg(OH)₂ was used as a reference. Authentic Mg(OH)₂ and LiCl/Mg(OH)₂ was obtained. Conditions of dehydration are shown in **Section 3.2.2** and **3.2.3**.

3.2.2 Characterization techniques

3.2.2.1 Scanning electron microscopy

Authentic Mg(OH)₂ and LiCl/Mg(OH)₂ was dehydrated by the thermobalance to obtain authentic MgO or LiCl/MgO. First, the samples were dried at 120°C for 30 min under argon gas flow (flow rate 100 mL min⁻¹). Then, the samples were heated up to the dehydration temperature (T_d , 300 °C) at a rate of 20 °C min⁻¹ under argon gas flow (flow rate 100 mL min⁻¹). The sample was kept at the dehydration temperature for 30 min.

Scanning electron microscopy (SEM) was performed to identify the microstructures and surface morphologies of the samples. A scanning electron microscope (SM-200, TOPCON Corp.) was used. An acceleration voltage was 8 kV.

3.2.2.2 Powder X-ray diffraction analysis

Authentic $Mg(OH)_2$ and $LiCl/Mg(OH)_2$ was dehydrated by the thermobalance to obtain MgO or LiCl/MgO. The procedure of dehydration was same as **Section 3.2.2.1**.

Powder X-ray diffraction (XRD) measurements were carried out under atmospheric conditions at room temperature using an X-ray diffractometer (Ultima IV, Rigaku Corp.) through a 2θ range 10° – 90° at a scan speed of 1° min⁻¹ using monochromatic CuK α radiation, 40 kV generator voltage, and 40 mA current.

3.2.3 Hydration measurement with thermogravimetry

The weight changes of the samples in the course of dehydration and hydration operation were measured by a thermobalance (TGD9600, Ulvac-Riko, Inc.). The samples were charged into a Pt cell of the balance. First, the samples were dried at 120° C for 30 min under argon gas flow (flow rate: 100 mL min⁻¹) to remove the sorbed water. Then, the samples were heated up to the dehydration temperature (T_d , 300°C or 350°C) at a rate of 20°C min⁻¹ under argon gas flow (flow rate: 100 mL min⁻¹). The sample weight at 200°C was defined as an initial weight. The sample was kept at the dehydration temperature for 30 min, after which it cooled down to the hydration temperature (T_h , 110–200°C) at a rate of 20°C min⁻¹. The hydration operation was induced by introducing a mixture of water vapor and argon (carrier gas) at the hydration temperature. Time for vapor supply (t_v) was examined between 2 min and 280 min. The partial pressures of water vapor (as an argon balance) were examined in the range of 7.4 to 57.8 kPa. Table 1 shows the relationship between water vapor pressure (t_h) and saturated vapor temperature (t_h).

Table 3.2-1 The relationship between water vapor pressure $(p_{\rm H2O})$ and saturated vapor temperature $(T_{\rm s})$.

$p_{ m H2O}$	[kPa]	7.4	12.3	19.9	31.2	47.4	57.8
$T_{ m s}$	[°C]	40	50	60	70	80	85

After the hydration operation was complete, vapor flow was stopped and dry argon gas was introduced

at the same hydration temperature for 50 min to remove the sorbed water (drying operation).

Mole fraction of $Mg(OH)_2$ (x [mol/mol]) in the particles consisting of MgO and $Mg(OH)_2$ was calculated using the Eq. (3-1).

$$x \text{ [mol/mol]} = \left[1 + \frac{\Delta w / M_{\text{H}_2\text{O}}}{w_{\text{hydroxide}} / M_{\text{hydroxide}}}\right]$$
(3-1)

where Δw [kg] is the weight change of the sample, $M_{\rm H2O}$ [kg mol⁻¹] is the molecular weight of water, $w_{\rm hydroxide}$ [kg] is the initial sample weight, and $M_{\rm hydroxide}$ [kg mol⁻¹] is the molecular weight of magnesium hydroxide (Mg(OH)₂).

Figure 3.2-1 shows a dehydration and hydration profiles of LiCl/Mg(OH)₂. The mole fraction of Mg(OH)₂ after the dehydration reaction is denoted as x_0 [mol/mol], that of Mg(OH)₂ at the end of the vapor supply period is denoted as x_h [mol/mol], and that of Mg(OH)₂ after the drying operation is denoted as x_c [mol/mol], respectively. The conversion of the hydration (Δx_1 [mol/mol]) is defined as $\Delta x_1 = x_c - x_0$, and the apparent change of x by sorption (Δx_2 [mol/mol]) is defined as $\Delta x_2 = x_h - x_c$.

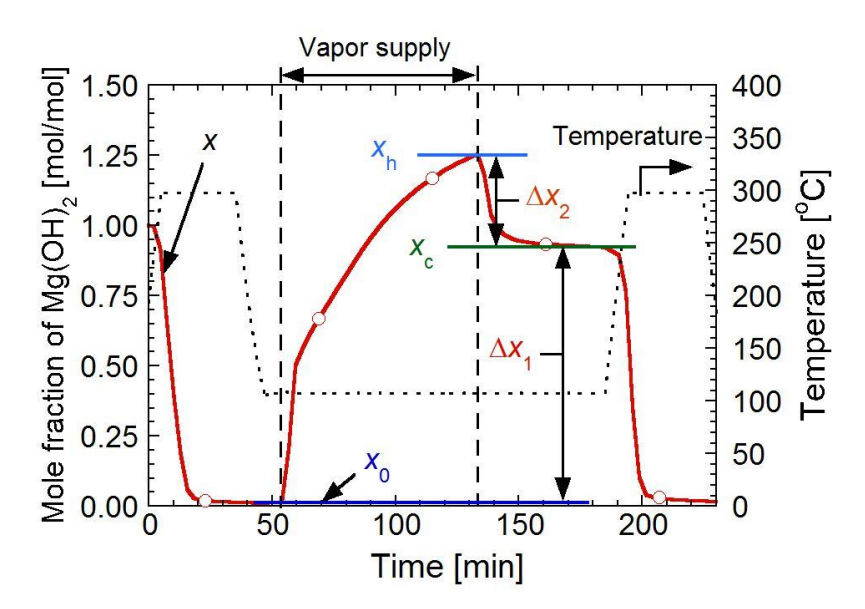


Figure 3.2-1 Example of dehydration and hydration profiles of LiCl/Mg(OH)₂.

The heat output capacity was calculated from the enthalpy changes in the reaction and the sorption of water vapor. In this study, the heat output capacity was expressed as heat output per unit initial weight of the starting material (LiCl/Mg(OH)₂) [kJ kg⁻¹]. It was assumed that the enthalpy change by the sorption of water vapor was equal to enthalpy change by the condensation of water.

$$Q_{\text{total}} = Q_{\text{r}} + Q_{\text{a}} \tag{3-2}$$

$$Q_{\rm r} = \frac{-\Delta H_{\rm r}}{M_{\rm sample}} \times \Delta x_{\rm l} \tag{3-3}$$

$$Q_{\rm a} = \frac{-\Delta H_{\rm s}}{M_{\rm sample}} \times \Delta x_2 \tag{3-4}$$

Here, Q_{total} [kJ kg⁻¹]: heat output capacity of the material; Q_r [kJ kg⁻¹]: heat output by hydration; Q_a [kJ kg⁻¹]: heat output by sorption; ΔH_r [kJ mol⁻¹]: enthalpy change by reaction; ΔH_s [kJ mol⁻¹]: enthalpy change by sorption; Δx_1 [mol/mol]: conversion of the hydration; Δx_2 [mol/mol]: apparent change of x by sorption; M_{sample} [kg mol⁻¹]: molecular weight of the sample, respectively.

The mean heat output rate (W [W kg⁻¹]) is evaluated by time for vapor supply (t_v [s]) and Q_{total} [kJ kg⁻¹].

$$W = \frac{Q_{\text{total}}}{t_{\text{v}}} \times 10^3 \tag{3-5}$$

3.3 Results

3.3.1 Characterization of samples

3.3.1.1 Surface morphology of lithium chloride-modified magnesium oxide

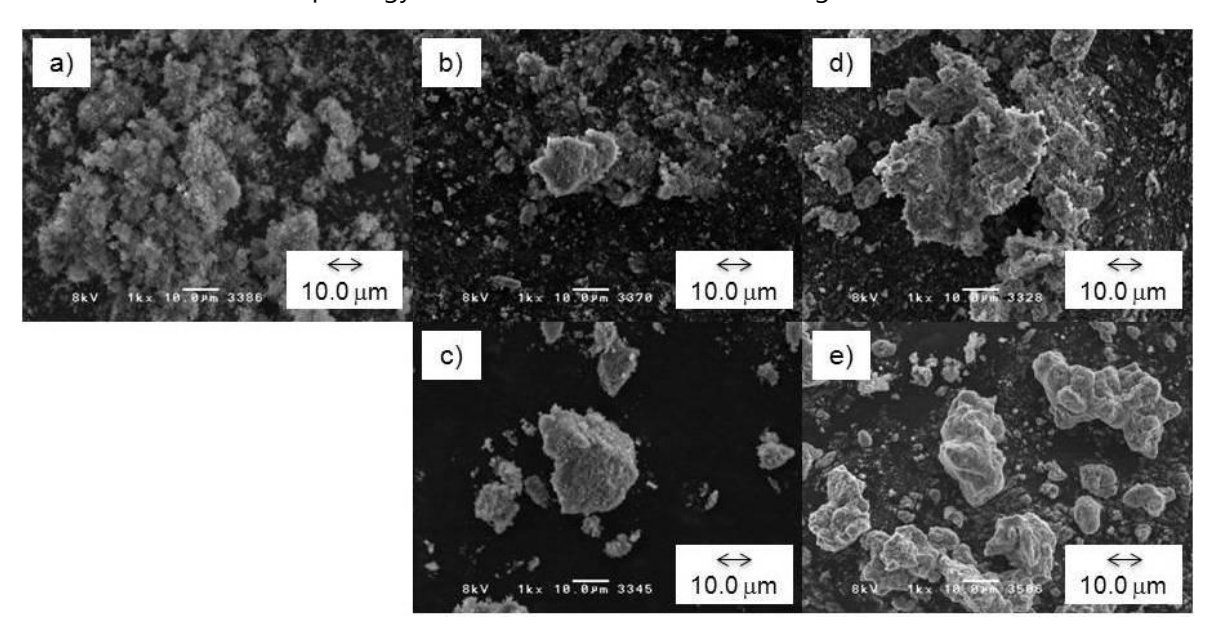


Figure 3.3-1 SEM micrographs of authentic Mg(OH)₂, and LiCl/Mg(OH)₂ (α = 0.02, 0.10, 0.30) after dehydration operation. The graph is magnified a 1000 times. Starting materials are as follows; (a) authentic Mg(OH)₂, (b) LiCl/Mg(OH)₂ (α = 0.02), (c) LiCl/Mg(OH)₂ (α = 0.05), (d) LiCl/Mg(OH)₂ (α = 0.10), and (e) LiCl/Mg(OH)₂ (α = 0.30).

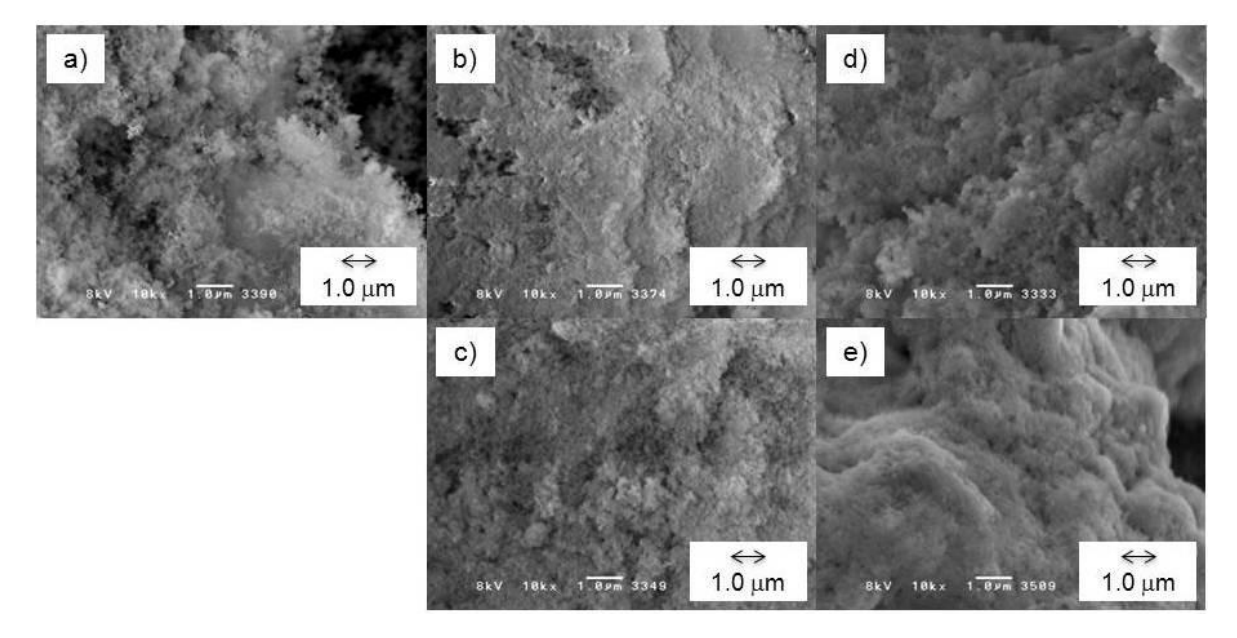


Figure 3.3-2 SEM micrographs of authentic Mg(OH)₂, and LiCl/Mg(OH)₂ (α = 0.02, 0.10, 0.30) after dehydration operation. The graph is magnified a 10000 times. Starting materials are as follows; (a) authentic Mg(OH)₂, (b) LiCl/Mg(OH)₂ (α = 0.02), (c) LiCl/Mg(OH)₂ (α = 0.05), (d) LiCl/Mg(OH)₂ (α = 0.10), and (e) LiCl/Mg(OH)₂ (α = 0.30).

SEM micrographs of authentic $Mg(OH)_2$, and $LiCl/Mg(OH)_2$ ($\alpha = 0.02, 0.10, 0.30$) after dehydration operation are shown in **Figure 3.3-1** and **Figure 3.3-2**. The needle-like crystals of LiCl were not found from these micrographs. This result indicates that the LiCl was highly dispersed on the samples after dehydration operation.

3.3.1.2 Crystal structure of lithium chloride-modified magnesium oxide

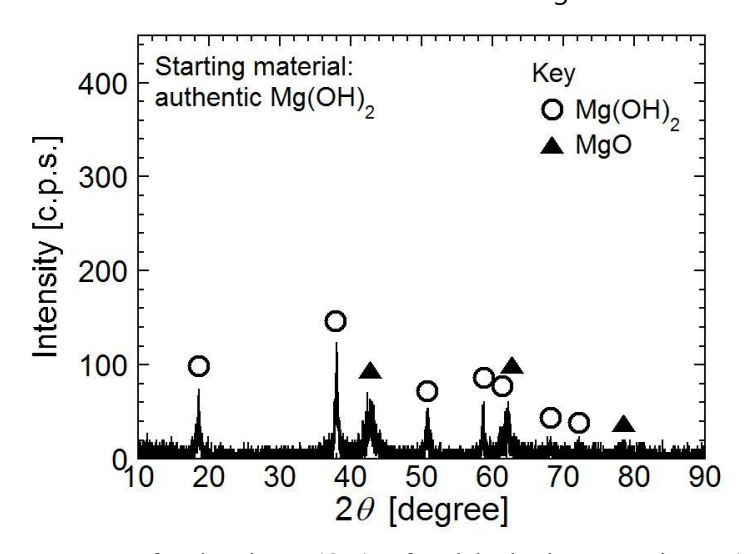


Figure 3.3-3 XRD pattern of authentic $Mg(OH)_2$ after dehydration operation. (\circ) indicates reference peak of $Mg(OH)_2$ (ICDD 10830114), and (\triangle) indicates reference peak of MgO (ICDD 10711176).

XRD pattern of authentic Mg(OH)₂ after dehydration operation are shown in Figure 3.3-3.

The characteristic peaks of Mg(OH)₂ and MgO were identified. Some of Mg(OH)₂ was remained after 30 min of dehydration at 300°C.

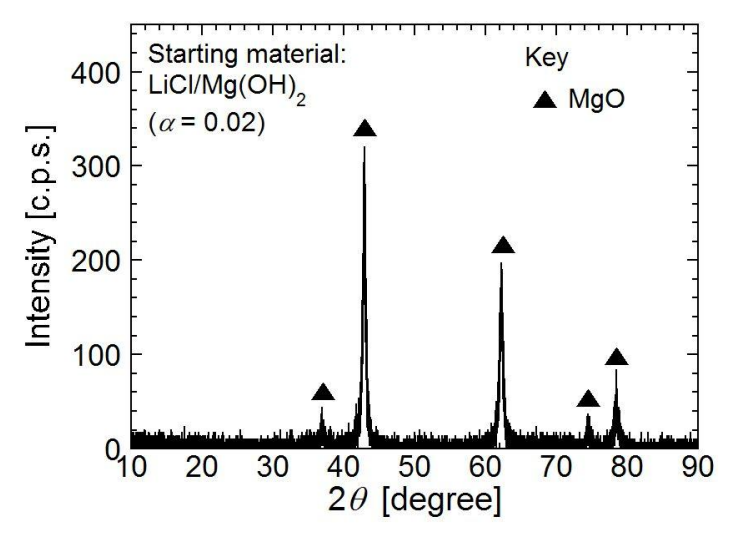


Figure 3.3-4 XRD pattern of LiCl/Mg(OH)₂ ($\alpha = 0.02$) after dehydration operation. (\blacktriangle) indicates reference peak of MgO (ICDD 10711176).

XRD pattern of LiCl/Mg(OH)₂ ($\alpha = 0.02$) after dehydration operation are shown in **Figure 3.3-4**. The characteristic peaks of MgO were identified.

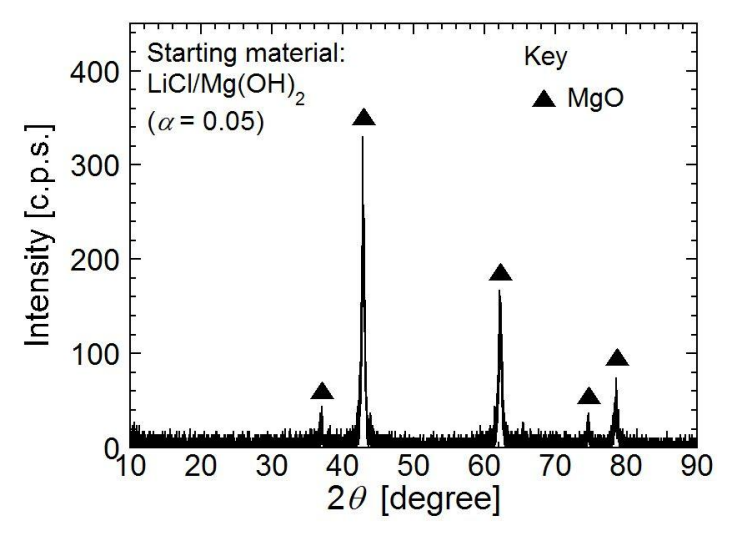


Figure 3.3-5 XRD pattern of LiCl/Mg(OH)₂ ($\alpha = 0.05$) after dehydration operation. (\blacktriangle) indicates reference peak of MgO (ICDD 10711176).

XRD pattern of LiCl/Mg(OH)₂ ($\alpha = 0.05$) after dehydration operation are shown in **Figure 3.3-5**. The characteristic peaks of MgO were identified.

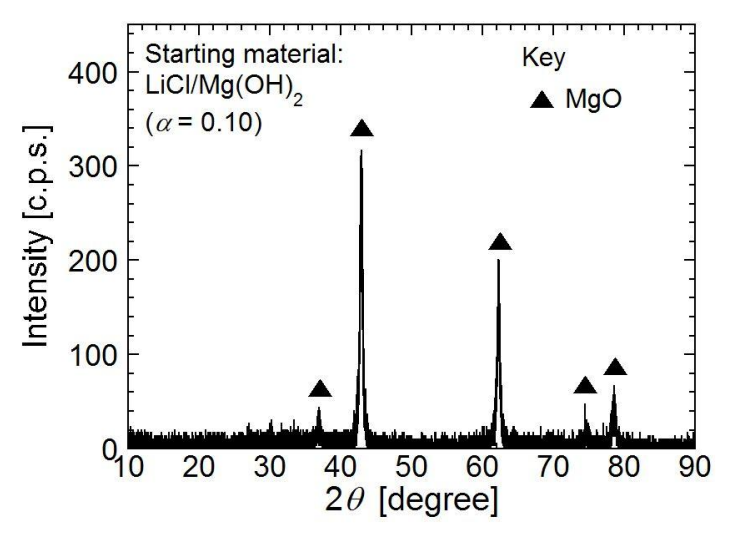


Figure 3.3-6 XRD pattern of LiCl/Mg(OH)₂ ($\alpha = 0.10$) after dehydration operation. (\blacktriangle) indicates reference peak of MgO (ICDD 10711176).

XRD pattern of LiCl/Mg(OH)₂ ($\alpha = 0.10$) after dehydration operation are shown in **Figure 3.3-6**. The characteristic peaks of MgO were identified.

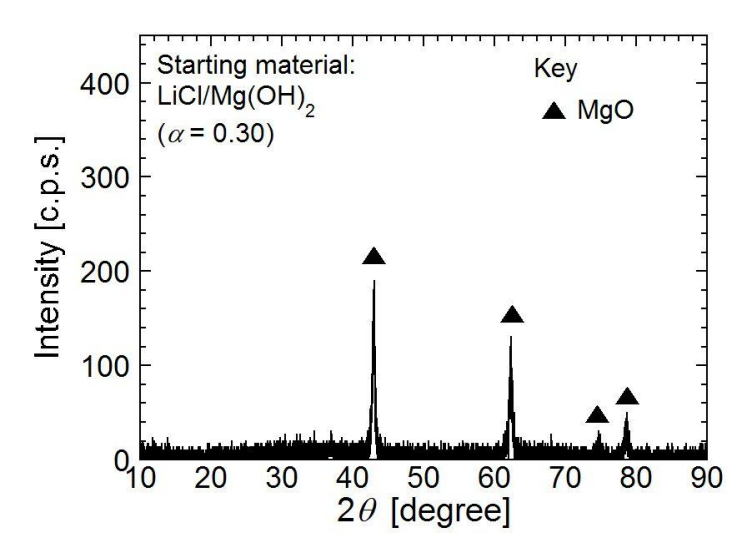


Figure 3.3-7 XRD pattern of LiCl/Mg(OH)₂ ($\alpha = 0.30$) after dehydration operation. (\blacktriangle) indicates reference peak of MgO (ICDD 10711176).

XRD pattern of LiCl/Mg(OH)₂ ($\alpha = 0.30$) after dehydration operation are shown in **Figure 3.3-7**. The characteristic peaks of MgO were identified.

3.3.2 Hydration measurement with thermogravimetry

3.3.2.1 Relationship between composition and hydration behavior

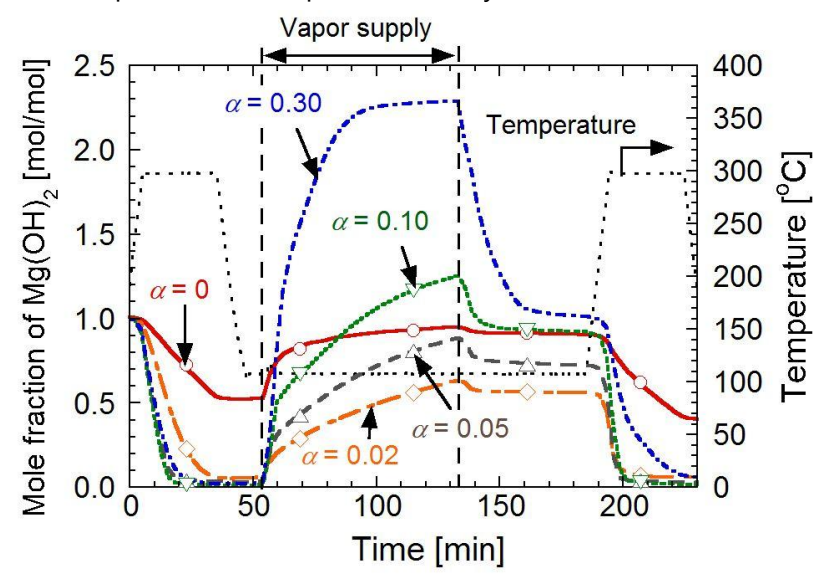


Figure 3.3-8 Dehydration–hydration profiles of LiCl/Mg(OH)₂ at mixing ratios $\alpha = 0$ –0.30, $T_{\rm d} = 300$ °C, $T_{\rm h} = 110$ °C, $p_{\rm H2O} = 57.8$ kPa, and $t_{\rm v} = 80$ min.

The dehydration–hydration profiles of LiCl/Mg(OH)₂ at several mixing ratios at $T_h = 110^{\circ}$ C are shown in **Figure 3.3-8**. The water vapor pressure (p_{H2O}) was fixed as 57.8 kPa. Authentic Mg(OH)₂ (LiCl/Mg(OH)₂ ($\alpha = 0$)) did not dehydrate enough ($x_0 = 0.521$ mol/mol), but LiCl/Mg(OH)₂ mixtures ($\alpha = 0.02$, 0.05, 0.10, 0.30) dehydrated well at 300°C during 30 min. These results agreed with the results of XRD. LiCl/Mg(OH)₂ ($\alpha = 0.10$) showed the fastest dehydration rate. The materials ($\alpha = 0.02$, 0.05, 0.10, 0.30) hydrated at 110°C with water vapor pressure of 57.8 kPa.

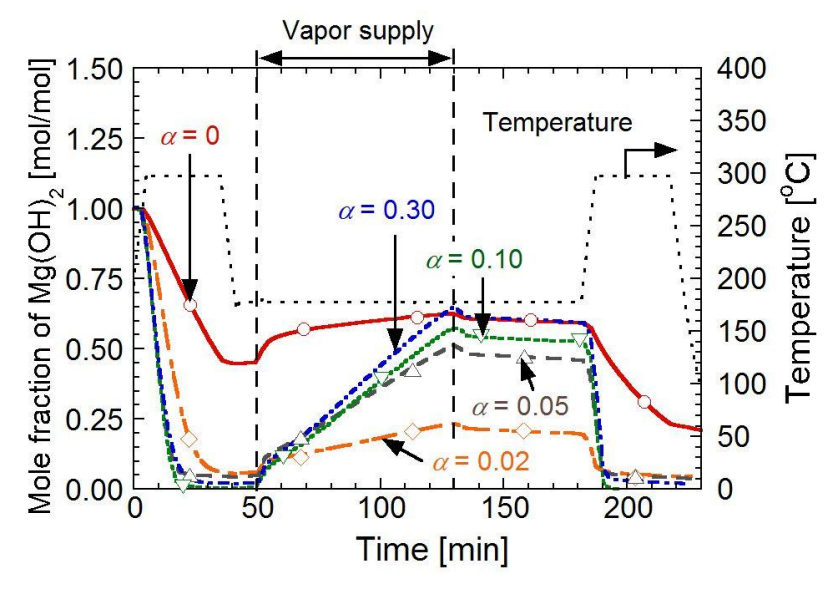


Figure 3.3-9 Dehydration–hydration profiles of LiCl/Mg(OH)₂ at mixing ratios $\alpha = 0$ –0.30, $T_{\rm d} = 300$ °C, $T_{\rm h} = 180$ °C, $p_{\rm H2O} = 57.8$ kPa, and $t_{\rm v} = 80$ min.

The dehydration–hydration profiles of LiCl/Mg(OH)₂ at $T_h = 180$ °C at various mixing ratios are shown in **Figure 3.3-9**. The materials ($\alpha = 0.05, 0.10, 0.30$) hydrated partially at 180°C with water vapor pressure of 57.8 kPa. On the other hand, LiCl/Mg(OH)₂ ($\alpha = 0.02$) dehydrated well at 300°C during 30 min, but did not hydrate enough at 180°C with water vapor pressure of 57.8 kPa.

3.3.2.2 Relationship between hydration temperature and hydration behavior

In this section, authentic Mg(OH)₂ was dehydrated at 350°C, and then hydrated at 110°C or 180°C, $p_{\rm H2O} = 57.8$ kPa. Authentic Mg(OH)₂ dehydrated at 350°C for 30 min ($x_0 = 0.12$ mol/mol). Hydration profiles of authentic Mg(OH)₂ at these conditions are shown in **Figure 3.3-10**. In the figure, the x-axis indicates the time from vapor supply start, and y-axis shows the change of the mole fraction of Mg(OH)₂ (Δx). Here, Δx is defined as $\Delta x = x - x_0$ in the hydration operation. Authentic MgO hydrated well at 110°C, $p_{\rm H2O} = 57.8$ kPa, and $t_{\rm v} = 80$ min ($\Delta x_1 = 0.719$ mol/mol). On the other hand, it hydrated slightly at 180°C, $p_{\rm H2O} = 57.8$ kPa, and $t_{\rm v} = 80$ min ($\Delta x_1 = 0.082$ mol/mol).

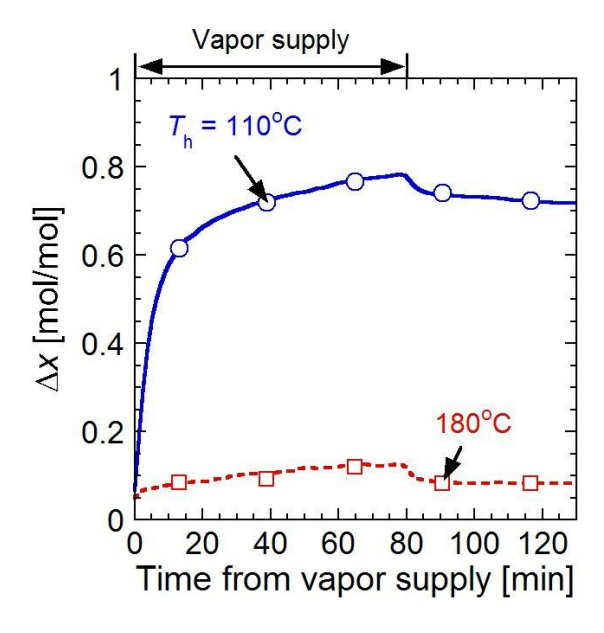


Figure 3.3-10 Hydration profiles of authentic MgO at $T_d = 350^{\circ}\text{C}$, $T_h = 110^{\circ}\text{C}$ and 180°C , $p_{\text{H2O}} = 57.8$ kPa, and $t_v = 80$ min.

LiCl/Mg(OH)₂ was dehydrated at 300°C, and then hydrated at 110–200°C, $p_{\rm H2O} = 57.8$ kPa, and $t_{\rm v} = 80$ min. The hydration profiles of LiCl/MgO ($\alpha = 0.10$) with several $T_{\rm h}$ are shown from **Figure 3.3-11** to **Figure 3.3-13**. Kinetic analysis is performed at Section 3.4.2.2 and calculated profiles are obtained at the section. The water vapor pressure ($p_{\rm H2O}$) was fixed as 57.8 kPa. In these figures, the x-axis indicates the time from vapor supply start, and y-axis shows the change of the mole fraction of Mg(OH)₂ (Δx). The hydration profile shows a convex upward curve at 110–150°C. On the other hand, it shows a linear shape at 180–190°C. The hydration profile at 160°C and 170°C appeared as an intermediate shape. These results suggest that the hydration mechanism was changed by hydration temperature. The hydration profile at 195°C and 200°C increased gradually for first 20

min, and then it increased steeply and linearly. This result suggests an existence of induction time for hydration (t_{ind}).

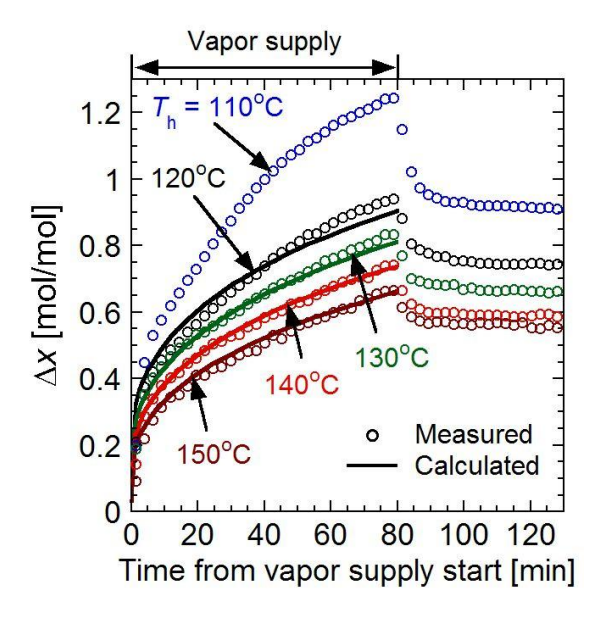


Figure 3.3-11 Hydration profiles of LiCl/MgO (α = 0.10) at $T_{\rm d}$ = 300°C, $T_{\rm h}$ = 110–150°C, $p_{\rm H2O}$ = 57.8 kPa, and $t_{\rm v}$ = 80 min. Calculated profiles are obtained at **Section 3.4.2.2**. Blue line: calculated line at 110°C, black line: calculated line at 120°C, green line: calculated line at 130°C, red line: calculated line at 140°C, brown line: calculated line at 150°C, respectively.

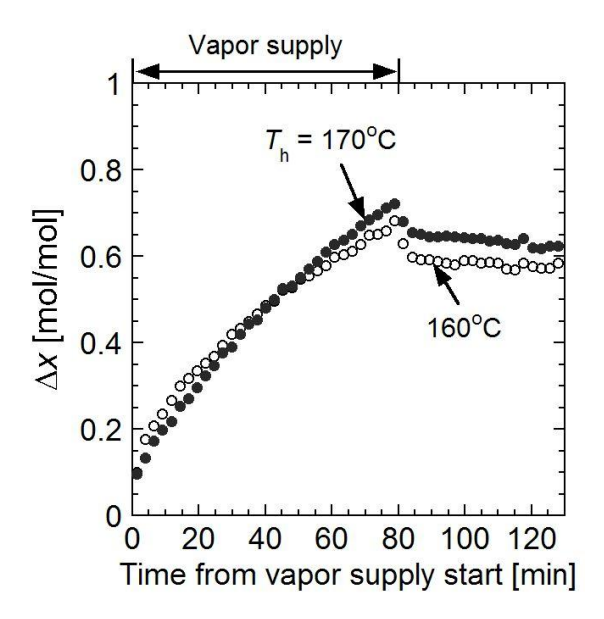


Figure 3.3-12 Hydration profiles of LiCl/MgO (α = 0.10) at $T_{\rm d}$ = 300°C, $T_{\rm h}$ = 160°C and 170°C, $p_{\rm H2O}$ = 57.8 kPa, and $t_{\rm v}$ = 80 min.

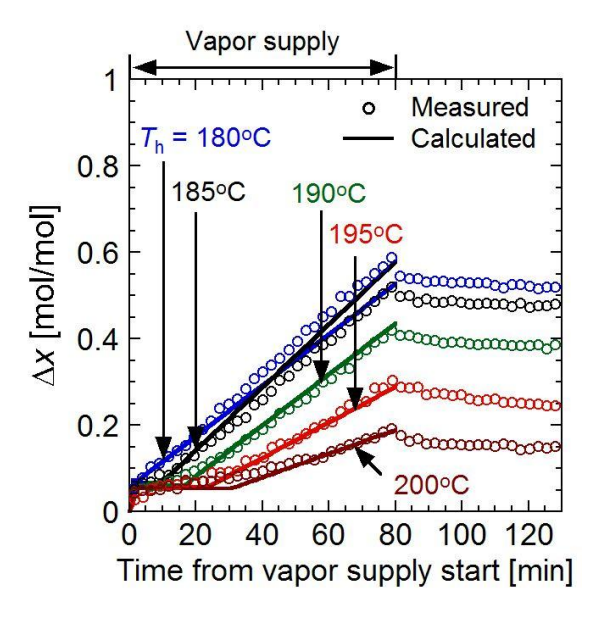


Figure 3.3-13 Hydration profiles of LiCl/MgO (α = 0.10) at $T_{\rm d}$ = 300°C, $T_{\rm h}$ = 180–200°C, $p_{\rm H2O}$ = 57.8 kPa, and $t_{\rm v}$ = 80 min. Calculated profiles are obtained at **Section 3.4.2.2**. Blue line: calculated line at 180°C, black line: calculated line at 185°C, green line: calculated line at 190°C, red line: calculated line at 195°C, brown line: calculated line at 200°C, respectively.

3.3.2.3 Relationship between vapor pressure and hydration behavior

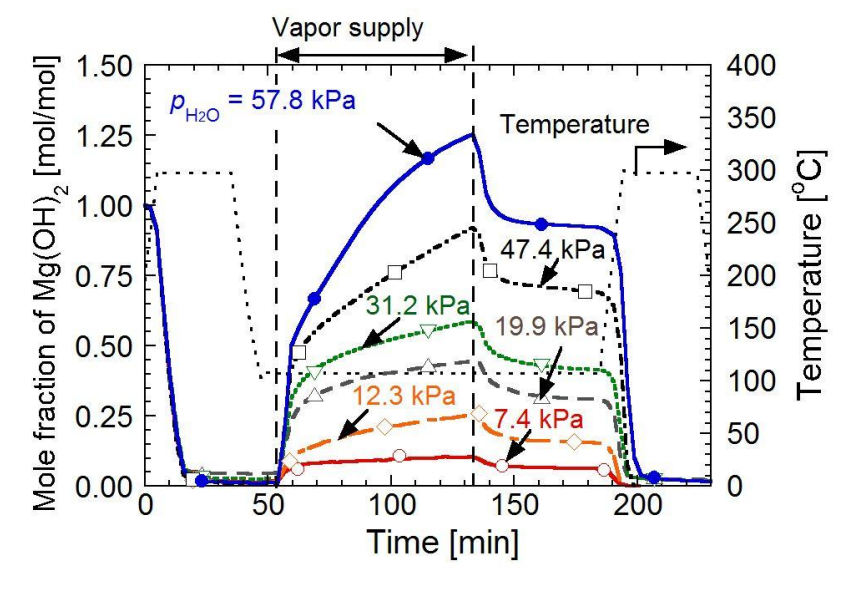


Figure 3.3-14 Dehydration–hydration profiles of LiCl/Mg(OH)₂ ($\alpha = 0.10$) at $T_d = 300$ °C, $T_h = 110$ °C, $p_{\text{H2O}} = 7.4 - 57.8$ kPa, and $t_v = 80$ min.

The dehydration–hydration profiles of LiCl/Mg(OH)₂ (α = 0.10) with different values of $p_{\rm H2O}$ are shown in **Figure 3.3-14**. The hydration temperature ($T_{\rm h}$) was fixed as 110°C. The value of Δx_1 increased by increase of the water vapor pressure ($p_{\rm H2O}$).

3.3.2.4 Relationship between time for vapor supply and hydration behavior

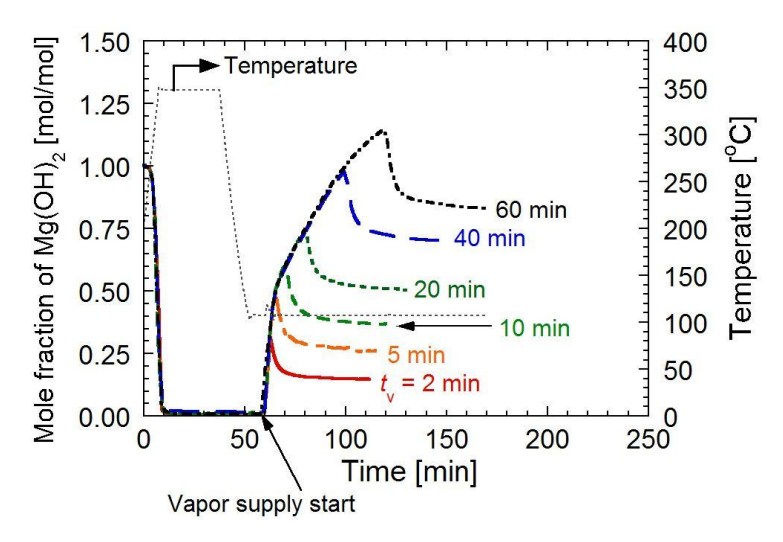


Figure 3.3-15 Dehydration–hydration profiles of LiCl/Mg(OH)₂ (α = 0.10) at $T_{\rm d}$ = 350°C, $T_{\rm h}$ = 110°C, $p_{\rm H2O}$ = 57.8 kPa, and $t_{\rm v}$ = 2–60 min.

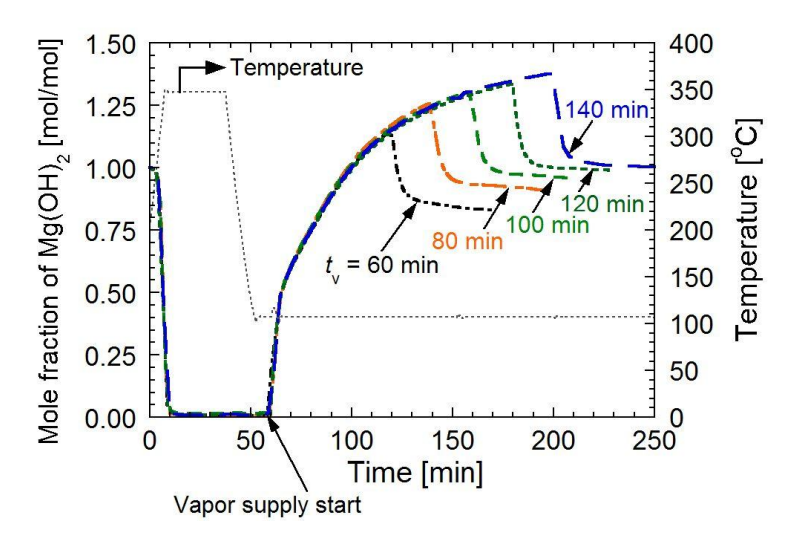


Figure 3.3-16 Dehydration–hydration profiles of LiCl/Mg(OH)₂ (α = 0.10) at $T_{\rm d}$ = 350°C, $T_{\rm h}$ = 110°C, $p_{\rm H2O}$ = 57.8 kPa, and $t_{\rm v}$ = 60–140 min.

The dehydration–hydration profiles of LiCl/Mg(OH)₂ ($\alpha = 0.10$) at 110°C with several hydration periods are shown in **Figure 3.3-15** and **Figure 3.3-16**. The water vapor pressure ($p_{\rm H2O}$) was fixed as 57.8 kPa. The hydration was proceeded with time. The hydration was completed at which $x_{\rm c}$ reached to 1.00 mol/mol at $t_{\rm v} = 140$ min.

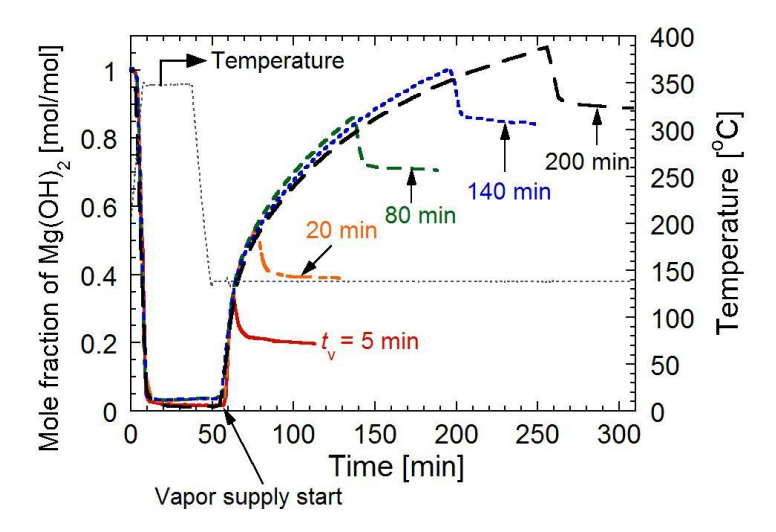


Figure 3.3-17 Dehydration–hydration profiles of LiCl/Mg(OH)₂ (α = 0.10) at $T_{\rm d}$ = 350°C, $T_{\rm h}$ = 140°C, $p_{\rm H2O}$ = 57.8 kPa, and $t_{\rm v}$ = 5–200 min.

The dehydration–hydration profiles of LiCl/Mg(OH)₂ ($\alpha = 0.10$) at 140°C with several hydration periods are shown in **Figure 3.3-17**. The water vapor pressure ($p_{\rm H2O}$) was fixed as 57.8 kPa. The hydration was proceeded with time.

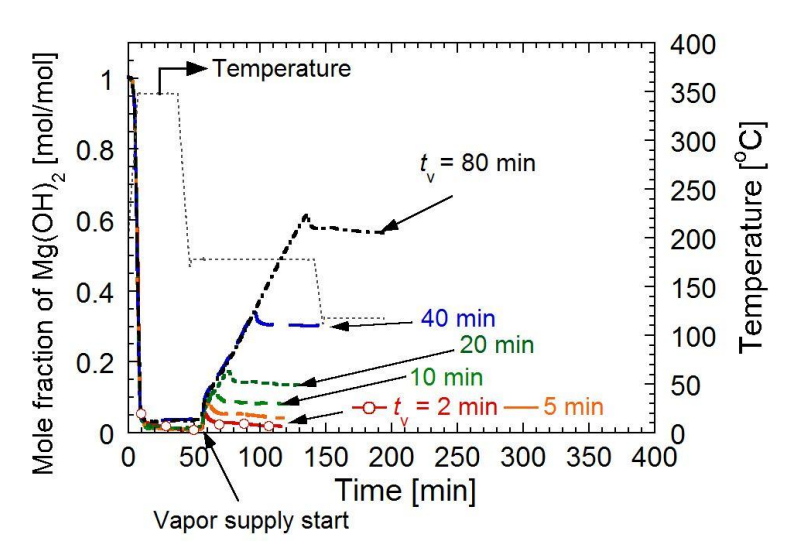


Figure 3.3-18 Dehydration–hydration profiles of LiCl/Mg(OH)₂ (α = 0.10) at $T_{\rm d}$ = 350°C, $T_{\rm h}$ = 180°C, $p_{\rm H2O}$ = 57.8 kPa, and $t_{\rm v}$ = 2–80 min.

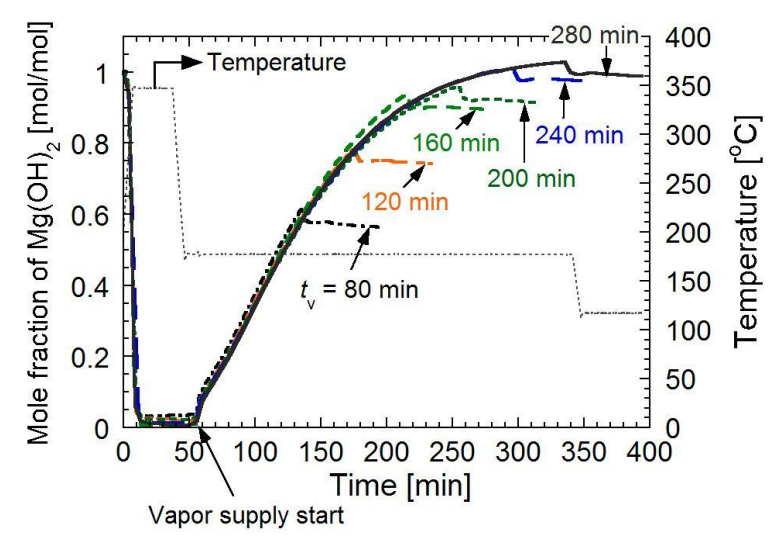


Figure 3.3-19 Dehydration–hydration profiles of LiCl/Mg(OH)₂ ($\alpha = 0.10$) at $T_d = 350$ °C, $T_h = 180$ °C, $p_{H2O} = 57.8$ kPa, and $t_v = 80-280$ min.

The dehydration–hydration profiles of LiCl/Mg(OH)₂ ($\alpha = 0.10$) at 180°C with several hydration periods are shown in **Figure 3.3-18** and **Figure 3.3-19**. The water vapor pressure ($p_{\rm H2O}$) was fixed as 57.8 kPa. Temperature in the reactor was cooled down at 120°C after vapor supply to avoid dehydration of the samples under the drying operation. The hydration was proceeded with time. The hydration was almost completed at which $x_{\rm c}$ reached 0.990 mol/mol at $t_{\rm v} = 280$ min.

3.4 Discussion

3.4.1 Heat output capacity

3.4.1.1 Relationship between composition and heat output capacity

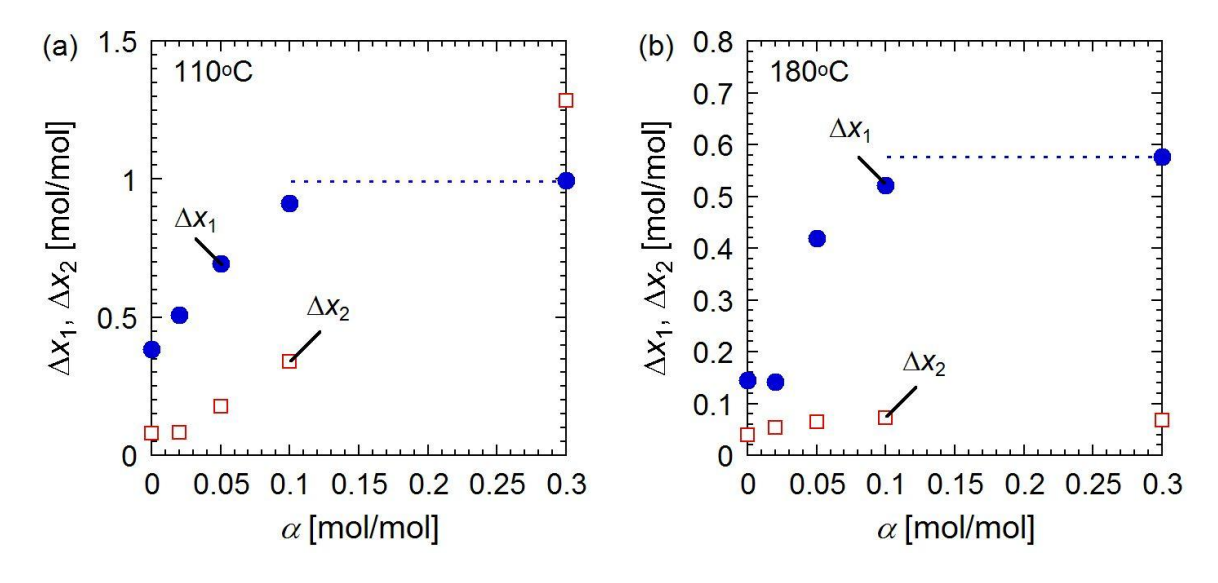


Figure 3.4-1 Relationship between α and Δx_1 , Δx_2 of the materials at $T_d = 300$ °C, $p_{H2O} = 57.8$ kPa, and 80 min for vapor supply. Starting materials were LiCl/Mg(OH)₂ ($\alpha = 0$ –0.30): (a) $T_h = 110$ °C; (b) $T_h = 180$ °C.

A Relationship between LiCl mixing ratio (α) of the samples and Δx_1 , Δx_2 of the materials at $T_d = 300^{\circ}\text{C}$, $T_h = 110^{\circ}\text{C}$, 180°C , $p_{\text{H2O}} = 57.8$ kPa is shown in **Figure 3.4-1**. The value of Δx_1 for LiCl/Mg(OH)₂ was increased by α for LiCl/Mg(OH)₂ ($\alpha = 0, 0.02, 0.05, 0.10$). On the other hand, that of Δx_1 for LiCl/Mg(OH)₂ ($\alpha = 0.10, 0.30$) was similar. The value of Δx_1 for LiCl/Mg(OH)₂ ($\alpha = 0.10, 0.30$) was higher than 0.90 mol/mol at $T_h = 110^{\circ}\text{C}$. **Figure 3.4-2** shows the heat output capacity of LiCl/Mg(OH)₂ with each mixing ratio at $T_h = 110^{\circ}\text{C}$. The heat output capacity increased with increase of α . Specifically, the heat output capacity of LiCl/Mg(OH)₂ at mixing ratios $\alpha = 0.05, 0.10$, and 0.30 was greater than 1000 kJ kg⁻¹. **Figure 3.4-3** shows the heat output capacity of LiCl/Mg(OH)₂ with each mixing ratio at $T_h = 180^{\circ}\text{C}$. The maximum value of heat output capacity was 724 kJ kg⁻¹ for LiCl/Mg(OH)₂ ($\alpha = 0.10$).

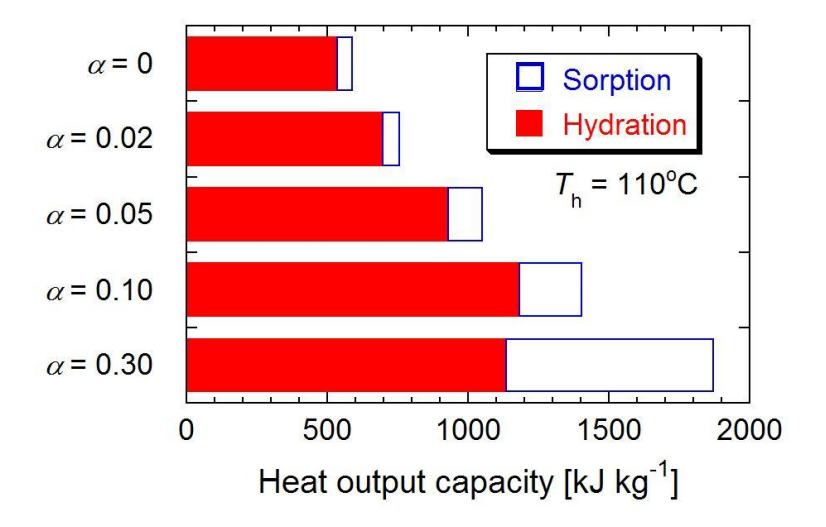


Figure 3.4-2 Heat output capacities of LiCl/Mg(OH)₂ at mixing ratios $\alpha = 0$ –0.30, $T_{\rm d} = 300$ °C, $T_{\rm h} = 110$ °C, $p_{\rm H2O} = 57.8$ kPa, and $t_{\rm v} = 80$ min.

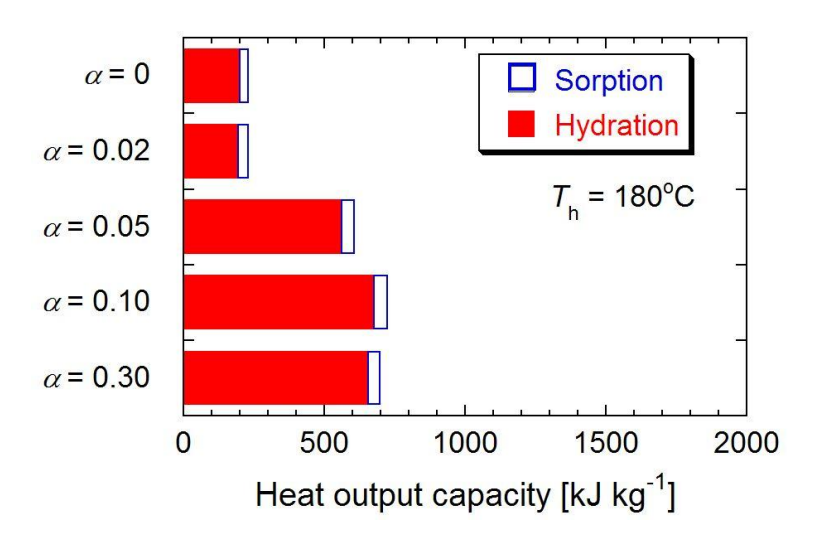


Figure 3.4-3 Heat output capacities of LiCl/Mg(OH)₂ at mixing ratios $\alpha = 0$ –0.30, $T_{\rm d} = 300$ °C, $T_{\rm h} = 180$ °C, $p_{\rm H2O} = 57.8$ kPa, and $t_{\rm v} = 80$ min.

3.4.1.2 Relationship between hydration temperature and heat output capacity

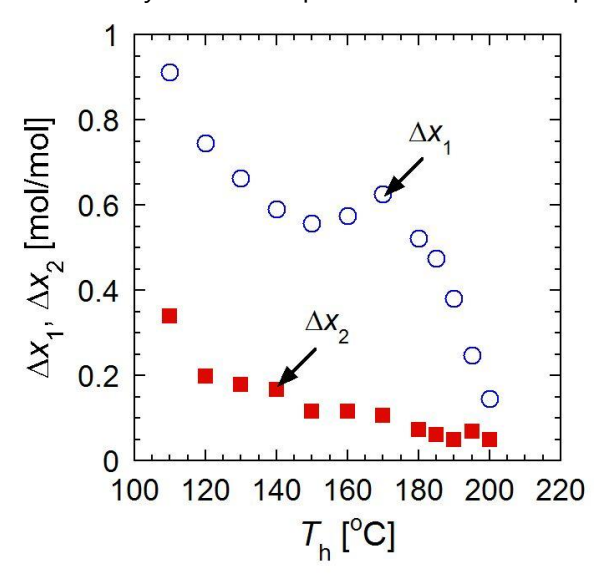


Figure 3.4-4 Relationship between T_h and Δx_1 , Δx_2 of the materials at $T_d = 300$ °C, $T_h = 110-200$ °C, $p_{\rm H2O} = 57.8$ kPa, and 80 min for vapor supply. Starting materials were LiCl/Mg(OH)₂ ($\alpha = 0.10$).

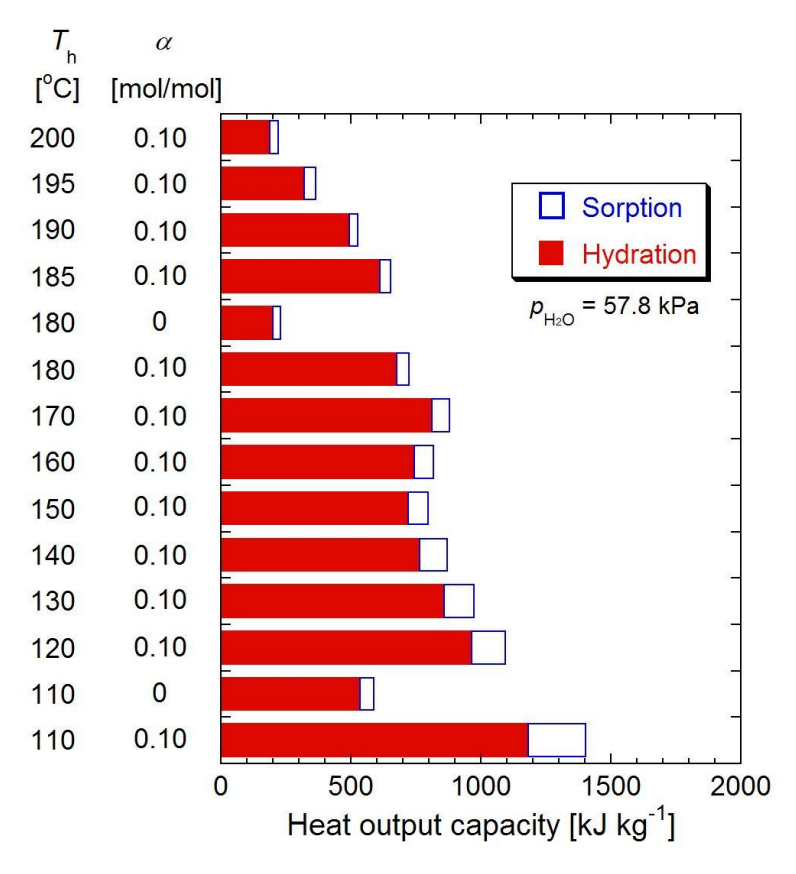


Figure 3.4-5 Heat output capacities of LiCl/Mg(OH)₂ at mixing ratios $\alpha = 0$ (authentic Mg(OH)₂) and 0.10, $T_d = 300$ °C, $T_h = 110-200$ °C, $T_{H2O} = 57.8$ kPa, and $T_{H2O} = 57.8$ kPa.

A relationship between T_h and Δx_1 , Δx_2 of the materials ($\alpha = 0.10$) at several hydration

temperature (T_h) is shown in **Figure 3.4-4**. The value of Δx_1 decreased with T_h at 110–150°C, and it increased with T_h at 150–170°C, then decreased with T_h at 170–200°C. This behavior would be caused by a change of the rate controlling step for an overall hydration of the sample. On the other hand, the value of Δx_2 shows downward trend at T_h at 110–200°C. The value of Δx_2 at 110°C was specifically large compared with that of Δx_2 at 120–200°C.

Figure 3.4-5 shows the heat output capacity of authentic Mg(OH)₂ (LiCl/Mg(OH)₂ ($\alpha = 0$)) and LiCl/Mg(OH)₂ ($\alpha = 0.10$) with several values of T_h . The heat output capacity of authentic Mg(OH)₂ at 110°C and 180°C are obtained from **Figure 3.4-2** and **Figure 3.4-3**. The heat output capacity at 180°C was 229 kJ kg⁻¹ for authentic Mg(OH)₂ and 724 kJ kg⁻¹ for LiCl/Mg(OH)₂ ($\alpha = 0.10$), and the heat output capacity at 110°C was 589 kJ kg⁻¹ for authentic Mg(OH)₂ and 1.40 × 10³ kJ kg⁻¹ for LiCl/Mg(OH)₂ ($\alpha = 0.10$). The heat output capacity was increased more than twice by LiCl-modification. The heat output capacities for LiCl/Mg(OH)₂ at $T_h = 110-180$ °C were higher than the heat output capacity of latent heat storage (around 100–500 kJ kg⁻¹) [6,7].

3.4.1.3 Relationship between vapor pressure and heat output capacity

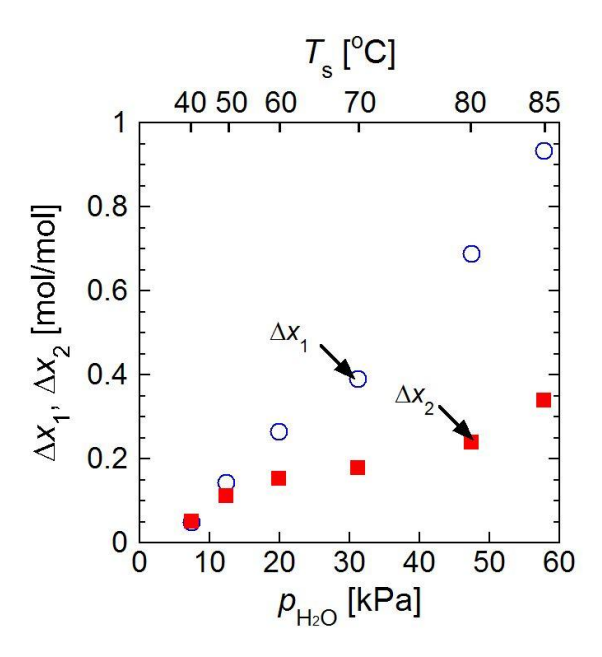


Figure 3.4-6 Relationship between $p_{\rm H2O}$ and Δx_1 , Δx_2 of LiCl/MgO ($\alpha = 0.10$) at $T_{\rm d} = 300^{\circ}$ C, $T_{\rm h} = 110^{\circ}$ C and 80 min for vapor supply. $T_{\rm s}$ indicates saturated vapor temperature.

Figure 3.4-6 shows the relationship between $p_{\rm H2O}$ and Δx_1 , Δx_2 . Both Δx_1 and Δx_2 show a linear trend for $p_{\rm H2O}$. This suggests that the hydration rate of LiCl/MgO depends linearly on $p_{\rm H2O}$.

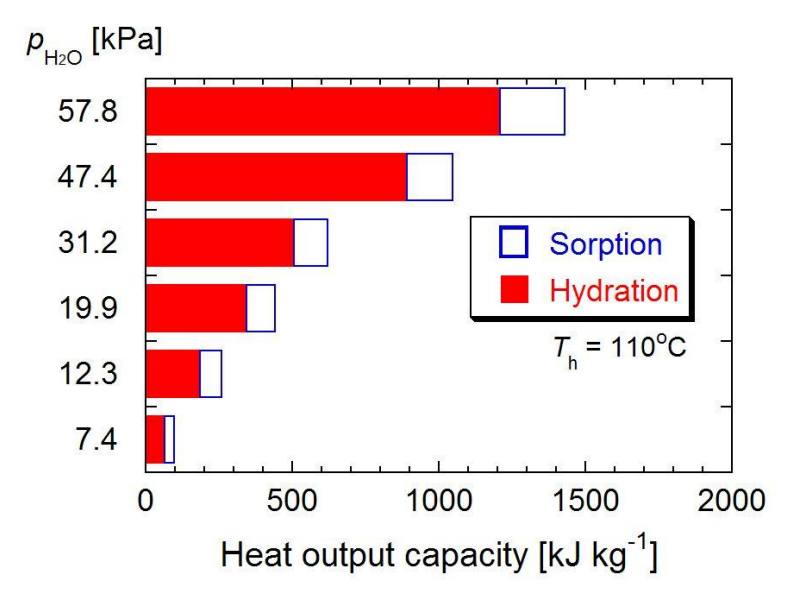


Figure 3.4-7 Heat output capacities of LiCl/Mg(OH)₂ (α = 0.10) at $T_{\rm d}$ = 300°C, $T_{\rm h}$ = 110°C, $p_{\rm H2O}$ = 7.4–57.8 kPa, and $t_{\rm v}$ = 80 min.

Figure 3.4-7 shows the heat output capacities of LiCl/Mg(OH)₂ ($\alpha = 0.10$) with each $p_{\rm H2O}$. The maximum value of heat output capacity was 1.43×10^3 kJ kg⁻¹ for $p_{\rm H2O} = 57.8$ kPa.

3.4.1.4 Relationship between time for vapor supply and heat output capacity

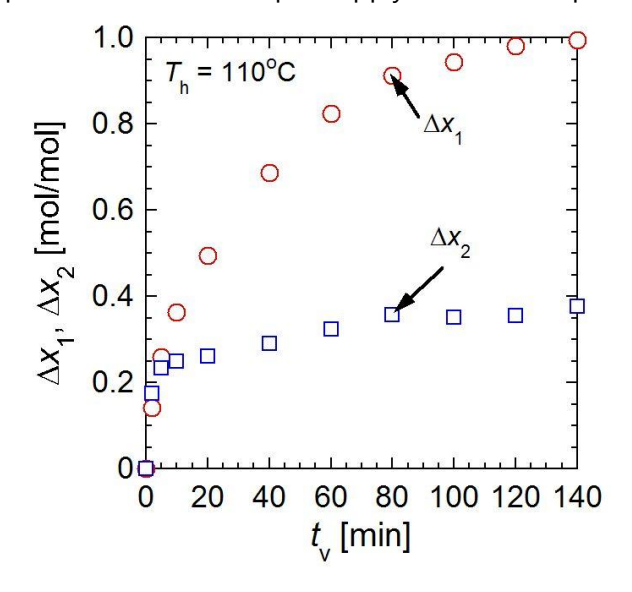


Figure 3.4-8 Relationship between t_v and Δx_1 , Δx_2 of the materials at $T_d = 350$ °C, $T_h = 110$ °C, and $p_{\text{H2O}} = 57.8$ kPa. Starting materials were LiCl/Mg(OH)₂ ($\alpha = 0.10$).

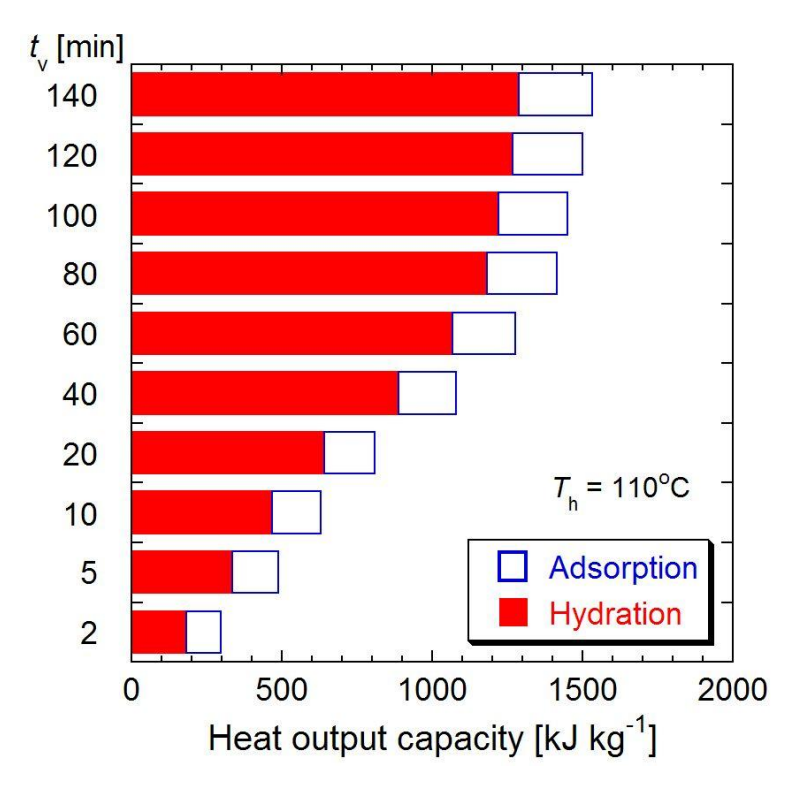


Figure 3.4-9 Heat output capacities of LiCl/Mg(OH)₂ (α = 0.10) at $T_{\rm d}$ = 350°C, $T_{\rm h}$ = 110°C, $p_{\rm H2O}$ = 57.8 kPa, and $t_{\rm v}$ = 2–140 min.

Figure 3.4-8 shows the relationship between t_v and Δx_1 , Δx_2 of the sample ($\alpha = 0.10$) at $T_h = 110$ °C and $p_{\rm H2O} = 57.8$ kPa. The plots of Δx_1 showed convex upward curve. On the other hand, the plots of Δx_2 rose steeply for first 5 min, and then increased gradually and linearly for 5–140 min.

Figure 3.4-9 shows the heat output capacities of LiCl/Mg(OH)₂ ($\alpha = 0.10$) with each t_v (2–140 min). The heat output capacity was varied from 297 kJ kg⁻¹ to 1.53×10^3 kJ kg⁻¹. The heat output capacity increased only 8.4% from $t_v = 80$ min (1.41×10^3 kJ kg⁻¹) to $t_v = 140$ min (1.53×10^3 kJ kg⁻¹). When the change of heat output capacity between current period and next period was less than 10%, it is assumed that the current heat output capacity was enough and representative value under the condition. The result suggests 80 min of vapor supply is enough for heat output operation at 110°C.

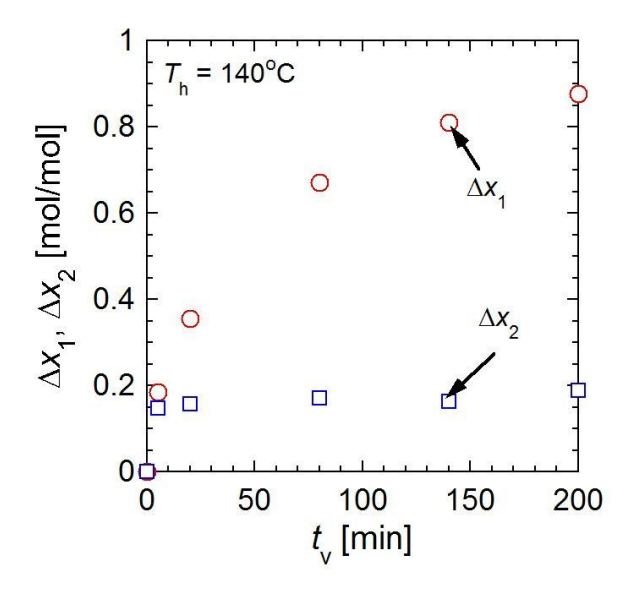


Figure 3.4-10 Relationship between t_v and Δx_1 , Δx_2 of the materials at $T_d = 350$ °C, $T_h = 140$ °C, and $p_{\text{H2O}} = 57.8 \text{ kPa}$. Starting materials were LiCl/Mg(OH)₂ ($\alpha = 0.10$).

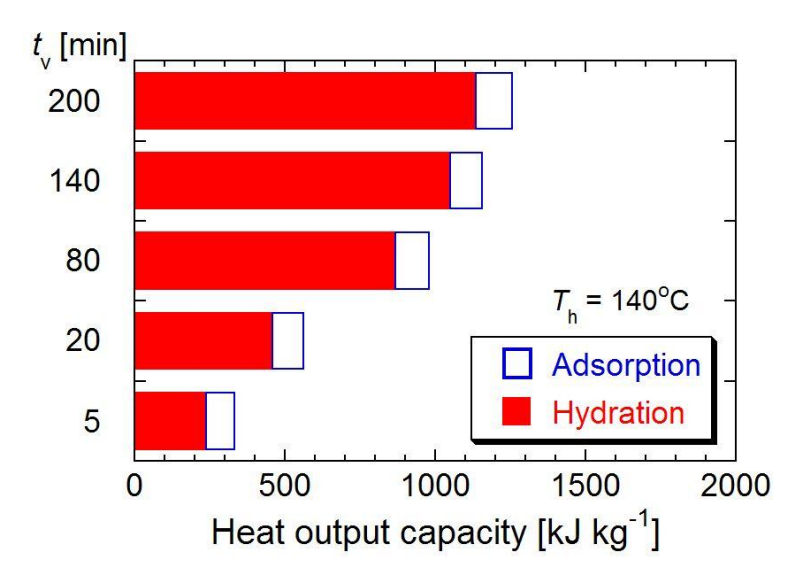


Figure 3.4-11 Heat output capacities of LiCl/Mg(OH)₂ ($\alpha = 0.10$) at $T_d = 350$ °C, $T_h = 140$ °C, $p_{H2O} = 57.8$ kPa, and $t_v = 5-200$ min.

Figure 3.4-10 shows the relationship between t_v and Δx_1 , Δx_2 of the sample ($\alpha = 0.10$) at $T_h = 140$ °C and $p_{H2O} = 57.8$ kPa. The plots of Δx_1 showed convex upward curve. On the other hand, the plots of Δx_2 rose steeply for first 5 min, and then it remained around 0.17 mol/mol for 5–200 min.

Figure 3.4-11 shows the heat output capacities of LiCl/Mg(OH)₂ (α = 0.10) with each t_v (5–200 min). The heat output capacity was varied from 334 kJ kg⁻¹ to 1.26 × 10³ kJ kg⁻¹. The heat output capacity increased only 8.7% from t_v = 140 min (1.16 × 10³ kJ kg⁻¹) to t_v = 200 min (1.26 × 10³ kJ kg⁻¹). It suggests 140 min of vapor supply is enough for heat output operation at 140°C.

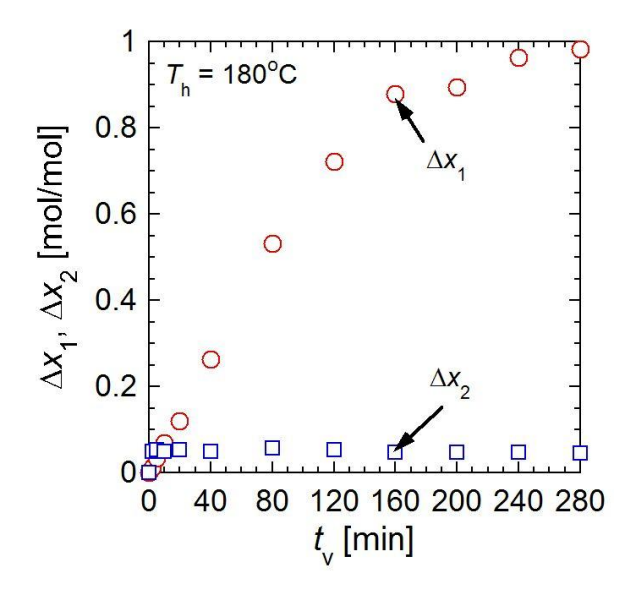


Figure 3.4-12 Relationship between t_v and Δx_1 , Δx_2 of the materials at $T_d = 350^{\circ}\text{C}$, $T_h = 180^{\circ}\text{C}$, and $p_{\text{H2O}} = 57.8 \text{ kPa}$. Starting materials were LiCl/Mg(OH)₂ ($\alpha = 0.10$).

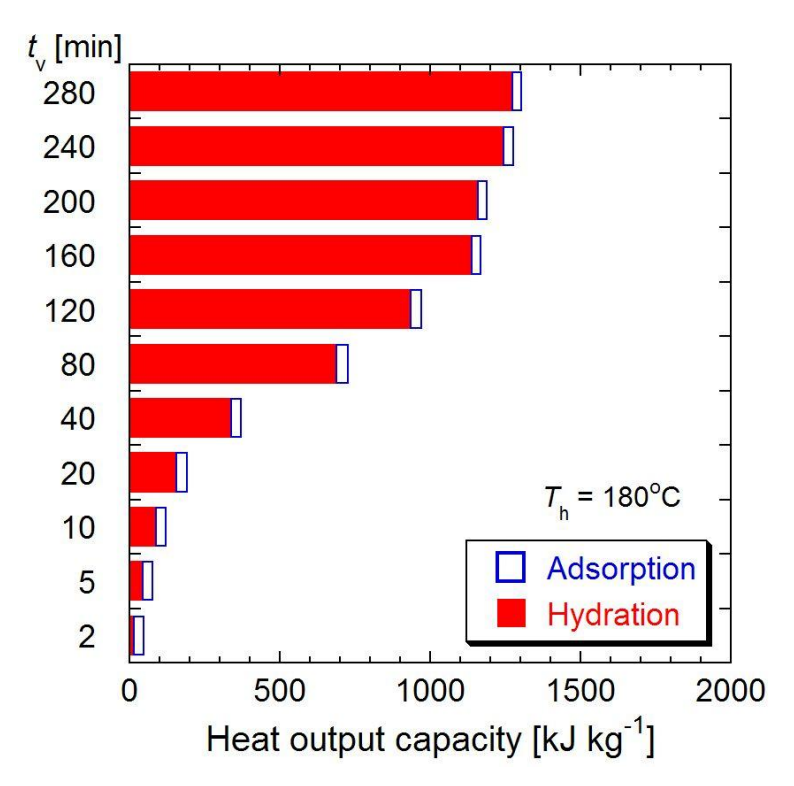


Figure 3.4-13 Heat output capacities of LiCl/Mg(OH)₂ (α = 0.10) at $T_{\rm d}$ = 350°C, $T_{\rm h}$ = 110°C, $p_{\rm H2O}$ = 57.8 kPa, and $t_{\rm v}$ = 2–280 min.

Figure 3.4-12 shows the relationship between t_v and Δx_1 , Δx_2 of the sample ($\alpha = 0.10$) at $T_h = 180$ °C and $p_{\rm H2O} = 57.8$ kPa. The plots of Δx_1 showed linear relation for 0–120 min, and then it showed convex upward curve for 120–280 min. On the other hand, the plots of Δx_2 rose steeply for first 2 min,

and then it showed almost constant value (0.05) for 2–280 min.

Figure 3.4-13 shows the heat output capacities of LiCl/Mg(OH)₂ (α = 0.10) with each t_v (2–280 min). The heat output capacity was varied from 47 kJ kg⁻¹ to 1.30 × 10³ kJ kg⁻¹. The heat output capacity increased only 1.8% from t_v = 160 min (1.17 × 10³ kJ kg⁻¹) to t_v = 200 min (1.19 × 10³ kJ kg⁻¹). It suggests 160 min of vapor supply is enough for heat output operation at 180°C.

3.4.2 Kinetic analysis of hydration for lithium chloride-modified magnesium oxide

3.4.2.1 Shrinking core model

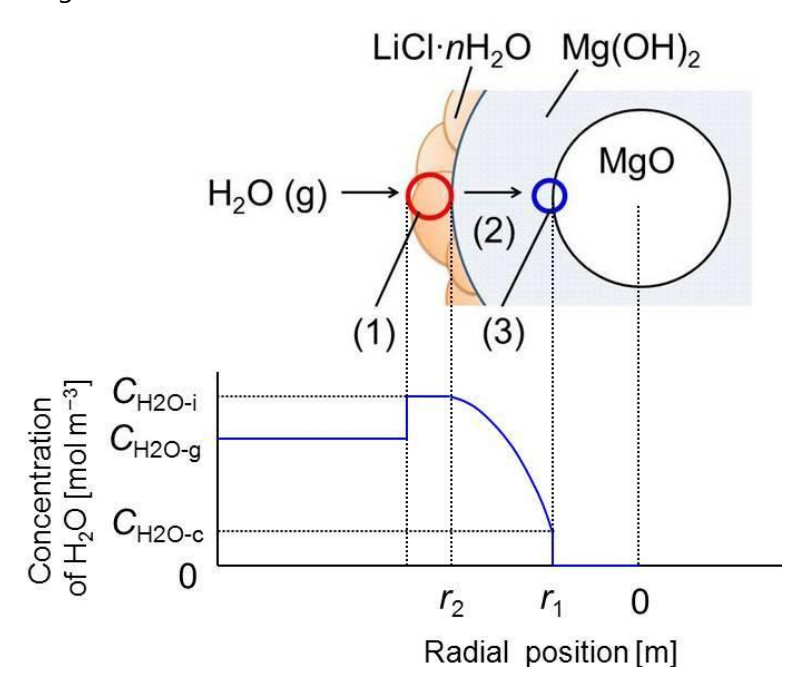


Figure 3.4-14 Scheme of the shrinking core model for hydration of LiCl/MgO (not to actual scale).

As mentioned at **Section 3.1**, several gas-solid reaction models have been proposed. A specific surface area of LiCl/Mg(OH)₂ (α = 0.10) was 24.6 m² g⁻¹, thereby LiCl/MgO (α = 0.10) would not be a porous material. Hence, the pore model was not employed in this work. LiCl/MgO was used as powders. Consequently, LiCl/MgO was not pellets consist of "grains". Hence, the grain model was excluded. The shrinking model was applied in this work. Shrinking core model has been applied to many gas-solid reaction systems [8–12]. In this study, shrinking core model with surface modification is studied. **Figure 3.4-14** shows a scheme of the model for hydration of LiCl/MgO. The concentration of H₂O in the LiCl·nH₂O layer is thought to be higher than that of H₂O in the main body of gas because LiCl is a hygroscopic compound. LiCl·nH₂O (n > 1) is considered as a media for H₂O transportation. The processes of H₂O transport and consumption consists of three components; (1) H₂O absorption at LiCl·nH₂O, (2) H₂O diffusion in the Mg(OH)₂ (ash) layer, (3) Hydration at the interface of the shrinking core. In this work the flow rate of the gas mixture (77 mL min⁻¹) is enough high to avoid the overall hydration was controlled by gas film diffusion. Shrinking core model with

surface modification has some assumptions; (a) isothermal condition in the particle, (b) a particle size will not be changed, (c) first-order irreversible reaction at the interface of the shrinking core, (d) pseudo-steady assumption for concentration distribution of H_2O . In this paper, concentration of H_2O is expressed as C_{H2O} [mol m⁻³]. Subscript of i indicates interface between LiCl· nH_2O and Mg(OH)₂, and that of c indicates shrinking core.

In this section, the hydration of LiCl/MgO ($\alpha = 0.10$) at $T_h = 110-200$ °C, $p_{H2O} = 57.8$ kPa is studied. An overall rate equation would be simplified when one process is a rate controlling step. $f(\Delta x_1)$ in the following equations indicates a function of rate analysis.

(a) Controlled by water absorption of LiCl·nH2O

The water absorption rate at $LiCl \cdot nH_2O$ under a constant water vapor pressure would be express as below.

$$k_{\text{abs}} t_{\text{V}} = \Delta x_{1} \equiv f_{\text{L}} (\Delta x_{1}) \tag{3-6}$$

Here, k_{abs} [s⁻¹]: absorption rate constant.

For ash diffusion control or interface reaction control, relationships between time for vapor supply (t_v) and conversion of the hydration (Δx_1) is expressed as below [12].

(b) Controlled by diffusion in Mg(OH)2 (ash) layer

$$\frac{t_{V}}{t^{*}} = 1 - 3(1 - \Delta x_{1})^{2/3} + 2(1 - \Delta x_{1}) \equiv f_{A}(\Delta x_{1})$$
(3-7)

$$t^* = \frac{\rho r_2^2}{6C_{\text{H2O},i}D_{\text{aP}}} \tag{3-8}$$

Here, ρ [mol m⁻³]: molar density, r_2 [m]: radius of the particle, D_{eP} [m² s⁻¹]: effective diffusion coefficient in the Mg(OH)₂ layer, t^* [s]: characteristic time.

(c) Controlled by the hydration at interface

$$\frac{t_{\rm V}}{t^*} = 1 - \left(1 - \Delta x_{\rm l}\right)^{1/3} \equiv f_{\rm R} \left(\Delta x_{\rm l}\right)$$
 (3-9)

$$t^* = \frac{\rho r_2}{C_{\text{H2O-i}} k_i} \tag{3-10}$$

Here, k_i [m s⁻¹]: hydration rate constant per unit area at the interface of shrinking core.

First, the relationship between t_v and $f_G(\Delta x_1)$, $f_A(\Delta x_1)$, or $f_R(\Delta x_1)$ were plotted. Then, a rate controlling process can be known by the function which has a best linearity.

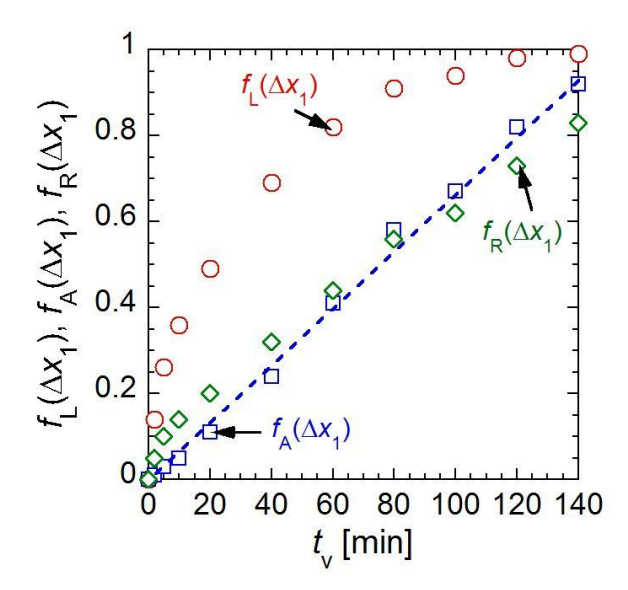


Figure 3.4-15 Test plots for kinetic analysis by shrinking core model for LiCl/MgO ($\alpha = 0.10$) at 110°C.

Test plots for kinetic analysis by shrinking core model for LiCl/MgO (α = 0.10) at 110°C are shown in **Figure 3.4-15**. The function of ash diffusion control shows best linearity. Hence, ash diffusion is assumed to be the rate controlling process of overall hydration rate at 110°C.

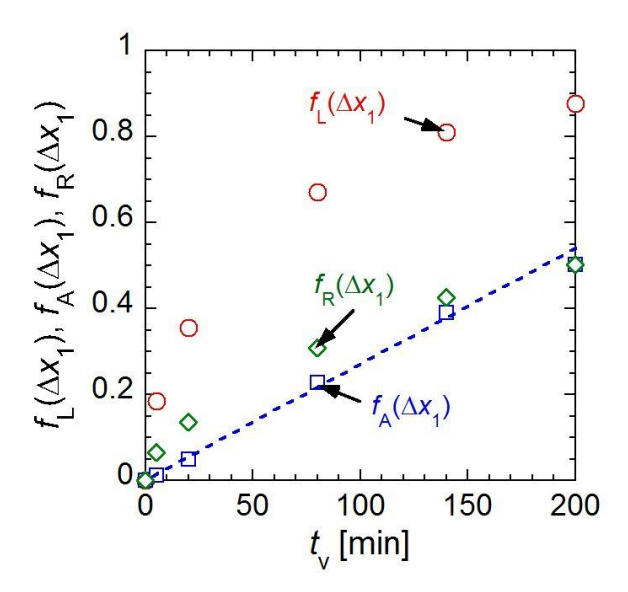


Figure 3.4-16 Test plots for kinetic analysis by shrinking core model for LiCl/MgO ($\alpha = 0.10$) at 140°C.

Test plots for kinetic analysis by shrinking core model for LiCl/MgO (α = 0.10) at 140°C are shown in **Figure 3.4-16**. The function of ash diffusion control shows best linearity. Hence, ash diffusion is also assumed to be the rate controlling process of overall hydration rate at 140°C.

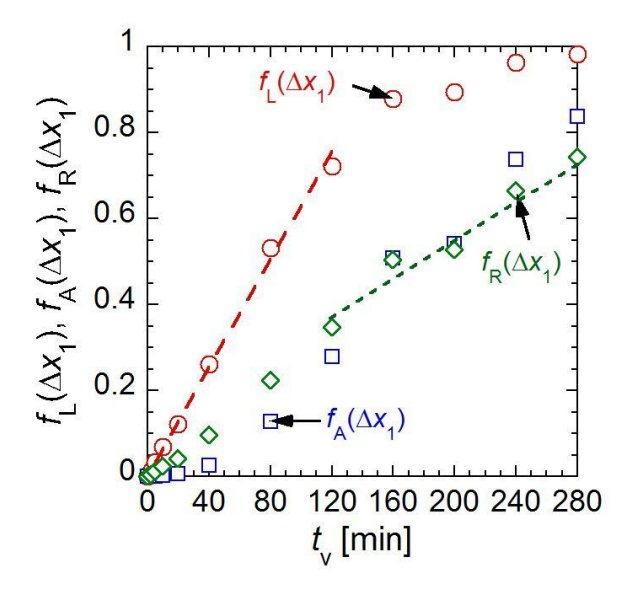


Figure 3.4-17 Test plots for kinetic analysis by shrinking core model for LiCl/MgO ($\alpha = 0.10$) at 180°C.

Test plots for kinetic analysis by shrinking core model for LiCl/MgO ($\alpha = 0.10$) at 180°C are shown in **Figure 3.4-17**. The function of water absorption of LiCl·nH₂O control shows best linearity at $t_v = 0$ –120 min, and the function of interface reaction control shows best linearity at $t_v = 120$ –280 min. Hence, water absorption at LiCl·nH₂O is the rate controlling process of overall hydration rate at $t_v = 0$ –120 min ($\Delta x_1 \le 0.72$ mol/mol), and interface reaction is assumed to be the rate controlling process of overall hydration rate at $t_v = 120$ –280 min ($\Delta x_1 \ge 0.72$ mol/mol).

3.4.2.2 Hydration rate equations and kinetic parameters

The change of the mole fraction of Mg(OH)₂ (Δx) consists of conversion of the hydration (Δx_1) and the apparent change of x by sorption (Δx_2).

$$\Delta x = \Delta x_1 + \Delta x_2 \tag{3-11}$$

Usually, sorption rate is much faster than chemical reaction rate. In this work, it is assumed sorption rate is expressed as zero-order rate equation and the sorption process reach achieve equilibrium for 60 s (Eq. (3-12)).

$$\Delta x_2 = k_{\text{srp}} t_V \quad (t_V \le 60 \text{ s}), \ k_{\text{srp}} = \Delta x_{2-\text{eq}} / 60[\text{s}]$$

$$\Delta x_2 = \Delta x_{2-\text{eq}} \quad (t_V > 60 \text{ s})$$
(3-12)

Here, Δx_{2a-eq} [mol/mol]: sorbed amount of H₂O per unit mole of LiCl/MgO at equilibrium.

From experimental results, temperature dependence of Δx_2 at 120–200°C would be formulated as Eq. (3-13). The value of Δx_2 at 110°C was specifically large (**Figure 3.4-4**). Thus, the temperature

range of 120-200°C was selected.

$$\Delta x_{2-\text{eq}} = 1.56 \times 10^{-6} \times \exp\left(\frac{2.78 \times 10^4}{RT}\right)$$
 (3-13)

Here, R [J mol⁻¹ K⁻¹]: gas constant, and T [K]: absolute temperature. **Figure 3.4-18** shows measured and calculated values of Δx_2 at $t_v = 80$ min and $p_{\rm H2O} = 57.8$ kPa. The values of Δx_2 can be calculated by Eq. (3-13).

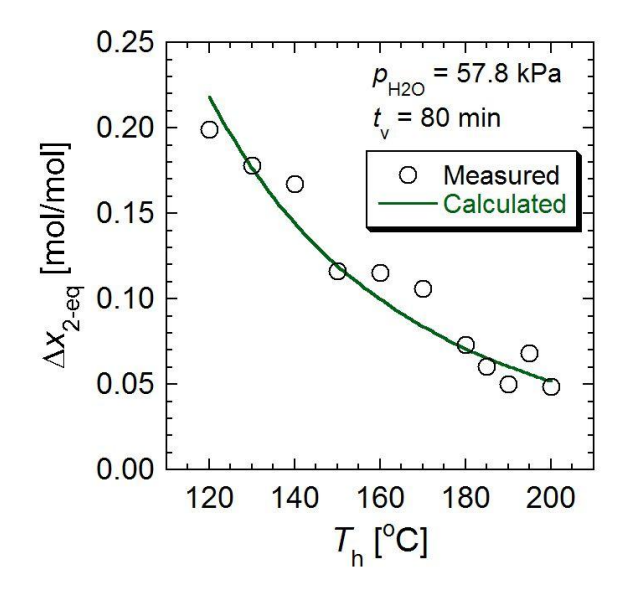


Figure 3.4-18 Measured and calculated values of Δx_{2-eq} at $t_v = 80$ min and $p_{H2O} = 57.8$ kPa.

Calculation of Δx_1 depends on the rate controlling process. Hydration rates at $120^{\circ}\text{C} \leq T_h \leq 150^{\circ}\text{C}$ and $180^{\circ}\text{C} \leq T_h \leq 200^{\circ}\text{C}$ are discussed at following discussions. In this work, hydration rate at 110°C is not examined because Δx_2 shows specifically behavior, and hydration rate at 160°C and 170°C are not analyzed because hydration would be a transition region at these temperatures.

$120^{\circ}\text{C} \le T_{\text{h}} \le 150^{\circ}\text{C}$

From the discussion at **Section 3.4.2.1**, ash diffusion would be expected as the rate controlling process of overall hydration rate at 120°C $\leq T_h \leq 150$ °C.

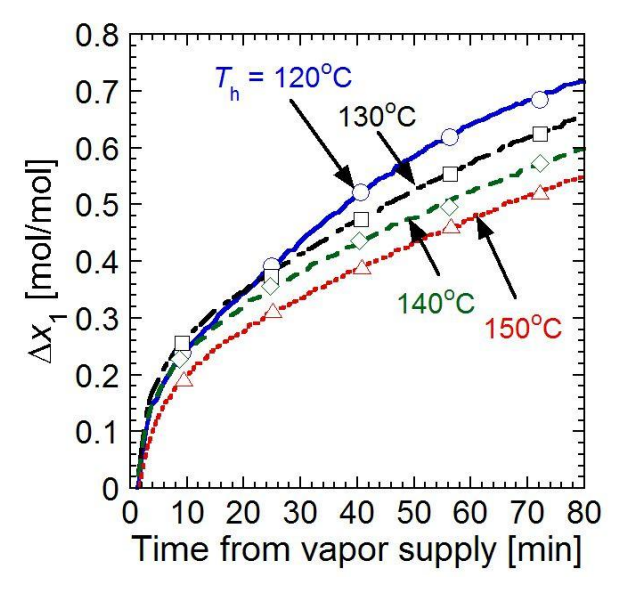


Figure 3.4-19 Calculated Δx_1 profile for each T_h (120°C $\leq T_h \leq$ 150°C).

The values of Δx_1 were obtained from the relationship of Eq. (3-11). The values of Δx were obtained from **Figure 3.3-11**, and the values of Δx_2 were calculated by Eq. (3-13). **Figure 3.4-19** shows calculated Δx_1 profile for each T_h (120°C $\leq T_h \leq 150$ °C). The values of t^* were obtained from the relationship of Eq. (3-7). Relationship between hydration temperature and characteristic time is shown in **Table 3.4-1**.

Table 3.4-1 Relationship between hydration temperature and characteristic time.

$T_{ m h}$	[°C]	120	130	140	150
t^*	[s]	1.72×10^{4}	2.22×10^{4}	2.87×10^{4}	3.56×10^4

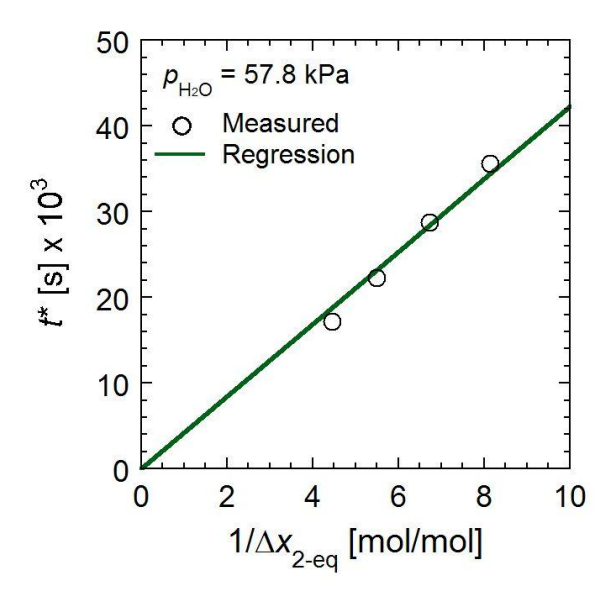


Figure 3.4-20 Relationship between $1/\Delta x_{2-eq}$ and t^* .

From Eq. (3-8), the value of t^* depends on the value of $1/C_{\rm H2O-i}$ (concentration of H₂O at interface between LiCl·nH₂O and Mg(OH)₂), and their relationship should be a line from the origin. $1/C_{\rm H2O-c}$ should correspond to $1/\Delta x_{2-\rm eq}$. Thus, the relationship between $1/\Delta x_{2-\rm eq}$ and t^* is plotted in **Figure 3.4-20**. The linear relation is found and the line is passing through the origin. Hence, the assumption in this section is valid. An empirical formula of the relationship between $1/\Delta x_{2-\rm eq}$ and t^* is expressed as follows.

$$t^* [s] = \frac{4.22 \times 10^3}{\Delta x_{2-eq} [mol/mol]}$$
 (3-14)

Comparisons between measured profiles and calculated profiles of Δx at 120°C and 150°C are shown in **Figure 3.4-21** and **Figure 3.4-22**. The submitted model can express the profiles of Δx .

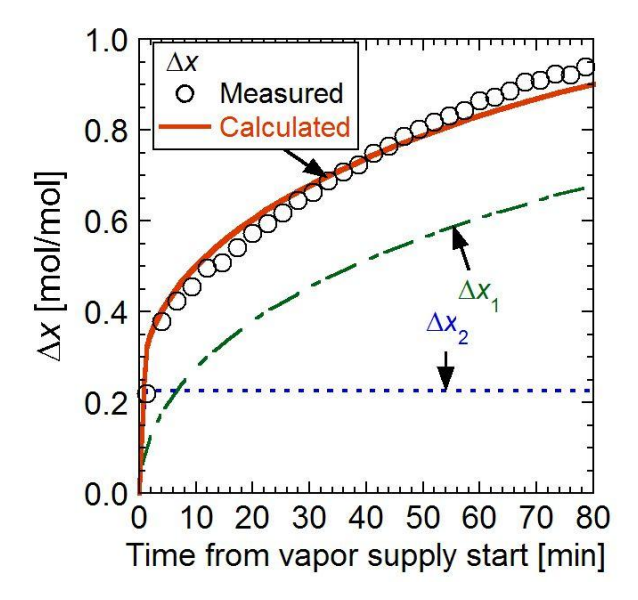


Figure 3.4-21 Comparison between calculated and measured value of Δx of LiCl/MgO ($\alpha = 0.10$) at $T_{\rm d} = 300^{\circ}$ C, $T_{\rm h} = 120^{\circ}$ C, $p_{\rm H2O} = 57.8$ kPa, and $t_{\rm v} = 80$ min.

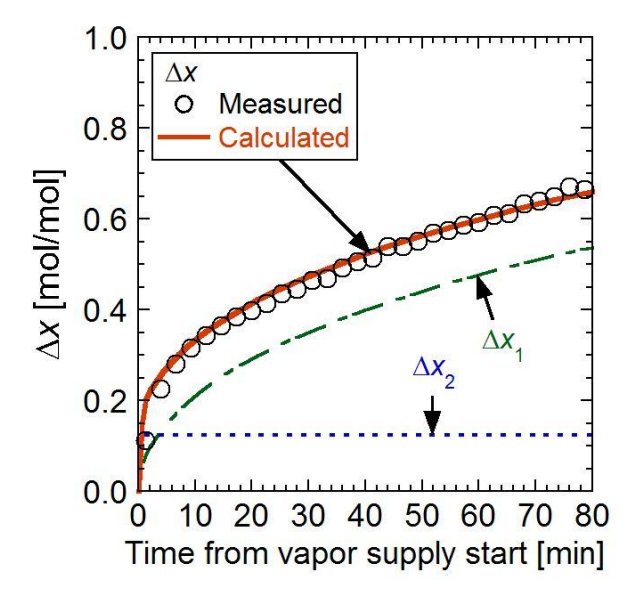


Figure 3.4-22 Comparison between calculated and measured value of Δx of LiCl/MgO (α = 0.10) at $T_{\rm d}$ = 300°C, $T_{\rm h}$ = 150°C, $p_{\rm H2O}$ = 57.8 kPa, and $t_{\rm v}$ = 80 min.

180°C $\leq T_{\rm h} \leq 200$ °C

From the discussion at **Section 3.4.2.1**, water absorption at LiCl·nH₂O is the rate controlling process of overall hydration rate at 180°C $\leq T_h \leq 200$ °C, $\Delta x_1 \leq 0.72$ mol/mol. From the results at **Section 3.3.2.2**, existence of induction time for hydration (t_{ind}) was indicated. The values of Δx_1 were obtained from the relationship of Eq. (3-11). The values of Δx were obtained from **Figure 3.3-13**, and the values of Δx_2 were calculated by Eq. (3-13). **Figure 3.4-23** shows calculated Δx_1 profile for each T_h (180°C $\leq T_h \leq 200$ °C).

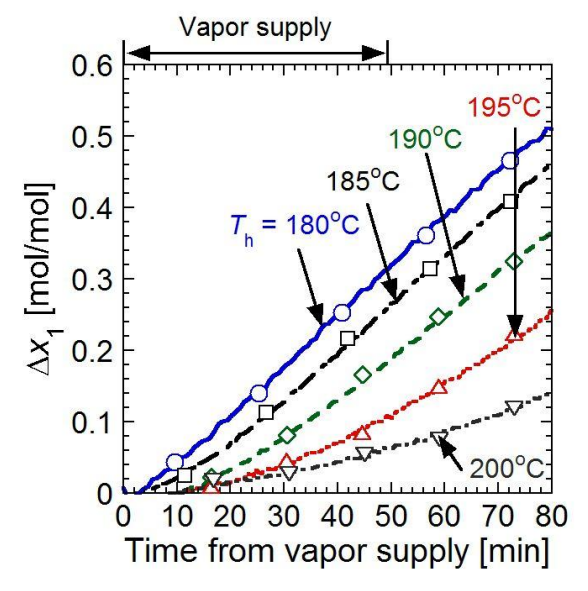


Figure 3.4-23 Calculated Δx_1 profile for each T_h (180°C $\leq T_h \leq$ 200°C).

The profiles of Δx_1 show good linearity from 50 min to 80 min. The regression line at 50–80

min was extrapolated, and intersection point at $\Delta x_1 = 0$ is calculated as t_{ind} in this work (**Figure 3.4-24**). The relationship between hydration temperature (T_h) and induction time for hydration (t_{ind}) is shown in **Figure 3.4-25**. A linear correlation is found. An empirical formula of the relationship between T_h and t_{ind} is expressed as Eq. (3-15).

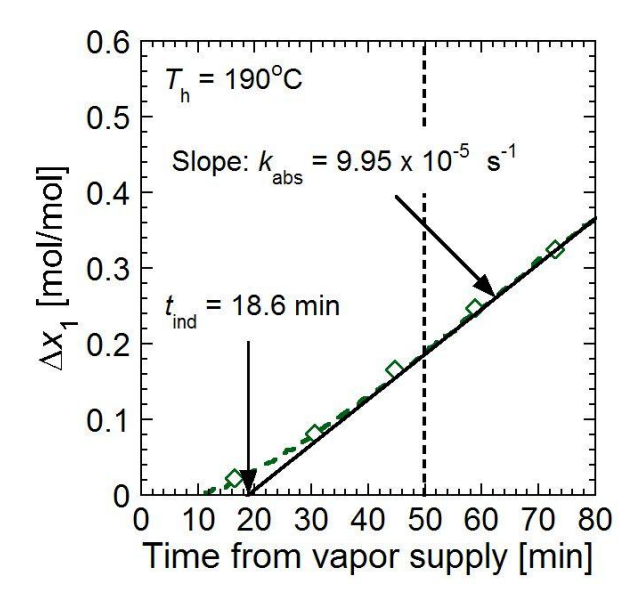


Figure 3.4-24 Calculation procedure of t_{ind} and k_{abs} . The solid line indicates regression line of Δx_1 .

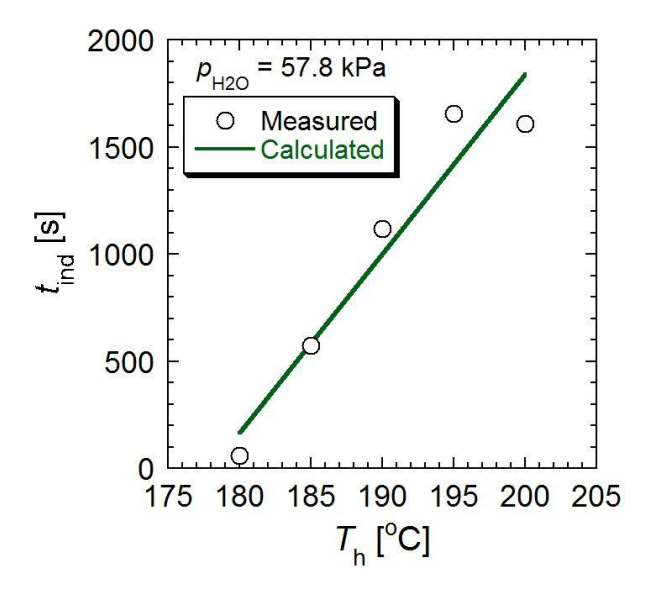


Figure 3.4-25 Relationship between hydration temperature (T_h) and induction time for hydration (t_{ind}) .

$$t_{\text{ind}} [s] = 83.7 \times T_{\text{h}} [^{\circ}\text{C}] - 1.49 \times 10^{4}$$
 (3-15)

The absorption rate constant (k_{abs}) was obtained from a slope of regression line of Δx_1 at 50–80 min (**Figure 3.4-24**).

The elementary reactions for hydration of LiCl·nH₂O are assumed.

$$\operatorname{LiCl} \cdot n \operatorname{H}_{2} \operatorname{O} + \operatorname{H}_{2} \operatorname{O} (g) \xrightarrow{k_{L1}} \operatorname{LiCl} \cdot (n+1) \operatorname{H}_{2} \operatorname{O}^{*} \xrightarrow{k_{L3}} \operatorname{LiCl} \cdot (n+1) \operatorname{H}_{2} \operatorname{O}$$
 (3-16)

Here, LiCl·(n+1)H₂O^{*} in Eq. (3-16) is an intermediate, k_{L1} [kPa⁻¹ s⁻¹], k_{L2} [s⁻¹], and k_{L3} [s⁻¹] are rate constants for each elementary reaction. A rate equation of overall hydration is expressed as follows.

$$\frac{dx}{dt} = k_{\text{abs}} = \frac{k_{\text{L1}}}{1 + (k_{\text{L2}}/k_{\text{L3}})} p_{\text{H2O}} \text{ [LiCl]}$$
(3-17)

The measured values for k_{abs} at 180–200°C are shown in **Figure 3.4-26**.

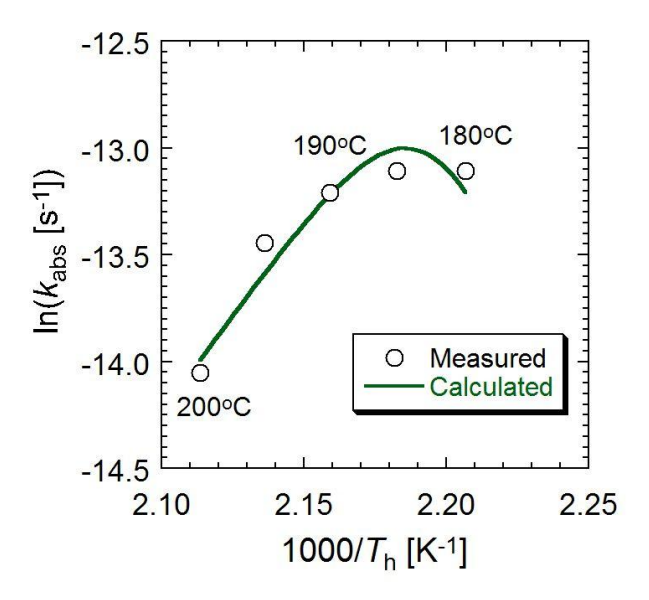


Figure 3.4-26 Measured and calculated values for k_{abs} at 180–200°C.

The measured values for $k_{\rm abs}$ at 190–200°C showed downward tendency. Thus, a reverse reaction (from LiCl·(n+1)H₂O* to LiCl·nH₂O and H₂O) is thought to be dominant at 180–200°C. Hence, $k_{\rm L2}$ is much greater than $k_{\rm L3}$ at 190–200°C. Eq. (3-17) is simplified by using the relation, $k_{\rm L2} >> k_{\rm L3}$.

$$\frac{dx}{dt} = k_{\text{abs}} = \frac{k_{\text{L1}} k_{\text{L3}}}{k_{\text{L2}}} p_{\text{H2O}} \text{ [LiCl]}$$
 (3-18)

A following relationship is obtained from measured values for k_{abs} at 190–200°C.

$$\frac{k_{L1} k_{L3}}{k_{L2}} = 9.17 \times 10^{-24} \exp\left(\frac{1.54 \times 10^5}{RT}\right)$$
 (3-19)

Then, a relationship between k_{L1} and temperature is obtained from the measured values for k_{abs} at 180–190°C and coming relationship (Eq. (3-20)).

$$\frac{1}{k_{L1}} = \frac{1}{k_{abs}} - \frac{k_{L2}}{k_{L1} k_{L3}} \tag{3-20}$$

$$k_{\rm L1} = 1.80 \times 10^{37} \exp\left(-\frac{3.71 \times 10^5}{RT}\right)$$
 (3-21)

A relationship between $k_{\rm L2}/k_{\rm L3}$ and temperature is obtained from Eqs. (3-19) and (3-21).

$$\frac{k_{12}}{k_{13}} = 1.96 \times 10^{60} \exp\left(-\frac{5.25 \times 10^5}{RT}\right)$$
 (3-22)

The values for k_{abs} at 180–200°C are calculated by Eqs. (3-17), (3-219, and (3-22). The calculated values for k_{abs} are shown in **Figure 3.4-26**.

Comparisons between measured profiles and calculated profiles of Δx at 180°C and 200°C are shown in **Figure 3.4-27** and **Figure 3.4-28**. The submitted model can express the profiles of Δx . The obtained kinetic equations for hydration of LiCl/MgO (α = 0.10) are summarized at **Table 3.4-2**.

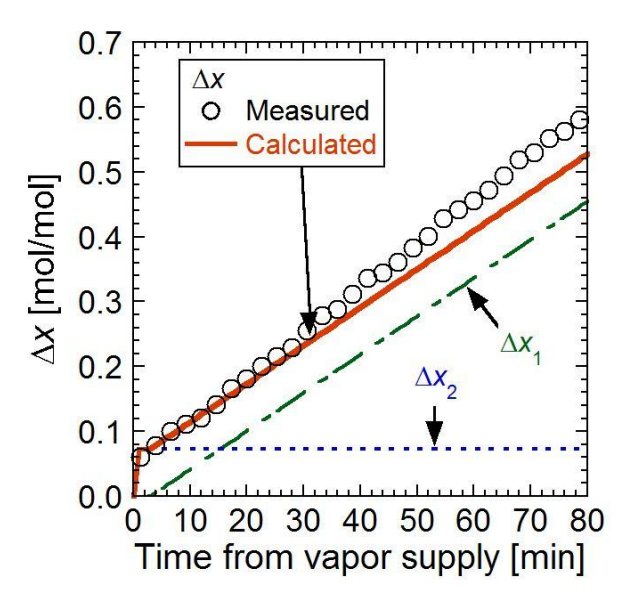


Figure 3.4-27 Comparison between calculated and measured value of Δx of LiCl/MgO (α = 0.10) at $T_{\rm d}$ = 300°C, $T_{\rm h}$ = 180°C, $p_{\rm H2O}$ = 57.8 kPa, and $t_{\rm v}$ = 80 min.

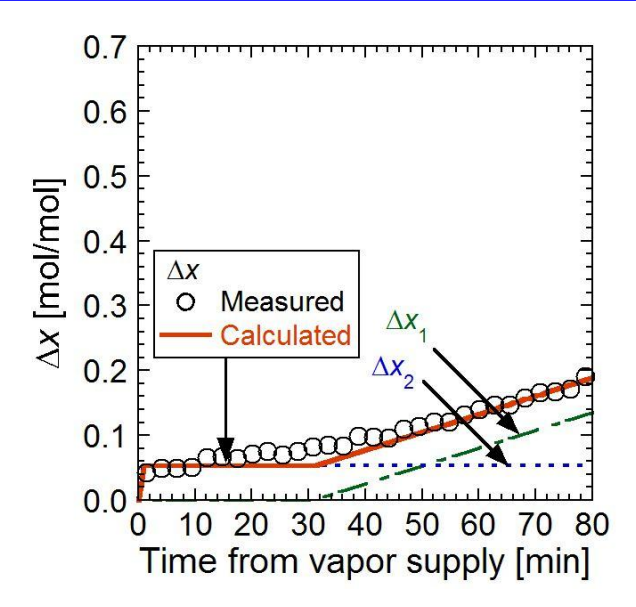


Figure 3.4-28 Comparison between calculated and measured value of Δx of LiCl/MgO (α = 0.10) at $T_{\rm d}$ = 300°C, $T_{\rm h}$ = 200°C, $p_{\rm H2O}$ = 57.8 kPa, and $t_{\rm v}$ = 80 min.

Table 3.4-2 Obtained kinetic equations for hydration of LiCl/MgO ($\alpha = 0.10$).

Temperature [°C]	Equations for Δx_1		
120–150	$1 - 3(1 - \Delta x_1)^{2/3} + 2(1 - \Delta x_1) = \frac{t_V}{t^*}$	$t^* [s] = \frac{4.22 \times 10^3}{\Delta x_{2-eq} [mol/mol]}$	
	$\Delta x_1 = 0 \ \left(t_{\rm V} < t_{\rm ind} \right)$	$t_{\text{ind}} [s] = 83.7 \times T_{\text{h}} [^{\circ}\text{C}] - 1.49 \times 10^{4}$	
180–200	$\Delta x_{\mathrm{l}} = k_{\mathrm{abs}} \ t_{\mathrm{V}} \ \left(t_{\mathrm{V}} \ge t_{\mathrm{ind}} \right)$	$k_{\text{abs}} = \frac{k_{\text{L1}}}{1 + (k_{\text{L2}}/k_{\text{L3}})} p_{\text{H2O}} \text{ [LiCl]}$	
		$k_{\rm L1} = 1.80 \times 10^{37} \exp\left(-\frac{3.71 \times 10^5}{RT}\right)$	
		$\frac{k_{1.2}}{k_{1.3}} = 1.96 \times 10^{60} \exp\left(-\frac{5.25 \times 10^5}{RT}\right)$	

Temperature [°C]	Equations for Δx_2		
	$\Delta x_2 = k_{\rm srp} t_{\rm V} \left(t_{\rm V} \le 60 \text{ s} \right)$	$k_{\rm srp} = \Delta x_{2-\rm eq} / 60[\rm s]$	
120–200	$\Delta x_2 = \Delta x_{2-\text{eq}} \left(t_{\text{V}} > 60 \text{ s} \right)$	$\Delta x_{2-\text{eq}} = 1.56 \times 10^{-6} \times \exp\left(\frac{2.78 \times 10^4}{RT}\right)$	

3.4.2.3 Effect of lithium chloride modification on hydration

The value of Δx_1 for authentic MgO was 0.082 mol/mol at $T_d = 350$ °C, $T_h = 180$ °C, $p_{H2O} =$

57.8 kPa, and $t_v = 80$ min. On the other hand, that of Δx_1 for LiCl/MgO ($\alpha = 0.10$) was 0.522 mol/mol at $T_d = 300$ °C, $T_h = 180$ °C, $p_{H2O} = 57.8$ kPa, and $t_v = 80$ min. The hydration reactivity was enhanced by LiCl-modification. The enhancement would be caused by relatively high concentration of H₂O at the interface between LiCl·nH₂O and Mg(OH)₂ compared with concentration of H₂O at the surface of authentic MgO.

3.4.3 Heat output rate

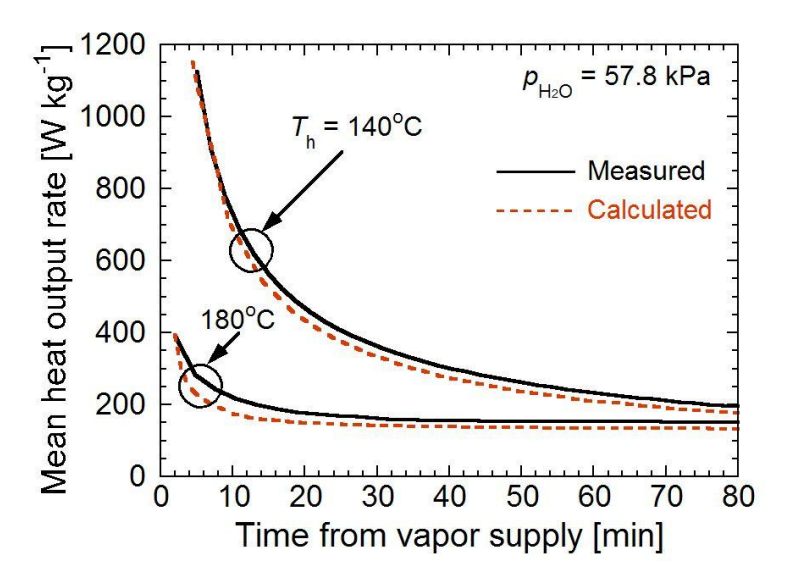


Figure 3.4-29 Comparison between measured and calculated value of mean heat output rates (W) of the material at $p_{\rm H2O} = 57.8$ kPa. Starting materials was LiCl/Mg(OH)₂ ($\alpha = 0.10$).

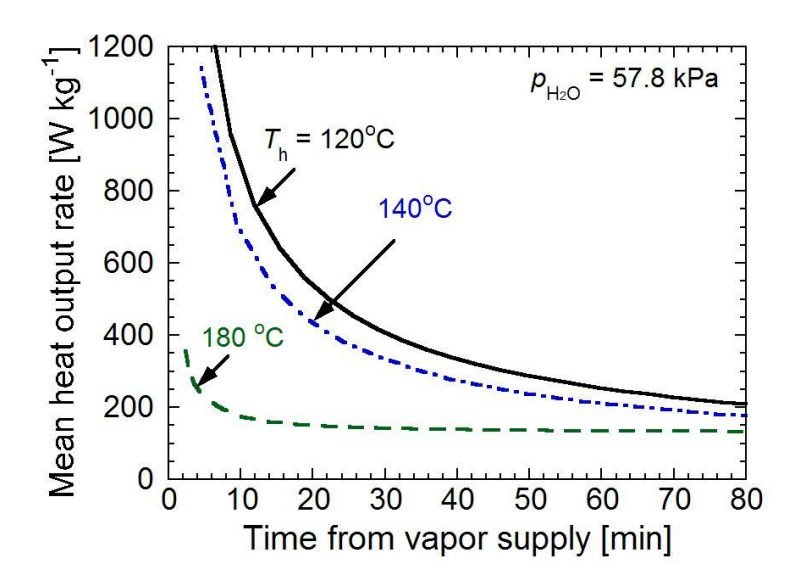


Figure 3.4-30 Calculated mean heat output rates (*W*) of the material at $p_{\rm H2O} = 57.8$ kPa. Starting materials was LiCl/Mg(OH)₂ ($\alpha = 0.10$).

Comparison between measured and calculated value of mean heat output rates (W) of the

material at $p_{\rm H2O} = 57.8$ kPa is shown in **Figure 3.4-29**. The value of W for calculated curve was little under estimated against measured curve. The relative error at 5 min was 4.9% for $T_h = 140$ °C, and was 17% for $T_h = 180$ °C. The relative error at 20 min was 6.9% for $T_h = 140$ °C, and was 6.3% for $T_h = 140$ °C. 180°C. Figure 3.4-30 shows calculated mean heat output rates (W) of the material at $p_{\rm H2O} = 57.8$ kPa. Lower temperature showed higher heat output rate. W was 535 W kg⁻¹ at 120° C, 435 W kg⁻¹ at 140° C, and 163 W kg⁻¹ at 180°C for initial 20 min. The heat output rate was higher than 150 W kg⁻¹ for first 50 min at $T_h = 120-180$ °C. Lahmidi et al. reported the mean heat output rate of a composite material, expanded natural graphite-SrBr₂·H₂O, was 36 kW m⁻³ at $T_h = 35$ °C and $p_{H2O} = 2.3$ kPa [13]. The bulk density of LiCl/Mg(OH)₂ ($\alpha = 0.10$) is 716 kg m⁻³. Thus the heat output of LiCl/Mg(OH)₂ (W > 107kW m⁻³) at $T_h = 120-180$ °C and $p_{H2O} = 57.8$ kPa was greater than the TCM of metal salt hydrate. Kim et al. reported the mean heat output rate of Expanded graphite/MgO/CaCl₂ at $T_h = 110$ °C was 320.0 W kg^{-1} for first 10 min [5]. The mean heat output rate of LiCl/MgO at $T_h = 120$ °C was 832 W kg^{-1} for first 10 min, and it was higher than the composite material, expanded graphite/MgO/CaCl₂. Because expanded graphite/MgO/CaCl₂ is introduced expanded graphite for thermal conductivity enhancement, then, heat capacity per mass is relatively smaller than the materials in this work. However, LiCl/Mg(OH)₂ is also expected to have potential as a high-performance TCM.

3.5 Summary

The effects of LiCl mixing ratio, hydration temperature, and water vapor pressure on the hydration behavior of LiCl/MgO were studied, and the heat output capacities at different experimental conditions were calculated. The kinetic analysis of hydration was performed by using shrinking core model.

The conversions of the hydration increased with higher LiCl mixing ratios in the samples, with an increase in water vapor pressure, or with lower hydration temperature. Both the conversion of hydration and the apparent change of the mole fraction of Mg(OH)₂ by sorption show a linear dependence on water vapor pressure. The heat output capacities of the material ($\alpha = 0.10$) at $p_{\rm H2O} = 57.8$ kPa were 724 kJ kg⁻¹ at hydration temperature of 180°C and 1.40 × 10³ kJ kg⁻¹ at 110°C. These were higher than the heat output capacity of authentic Mg(OH)₂. The rate controlling process of overall hydration was changed by temperature. H₂O diffusion in Mg(OH)₂ layer was the rate controlling process at 110–150°C, $p_{\rm H2O} = 57.8$ kPa, and water absorption at LiCl·nH₂O is the rate controlling process of overall hydration rate at 180–200°C, $p_{\rm H2O} = 57.8$ kPa, $\Delta x_1 \leq 0.72$ mol/mol. Hydration rate equations and kinetic parameters of LiCl/MgO ($\alpha = 0.10$) are submitted (Table 3.4-2), and heat output rate is evaluated. The submitted rate equations predicted well hydration profile of LiCl/MgO ($\alpha = 0.10$). Hence it was demonstrated that the proposed hydration model by using shrinking core model was valid for hydration of LiCl/MgO ($\alpha = 0.10$). LiCl/Mg(OH)₂ was expected to be used as a new TCM.

3.6 References

- [1] G. Layden, G. Brindley; Kinetics of vapor-phase hydration of magnesium oxide, *J. Amer. Ceram. Soc.*, **46**, 518–522 (1963)
- [2] Y. Kato, J. Nakahata, Y. Yoshizawa; Durability characteristics of the hydration of magnesium oxide under repetitive reaction, *J. Mater. Sci.*, **34**, 475–480 (1999)
- [3] H. Matsuda, T. Ishizu, S.K. Lee, M. Hasatani; Kinetic study of Ca(OH)₂/CaO reversible thermochemical reaction for thermal energy storage by means of chemical reaction, *Kagaku Kougaku Ronbunshu* (in Japanese with English abstract), **11**, 542–548 (1985)
- [4] M. Aihara, T. Yoshii, Y. Shimazaki, T. Takeuchi, H. Habuka; Dacarbonation and pore structural change of Ca-solid reactant for CaO/CO₂ chemical heat pump, *J. Chem. Eng. Jpn.*, **41**, 513–518 (2008)
- [5] S.T. Kim, J. Ryu, Y. Kato; Reactivity enhancement of chemical materials used in packed bed reactor of chemical heat pump, *Prog. Nucl. Energy*, **53**, 1027–1033 (2011)
- [6] M. Liu, W. Saman, F. Bruno; Review on storage materials and thermal performance enhancement techniques for high temperature phase change thermal storage systems, *Renew. Sustainable Energy Rev.*, **16**, 2118–2132 (2012)
- [7] H. Michels, R. Pitz-Paal; Cascaded latent heat storage for parabolic trough solar power plants, *Sol. Energy*, **81**, 829–837 (2007)
- [8] Yagi, S., Kunii, D. Kogyo Kagaku Zassi (in Japanese), **56**, 131–135 (1953)
- [9] A. Gokarn, L. Doraiswamy; A modek for solid-gas reactions, *Chem. Eng. Sci.*, **26**, 1521–1533 (1971)
- [10] T. Takemura, K. Yoshida, D. Kunii; Kinetic study of oxidation of zinc sulfide pellets, *J. Chem. Eng. Jpn.*, 7, 276–280 (1974)
- [11] P. Weisz, R. Goodwin; Combustion of carbonaceous deposits within porous catalyst particles I. diffusion-controlled kinetics, *J. Catal.*, **2**, 397–404 (1963)
- [12] Levenspiel, O. *Chemical Reaction Engineering*, third ed., John Wiley & Sons, Hoboken, U.S., Third Edition, 566–583 (1999)
- [13] H. Lahmidi, S. Mauran, V. Goetz; Definition, test and simulation of a thermochemical storage process adapted to solar thermal systems, *Sol. Energy*, **80**, 883–893 (2006)

Chapter 4 Near infrared spectroscopy for hydration observation of lithium chloride-modified magnesium oxide

4.1 Introduction

The reaction conversion of the hydration for LiCl/MgO (α = 0.10) was larger than that of hydration for authentic MgO at same hydration temperature and water vapor pressure (**Chapter 3**). Hydration of LiCl/MgO was enhanced compared with authentic MgO by introduction of LiCl. However, a mechanism of the hydration for LiCl/MgO is unclear. It is not easy to identify the hydration mechanism by thermogravimetry. It is necessary to understand the effects of metal-salt modification in order to develop new thermochemical energy storage materials (TCMs). The hydration mechanism is important information to develop new TCMs.

In this chapter, hydration of authentic MgO and LiCl/MgO (α = 0.10) was examined by near infrared (NIR) spectroscopy. The NIR absorption spectrum under the hydration process is consists of elementary spectrum of Mg(OH)₂ and adsorbed/absorbed water. Thus, peak positions of each component should be clarified to deconvolute measured spectrum into components. Thus, NIR absorption spectrum of authentic Mg(OH)₂ at 110°C was observed to obtain a peak position of stretching first overtone for Mg(OH)₂. NIR absorption spectra of authentic Mg(OH)₂ under vapor supply were observed to clarify a peak position of adsorbed water, and that of LiCl/Mg(OH)₂ (α = 0.10) under vapor supply were observed to clarify a peak position of adsorbed and absorbed (sorbed) water

Then, NIR absorption spectra of authentic MgO and LiCl/MgO (α = 0.10) under vapor supply were observed to analyze hydration mechanism. The obtained NIR absorption spectra of authentic MgO and LiCl/MgO (α = 0.10) under hydration process is deconvoluted into each components (Mg(OH)₂ and adsorbed/absorbed water). The hydration mechanism was discussed by profile of peak area for each component with time.

4.2 Experimental

4.2.1 Sample preparation

LiCl/Mg(OH)₂ was prepared as a precursor of LiCl/MgO. A detail of the preparation procedure was shown in **Section 2.2.1**. In this chapter, LiCl/Mg(OH)₂ (α = 0.10) was employed, and authentic MgO was used as a reference. Authentic Mg(OH)₂ and LiCl/Mg(OH)₂ was dehydrated at 400°C under Ar gas flow (flow rate 50 mL min⁻¹) for 1 h, and then authentic MgO and LiCl/MgO was obtained.

4.2.2 Observation of hydration by near infrared spectroscopy

The spectra of the samples were observed by near infrared (NIR) spectroscopy. The NIR

absorption spectra were measured by the diffuse reflectance (DR) method. The spectra were recorded on a UV-vis-NIR spectrophotometer equipped with a portable integrating sphere (V-670, JASCO Corporation). The background for the NIR spectra was calibrated with α -Al₂O₃ powder using the diffuse reflectance mode. The obtained absorption spectra were converted into KM function [1].

$$f(R) \equiv \frac{K}{S} = \frac{\left(1 - R\right)^2}{2R} \tag{4-1}$$

$$R = \frac{\text{Diffuse reflectance of the sample}}{\text{Diffuse reflectance of } \alpha - \text{Al}_2\text{O}_3}$$
 (4-2)

Here, f(R): KM function, K: absorption coefficient, S: scatter coefficient, R: relative diffuse reflectance, respectively. The scanning speed was fixed at $10000 \text{ cm}^{-1} \text{ min}^{-1}$. A schematic diagram of the NIR spectroscopic measurement system is shown in **Figure 4.2-1**.

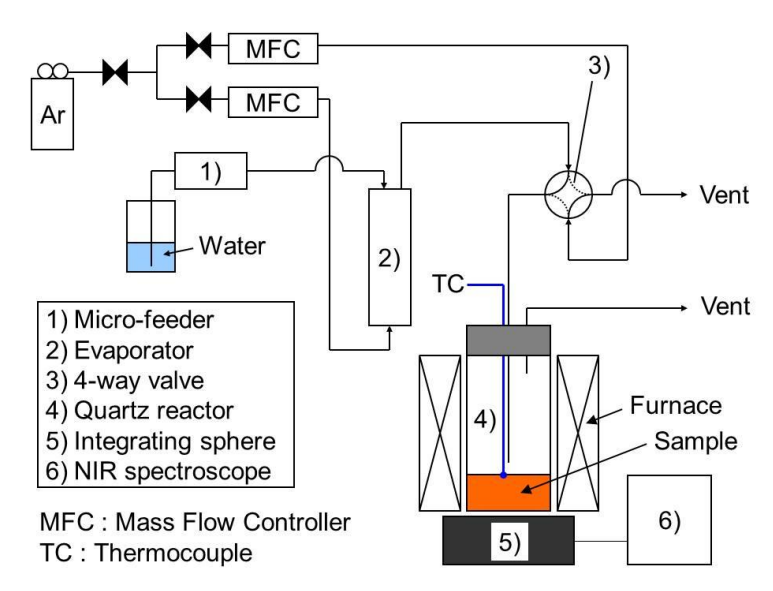


Figure 4.2-1 Schematic diagram of the NIR spectroscopic measurement system.

Water adsorption, water absorption, and hydration are thought to be proceeded simultaneously for hydration of LiCl/MgO. Stretching and bending vibrations for adsorbed water on MgO, stretching and bending vibrations for adsorbed water on LiCl $\cdot nH_2O$, stretching and bending vibrations for hydrated species in LiCl $\cdot nH_2O$, and stretching vibrations for Mg(OH)₂ were observed by NIR spectroscopy. A schematic model for hydration of LiCl/Mg(OH)₂ is shown in **Figure 4.2-2**. Names of observed compounds by NIR spectroscopy are shown in red characters in **Figure 4.2-2**.

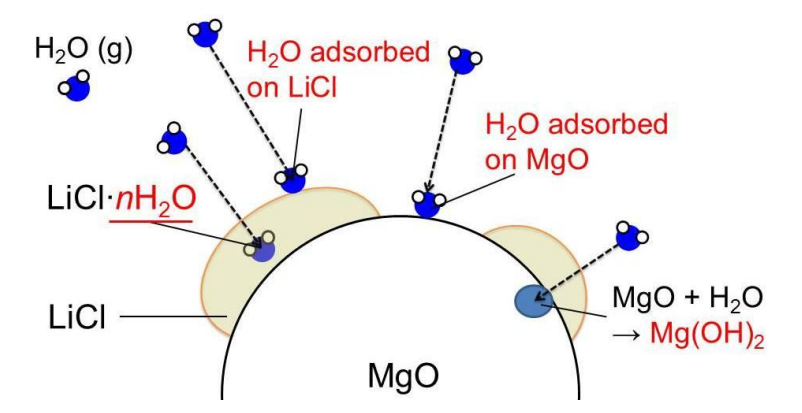


Figure 4.2-2 Schematic model for hydration of LiCl/Mg(OH)₂. Names of observed compounds by NIR spectroscopy are shown in red characters.

Spectrum measurement to identify peak position

Spectrum of authentic Mg(OH)₂ under Ar flow was observed to identify the peak position of stretching first overtone for Mg(OH)₂. 200 mg of authentic Mg(OH)₂ was placed in the quartz reactor. The reactor was heated at 110°C or 180°C under Ar flow, and DR-NIR spectra of authentic Mg(OH)₂ were recorded.

Spectra of authentic $Mg(OH)_2$ under vapor supply were observed to identify the peak position of adsorbed water at $110^{\circ}C$. 200 mg of authentic $Mg(OH)_2$ (0.07-µm diameter, 99.9%, Wako Pure Chemical Industries, Ltd.) was placed in the reactor. The reactor was heated at $110^{\circ}C$ under Ar flow. A mixture of water vapor and Ar (carrier gas) was produced at the evaporator. The water vapor pressure (p_{H2O}) was fixed at 57.8 kPa. The gas mixture was supplied (flow rate: 10 mL min⁻¹) into the reactor for 20 min at $110^{\circ}C$ for adsorption measurement, and DR-NIR spectra of the samples were recorded. The spectra were measured every 4 min.

Spectra of LiCl/Mg(OH)₂ (α = 0.10) under vapor supply were observed to identify the peak position of adsorbed and absorbed water at 110°C or 180°C. 200 mg of LiCl/Mg(OH)₂ (α = 0.10) was placed in the quartz reactor. The reactor was heated at 110°C or 180°C under Ar flow. The gas mixture ($p_{\rm H2O}$ = 57.8 kPa) was supplied (flow rate: 10 mL min⁻¹) into the reactor for 20 min at 110°C or 180°C for sorption measurement, and DR-NIR spectra of the samples were recorded. The spectra were measured every 4 min.

Spectrum measurement for analysis of hydration

Spectra of authentic MgO under vapor supply were observed to analyze hydration of authentic MgO. The gas mixture ($p_{\rm H2O} = 57.8$ kPa) was supplied (flow rate: 10 mL min^{-1}) into the reactor for 40 min at 110° C for hydration measurement, and DR-NIR spectra of the samples were recorded. The spectra was measured every 4 min. The flow rate of the gas mixture for NIR measurement (10 mL min^{-1}) was smaller than flow rate of the gas mixture for thermogravimetry (77 mL min^{-1}) to observe a detail of initial hydration state for the samples. The obtained spectra were deconvoluted into

components. It is assumed that the profile of each component can be expressed by Gaussian function.

Spectra of LiCl/MgO (α = 0.10) under vapor supply were observed to analyze hydration LiCl/MgO (α = 0.10). The gas mixture ($p_{\rm H2O}$ = 57.8 kPa) was supplied (flow rate: 10 mL min⁻¹) into the reactor for 40 min at 110°C or 180°C for hydration measurement, and DR-NIR spectra of the samples were recorded. The spectra was measured every 4 min. The obtained spectra were deconvoluted into components. It is assumed that the profile of each component can be expressed by Gaussian function.

4.3 Results

4.3.1 Spectrum measurement to identify peak position

4.3.1.1 Spectra of authentic magnesium hydroxide

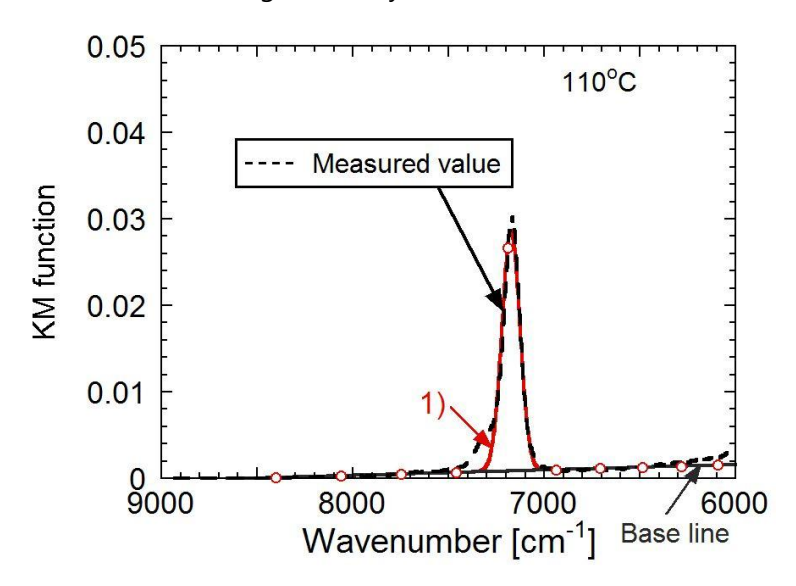


Figure 4.3-1 DR-NIR spectrum for authentic $Mg(OH)_2$ at $110^{\circ}C$. 1) indicates a fitted curve of $Mg(OH)_2$ first overtone (7174 cm⁻¹).

Spectrum of authentic Mg(OH)₂ under Ar flow was observed to identify the peak position of first overtone for Mg(OH)₂. DR-NIR spectrum for authentic Mg(OH)₂ at 110°C, under Ar atmosphere is shown in **Figure 4.3-1**, and the spectrum at 180°C, under Ar atmosphere is shown in **Figure 4.3-2**. Red colored curve, 1), indicates fitting curve by using Gaussian function. Martens and Freund reported that a peak position of first overtone for Mg(OH)₂ is 7154 cm⁻¹ [1]. In this work, the peak position of first overtone for Mg(OH)₂ at 110°C and 180°C is estimated as 7174 cm⁻¹ from the results of curve fitting.

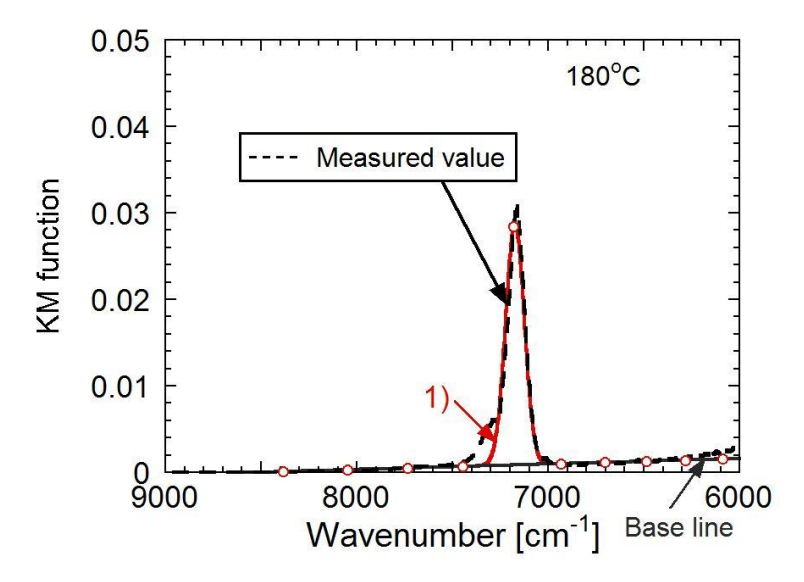


Figure 4.3-2 DR-NIR absorption spectrum for authentic Mg(OH)₂ at 180°C: 1) indicates a fitted curve of Mg(OH)₂ first overtone (7174 cm⁻¹).

4.3.1.2 Water adsorption on authentic magnesium hydroxide

Spectra of authentic Mg(OH)₂ under vapor supply were observed to clarify the peak position of adsorbed water at 110°C. DR-NIR spectra of authentic Mg(OH)₂ under vapor supply at 110°C, $p_{\rm H2O}$ = 57.8 kPa, and vapor supply time ($t_{\rm v}$) of 0–20 min are shown in **Figure 4.3-3**. The peak at 7174 cm⁻¹ (first overtone of Mg(OH)₂) was observed at first 8 min of vapor supply. Then, a shoulder peak at around 7000 cm⁻¹ and a sharp peak at around 5300 cm⁻¹ were observed after 12 min of vapor supply.

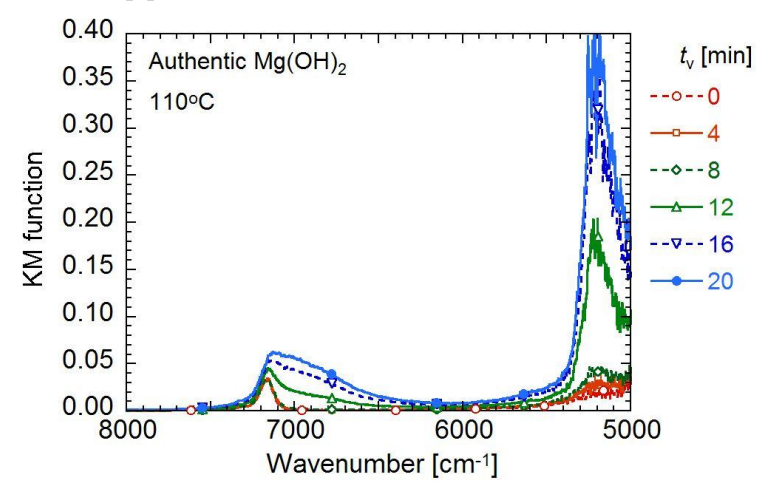


Figure 4.3-3 DR-NIR spectra of authentic Mg(OH)₂ under vapor supply at 110°C, $p_{\rm H2O} = 57.8$ kPa, and $t_{\rm v} = 0$ –20 min.

To remove a contribution of first overtone for Mg(OH)₂ to the spectra, DR-NIR difference spectra were calculated. The difference between a spectrum at $t_v \ge 4$ min and a spectrum at $t_v = 0$ min was calculated. **Figure 4.3-4** shows NIR difference spectra of authentic Mg(OH)₂ under vapor supply at 110°C, $p_{\text{H2O}} = 57.8$ kPa, and $t_v = 4-20$ min. A shoulder peak at around 7100 cm⁻¹ and a sharp peak

at around 5200 cm⁻¹ were observed after $t_v = 12$ min.

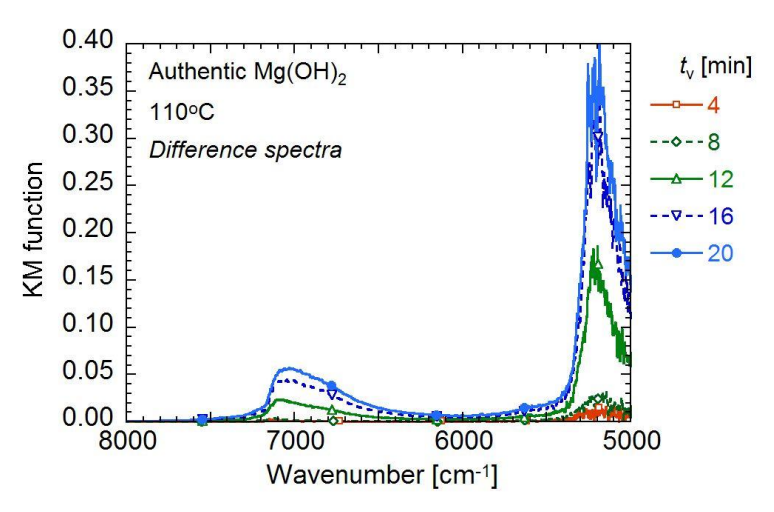


Figure 4.3-4 NIR difference spectra of authentic Mg(OH)₂ under vapor supply at 110°C, $p_{\rm H2O} = 57.8$ kPa, and $t_{\rm v} = 0$ –20 min.

4.3.1.3 Water sorption at lithium chloride-modified magnesium hydroxide

Spectra of LiCl/Mg(OH)₂ ($\alpha = 0.10$) under vapor supply were observed to identify the peak position of adsorbed and absorbed water at 110°C or 180°C. DR-NIR spectra of LiCl/Mg(OH)₂ ($\alpha = 0.10$) under vapor supply at 110°C, $p_{\rm H2O} = 57.8$ kPa, and $t_{\rm v} = 0$ –20 min are shown in **Figure 4.3-5**. The peak at 7174 cm⁻¹ (first overtone for Mg(OH)₂) was observed at $t_{\rm v} = 0$ min. Then, a shoulder peak at around 6900 cm⁻¹ and a sharp peak at around 5200 cm⁻¹ were observed after 4 min of vapor supply.

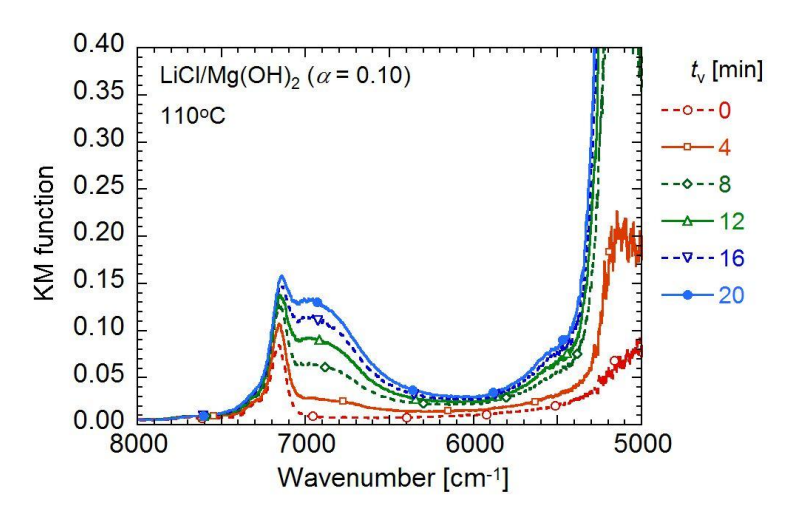


Figure 4.3-5 DR-NIR spectra of LiCl/Mg(OH)₂ (α = 0.10) under vapor supply at 110°C, $p_{\rm H2O}$ = 57.8 kPa, and $t_{\rm v}$ = 0–20 min.

To remove a contribution of first overtone for $Mg(OH)_2$ to the spectra, DR-NIR difference spectra were calculated from the DR-NIR spectra under sorption processes. The difference between a spectrum at $t_v \ge 4$ min and a spectrum at $t_v = 0$ min was calculated. **Figure 4.3-6** shows DR-NIR

difference spectra of LiCl/Mg(OH)₂ ($\alpha = 0.10$) under vapor supply at 110°C, $p_{\rm H2O} = 57.8$ kPa, and $t_{\rm v} = 4-20$ min. A broad peak at around 7000 cm⁻¹ and a sharp peak at around 5200 cm⁻¹ were observed after $t_{\rm v} = 12$ min.

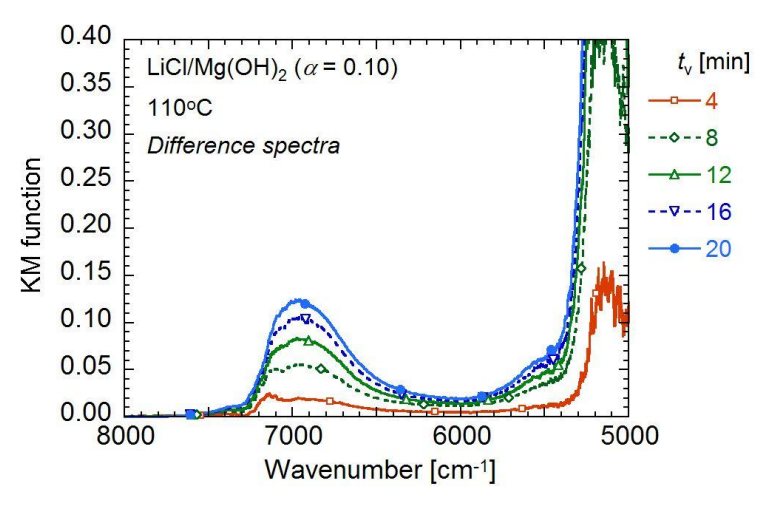


Figure 4.3-6 NIR difference spectra of LiCl/Mg(OH)₂ (α = 0.10) under vapor supply at 110°C, $p_{\rm H2O}$ = 57.8 kPa, and $t_{\rm v}$ = 0–20 min.

DR-NIR spectra of LiCl/Mg(OH)₂ ($\alpha = 0.10$) under vapor supply at 180°C, $p_{\rm H2O} = 57.8$ kPa, and $t_{\rm v} = 0$ –20 min are shown in **Figure 4.3-7**. The peak at 7174 cm⁻¹ (first overtone of Mg(OH)₂) was observed at $t_{\rm v} = 0$ min. Then, a shoulder peak at around 6900 cm⁻¹ and a sharp peak at around 5200 cm⁻¹ were observed after 4 min of vapor supply.

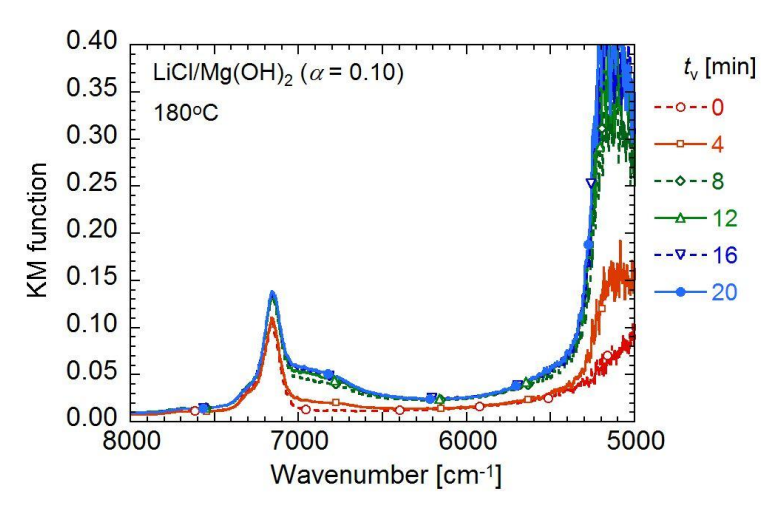


Figure 4.3-7 DR-NIR spectra of LiCl/Mg(OH)₂ (α = 0.10) under vapor supply at 180°C, $p_{\rm H2O}$ = 57.8 kPa, $t_{\rm v}$ = 0–20 min.

Figure 4.3-8 shows DR-NIR difference spectra of LiCl/Mg(OH)₂ ($\alpha = 0.10$) under vapor supply at 180°C, $p_{\rm H2O} = 57.8$ kPa, and $t_{\rm v} = 0$ –20 min. A broad peak at around 7000 cm⁻¹ and a sharp peak at around 5200 cm⁻¹ were observed after $t_{\rm v} = 8$ min.

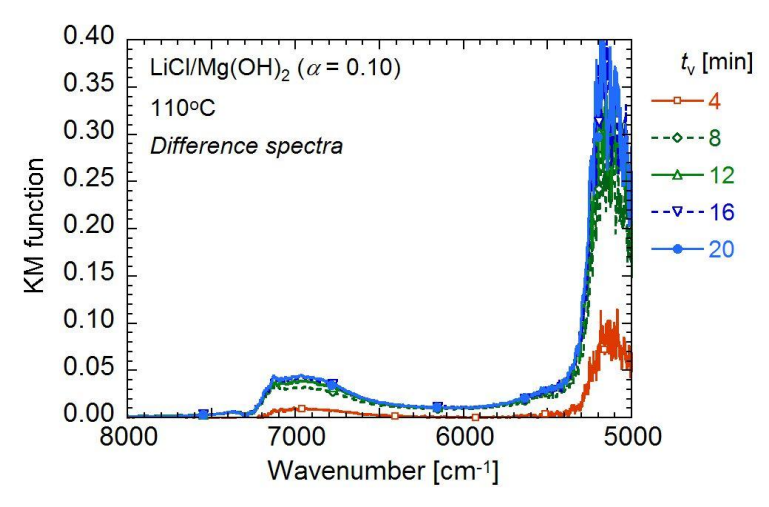


Figure 4.3-8 NIR difference spectra of LiCl/Mg(OH)₂ (α = 0.10) under vapor supply at 180°C, $p_{\rm H2O}$ = 57.8 kPa, and $t_{\rm v}$ = 0–20 min.

4.3.2 Spectrum measurement for analysis of hydration

4.3.2.1 Hydration of authentic magnesium oxide

Spectra of authentic MgO were observed to analyze hydration of authentic MgO. The changes in the DR-NIR spectra for the hydration process of authentic MgO at 110° C, and $p_{H2O} = 57.8$ kPa are shown in **Figure 4.3-9** and **Figure 4.3-10**. A peak at around 7174 cm⁻¹ was observed at $t_v = 24$ min. After 28 min of vapor supply, a shoulder peak at around 7000 cm⁻¹ and a sharp peak at around 5300 cm⁻¹ were observed. The peak area was increased by time.

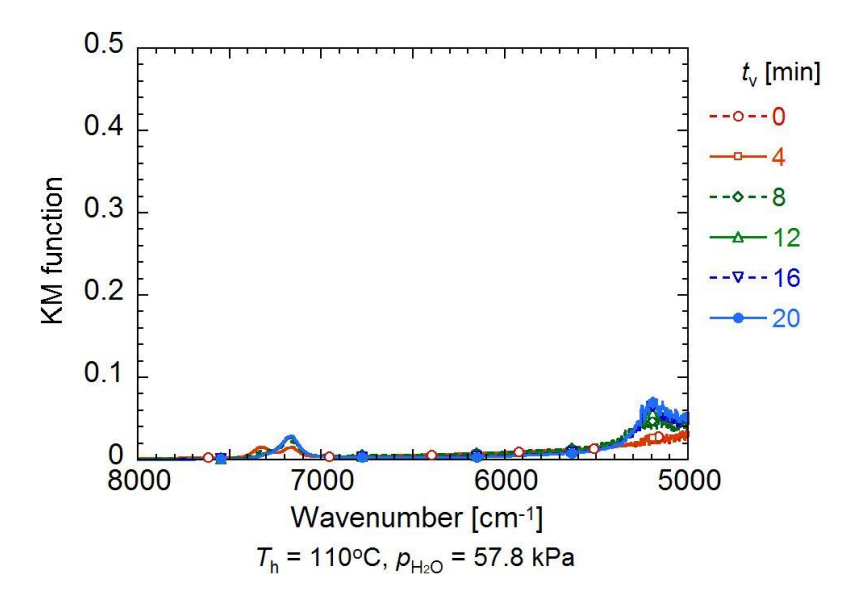


Figure 4.3-9 DR-NIR spectra of authentic MgO under vapor supply at 110°C, $p_{\rm H2O} = 57.8$ kPa, and $t_{\rm v} = 0-20$ min.

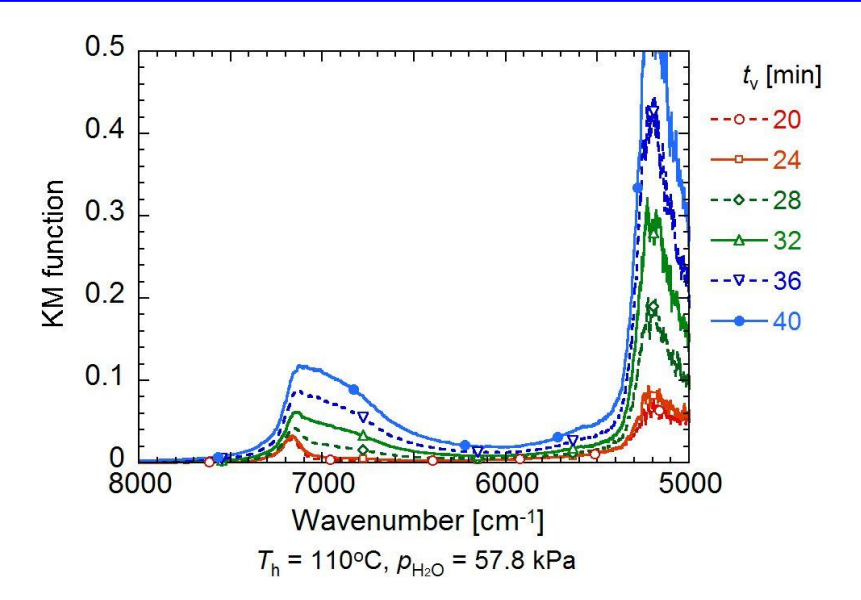


Figure 4.3-10 DR-NIR spectra of authentic MgO under vapor supply at 110°C, $p_{\rm H2O} = 57.8$ kPa, and $t_{\rm v} = 20$ –40 min.

4.3.2.2 Hydration of lithium chloride-modified magnesium oxide

Spectra of LiCl/MgO (α = 0.10) were observed to analyze hydration of LiCl/MgO (α = 0.10). The changes in the DR-NIR spectra for the hydration process of LiCl/MgO (α = 0.10) at 110°C, and $p_{\rm H2O}$ = 57.8 kPa are shown in **Figure 4.3-11** and **Figure 4.3-12**. A broad peak at around 7000 cm⁻¹ and a sharp peak at around 5200 cm⁻¹ were observed. The peak area was increased by time.

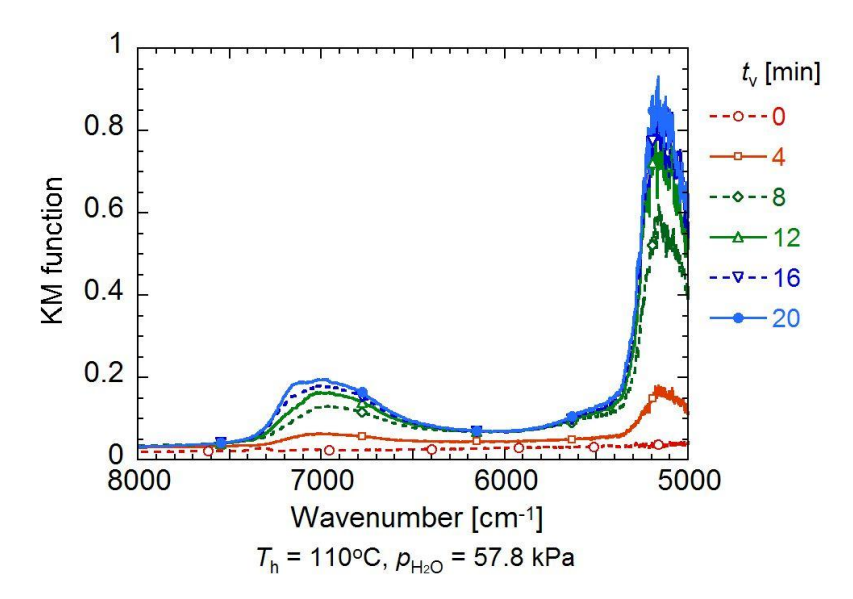


Figure 4.3-11 DR-NIR spectra of LiCl/MgO (α = 0.10) under vapor supply at 110°C, $p_{\rm H2O}$ = 57.8 kPa, and $t_{\rm v}$ = 0–20 min.

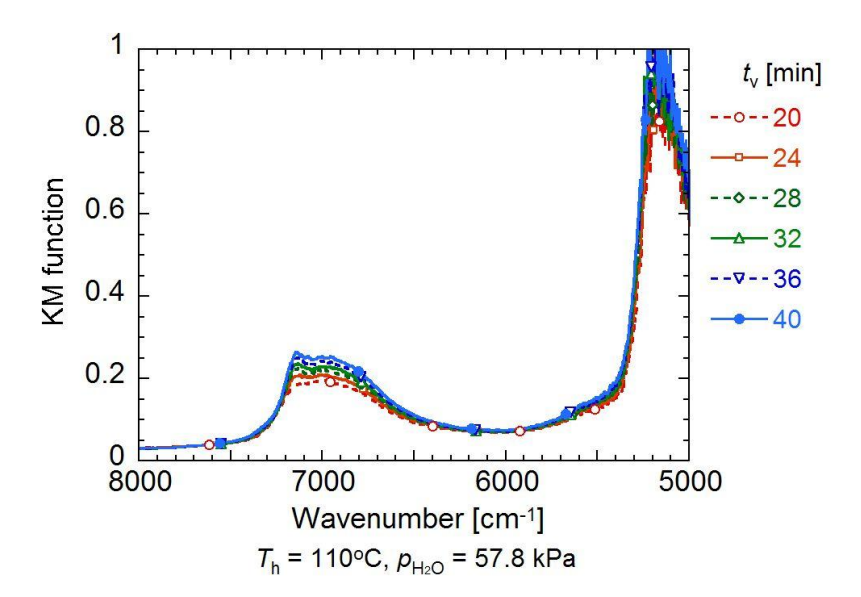


Figure 4.3-12 DR-NIR spectra of LiCl/MgO (α = 0.10) under vapor supply at 110°C, $p_{\rm H2O}$ = 57.8 kPa, and $t_{\rm v}$ = 20–40 min.

The changes in the DR-NIR spectra for the hydration process of LiCl/MgO ($\alpha = 0.10$) at 180°C, and $p_{\rm H2O} = 57.8$ kPa are shown in **Figure 4.3-13** and **Figure 4.3-14**. A broad peak at around 7000 cm⁻¹ and a peak at around 5200 cm⁻¹ were observed. The peak area was increased by time.

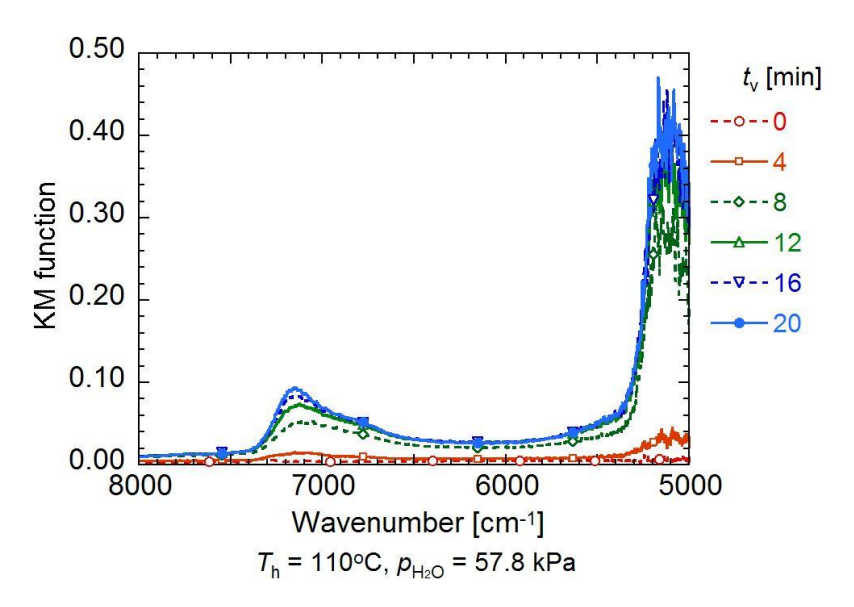


Figure 4.3-13 DR-NIR spectra of LiCl/MgO (α = 0.10) under vapor supply at 180°C, $p_{\rm H2O}$ = 57.8 kPa, and $t_{\rm v}$ = 0–20 min.

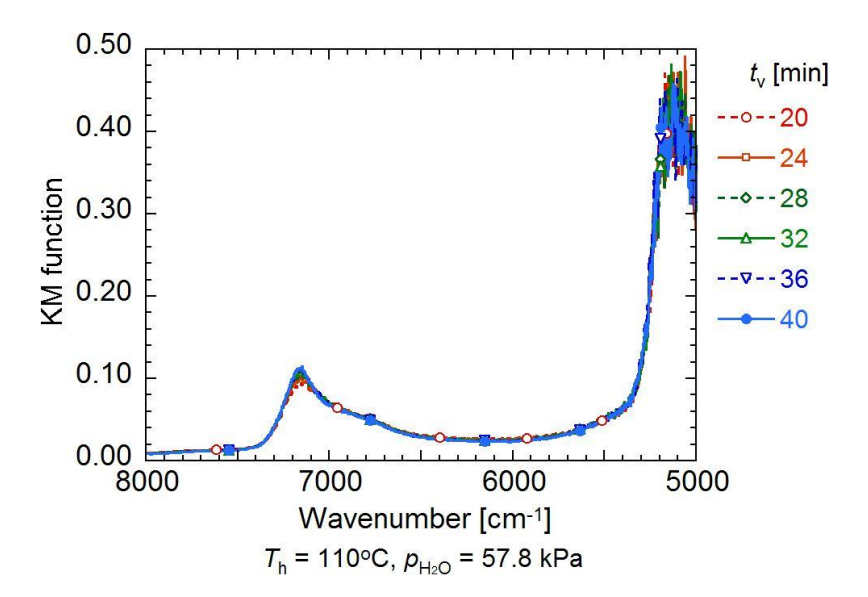


Figure 4.3-14 DR-NIR spectra of LiCl/MgO (α = 0.10) under vapor supply at 180°C, $p_{\rm H2O}$ = 57.8 kPa, and $t_{\rm v}$ = 20–40 min.

4.4 Discussion

4.4.1 Spectrum decomvolution for analysis of hydration process

4.4.1.1 Peak positions of each component

Peak positions of each component are estimated to perform spectrum deconvolution during hydration process. The peak position of first overtone for Mg(OH)₂ at 110°C and 180°C is estimated as 7174 cm⁻¹ from the spectra of authentic Mg(OH)₂ (Section 4.3.1.1).

The adsorbed water on the solid surface showed a different combination band depending on the hydrogen bond structure [2,3]. It was reported that a hydrogen bond increment causes a shift of the peak position to a lower wavenumber [2,3]. In this work, profile of adsorbed water on authentic Mg(OH)₂ was separated into two species; (a) free water (not hydrogen-bonded water), and (b) bound water (hydrogen-bonded water). **Figure 4.4-1** shows schematic model of water adsorption on Mg(OH)₂ under vapor supply.

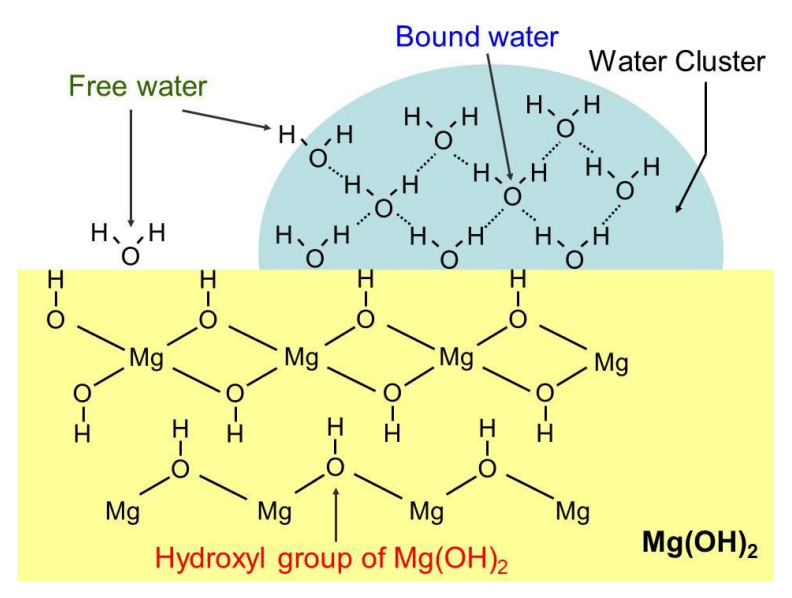


Figure 4.4-1 Schematic model of water adsorption on Mg(OH)₂ under vapor supply. (—) covalent bonds, (---) hydrogen bonds.

Figure 4.4-2 shows a deconvoluted difference spectrum of authentic Mg(OH)₂ at 110°C, p_{H2O} = 57.8 kPa, t_{v} = 12 min. It is assumed that the profile of each component is expressed by Gaussian function. The deconvolution was performed by curve fitting between measured value and calculated value. The calculated value was obtained from a summation of values of each component. The spectra is deconvoluted into four components; 2) free water ($v_1 + v_3$) (7055 cm⁻¹), 3) bound water ($v_1 + v_3$) (6848 cm⁻¹), 4) free water ($v_2 + v_3$) (5400 cm⁻¹), and 5) bound water ($v_2 + v_3$) (5216 cm⁻¹). Here, v_1 : symmetric stretch vibration, v_2 : bending vibration, v_3 : asymmetric stretching vibration of water, respectively.

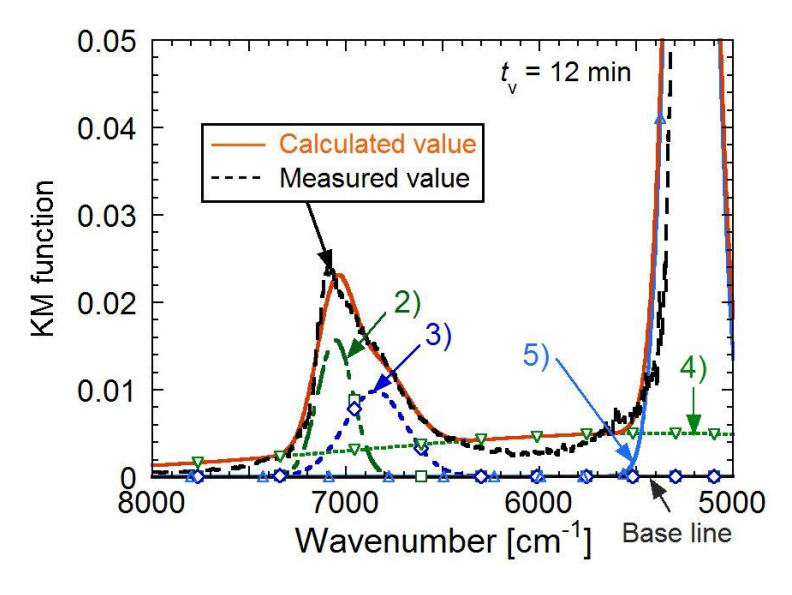


Figure 4.4-2 Deconvoluted difference spectrum of authentic Mg(OH)₂ at 110°C, $p_{\text{H2O}} = 57.8 \text{ kPa}$ and $t_{\text{v}} = 12 \text{ min: 2}$) free water ($v_1 + v_3$) (7055 cm⁻¹), 3) bound water ($v_1 + v_3$) (6848 cm⁻¹), 4) free water ($v_2 + v_3$) (5400 cm⁻¹), and 5) bound water ($v_2 + v_3$) (5216 cm⁻¹).

Water sorption at LiCl/Mg(OH)₂ (α = 0.10) would form hydrated species in LiCl. In this work, profile of adsorbed and absorbed water at LiCl/Mg(OH)₂ (α = 0.10) was separated into two species; (a) free water, and (b) hydrated species. **Figure 4.4-3** shows schematic model of water sorption at LiCl/Mg(OH)₂ under vapor supply.

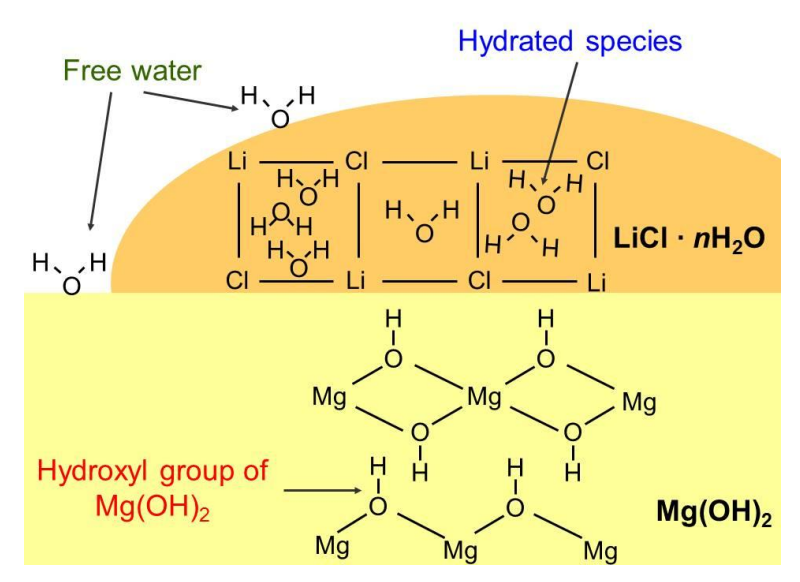


Figure 4.4-3 Schematic model of water sorption at LiCl/Mg(OH)₂ under vapor supply. (—) covalent bonds.

Figure 4.4-4 shows a deconvoluted difference spectrum of LiCl/Mg(OH)₂ (α = 0.10) at 110°C, $p_{\rm H2O}$ = 57.8 kPa and $t_{\rm v}$ = 12 min. It is assumed that the profile of each component can be expressed by Gaussian function. The spectra is deconvoluted into four components; 2) free water ($v_1 + v_3$) (7060 cm⁻¹), 3) hydrated species ($v_1 + v_3$) (6859 cm⁻¹), 4) free water ($v_2 + v_3$) (5469 cm⁻¹), and 5) hydrated species ($v_2 + v_3$) (5130 cm⁻¹).

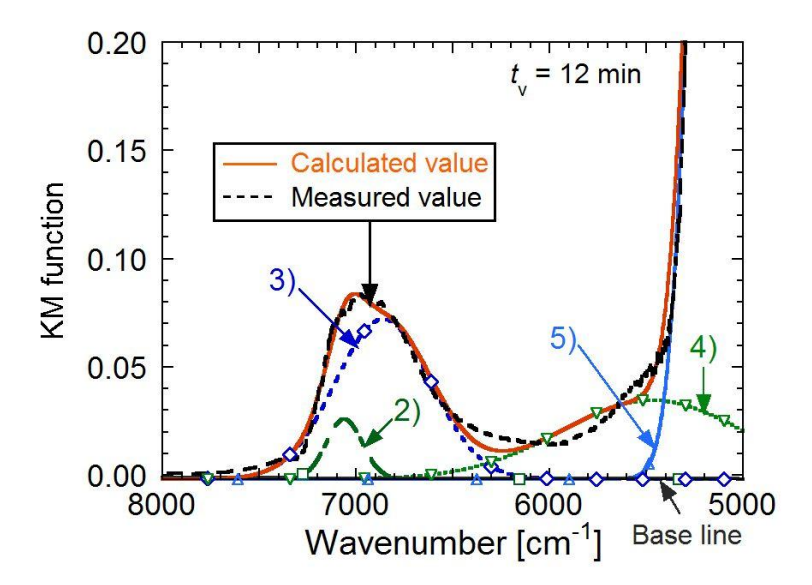


Figure 4.4-4 Deconvoluted difference of LiCl/Mg(OH)₂ (α = 0.10) at 110°C, p_{H2O} = 57.8 kPa and t_{v} = 12 min: 2) free water ($v_1 + v_3$) (7060 cm⁻¹), 3) hydrated species ($v_1 + v_3$) (6859 cm⁻¹), 4) free water ($v_2 + v_3$) (5469 cm⁻¹), and 5) hydrated species ($v_2 + v_3$) (5130 cm⁻¹).

Figure 4.4-5 shows a deconvoluted difference spectrum of LiCl/Mg(OH)₂ ($\alpha = 0.10$) at 180°C, $p_{\rm H2O} = 57.8$ kPa and $t_{\rm v} = 12$ min. The spectra is deconvoluted into four components; 2) free water ($v_1 + v_3$) (7060 cm⁻¹), 3) hydrated species ($v_1 + v_3$) (6859 cm⁻¹), 4) free water ($v_2 + v_3$) (5469 cm⁻¹), and 5) hydrated species ($v_2 + v_3$) (5130 cm⁻¹).

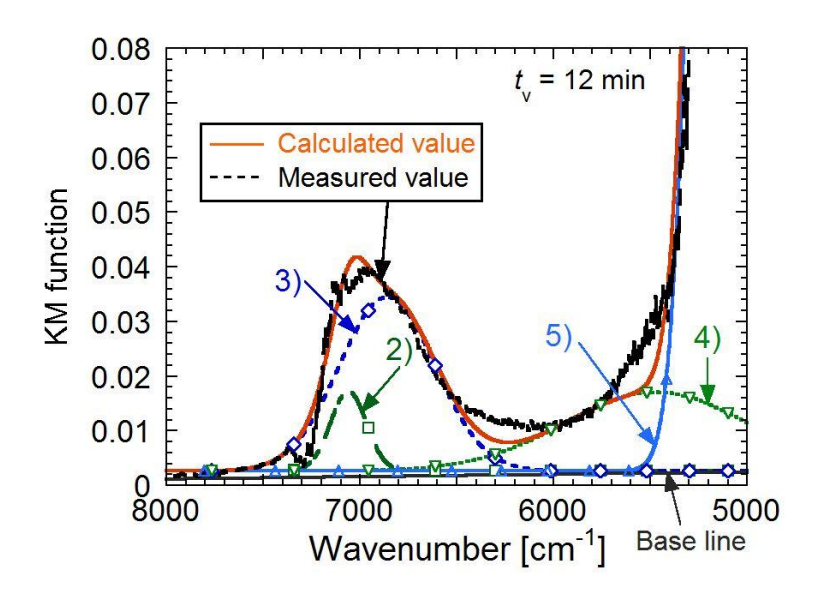


Figure 4.4-5 Deconvoluted difference spectrum of LiCl/Mg(OH)₂ ($\alpha = 0.10$) at 180°C, $p_{\text{H2O}} = 57.8$ kPa and $t_{\text{v}} = 12$ min: 2) free water ($v_1 + v_3$) (7060 cm⁻¹), 3) hydrated species ($v_1 + v_3$) (6859 cm⁻¹), 4) free water ($v_2 + v_3$) (5469 cm⁻¹), and 5) hydrated species ($v_2 + v_3$) (5130 cm⁻¹).

Assignment of each components of adsorbed water for authentic Mg(OH)₂ is shown in **Table**

4.4-1 and that of adsorbed and absorbed water for LiCl/Mg(OH)₂ (α = 0.10) is shown in **Table 4.4-2**.

Table 4.4-1	Assignment of each	components of adsorbed	I water for Authentic $Mg(OH)_2$.
--------------------	--------------------	------------------------	------------------------------------

	Free water	Bound water	Free water	Bound water
Temperature	$v_1 + v_3$	$v_1 + v_3$	$v_2 + v_3$	$v_2 + v_3$
[°C]	$[cm^{-1}]$	$[cm^{-1}]$	$[cm^{-1}]$	$[cm^{-1}]$
110	7055	6848	5400	5216

Table 4.4-2 Assignment of each components of adsorbed and absorbed water for LiCl/Mg(OH)₂ ($\alpha = 0.10$).

	Free water	Hydrated species	Free water	Hydrated species
Temperature	$v_1 + v_3$	$v_1 + v_3$	$v_2 + v_3$	$v_2 + v_3$
[°C]	$[cm^{-1}]$	$[cm^{-1}]$	$[cm^{-1}]$	$[cm^{-1}]$
110	7060	6859	5469	5130
180	7060	6859	5469	5130

4.4.1.2 Spectrum deconvolution of the samples under hydration process

The deconvolution of each spectrum under hydration process was performed with following conditions; (a) the peak position of each component was constant, (b) the standard deviation of the Gaussian function for each component was constant.

The deconvoluted spectrum of authentic MgO at 110°C, $p_{\rm H2O} = 57.8$ kPa and $t_{\rm v} = 20$ min is shown in **Figure 4.4-6**. The spectrum is deconvoluted into three components; 1) Mg(OH)₂ (first overtone) (7174 cm⁻¹), 4) free water ($v_2 + v_3$) (5400 cm⁻¹), and 5) bound water ($v_2 + v_3$) (5216 cm⁻¹).

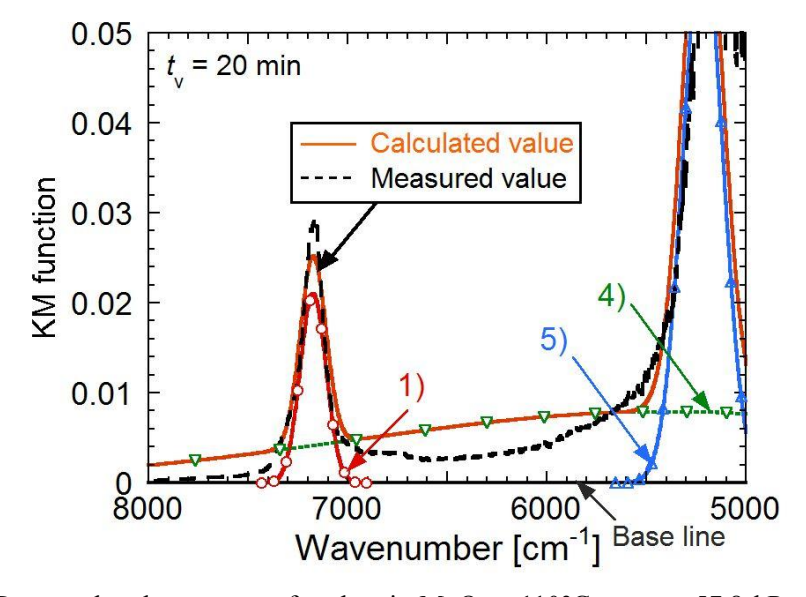


Figure 4.4-6 Deconvoluted spectrum of authentic MgO at 110°C, $p_{\text{H2O}} = 57.8$ kPa, $t_{\text{v}} = 20$ min: 1) Mg(OH)₂ first overtone (7174 cm⁻¹), 4) free water ($v_2 + v_3$) (5400 cm⁻¹), and 5) bound water ($v_2 + v_3$) (5216 cm⁻¹).

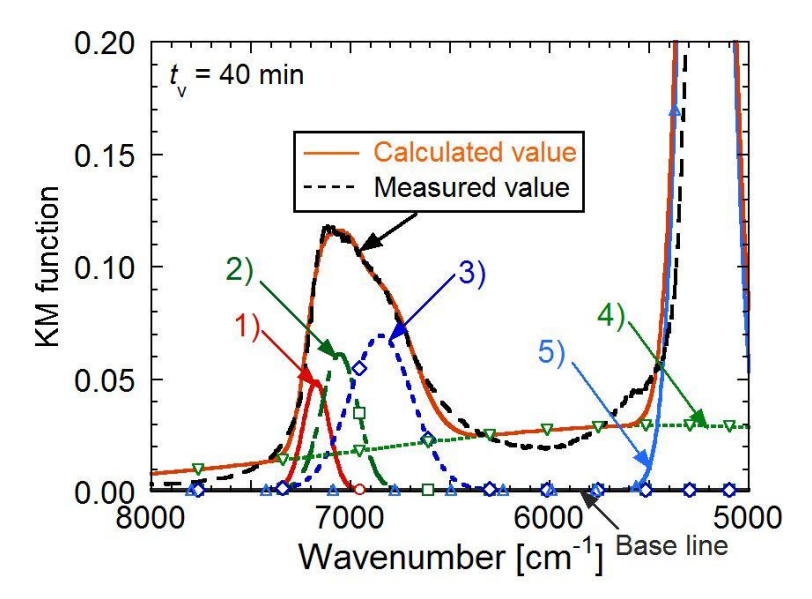


Figure 4.4-7 Deconvoluted spectrum of authentic MgO at 110°C, $p_{\text{H2O}} = 57.8 \text{ kPa}$ and, $t_{\text{v}} = 40 \text{ min}$: 1) Mg(OH)₂ (first overtone) (7174 cm⁻¹), 2) free water ($v_1 + v_3$) (7055 cm⁻¹), 3) bound water ($v_1 + v_3$) (6848 cm⁻¹), 4) free water ($v_2 + v_3$) (5400 cm⁻¹), and 5) bound water ($v_2 + v_3$) (5216 cm⁻¹).

The deconvoluted spectrum of authentic MgO at 110°C, $p_{\rm H2O} = 57.8$ kPa, and $t_{\rm v} = 40$ min is shown in **Figure 4.4-7**. The spectrum is deconvoluted into five components; 1) Mg(OH)₂ (first overtone) (7174 cm⁻¹), 2) free water ($v_1 + v_3$) (7055 cm⁻¹), 3) bound water ($v_1 + v_3$) (6848 cm⁻¹), 4) free water ($v_2 + v_3$) (5400 cm⁻¹), and 5) bound water ($v_2 + v_3$) (5216 cm⁻¹).

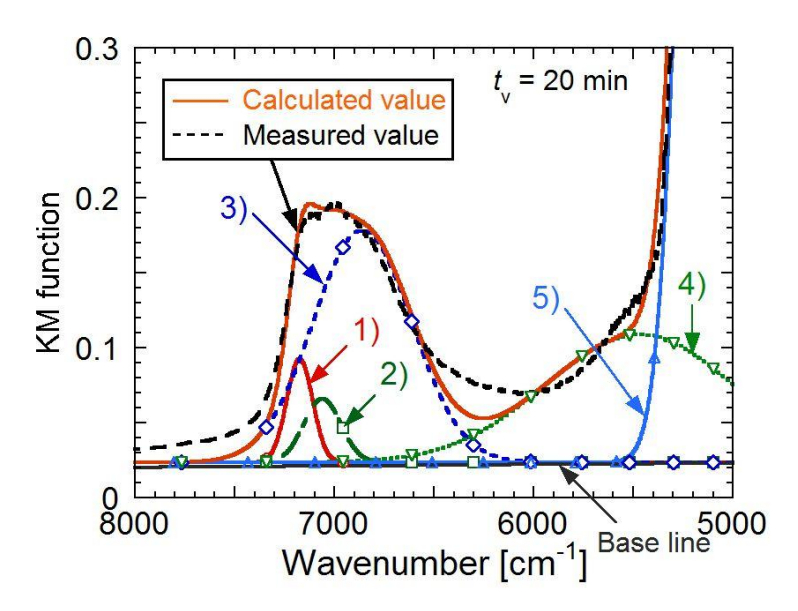


Figure 4.4-8 Deconvoluted spectrum of LiCl/MgO ($\alpha = 0.10$) at 110°C, $p_{\rm H2O} = 57.8$ kPa, $t_{\rm v} = 20$ min: 1) Mg(OH)₂ (first overtone) (7174 cm⁻¹), 2) free water ($v_1 + v_3$) (7060 cm⁻¹), 3) hydrated species ($v_1 + v_3$) (6859 cm⁻¹), 4) free water ($v_2 + v_3$) (5469 cm⁻¹), and 5) hydrated species ($v_2 + v_3$) (5130 cm⁻¹).

The deconvoluted spectrum of LiCl/MgO ($\alpha = 0.10$) at 110°C, $p_{\rm H2O} = 57.8$ kPa, and $t_{\rm v} = 20$ min is shown in **Figure 4.4-8**. The spectrum is deconvoluted into five components; 1) Mg(OH)₂ (first overtone) (7174 cm⁻¹), 2) free water ($v_1 + v_3$) (7060 cm⁻¹), 3) hydrated species ($v_1 + v_3$) (6859 cm⁻¹), 4) free water ($v_2 + v_3$) (5469 cm⁻¹), and 5) hydrated species ($v_2 + v_3$) (5130 cm⁻¹).

The deconvoluted spectrum of LiCl/MgO ($\alpha = 0.10$) at 110°C, $p_{\rm H2O} = 57.8$ kPa, and $t_{\rm v} = 40$ min is shown in **Figure 4.4-9**. The spectrum is deconvoluted into five components; 1) Mg(OH)₂ first overtone (7174 cm⁻¹), 2) free water ($v_1 + v_3$) (7060 cm⁻¹), 3) hydrated species ($v_1 + v_3$) (6859 cm⁻¹), 4) free water ($v_2 + v_3$) (5469 cm⁻¹), and 5) hydrated species ($v_2 + v_3$) (5130 cm⁻¹).

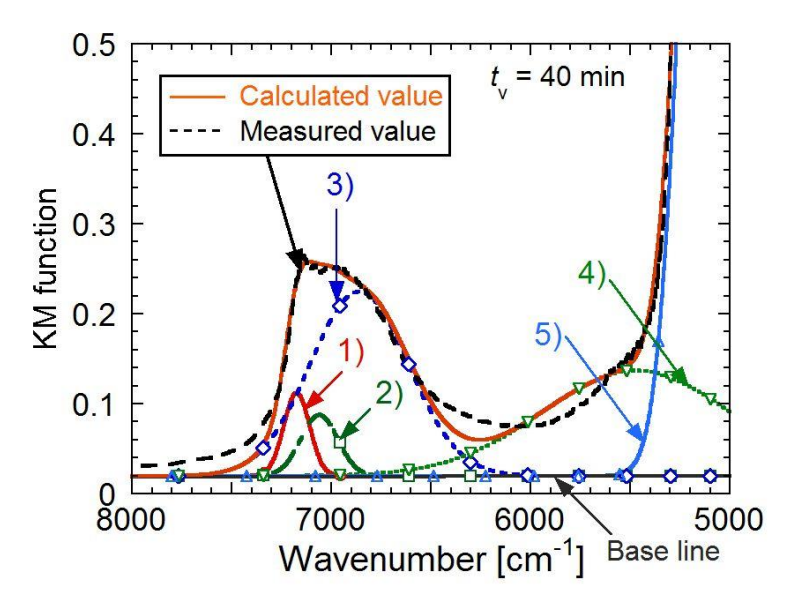


Figure 4.4-9 Deconvoluted spectrum of LiCl/MgO ($\alpha = 0.10$) at 110°C, $p_{\text{H2O}} = 57.8$ kPa, $t_{\text{v}} = 40$ min: 1) Mg(OH)₂ (first overtone) (7174 cm⁻¹), 2) free water ($v_1 + v_3$) (7060 cm⁻¹), 3) hydrated species ($v_1 + v_3$) (6859 cm⁻¹), 4) free water ($v_2 + v_3$) (5469 cm⁻¹), and 5) hydrated species ($v_2 + v_3$) (5130 cm⁻¹).

The deconvoluted spectrum of LiCl/MgO (α = 0.10) at 180°C, $p_{\rm H2O}$ = 57.8 kPa, $t_{\rm v}$ = 20 min is shown in **Figure 4.4-10**. The spectrum is deconvoluted into five components; 1) Mg(OH)₂ (first overtone) (7174 cm⁻¹), 2) free water ($v_1 + v_3$) (7060 cm⁻¹), 3) hydrated species ($v_1 + v_3$) (6859 cm⁻¹), 4) free water ($v_2 + v_3$) (5469 cm⁻¹), and 5) hydrated species ($v_2 + v_3$) (5130 cm⁻¹).

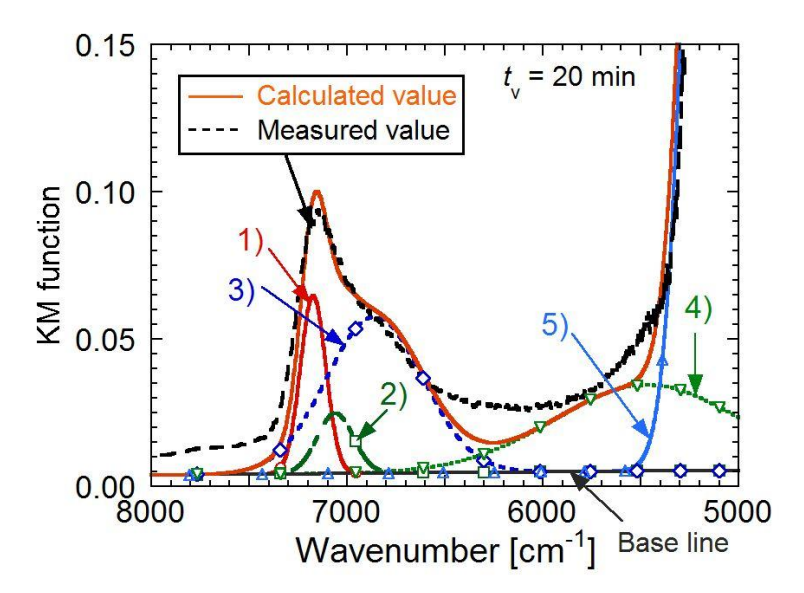


Figure 4.4-10 Deconvoluted spectrum of LiCl/MgO ($\alpha = 0.10$) at 180°C, $p_{H2O} = 57.8$ kPa, $t_v = 20$ min: 1) Mg(OH)₂ (first overtone) (7174 cm⁻¹), 2) free water ($v_1 + v_3$) (7060 cm⁻¹), 3) hydrated species ($v_1 + v_3$) (6859 cm⁻¹), 4) free water ($v_2 + v_3$) (5469 cm⁻¹), and 5) hydrated species ($v_2 + v_3$) (5130 cm⁻¹).

The deconvoluted spectrum of LiCl/MgO (α = 0.10) at 180°C, $p_{\rm H2O}$ = 57.8 kPa, $t_{\rm v}$ = 40 min is shown in **Figure 4.4-11**. The spectrum is deconvoluted into five components; 1) Mg(OH)₂ (first overtone) (7174 cm⁻¹), 2) free water ($v_1 + v_3$) (7060 cm⁻¹), 3) hydrated species ($v_1 + v_3$) (6859 cm⁻¹), 4) free water ($v_2 + v_3$) (5469 cm⁻¹), and 5) hydrated species ($v_2 + v_3$) (5130 cm⁻¹).

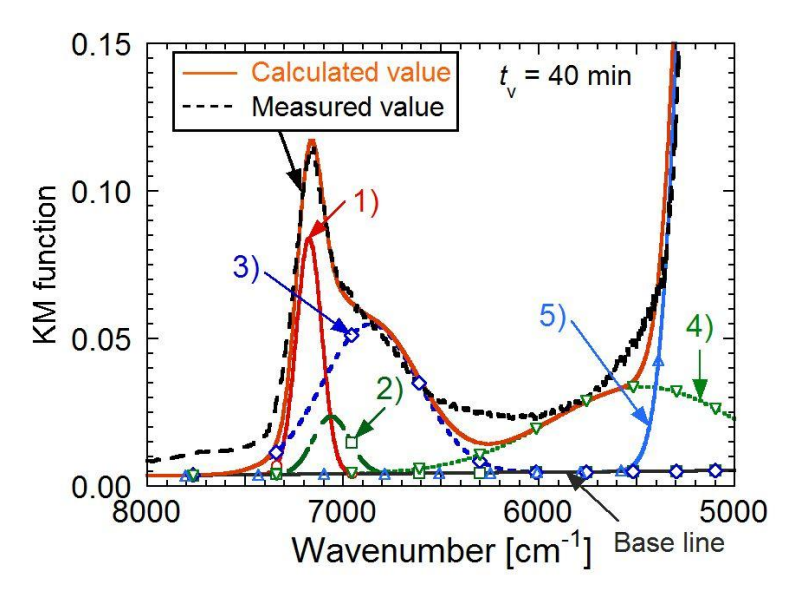


Figure 4.4-11 Deconvoluted spectrum of LiCl/MgO ($\alpha = 0.10$) at 180°C, $p_{\text{H2O}} = 57.8$ kPa, $t_{\text{v}} = 40$ min: 1) Mg(OH)₂ (first overtone) (7174 cm⁻¹), 2) free water ($v_1 + v_3$) (7060 cm⁻¹), 3) hydrated species ($v_1 + v_3$) (6859 cm⁻¹), 4) free water ($v_2 + v_3$) (5469 cm⁻¹), and 5) hydrated species ($v_2 + v_3$) (5130 cm⁻¹).

4.4.2 Hydration mechanism

4.4.2.1 Authentic magnesium oxide

A profile of peak area of Mg(OH)₂ (first overtone) for authentic MgO at 110°C and $p_{\rm H2O}$ = 57.8 kPa is shown in **Figure 4.4-12**. The peak area increased steeply from 4 to 12 min, gradually from 12 to 32 min, and steeply from 32 to 40 min. A profile of peak area of free water ($v_1 + v_3$) for authentic MgO at 110°C and $p_{\rm H2O}$ = 57.8 kPa is shown in **Figure 4.4-13**. The peak area was zero until 20 min, and increased linearly from 20 to 40 min. A profile of peak area of bound water ($v_1 + v_3$) for authentic MgO at 110°C and $p_{\rm H2O}$ = 57.8 kPa is shown in **Figure 4.4-14**. The peak area was zero until 24 min, and increased steeply from 20 to 40 min.

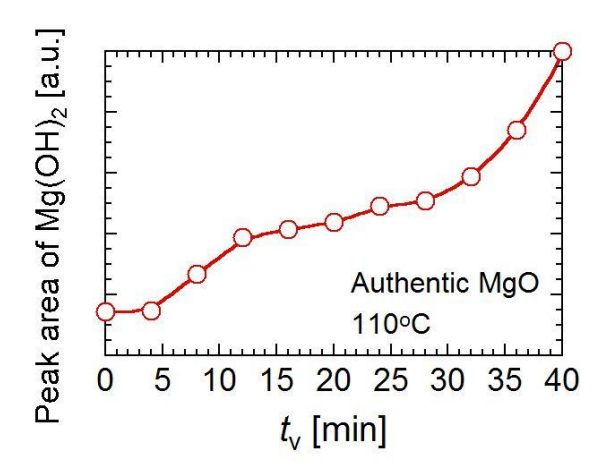


Figure 4.4-12 Profile of peak area of Mg(OH)₂ (first overtone) for authentic MgO at 110°C and $p_{\rm H2O}$ = 57.8 kPa.

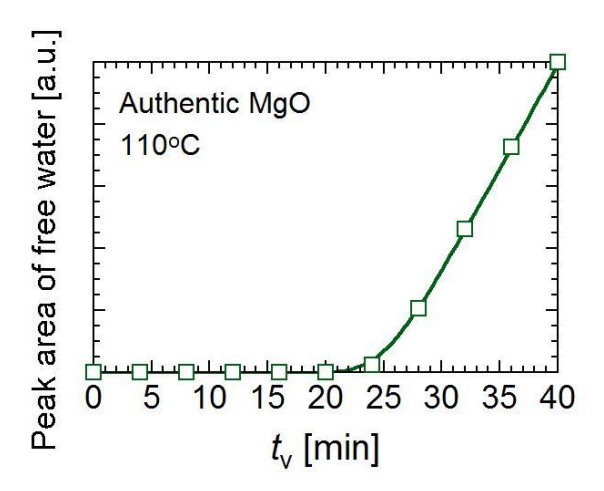


Figure 4.4-13 Profile of peak area of free water $(v_1 + v_3)$ for authentic MgO under hydration operation at 110°C and $p_{\rm H2O} = 57.8$ kPa.

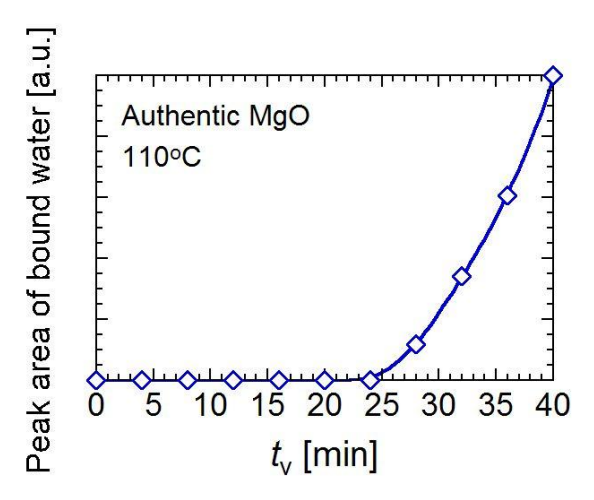


Figure 4.4-14 Profile of peak area of bound water $(v_1 + v_3)$ for authentic MgO under hydration operation at 110°C and $p_{\rm H2O} = 57.8$ kPa.

Differential peak areas are calculated to obtain information about rate of hydration or water sorption. Differential peak areas are evaluated from the central difference ($\Delta t = 8 \text{ min}$) of the original data. Differential peak area of Mg(OH)₂ (first overtone) for authentic MgO at 110°C and $p_{\text{H2O}} = 57.8 \text{ kPa}$ is shown in **Figure 4.4-15**, that of free water ($v_1 + v_3$) is shown in **Figure 4.4-16**, and that of bound water ($v_1 + v_3$) is shown in **Figure 4.4-17**, respectively. Differential peak area of Mg(OH)₂ (first overtone) showed relatively large value at $t_v = 4 \text{min}$. On the other hand, differential peak area of free water and bound water remained zero until $t_v = 16 \text{ min}$. These results indicate the supplied water vapor was consumed by hydration of MgO at surface until $t_v = 16 \text{ min}$. Differential peak area of Mg(OH)₂ (first overtone) increased after $t_v = 20 \text{ min}$, and then differential peak area of Mg(OH)₂ (first overtone) increased after $t_v = 28 \text{ min}$. These results indicate water adsorption on the surface was started at around $t_v = 20 \text{ min}$, and hydration of MgO at inner side was proceeded by diffusion of adsorbed water from surface to inner side.

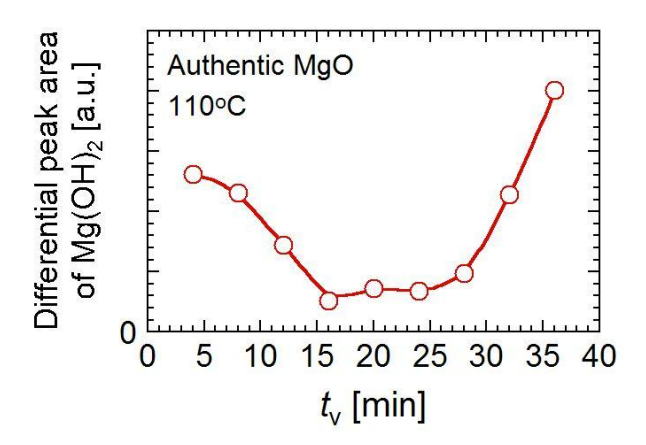


Figure 4.4-15 Differential profile of peak area of Mg(OH)₂ (first overtone) for authentic MgO under hydration operation at 110°C and $p_{\rm H2O}$ = 57.8 kPa.

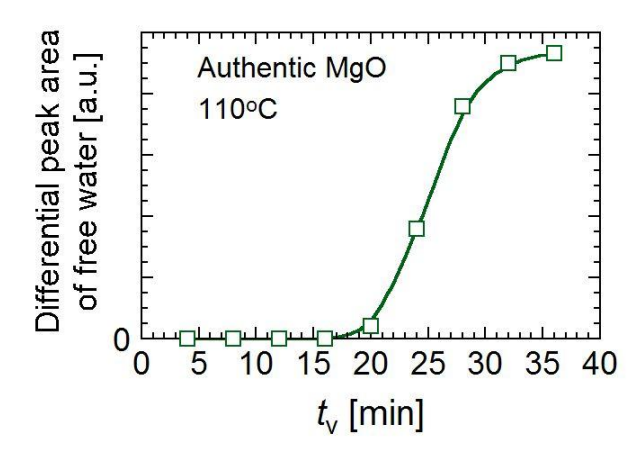


Figure 4.4-16 Differential profile of peak area of free water $(v_1 + v_3)$ for authentic Mg(OH)₂ under hydration operation at 110°C and $p_{\rm H2O} = 57.8$ kPa.

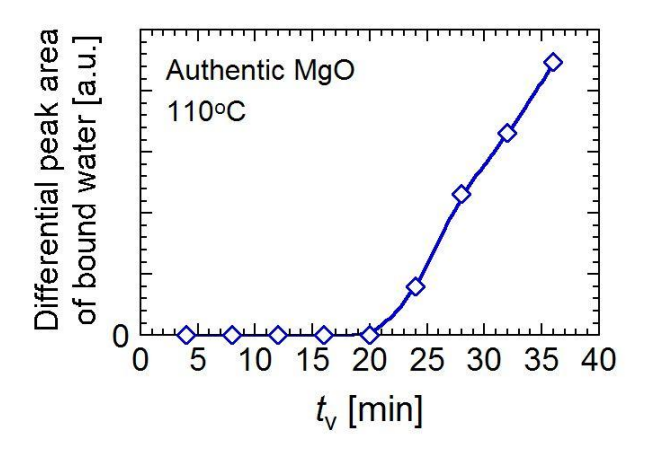


Figure 4.4-17 Differential profile of peak area of bound water $(v_1 + v_3)$ for authentic Mg(OH)₂ under hydration operation at 110°C and $p_{\rm H2O} = 57.8$ kPa.

4.4.2.1 Lithium chloride-modified magnesium oxide

A profile of peak area of Mg(OH)₂ (first overtone) for LiCl/MgO (α = 0.10) at 110°C and $p_{\rm H2O}$ = 57.8 kPa is shown in **Figure 4.4-18**. The peak area increased gradually until 12 min, steeply from 12 to 20 min, and gradually from 20 to 40 min. A profile of peak area of free water ($v_1 + v_3$) for LiCl/MgO (α = 0.10) at 110°C and $p_{\rm H2O}$ = 57.8 kPa is shown in **Figure 4.4-19**. The peak area increased linearly but the slope was changed at 12 min. A profile of peak area of hydrated species ($v_1 + v_3$) for LiCl/MgO (α = 0.10) at 110°C and $p_{\rm H2O}$ = 57.8 kPa is shown in **Figure 4.4-20**. The peak area increased steeply until 12 min, and increased gradually from 12 to 40 min.

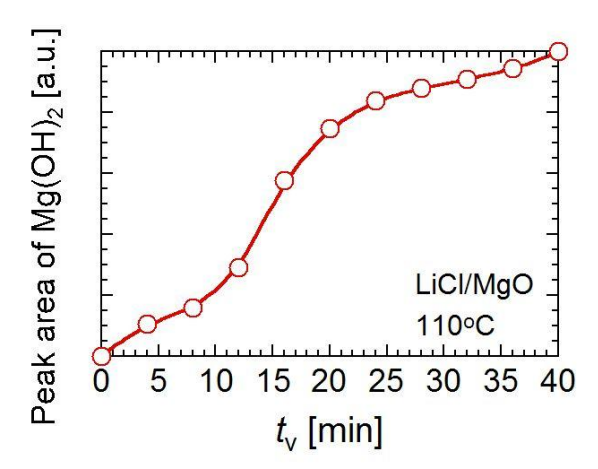


Figure 4.4-18 Profile of peak area of Mg(OH)₂ (first overtone) for LiCl/MgO ($\alpha = 0.10$) under hydration operation at 110°C and $p_{\rm H2O} = 57.8$ kPa.

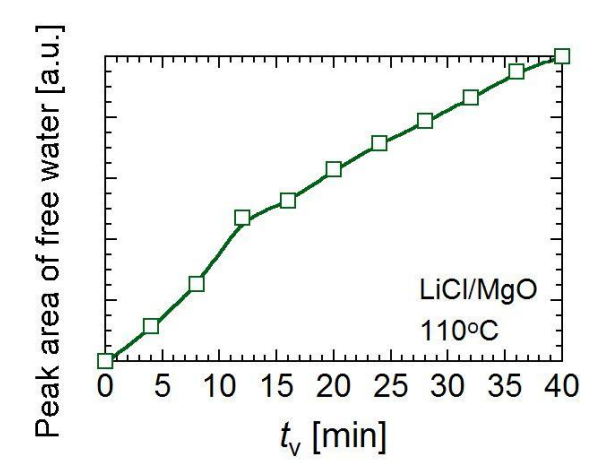


Figure 4.4-19 Profile of peak area of free water $(v_1 + v_3)$ for LiCl/MgO ($\alpha = 0.10$) under hydration operation at 110°C and $p_{\rm H2O} = 57.8$ kPa.

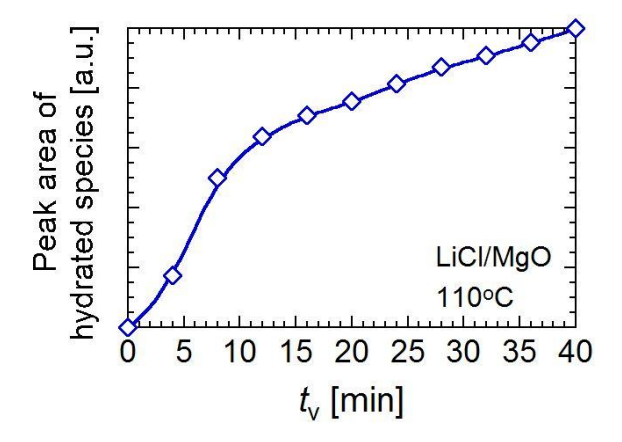


Figure 4.4-20 Profile of peak area of hydrated species ($v_1 + v_3$) for LiCl/MgO ($\alpha = 0.10$) under hydration operation at 110°C and $p_{\rm H2O} = 57.8$ kPa.

Differential peak area of Mg(OH)₂ (first overtone) for LiCl/MgO (α = 0.10) at 110°C and $p_{\rm H2O}$ = 57.8 kPa is shown in **Figure 4.4-21**, that of free water ($v_1 + v_3$) is shown in **Figure 4.4-22**, and that of hydrated species ($v_1 + v_3$) is shown in **Figure 4.4-23**, respectively. Differential peak area of Mg(OH)₂ (first overtone) showed peak at around t_v = 16 min. On the other hand, differential peak area of free water ($v_1 + v_3$) showed peak at t_v = 8 min, and that of hydrated species ($v_1 + v_3$) showed peak at t_v = 4 min. These results suggests supplied water vapor was consumed for formation of free water and hydrated species for first 8 min, and then hydration of MgO was proceeded. There are two possibilities of reaction paths for hydration of LiCl/MgO (α = 0.10) at 110°C. One of them is a cascaded relationship between water sorption at LiCl (Eq. (4-3)) and solid-solid reaction of LiCl·H₂O and MgO (Eq. (4-4)) (Reaction path A). The absorbed water was consumed for the hydration of MgO in this reaction path.

$$LiCl + H2O(g) \rightarrow LiCl \cdot nH2O$$
 (4-3)

$$LiCl \cdot n H_2O + MgO \rightarrow LiCl \cdot (n-1)H_2O + Mg(OH), \tag{4-4}$$

The other possibility is parallel relationship between water sorption of LiCl (Eq. (4-5)) and hydration of MgO (Eq. (4-6)) (Reaction path B). The absorbed water was not consumed for the hydration of MgO in this reaction path.

$$LiCl + H2O(g) \rightarrow LiCl \cdot nH2O$$
 (4-5)

$$MgO + H_2O(g) \rightarrow Mg(OH)_2$$
 (4-6)

It is not easy to identify the reaction path. However, hydration was enhanced by LiCl-modification (**Chapter 3**), the hydration mechanism of LiCl/MgO ($\alpha = 0.10$) can be explained by reaction path A.

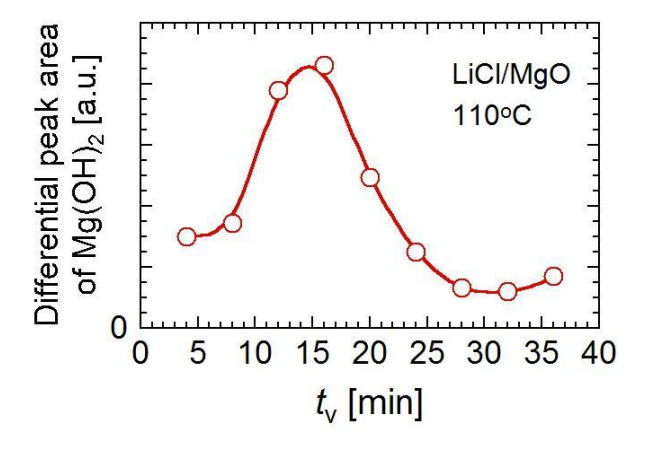


Figure 4.4-21 Differential profile of peak area of Mg(OH)₂ (first overtone) for LiCl/MgO (α = 0.10) under hydration operation at 110°C and $p_{\rm H2O}$ = 57.8 kPa.

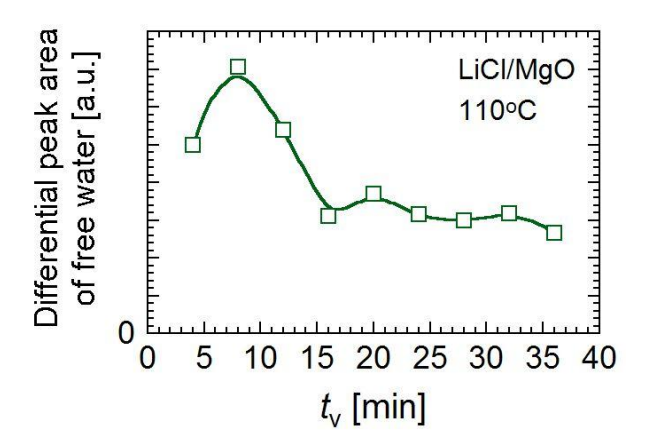


Figure 4.4-22 Differential profile of peak area of free water ($v_1 + v_3$) for LiCl/MgO ($\alpha = 0.10$) under hydration operation at 110°C and $p_{\rm H2O} = 57.8$ kPa.

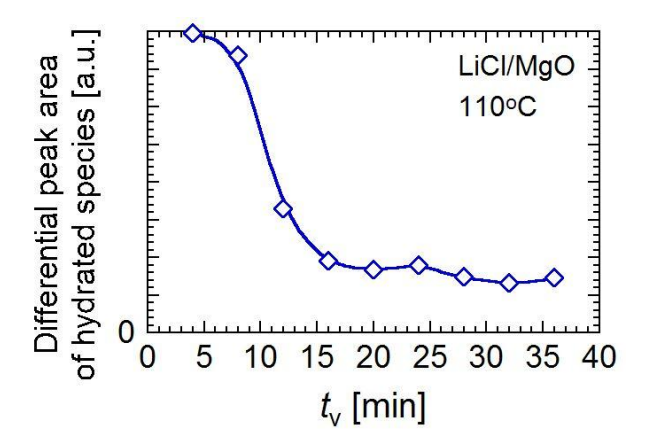


Figure 4.4-23 Differential profile of peak area of hydrated species ($v_1 + v_3$) for LiCl/MgO ($\alpha = 0.10$) under hydration operation at 110°C and $p_{\rm H2O} = 57.8$ kPa.

A profile of peak area of Mg(OH)₂ (first overtone) for LiCl/MgO (α = 0.10) at 180°C and $p_{\rm H2O}$ = 57.8 kPa is shown in **Figure 4.4-24**. The profile of peak area showed upward curve. A profile of peak area of free water ($v_1 + v_3$) for LiCl/MgO (α = 0.10) at 180°C and $p_{\rm H2O}$ = 57.8 kPa is shown in **Figure 4.4-25**. The peak area increased steeply until 16 min, and then it became almost constant. A profile of peak area of hydrated species ($v_1 + v_3$) for LiCl/MgO (α = 0.10) at 180°C and $p_{\rm H2O}$ = 57.8 kPa is shown in **Figure 4.4-26**. The peak area increased steeply until 12 min, and then it became almost constant.

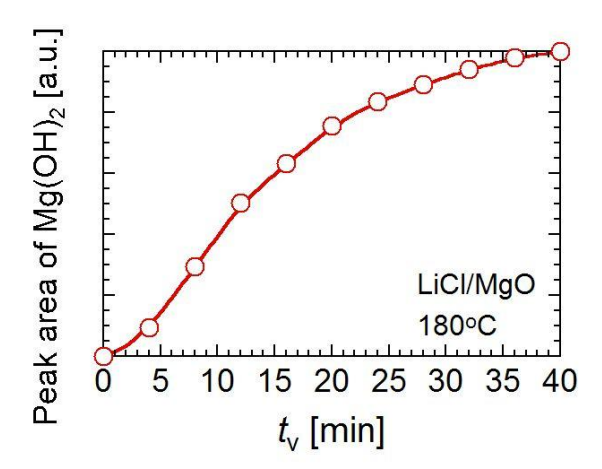


Figure 4.4-24 Profile of peak area of Mg(OH)₂ (first overtone) for LiCl/MgO ($\alpha = 0.10$) under hydration operation at 180°C and $p_{\rm H2O} = 57.8$ kPa.

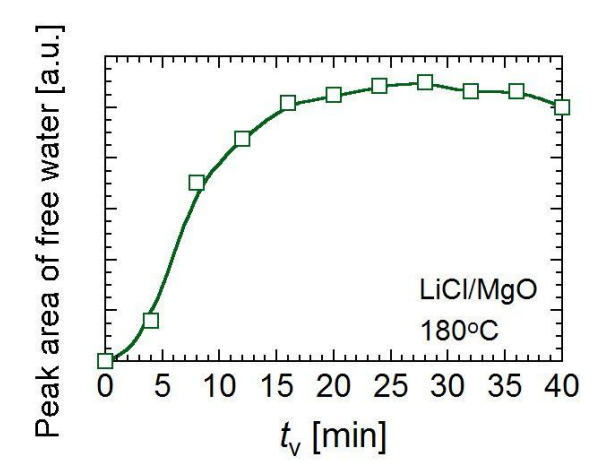


Figure 4.4-25 Profile of peak area of free water ($v_1 + v_3$) for LiCl/MgO ($\alpha = 0.10$) under hydration operation at 180°C and $p_{\rm H2O} = 57.8$ kPa.

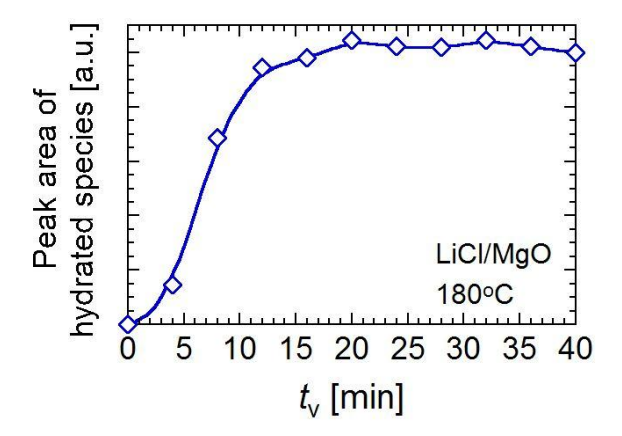


Figure 4.4-26 Profile of peak area of hydrated species ($v_1 + v_3$) for LiCl/MgO ($\alpha = 0.10$) under hydration operation at 180°C and $p_{\rm H2O} = 57.8$ kPa.

Differential peak area of Mg(OH)₂ (first overtone) for LiCl/MgO (α = 0.10) at 180°C and $p_{\rm H2O}$ = 57.8 kPa is shown in **Figure 4.4-27**, that of free water (v_1 + v_3) is shown in **Figure 4.4-28**, and that of hydrated species (v_1 + v_3) is shown in **Figure 4.4-29**, respectively. Differential peak area of free water (v_1 + v_3) and hydrated species (v_1 + v_3) showed peak at around t_v = 8 min, and then decreased until t_v = 20 min. On the other hand, differential peak area of Mg(OH)₂ (first overtone) showed peak at 8 min, and then decreased. These results suggest hydration of MgO and water sorption occurred almost simultaneously until t_v = 20 min. Finally, differential peak area of free water (v_1 + v_3) and hydrated species (v_1 + v_3) remained around zero after t_v = 24 min. This result indicates water sorption reached equilibrium state at around t_v = 24 min. There were two possibilities of reaction paths for hydration of LiCl/MgO (α = 0.10) at 180°C, same as hydration at 110°C. One of them is a cascaded relationship between water sorption of LiCl (Eq. (4-3)) and solid-solid reaction of LiCl·H₂O and MgO (Eq. (4-4)) (Reaction path A). The other possibility is parallel relationship between water sorption of LiCl (Eq. (4-5)) and hydration of MgO (Eq. (4-6)) (Reaction path B). The hydration at 180°C was enhanced by LiCl-modification (Chapter 3), the hydration mechanism of LiCl/MgO (α = 0.10) can be explained by reaction path A.

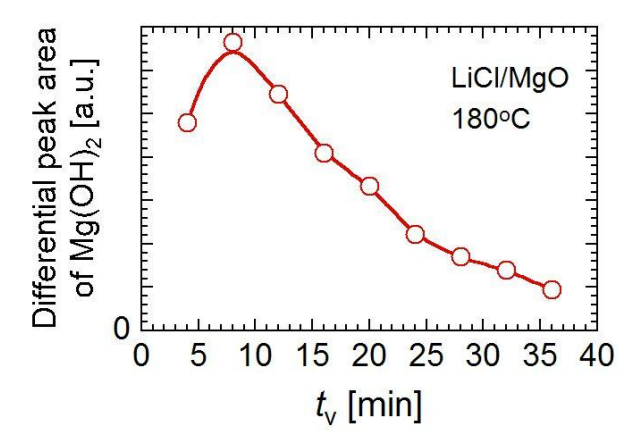


Figure 4.4-27 Differential profile of peak area of Mg(OH)₂ (first overtone) for LiCl/MgO (α = 0.10) under hydration operation at 180°C and $p_{\rm H2O}$ = 57.8 kPa.

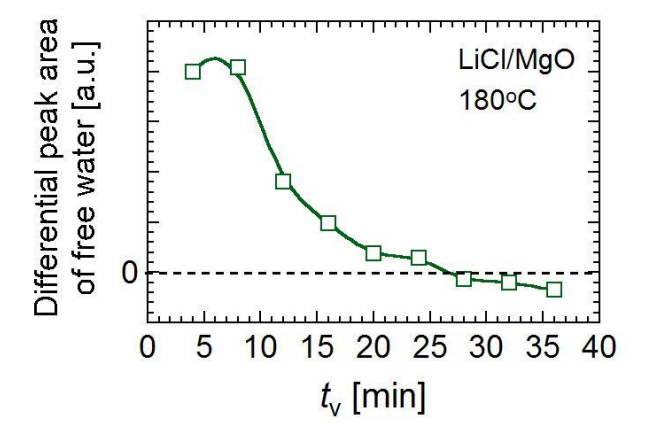


Figure 4.4-28 Differential profile of peak area of free water ($v_1 + v_3$) for LiCl/MgO ($\alpha = 0.10$) under hydration operation at 180°C and $p_{\rm H2O} = 57.8$ kPa.

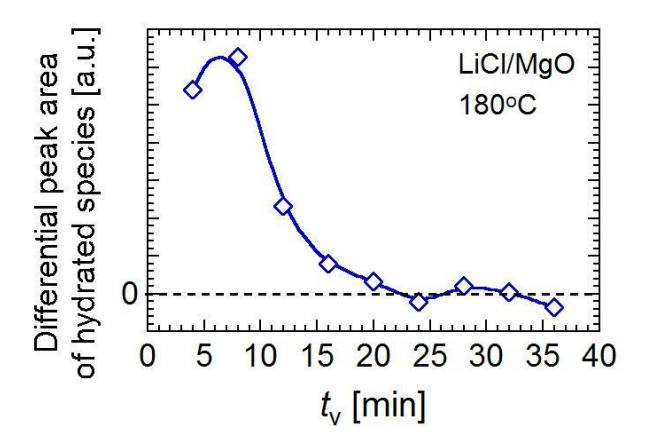


Figure 4.4-29 Differential profile of peak area of hydrated species ($v_1 + v_3$) for LiCl/MgO ($\alpha = 0.10$) under hydration operation at 180°C and $p_{\rm H2O} = 57.8$ kPa.

4.5 Summary

Hydrations of authentic MgO and LiCl/MgO (α = 0.10) were observed by near infrared spectroscopy to understand the contribution of LiCl-modification. The obtained spectra were deconvoluted into components (Mg(OH)₂, free water, and bound water or hydrated species). The spectrum of authentic MgO is deconvoluted into five components; 1) Mg(OH)₂ (first overtone), 2) free water ($v_1 + v_3$), 3) hydrated species ($v_1 + v_3$), 4) free water ($v_2 + v_3$), and 5) hydrated species ($v_2 + v_3$), and that of LiCl/MgO (α = 0.10) is deconvoluted into five components; 1) Mg(OH)₂ (first overtone), 2) free water ($v_1 + v_3$), 3) hydrated species ($v_1 + v_3$), 4) free water ($v_2 + v_3$), and 5) hydrated species ($v_2 + v_3$).

The hydration mechanism was discussed by profile of peak area for each component with time. For authentic MgO, supplied water vapor was consumed by hydration of MgO at surface until first 16 min, and water adsorption on the surface was started at $t_v = 20$ min. Hydration of MgO at inner side was proceeded by adsorbed water on the surface of MgO after $t_v = 28$ min. For LiCl/MgO ($\alpha = 0.10$) at 110°C, supplied water vapor was consumed for formation of free water and hydrated species for first 8 min, and then hydration of MgO was proceeded. For LiCl/MgO ($\alpha = 0.10$) at 180°C, hydration of MgO and water sorption was occurred almost simultaneously until $t_v = 20$ min., and water sorption was reached equilibrium state at around $t_v = 24$ min. There are two possibilities of reaction paths for hydration of LiCl/MgO ($\alpha = 0.10$). One of them is a cascaded relationship between water sorption of LiCl and solid-solid reaction of LiCl·H₂O and MgO (Reaction path A). The other possibility is parallel relationship between water sorption of LiCl and hydration of MgO (Reaction path B). The hydration was enhanced by LiCl-modification (**Chapter 3**), the hydration mechanism of LiCl/MgO ($\alpha = 0.10$) can be explained by reaction path A.

4.6 References

[1] W. N. Delgass, G. L. Haller, R. Kellerman, J. H. Lunsford; Spectroscopy in heterogeneous catalysis,

Academic press, New York, U.S. (1979)

- [2] R. Martens, F. Freund; The potential energy curve of the proton and the discussion energy of the OH- ion in Mg(OH)₂, *Phys. Status Solidi A*, **37**, 97–104 (1976)
- [3] M. Takeuchi, G. Martra, S. Coluccia, M. Anpo; Investigations of the structure of H₂O clusters adsorbed on TiO₂ surfaces by near-infrared absorption spectroscopy, *J. Phys. Chem. B*, **109**, 7387–7391 (2005)
- [4] M. Takeuchi, G. Martra, S. Coluccia, M. Anpo; Evaluation of the adsorption states of H₂O on oxide surfaces by vibrational absorption: near- and mid-infrared spectroscopy, *J. Near Infrared Spectrosc.*, **17**, 373–384 (2009)

Chapter 5 Durability of lithium chloride-modified magnesium hydroxide on repetitive reactions

5.1 Introduction

The dehydration and hydration reactivity of LiCl/Mg(OH)₂ were studied at **Chapter 2** and **Chapter 3**. From previous results, LiCl/Mg(OH)₂ is a candidate for thermochemical energy storage materials (TCM) to store heat at 250–300°C, and output heat at 110–180°C with 57.8 kPa of water vapor. The knowledge on durability properties of LiCl/Mg(OH)₂ is needed to study for practical application. For example, it is used to decide a period for replacement of TCM. The reason for the reactivity change should be explained. Although there have been some reports on the durability characteristics of TCMs [1-6]. However, the durability characteristics of metal-salt-modified material have not been reported.

In this chapter, the thermogravimetry was used to investigate the reactivity change of LiCl/Mg(OH)₂ in 105 dehydration/hydration cycles. The samples were dehydrated at 250°C and hydrated at 110°C. The number of cycle, 105, was selected to examine heat storage/output operations for one winter-season. It is assumed that one cycle of heat storage/output operation is performed every day for 105 days (from early December to middle of March, for example). A target value of durability property of the material is to keep heat output capacity as \pm 20% under 105 runs compared with initial value.

The surface state of LiCl/Mg(OH)₂ is quite important for its reactivity. Thus, samples were characterized before and after 1, 7, and 105 cyclic operational runs. Microstructures were observed using scanning electron microscopy. The crystal structures of the samples were examined using powder X-ray diffraction. Specific surface areas of samples were determined by the adsorption of nitrogen gas.

5.2 Experimental

5.2.1 Sample preparation

 $LiCl/Mg(OH)_2$ was prepared using an impregnation method. A detail of the procedure was shown in **Section 2.2.1**. In this chapter, $LiCl/Mg(OH)_2$ ($\alpha = 0.10$) was employed.

5.2.2 Repetitive dehydration—hydration measurement with thermogravimetry

The dehydration and hydration of the samples were measured by thermogravimetry using a thermobalance (TGD9600, ULVAC-RIKO, Inc.). LiCl/Mg(OH)₂ samples were charged into the Pt cell of the balance. The dehydration temperature (T_d) was 250°C and the hydration temperature (T_d) was 110°C, with heating and cooling rate of 20 °C min⁻¹ under argon gas flow (flow rate 100 mL min⁻¹).

Prior to dehydration, the samples were dried at 110°C for 110 min to remove sorbed water.

The sample weight at the first achievement of 200°C was defined as the initial weight. The samples were then dehydrated at 250°C for 200 min. The hydration operation was conducted by introducing a mixture of water vapor and argon (carrier gas) at a water vapor pressure of 57.8 kPa for 80 min. This vapor pressure corresponded to the saturated vapor pressure at 85°C. After the hydration operation was complete, the vapor supply was stopped and dry argon gas was introduced at the same hydration temperature for 50 min in order to remove sorbed water (drying operation). This set of dehydration–drying operations is designated as the cyclic operation. In this study, 105 runs of this cyclic operation were examined.

Mole fraction of Mg(OH)₂ (x) [mol/mol] in the particles consisting of MgO and Mg(OH)₂ was calculated using the Eq. (5-1), where Δw [kg] is the weight change of the sample, $M_{\rm H2O}$ [kg mol⁻¹] is the molecular weight of water, $M_{\rm hydroxide}$ [kg mol⁻¹] is the molecular weight of Mg(OH)₂, and $w_{\rm hydroxide}$ [kg] is the initial sample weight.

$$x [\text{mol/mol}] = \left[1 + \frac{\Delta w / M_{\text{H}_2\text{O}}}{w_{\text{hydroxide}} / M_{\text{hydroxide}}} \right]$$
 (5-1)

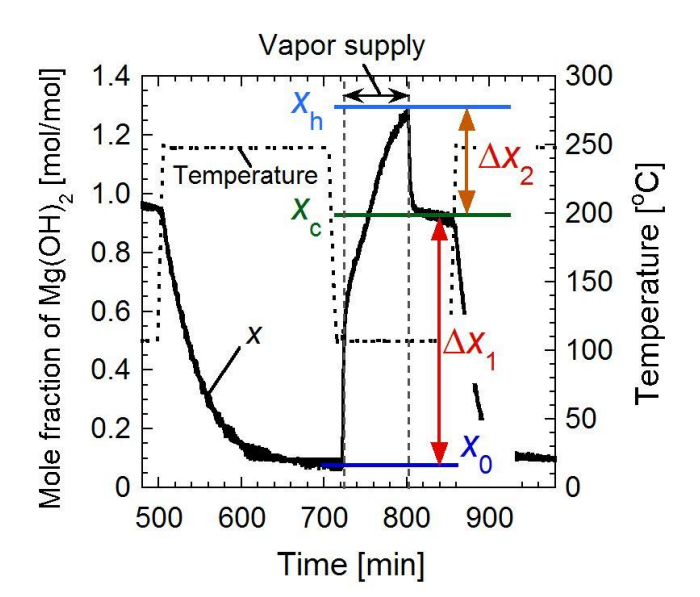


Figure 5.2-1 One cycle of the dehydration and hydration operation. x indicates mole fraction of Mg(OH)₂.

Figure 5.2-1 shows a dehydration and hydration profiles of LiCl/Mg(OH)₂ ($\alpha = 0.10$). The mole fraction of Mg(OH)₂ after the dehydration reaction is denoted as x_0 [mol/mol], that of Mg(OH)₂ at the end of the vapor supply period is denoted as x_h [mol/mol], and that of Mg(OH)₂ after the drying operation is denoted as x_c [mol/mol]. The conversion of the hydration (Δx_1 [mol/mol]) is defined as $\Delta x_1 = x_c - x_0$, and the apparent change of x by sorption (Δx_2 [mol/mol]) is defined as $\Delta x_2 = x_h - x_c$.

The heat output capacity was calculated from the enthalpy changes in the reaction and upon

the sorption of water vapor. The detail of the calculation was shown in **Section 3.2.3**.

5.2.3 Characterization techniques

5.2.3.1 Scanning electron microscopy

Scanning electron microscopy (SEM) was performed to identify the microstructures and surface morphologies of the samples. A scanning electron microscope (SM-200, TOPCON Corp.) was used. An acceleration voltage was 5–10 kV.

5.2.3.2 Powder X-ray diffraction analysis

Powder X-ray diffraction (XRD) measurements were carried out under atmospheric conditions at room temperature using an X-ray diffractometer (Ultima IV, Rigaku Corp.) through a 2θ range 10° – 90° at a scan speed of 1° min⁻¹ using monochromatic Cu K α radiation, 40 kV generator voltage, and 40 mA current.

5.2.3.3 Measurements of specific surface area

The nitrogen adsorption isotherm at 77.4 K was measured (Omnisorp 100CX, Beckman Coulter Inc.). The specific surface area of the samples was calculated using the BET method. Prior to nitrogen adsorption, the samples were evacuated at 120°C for 30 min as a pretreatment.

5.3 Results

5.3.1 Repetitive dehydration—hydration measurement with thermogravimetry

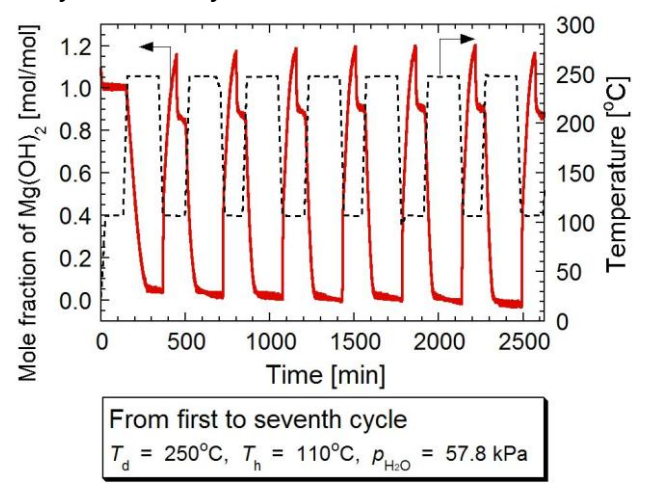


Figure 5.3-1 Dehydration and hydration profile of LiCl/Mg(OH)₂ (α = 0.10) from first cycle to seventh cycle.

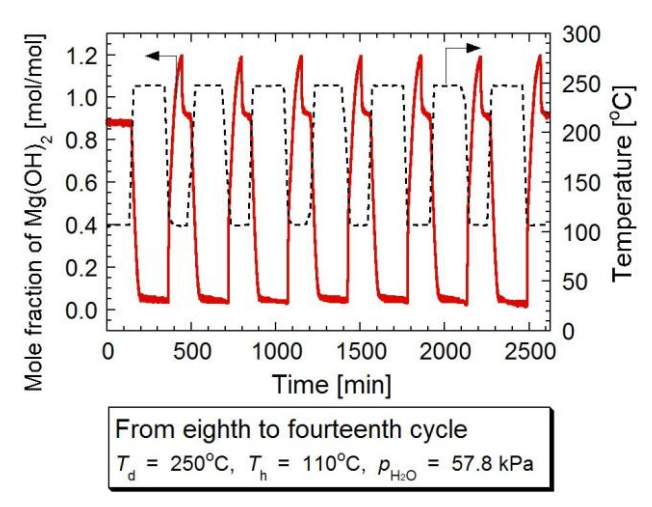


Figure 5.3-2 Dehydration and hydration profile of LiCl/Mg(OH)₂ ($\alpha = 0.10$) from eighth cycle to fourteenth cycle.

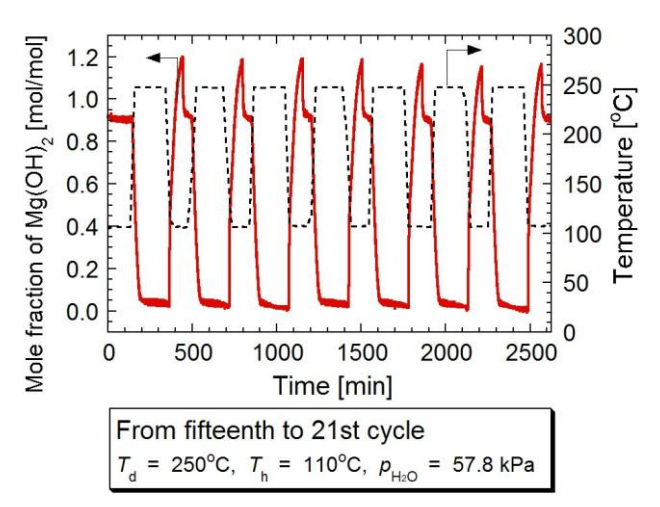


Figure 5.3-3 Dehydration and hydration profile of LiCl/Mg(OH)₂ ($\alpha = 0.10$) from fifteenth cycle to 21st cycle.

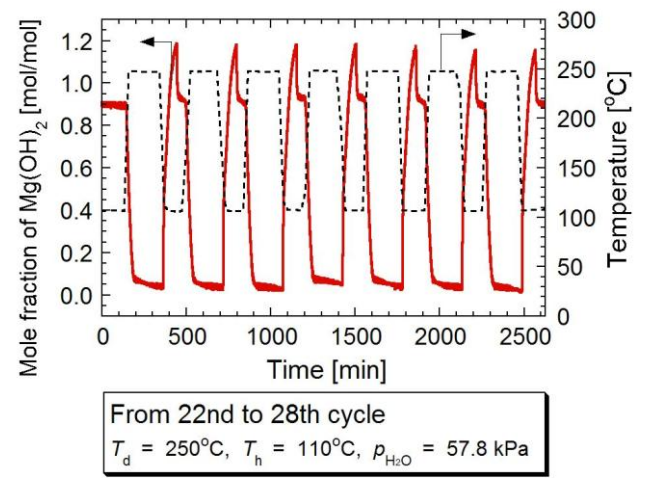


Figure 5.3-4 Dehydration and hydration profile of LiCl/Mg(OH)₂ (α = 0.10) from 22nd cycle to 28th cycle.

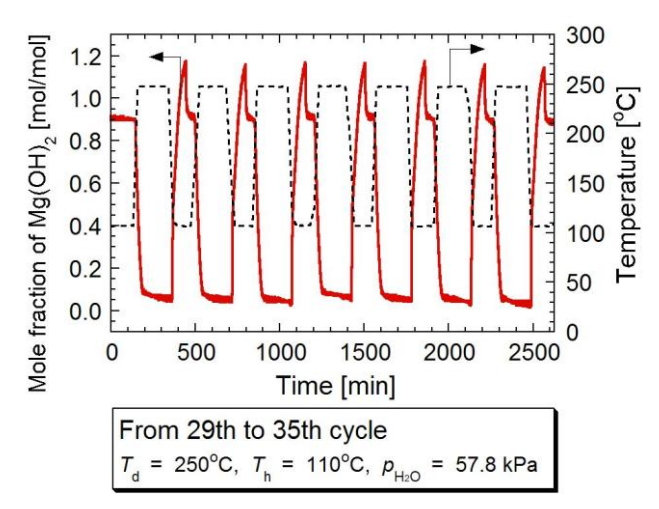


Figure 5.3-5 Dehydration and hydration profile of LiCl/Mg(OH)₂ ($\alpha = 0.10$) from 29th cycle to 35th cycle.

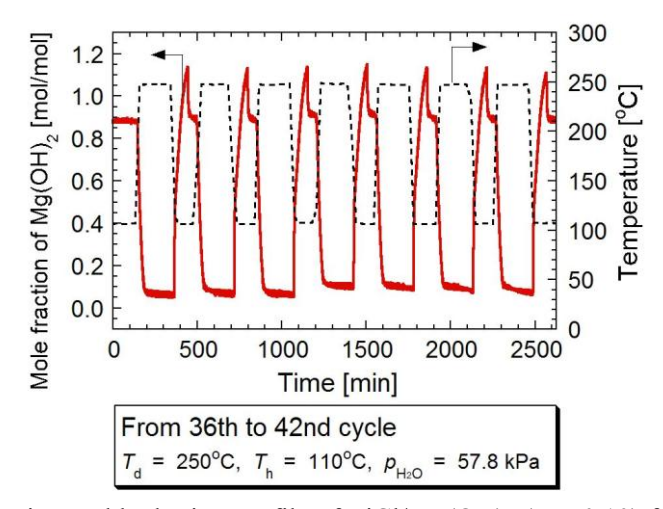


Figure 5.3-6 Dehydration and hydration profile of LiCl/Mg(OH)₂ (α = 0.10) from 36th cycle to 42nd cycle.

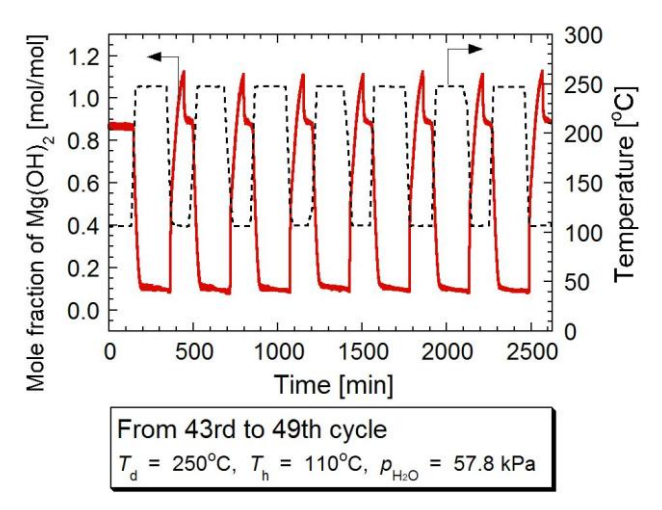


Figure 5.3-7 Dehydration and hydration profile of LiCl/Mg(OH)₂ ($\alpha = 0.10$) from 43rd cycle to 49th cycle.

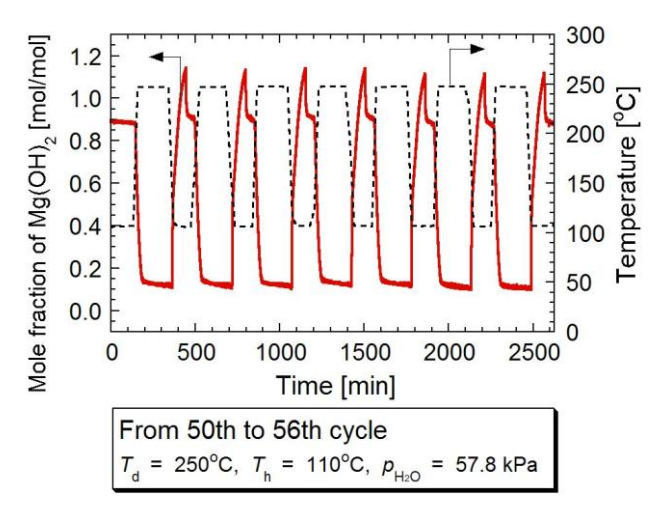


Figure 5.3-8 Dehydration and hydration profile of LiCl/Mg(OH)₂ ($\alpha = 0.10$) from 50th cycle to 56th cycle.

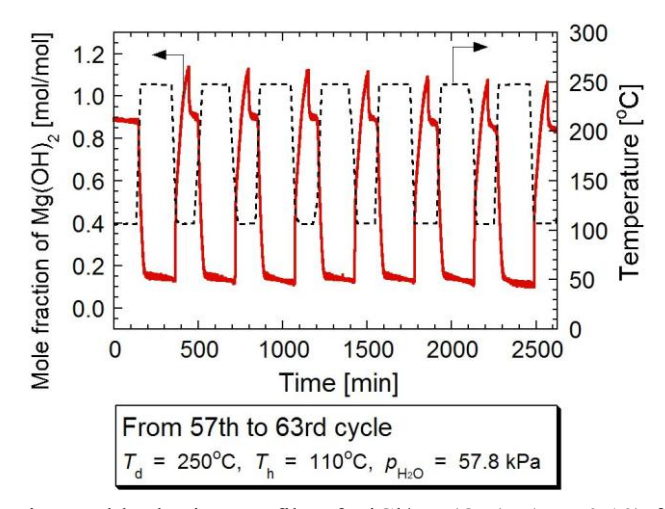


Figure 5.3-9 Dehydration and hydration profile of LiCl/Mg(OH)₂ ($\alpha = 0.10$) from 57th cycle to 63rd cycle.

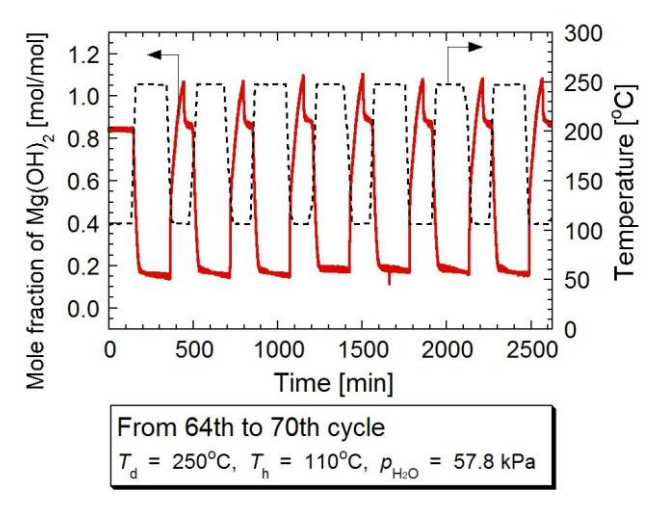


Figure 5.3-10 Dehydration and hydration profile of LiCl/Mg(OH)₂ (α = 0.10) from 64th cycle to 70th cycle.

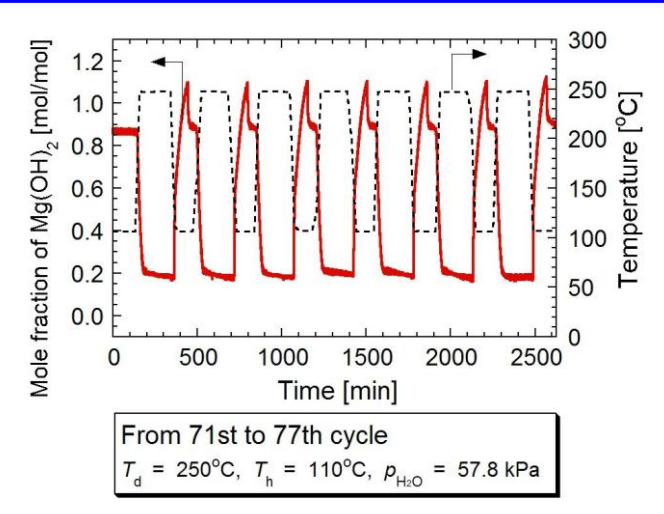


Figure 5.3-11 Dehydration and hydration profile of LiCl/Mg(OH)₂ ($\alpha = 0.10$) from 71st cycle to 77th cycle.

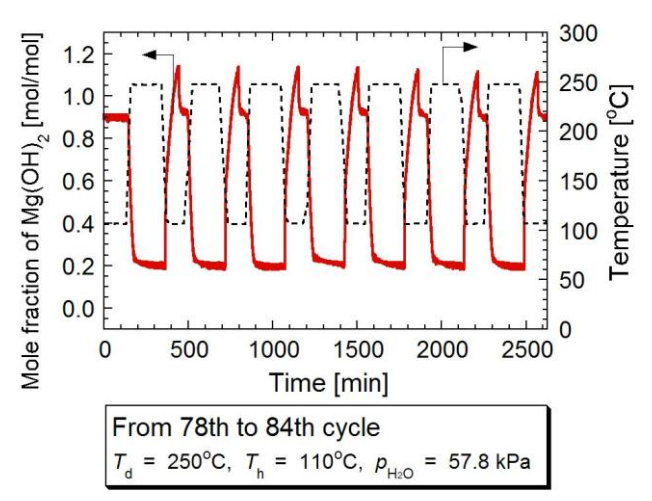


Figure 5.3-12 Dehydration and hydration profile of LiCl/Mg(OH)₂ (α = 0.10) from 78th cycle to 84th cycle.

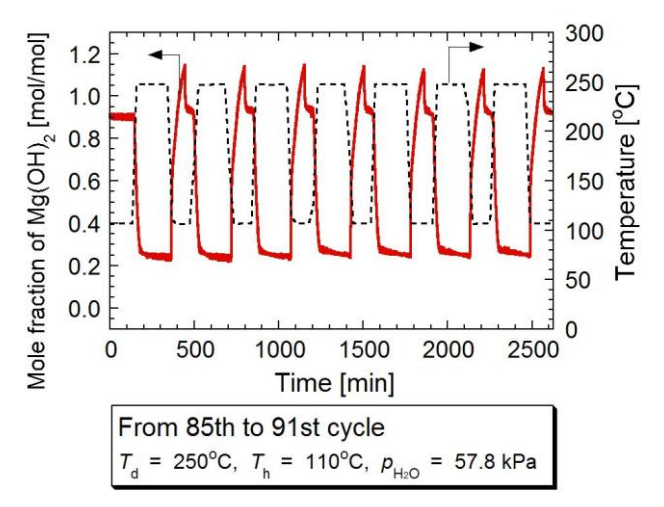


Figure 5.3-13 Dehydration and hydration profile of LiCl/Mg(OH)₂ (α = 0.10) from 85th cycle to 91st cycle.

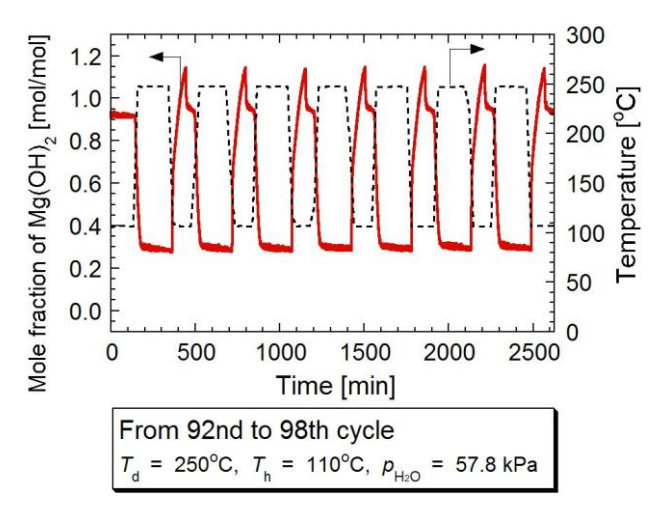


Figure 5.3-14 Dehydration and hydration profile of LiCl/Mg(OH)₂ (α = 0.10) from 92nd cycle to 98th cycle.

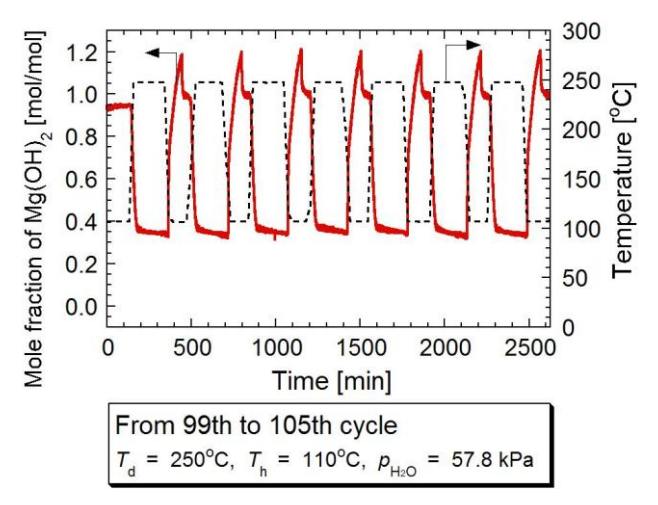


Figure 5.3-15 Dehydration and hydration profile of LiCl/Mg(OH)₂ ($\alpha = 0.10$) from 99th cycle to 105th cycle.

The Dehydration and hydration profiles of LiCl/Mg(OH)₂ from first cycle to 105-th cycle are shown in from **Figure 5.3-1** to **Figure 5.3-15**. **Figure 5.3-1** shows the dehydration and hydration profile of LiCl/Mg(OH)₂ from the first cycle to the seventh cycle. During these cycles, the value of x_0 decreased, while that of x_0 increased. The dehydration of LiCl/Mg(OH)₂ occurred in 200 min at 250°C. The maximum value of x_0 (= 0.901) was found at fourth cycle. **Figure 5.3-15** illustrates the dehydration and hydration profile of LiCl/Mg(OH)₂ from the 99th cycle to the 105th cycle (last seven cycles). The value of x_0 remained almost constant at around 0.99, while that of x_0 remained nearly constant at around 0.34. It was unclear whether any further decrease in dehydration reactivity had occurred.

Figure 5.3-16 shows the relationships between the cycle number, and x_0 , x_c , Δx_1 , respectively. The value of x_0 increased from 0.040 to 0.339 during the 105 cyclic operations, while the dehydration reactivity of LiCl/Mg(OH)₂ decreased. On the other hand, the value of x_c increased from 0.850 to 0.996 during the 105 runs. The value of Δx_1 , which corresponds to the heat output performance,

increased from the first cycle (0.810) to the fourth cycle (0.901) and then decreased from the sixth cycle (0.901) to the 105th cycle (0.657). This decrease in the value of Δx_1 is attributed to the reduction in the dehydration reactivity of the sample. The reason of the reduction in the dehydration reactivity is discussed at **Section 5.4.3.**

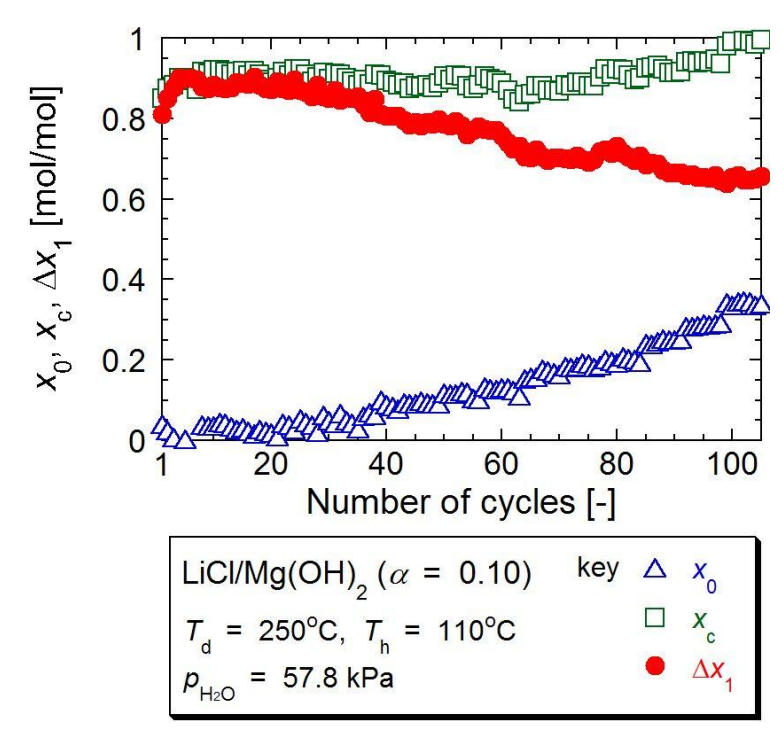


Figure 5.3-16 Relationships between number of cycles and x_0 , x_c , and Δx_1

5.3.2 Characterization of samples

5.3.2.1 Surface morphology of the material before and after cyclic operation

Figure 5.3-17 shows SEM micrographs of LiCl/Mg(OH)₂ (α = 0.10) before the cyclic operation and after 1, 7, and 105 runs. The major component in the sample is Mg(OH)₂ because the last operations performed were hydration and drying. The needle-like crystals of LiCl were not observed before the cyclic operation, after one run, and after seven runs, which indicates that the LiCl was highly dispersed. On the other hand, needle-like crystals of LiCl were observed in the sample after 105 runs.

SEM micrograph, which is magnified a 5000 times, of LiCl/Mg(OH)₂ (α = 0.10) after 105 runs is shown in **Figure 5.3-18**. It was observed that only a portion of the Mg(OH)₂ and MgO surfaces were covered with LiCl crystals after 105 runs of cyclic operation.

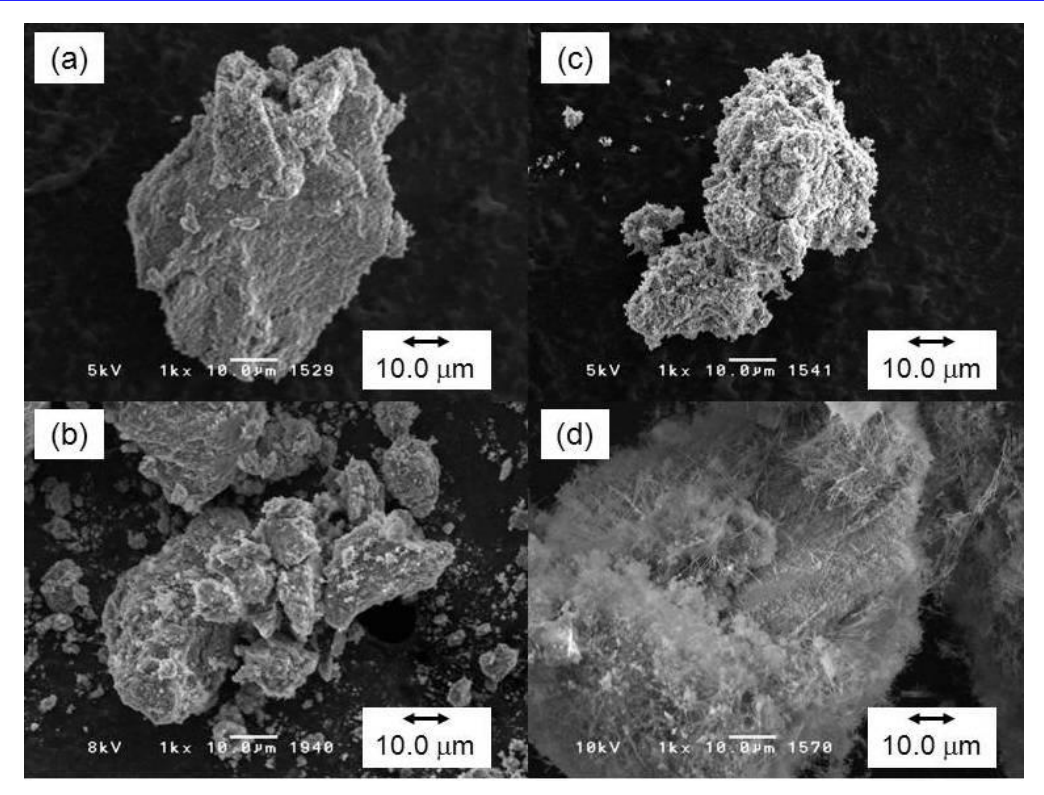


Figure 5.3-17 SEM micrograph of LiCl/Mg(OH)₂ (α = 0.10); (a) before cyclic operation, (b) after one run of cyclic operation, (c) after seven runs, and (d) after 105 runs. The graph is magnified a 1000 times.

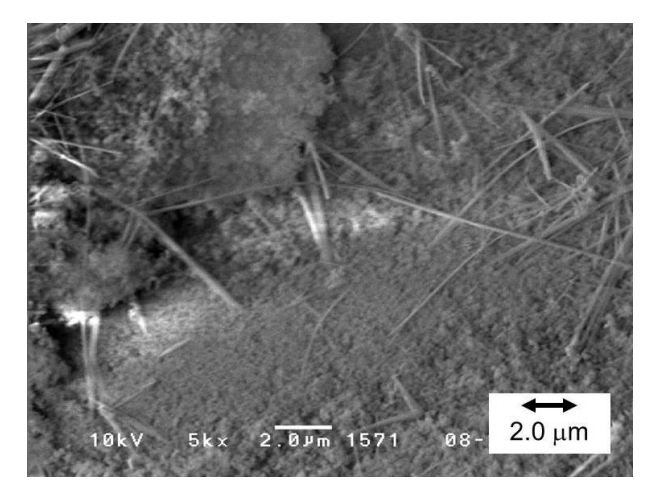


Figure 5.3-18 SEM micrograph of LiCl/Mg(OH)₂ (α = 0.10) after 105 runs. The graph is magnified a 5000 times.

5.3.2.2 Crystal structure of the material before and after cyclic operation

Figure 5.3-19 shows the XRD pattern for LiCl/Mg(OH)₂ before the cyclic operation and after 1, 7, and 105 runs. The major component in the sample was Mg(OH)₂. The characteristic peaks of Mg(OH)₂ and LiCl·H₂O were indeed identified in all of the samples. The peaks corresponding to LiCl were detected slightly at only after 105 runs. These results indicate that highly dispersed LiCl on the surface of Mg(OH)₂ at the initial state was aggregated and needle-like LiCl crystal was formed

gradually on the surface of Mg(OH)₂ between the seventh cycle and 105th cycle. The characteristic peaks for LiOH, MgCl₂, and hydrated form of these species which would be products of side reactions, were not identified in all of the patterns.

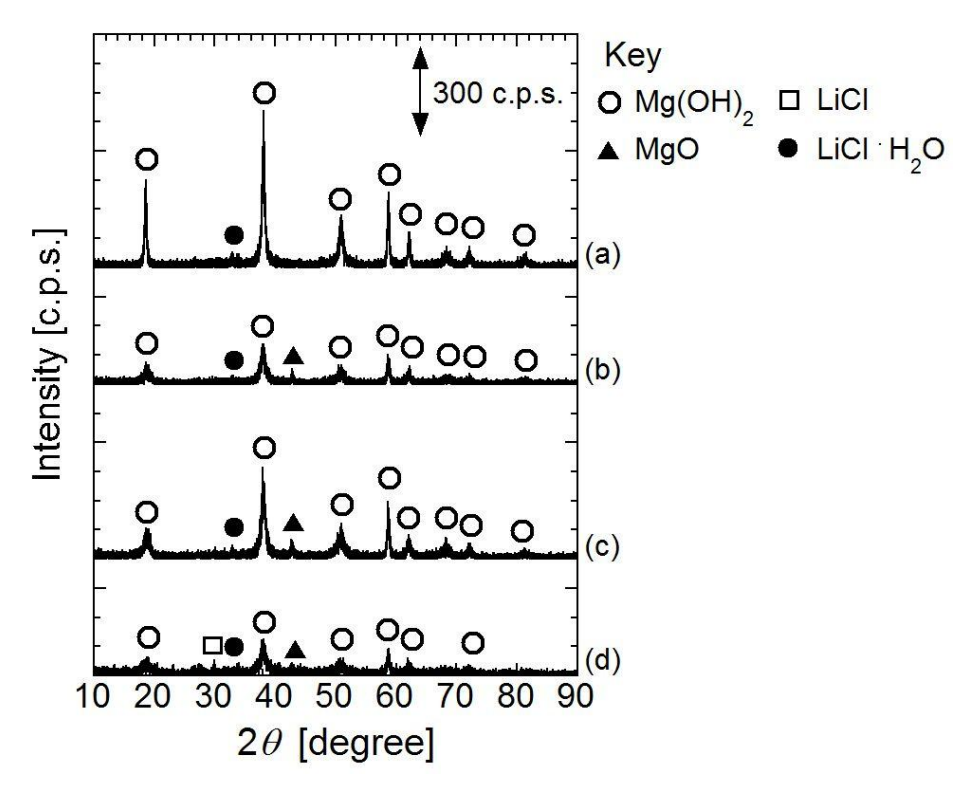


Figure 5.3-19 XRD pattern of LiCl/Mg(OH)₂; (a) before cyclic operation, (b) after first cyclic operation, (c) after seventh cyclic operation, and (d) after 105th cyclic operation.

5.3.2.3 Specific surface area of the material before and after cyclic operation

Table 5.3-1 Specific surface area of materials before and after cyclic operation.

Number of cycle	[-]	As prepared	1	7	105
Specific surface area	$[m^2 g^{-1}]$	24.6	55.7	55.6	51.6

Table 5.3-1 shows the specific surface area of the materials before and after the cyclic operation. The major component in the sample was Mg(OH)₂. The surface area of the sample was increased by one run of the cyclic operation. The first dehydration was divided the original grains into smaller grains. Subsequently, the specific surface areas were almost the same from the first cycle to the 105th cycle.

5.4 Discussion

5.4.1 Comparison with authentic magnesium hydroxide

In a previous study [2], the durability of authentic Mg(OH)₂ was examined. Authentic Mg(OH)₂ was dehydrated at 350°C for 60 min and hydrated at 110°C for 60 min under a vapor pressure

of 57.8 kPa. The conversion of the hydration reaction was around 0.50 in twelve runs of cyclic operation. In another previous study [3], high-purity Mg(OH)₂ was dehydrated at 350°C and hydrated at 110°C for 60 min under a vapor pressure of 48 kPa. High-purity MgO gave a conversion of approximately 0.50 for hydration at the 70th cycle. Reactivity of the material decreased during the initial five cycles. The LiCl/MgO showed higher conversion of hydration (Δx_1) than authentic MgO did. For example, Δx_1 was 0.874 after 12 runs of cyclic operation and Δx_1 was 0.704 after 70 runs. LiCl/Mg(OH)₂ (or LiCl/MgO) is thus a promising material for a thermochemical energy storage.

5.4.2 Change of heat output capacity

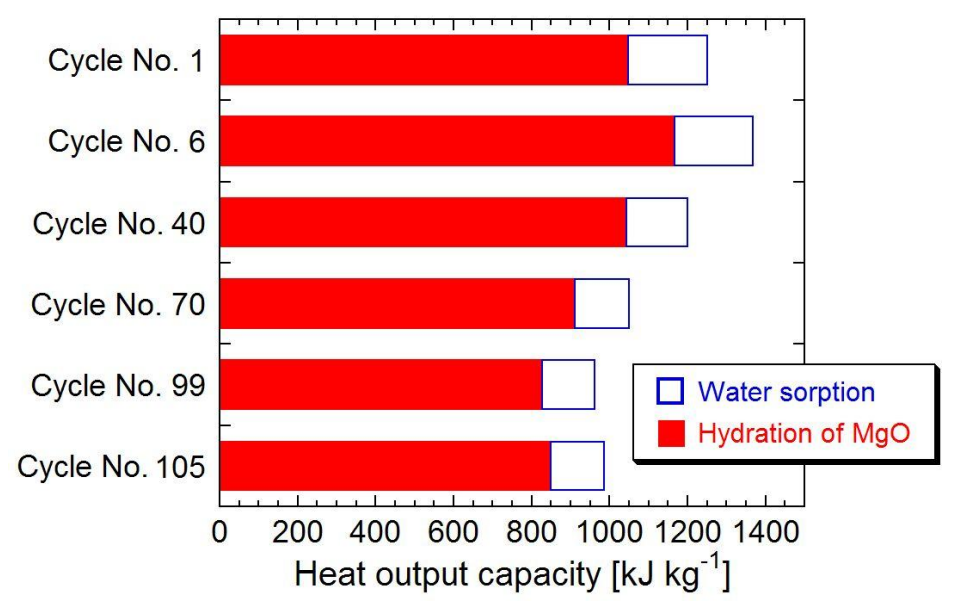


Figure 5.4-1 Heat output capacity of LiCl/Mg(OH)₂ (α = 0.10) after cyclic operations.

Figure 5.4-1 shows the heat output capacity of LiCl/Mg(OH)₂ (α = 0.10) after the first, sixth, 40th, 70th, 99th, and 105th runs of the cyclic operation. The initial value of the heat output capacity was 1.25×10^3 kJ kg⁻¹, and the value of the heat output capacity at the 105th cycle was 986 kJ kg⁻¹. The heat output capacity thus decreased by 21.1% from the first cycle to the 105th cycle. The maximum heat output capacity value was found to be 1.37×10^3 kJ kg⁻¹ (9.4% more than initial value) at the sixth cycle and the minimum heat output capacity value was 962 kJ kg⁻¹ (23% less than initial value) at the 99th cycle. The heat output capacity at 99th cycle and 105th cycle was lower than the target value of heat output capacity (\pm 20% compared with initial value). The durability of the LiCl/Mg(OH)₂ (α = 0.10) is needed to be improved in future work.

5.4.3 Change of surface state

From the SEM micrograph (**Figure 5.3-17(d)** and **Figure 5.3-18**), only a portion of the Mg(OH)₂ and MgO surfaces were covered with LiCl after 105 runs of cyclic operation. This result is corresponding to the XRD pattern (**Figure 5.3-19**) of the sample after 105 runs, which indicated the

formation of LiCl anhydride crystals. As discussion at **Section 2.4.3**, the uniform LiCl-coating accelerated the dehydration of $Mg(OH)_2$. From SEM micrographs, it was indicated that highly dispersed LiCl on the surface of $Mg(OH)_2$ at the initial state was aggregated and needle-like LiCl crystal was formed gradually on the surface of $Mg(OH)_2$ between the seventh cycle and 105th cycle (**Section 5.3.2.1**). A part of surface of $Mg(OH)_2$ was uncovered with LiCl. The change of the surface state was thought to be decreased the dehydration reactivity of the sample. Thereby, the heat output capacity of LiCl/ $Mg(OH)_2$ ($\alpha = 0.10$) decreased by 21.1% in the 105 runs.

On the other hand, the specific surface areas were almost the same from the first cycle to the 105th cycle (**Table 5.3-1**). This result indicates that the effect of sintering on decreasing dehydration reactivity is smaller than the effect of the changes of surface state.

Consequently, a regeneration of surface state is needed. For example, excess vapor is supplied to the material, and LiCl is deliquesced. Then the sample is dried, and homogeneously dispersed LiCl on the surface is obtained like material at the initial state.

One candidate method is that LiCl crystals are dissolved into water, and then water will be removed by evaporation. This procedure can disperse LiCl again.

5.5 Summary

In this chapter, the effect of 105 runs of a cyclic dehydration and hydration operation on LiCl/Mg(OH)₂ was examined. The heat output capacity of the material decreased by 21.1%, from 1.25 \times 10³ kJ kg⁻¹ to 986 kJ kg⁻¹, in the 105 runs of the cyclic operation.

A SEM micrograph revealed that LiCl was highly dispersed on the Mg(OH)₂ grains before the cyclic operation. In contrast, needle-like crystals of LiCl were observed on the Mg(OH)₂ grains after 105 runs of the cyclic operation. The XRD pattern showed no characteristic peak for LiCl in the sample prior to the cyclic operation. However, the peak did appear in the sample after 105 runs of the cyclic operation. These results indicate that highly dispersed LiCl on the surface of Mg(OH)₂ at the initial state was aggregated and needle-like LiCl crystal was formed gradually on the surface of Mg(OH)₂ during 105 runs of cyclic reactions. This change was thought to be decreased the reactivity of the material. The specific surface area of the material was almost unchanged between the first and 105th cycles. Hence, this sintering was thought to be a minor effect compared with the change in the surface state. Formed needle-like crystals of LiCl is needed to disperse again for regeneration of the material. A regeneration of surface state is needed to improve durability property of LiCl/Mg(OH)₂ (α = 0.10). For example, excess vapor is supplied to the material, and LiCl is deliquesced. Then the sample is dried, and homogeneously dispersed LiCl on the surface is obtained like material at the initial state.

5.6 References

[1] S. K. Lee, H. Matsuda, M. Hasatani; Fundamental studies of CaSO₄·(1/2)H₂O/CaSO₄ thermochemical reaction cycle for thermal energy storage by means of chemical reaction, *Kagaku*

Kogaku Ronbunshu (in Japanese with English abstract), 12, 75–82 (1986)

- [2] Y. Kato, J. Nakahata, Y. Yoshizawa; Durability characteristics of the hydration of magnesium oxide under repetitive reaction, *J. Mater. Sci.*, **34**, 475–480 (1999)
- [3] Y. Kato, T. Saito, T. Soga, J. Ryu, Y. Yoshizawa; Durable reaction material development for magnesium oxide/water chemical heat pump, *J. Chem. Eng. Jpn.*, **40**, 1264–1269 (2007)
- [4] M. Aihara, T. Nagai, J. Matsushita, Y. Negishi, H. Ohya; Development of the porous solid reactant for thermal-energy storage and temperature upgrade using carbonation/decarbonation reaction, *Appl. Energy*, **69**, 225–238 (2001)
- [5] M. Aihara, K. Tanaka, M. Watanabe, T. Takeuchi, H. Habuka; Carbonation/decarbonation of Ca-solid reactant derived from natural limestone for thermal-energy storage and temperature upgrade, *J. Chem. Eng. Jpn.*, **40**, 1270–1274 (2007)
- [6] T. Kito, N. Kobayashi; Evaluation of output power characteristics of chemical heat pump by using CaO-LiCl compound reactant, *Kagaku Kougaku Ronbunshu* (in Japanese with English abstract), **38**, 172–175 (2012)

Chapter 6 Rare earth mixed hydroxide for thermochemical energy storage

6.1 Introduction

Authentic magnesium hydroxide $(Mg(OH)_2)$ and Lithium chloride-modified magnesium hydroxide $(LiCl/Mg(OH)_2)$ were studied as a thermochemical energy storage materials (TCMs) at previous chapters (Chapters 2, 3, and 4). However, these materials require water vapor pressure (p_{H2O}) at $p_{H2O} \ge 31.2$ kPa for hydration. It means the thermochemical energy storage (TcES) system requires heat over 70° C for evaporation of water for the hydration, and extra heat sources such as exhaust heats from cooling media of internal combustion engines, polymer electrolyte fuel cells, or industrial plants are needed for the water evaporation. However, it is hard to prepare these heat sources on the requirement for hydration operation. Hence, it is necessary to develop new materials that can be used at a lower water vapor pressure (lower heat source temperature) for hydration, that is, heat output operation.

Batsanov et al. [1] and Yamamoto et al. [2] reported that the temperatures of first dehydration for rare earth hydroxides ($T_{\rm fd}$) proceeds at 250–410°C (**Table 6.1-1**). Thus, rare earth hydroxides would store thermal energy from chemical plants, steel plants, and light-water reactors. Nagao et al. reported that La₂O₃ shows high hydration reactivity at 25°C with saturated water vapor [3]. However, a technical problem is that the first dehydration of La(OH)₃ does not proceed enough at 300°C or lower temperatures [4]. Pure La(OH)₃ is not suitable for TCM to store industrial waste heat lower than 300°C.

The dehydration (endothermic reaction) and hydration (exothermic reaction) of a rare earth (R) hydroxide (R(OH)₃, R indicates a rare earth element) is expressed generally as follows:

$$R(OH)_3$$
 (s) \rightleftharpoons $ROOH$ (s) + H_2O (g) (6-1)

ROOH (s)
$$\longleftrightarrow \frac{1}{2} R_2 O_3$$
 (s) $+ \frac{1}{2} H_2 O$ (g) (6-2)

The second dehydration of rare earth hydroxides generally occur at over 400°C [1]. In this chapter, only the first dehydration of rare earth hydroxides was studied because this study's main subject is heat storage at lower than around 300°C.

Table 6.1-1	Temperatures of	first dehydratic	on for rare earth	hvdroxides ($(R(OH)_3).$
--------------------	-----------------	------------------	-------------------	--------------	--------------

	. 1			J				(- /3/-		
Metal (R)	Y	La	Nd	Sm	Gd	Dy	Но	Er	Tm	Reference
T_{fd} [°C]	310	410	375	345	330	295	290	250	270	[1]
T_{fd} [°C]	264	310	335	290	270					[2]

As mentioned at **Chapter 1**, TCMs based on mixed hydroxides such as magnesium-cobalt and magnesium-nickel mixed hydroxides can store thermal energy at 280°C [5], and dehydration temperatures of brucite-type hydroxides are affected by electronegativity of cation. The relationship of temperatures of first dehydration for rare earth hydroxides in **Table 6.1-1** and electronegativity of cation are shown in **Figure 6.1-1**. Temperatures of first dehydration are decreased with increase of electronegativity of cation.

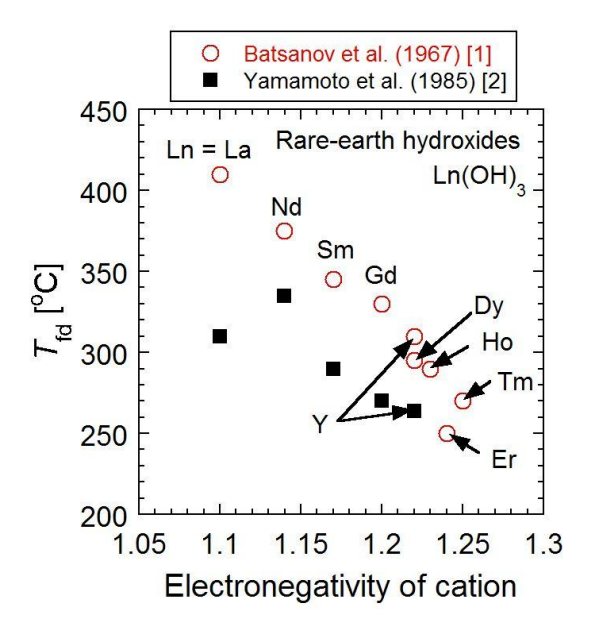


Figure 6.1-1 Relationship between electronegativity of cation and first dehydration temperature for rare earth pure hydroxide. The values of electronegativity in a reference [6] are employed.

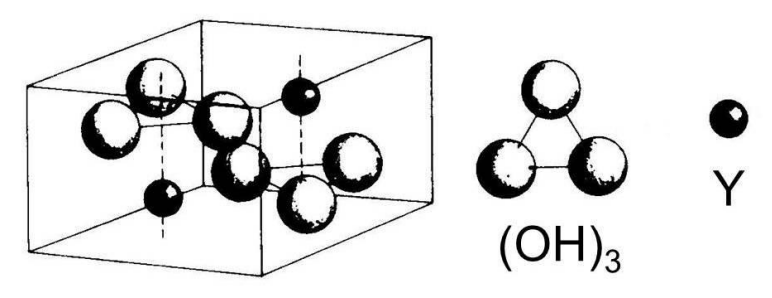


Figure 6.1-2 The $Y(OH)_3$ -type structure [7].

It is known that rare earth hydroxides have a same structure, yttrium hydroxide (Y(OH)₃-type structure, **Figure 6.1-2**) [8]. Ionic radiuses of lanthanum (La), neodymium (Nd), gadolinium (Gd), and

yttrium (Y) are shown in **Table 6.1-2**. Their radius was 1.10 ± 0.07 Å. Lanthanum hydroxide (La(OH)₃), neodymium hydroxide (Nd(OH)₃), gadolinium hydroxide (Gd(OH)₃), and yttrium hydroxide (Y(OH)₃) have same structure and similar ionic radius. Hence, different rare earths are able to be mixed together under wide mixing ratio, and rere earth mixed hydroxides can be prepared. The dehydration/hydration reactivity of rare earth mixed hydroxides can be enhanced by modifying the metal ion composition. **Table 6.1-3** shows crustal abundances of rare earth, common metals, and uranium. The abundances of Y, La, Nd and Gd are smaller than that of magnesium (Mg), aluminum (Al), and iron (Fe), while the abundances of the rare earth metals are similar to that of cobalt (Co), and bigger than uranium (U). The abundances of rare earth elements are not extremely "rare". Therefore, La(OH)₃, Nd(OH)₃, Gd(OH)₃, Y(OH)₃ and their mixed hydroxides would be candidates for TCMs.

Table 6.1-2 Ionic radiuses of La, Nd, Gd, and Y (coordination number: 6) [9].

Metal ion	La	Nd	Gd	Y
r [Å]	1.17	1.12	1.08	1.04

Table 6.1-3 Crustal abundances of rare earth, common metals, and uranium [9].

			= =	
Mg	Al	Fe	Co	U
3.2×10^4	8.4×10^4	7.1×10^{4}	29	0.91
				_
Y	La	Nd	Gd	
20	16	16	3.3	_
	3.2×10^4	3.2×10^4 8.4×10^4 Y La	3.2×10^4 8.4×10^4 7.1×10^4 Y La Nd	3.2×10^4 8.4×10^4 7.1×10^4 29

Reaction enthalpies of Eq. (6-1) for rare earth pure/mixed hydroxides are needed to evaluate heat output capacities of TCMs. Reaction enthalpies can be calculated from formation enthalpies of hydroxides and oxyhydroxides. However, only few values of them are known (**Table 6.1-4**). Thus, reaction enthalpies (reaction heats) of the rare earth pure/mixed hydroxides are needed to measure.

Table 6.1-4 Standard enthalpies of formation for rare earth pure hydroxides and oxyhydroxides.

Compound	$\Delta H_{\mathrm{f}}^{\circ} [\mathrm{kJ} \; \mathrm{mol}^{-1}]$	Reference	•	Compound	$\Delta H_{\rm f}^{\circ} [{\rm kJ \ mol}^{-1}]$	Reference
La(OH) ₃	-1343.29	[10]		Nd(OH) ₃	-1403.7	[13]
$La(OH)_3$	-1415.5	[11]		$Nd(OH)_3$	-1436	[12]
La(OH) ₃	-1442	[12]		$Gd(OH)_3$	-1410	[12]
LaOOH	-1045.45	[10]		$Y(OH)_3$	-1398.96	[10]
LaOOH	-1078.6	[11]		YOOH	-1101.96	[10]

In this chapter, rare earth pure/mixed hydroxides were prepared by the precipitation/coprecipitation method. Microstructures and surface morphologies of the samples were identified by scanning electron microscopy. The crystal structures of the samples were examined by

powder X-ray diffractometry. Infrared (IR) spectroscopy was performed to clarify formation of homogeneous mixed hydroxides. Thermal decomposition profiles and dehydration/hydration behavior of the rare earth pure/mixed hydroxides were measured by thermogravimetry. Reaction heats of the samples were measured by differential scanning calorimetry. Then heat output capacities of the samples were evaluated.

6.2 Experimental

6.2.1 Sample preparation

Rare earth pure/mixed hydroxides, $La_xNd_{1-x}(OH)_3$, $La_xGd_{1-x}(OH)_3$, and $La_xY_{1-x}(OH)_3$ (x = 0, 0.25, 0.50, 0.75, 1), were prepared by the precipitation/coprecipitation method. $La(NO_3)_3 \cdot 6H_2O$ (99.9%, Wako Pure Chemical Industries, Ltd.), $Nd(NO_3)_3 \cdot 6H_2O$ (99.5%, Wako Pure Chemical Industries, Ltd.), and $Y(NO_3)_3 \cdot nH_2O$ (99.9%, Wako Pure Chemical Industries, Ltd.) were used as precursors of the hydroxides. The value of n was determined previously by thermogravimetry, and it was 5.29. An aqueous solution of the rare earth nitrate(s) was added to 1 M aqueous NaOH solution. The resulting precipitates were washed five or more times with pure water and thermally decomposed by heating at 800°C for 5 h. Then, hydrothermal treatment was performed by using an PTFE autoclave (inner diameter 34 mm × depth 80 mm). 1 g of thermal decomposition product and 30 mL of water were charged into the autoclave. Hydrothermal conditions for each sample are shown in **Table 6.2-1**. The sample preparation procedure for rare earth pure/mixed hydroxides is shown in **Figure 6.2-1** as a flowchart.

Table 6.2-1 Hydrothermal conditions for $La_xNd_{1-x}(OH)_3$, $La_xGd_{1-x}(OH)_3$, and $La_xY_{1-x}(OH)_3$ without $Y(OH)_3$.

	x = 0	x = 0.25	x = 0.50	x = 0.75	x = 1
$La_xNd_{1-x}(OH)_3$	120°C, 3 h	120°C, 3 h	120°C, 3 h	120°C, 3 h	120°C, 3 h
$La_xGd_{1-x}(OH)_3$	160°C, 24h	120°C, 3 h	120°C, 3 h	120°C, 3 h	120°C, 3 h
$La_xY_{1-x}(OH)_3$	_	180°C, 24 h	120°C, 3 h	120°C, 3 h	120°C, 3 h

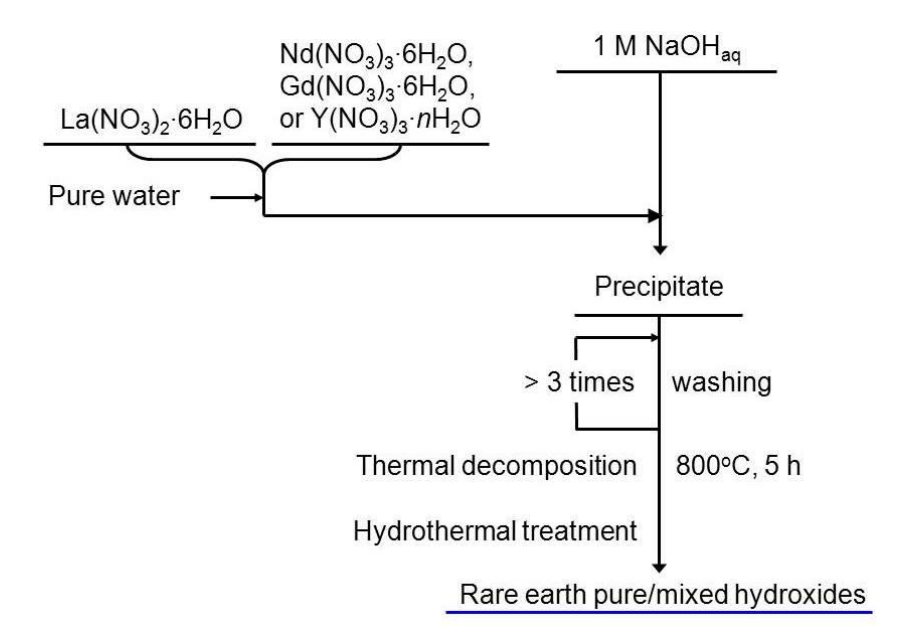


Figure 6.2-1 Sample preparation procedure for $La_xNd_{1-x}(OH)_3$ (x = 0, 0.25, 0.50, 0.75, 1), $La_xGd_{1-x}(OH)_3$ (x = 0, 0.25, 0.50, 0.75, 1), and $La_xY_{1-x}(OH)_3$ (x = 0.25, 0.50, 0.75, 1).

For $Y(OH)_3$ preparation, an aqueous solution of the $Y(NO_3)_3$ was added to 1 M aqueous NaOH solution. The resulting precipitate was hydrothermally treated at 160° C, 24 h, and thermal decomposition was not performed. The obtained powders were washed three times with pure water. The sample preparation procedure for $Y(OH)_3$ is shown in Figure 6.2-2 as a flowchart.

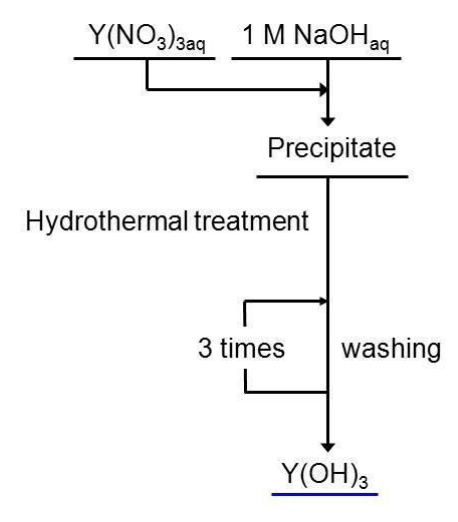


Figure 6.2-2 Sample preparation procedure for Y(OH)₃.

Authentic $Mg(OH)_2$ (0.07- μm diameter, 99.9%, Wako Pure Chemical Industries, Ltd.) was examined as a reference material.

6.2.2 Characterization

6.2.2.1 Scanning electron microscopy

Scanning electron microscopy (SEM) was performed to identify the microstructures and surface morphologies of the samples. A scanning electron microscope (SM-200, TOPCON Corp.) was used. An acceleration voltage was 8 kV. The samples were pretreated at 120°C for 30 min (or more).

6.2.2.2 Powder X-ray diffraction analysis

Powder X-ray diffractometry (XRD) measurements were carried out using an Ultima IV diffractometer (Rigaku Corporation). For a qualitative analysis, the 2θ range was at 10– 90° and a scan speed was 0.5° min⁻¹. For a lattice constant measurement, the step scan was employed with 2θ range at 35–90° with step width of 0.01° . A diffracted X-ray was counted among 3 s for each angle. Si crystal was used for an internal standard. The measurement of lattice constant was performed at $21 \pm 2^{\circ}$ C. Monochromatic CuK α radiation was used, and the generator voltage and current were 40 kV and 40 mA, respectively.

6.2.2.3 Infrared spectroscopy

Infrared (IR) spectroscopy was performed by using Fourier transform (FT) IR spectrophotometer (FT/IR-4200, JASCO Corporation). Resolution of spectrum was 1 cm⁻¹. The powder samples were mixed with KBr powder, and disk was prepared by compression of powder mixture. The measurements were carried out under atmospheric condition at room temperature.

6.2.3 Thermal decomposition measurement with thermogravimetry

The thermal decomposition curves for the samples as hydroxide state were measured by thermogravimetry (TG) using a TGD9600 thermobalance (Ulvac-Riko Inc.). Before the analysis, the samples were dried at 120°C for 30 min to remove the adsorbed water. The samples were heated to 400°C at the rate of 5°C min⁻¹ under argon gas flow (flow rate: 100 mL min⁻¹).

The mole fraction of the hydroxide (X [mol/mol]) was calculated from the weight change in the samples.

$$X \left[\%\right] = 1 + \frac{\Delta w / (n \cdot M_{\text{H2O}})}{w_{\text{ini}} / M_{\text{hydroxide}}}$$
(6-3)

Here, Δw [g]: weight change in the sample, n [–]: the stoichiometric factor (1 for Mg(OH)₂; 1.5 for rare earth pure/mixed hydroxides), $M_{\rm H2O}$ [g mol⁻¹] the molecular weight of water, $M_{\rm hydroxide}$ [g mol⁻¹]: the molecular weight of the pure/mixed hydroxide, and $w_{\rm ini}$ [g]: the initial sample weight, respectively. For rare earth compounds, X = 1, 0.33, or 0 would imply that the sample is a pure hydroxide, oxyhydroxide, or pure oxide, respectively.

In this study, the temperature at which the derivative thermogravimetric curve shows a maximum is defined as the first dehydration temperature ($T_{\rm fd}$).

6.2.4 Dehydration-hydration measurement with thermogravimetry

Dehydration-hydration behavior of the samples as hydroxide state was determined by thermogravimetry. The dehydration operation was carried out at 300°C ($T_d = 300$ °C) for 30 min, and the hydration-operation was performed at 110°C ($T_h = 110$ °C) for 80 min. During hydration operation, a mixture of water vapor and argon (carrier gas) at a water vapor pressure (p_{H2O}) of 7.4 kPa was introduced. This vapor pressure corresponds to the saturated water vapor pressure at 40°C. After the hydration operation had completed, the vapor supply was stopped, and dry argon gas was introduced at the same hydration operation temperature (110°C) for 50 min to remove the adsorbed water (drying operation). The dehydration-hydration-drying operation was carried out at heating and cooling rates of 20°C min⁻¹ and at an argon gas flow rate of 100 mL min⁻¹.

Figure 6.2-3 shows an example of dehydration and hydration profiles for rare earth mixed hydroxide. The definition of the mole fraction of hydroxide (X) is same as Eq. (6-3). The mole fraction of hydroxide after the dehydration reaction is denoted as X_0 [mol/mol], that of hydroxide at the end of the vapor supply period is denoted as X_h [mol/mol], and that of hydroxide after the drying operation is denoted as X_c [mol/mol]. The conversion of the dehydration (ΔX_d [mol/mol]) is defined as $\Delta X_d = 1 - X_0$, the conversion of the hydration (ΔX_1 [mol/mol]) is defined as $\Delta X_1 = X_c - X_0$, and the apparent change of X by adsorption (ΔX_2 [mol/mol]) is defined as $\Delta X_2 = X_h - X_c$.

The heat output capacity was calculated from the enthalpy changes in the reaction and upon the adsorption of water vapor. In this chapter, the heat output capacity was expressed as heat output [kJ] per unit initial weight of the sample (rare earth pure/mixed hydroxide) [kg]. It was assumed that the enthalpy change of the adsorption of water vapor was equal to that of the condensation of water.

$$Q_{\text{total}} = Q_{\text{r}} + Q_{\text{a}} \tag{6-4}$$

$$Q_{\rm r} = \frac{-\Delta H_{\rm r}}{M_{\rm sample}} \times \Delta X_1 \tag{6-5}$$

$$Q_{\rm a} = \frac{-\Delta H_{\rm a}}{M_{\rm sample}} \times \Delta X_2 \tag{6-6}$$

Here, Q_{total} [kJ kg⁻¹]: heat output capacity of the material, Q_{r} [kJ kg⁻¹]: heat output by reaction, Q_{a} [kJ kg⁻¹]: heat output by adsorption, ΔH_{r} [kJ mol⁻¹]: enthalpy change by reaction, ΔH_{a} [kJ mol⁻¹]: enthalpy change by adsorption, ΔX_{1} [mol/mol]: change of X by hydration; ΔX_{2} [mol/mol]: apparent change of X by adsorption, M_{sample} [kg mol⁻¹]: molecular weight of the sample. Since some of enthalpy changes by reaction for rare earth pure/mixed hydroxides are unknown, reaction heats were measured at **Section 6.2.5**.

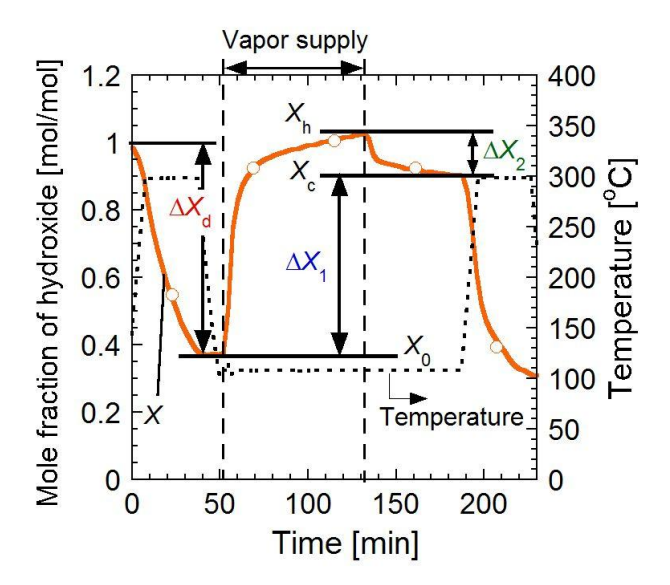


Figure 6.2-3 Example of dehydration and hydration profiles for rare earth mixed hydroxide. X indicates mole fraction of hydroxide.

6.2.5 Measurement of reaction heat with differential scanning calorimetry

The reaction heats (dehydration heats) of rare earth pure/mixed hydroxides were measured by differential scanning calorimetry (DSC). A differential scanning calorimeter (Thermo plus DSC8320, Rigaku Corporation) was used. The samples were charged into Al pans, and closed by Al lids. The samples were heated to 500° C at the rate of 5° C min⁻¹ under argon gas flow (flow rate: 100 mL min^{-1}). The measurement was performed five times. Average value and standard deviation (σ) of reaction heats were evaluated. In this chapter, error-bar indicates 3σ .

6.3 Results

6.3.1 Characterization

6.3.1.1 Surface morphology of rare earth mixed hydroxide

SEM micrographs of authentic La_xNd_{1-x}(OH)₃, La_xGd_{1-x}(OH)₃, and La_xY_{1-x}(OH)₃ (x = 0, 0.25, 0.50, 0.75, 1) are shown in from **Figure 6.3-1** to **Figure 6.3-6**. Secondary particles were consisted of spherical primary particles for La_xNd_{1-x}(OH)₃ (x = 0, 0.25, 0.50, 0.75, 1), La_{0.75}Gd_{0.25}(OH)₃, and La_{0.75}Y_{0.25}(OH)₃. On the other hand, secondary particles were consisted of columnar crystals for La_xGd_{1-x}(OH)₃ (x = 0.50, 0.75, 1), and La_xY_{1-x}(OH)₃ (x = 0.50, 0.75). Larger columnar crystals were observed for Y(OH)₃, and their size were around 10 μ m.

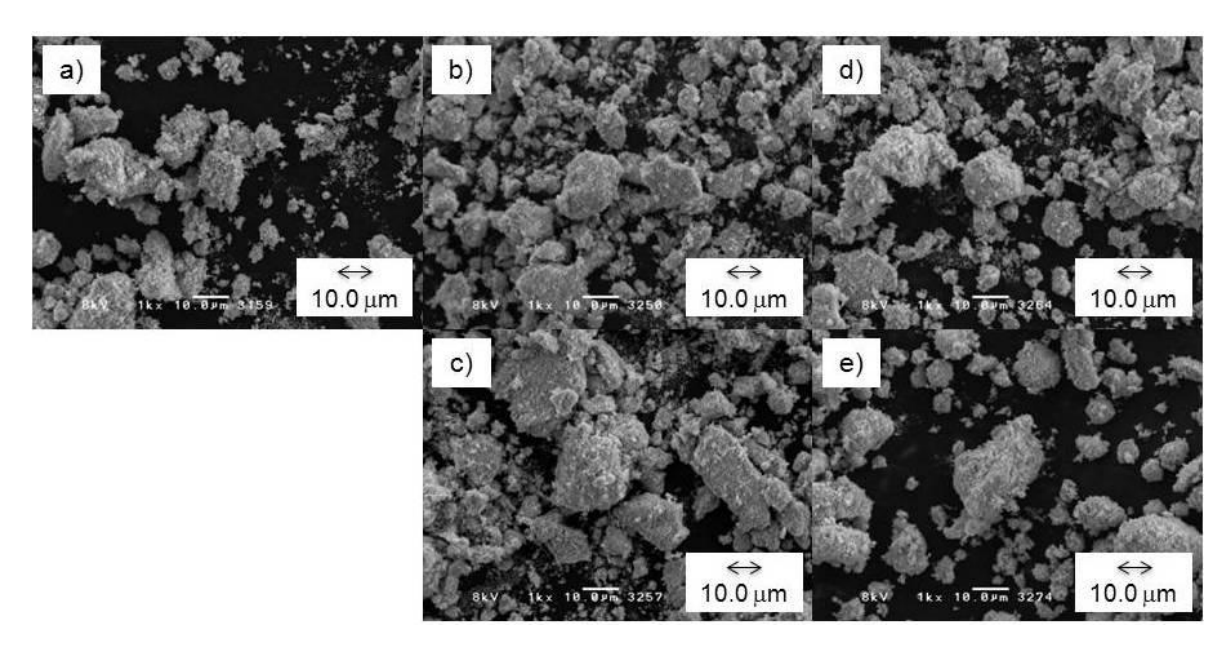


Figure 6.3-1 SEM micrographs of authentic $La_xNd_{1-x}(OH)_3$ (x = 0, 0.25, 0.50, 0.75, 1). The graph is magnified a 1000 times. a) $La(OH)_3$, b) $La_{0.75}Nd_{0.25}(OH)_3$, c) $La_{0.50}Nd_{0.50}(OH)_3$, d) $La_{0.25}Nd_{0.75}(OH)_3$, e) $Nd(OH)_3$.

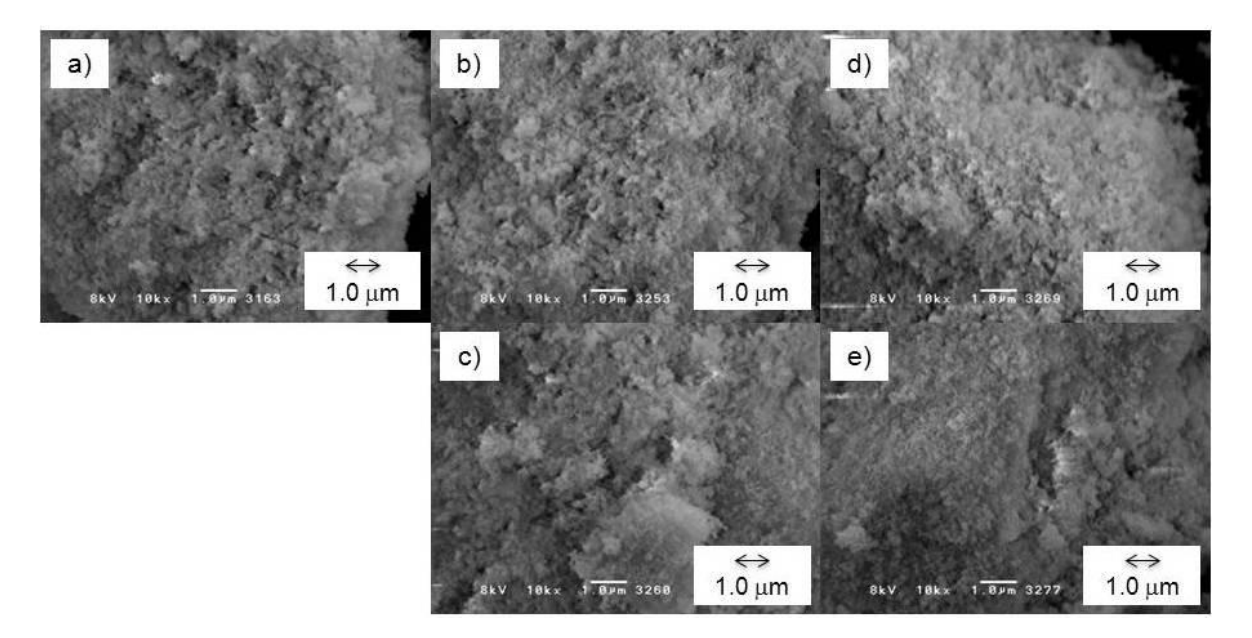


Figure 6.3-2 SEM micrographs of authentic $La_xNd_{1-x}(OH)_3$ (x = 0, 0.25, 0.50, 0.75, 1). The graph is magnified a 10000 times. a) $La(OH)_3$, b) $La_{0.75}Nd_{0.25}(OH)_3$, c) $La_{0.50}Nd_{0.50}(OH)_3$, d) $La_{0.25}Nd_{0.75}(OH)_3$, e) $Nd(OH)_3$.

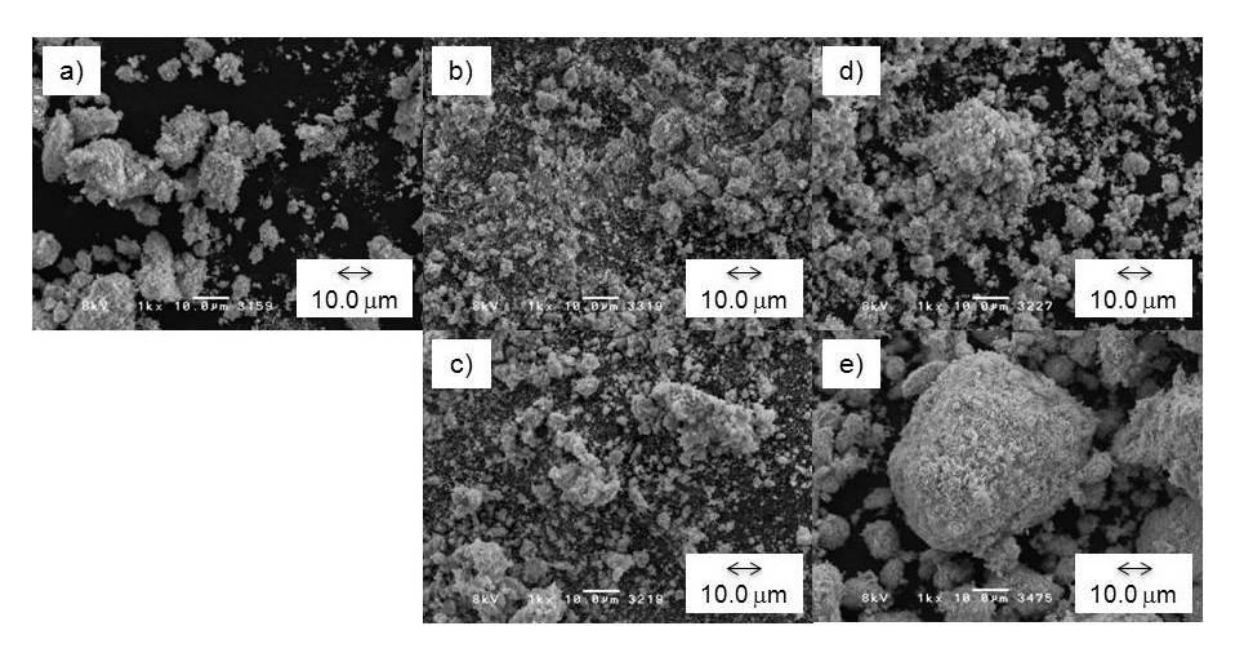


Figure 6.3-3 SEM micrographs of authentic $La_xGd_{1-x}(OH)_3$ (x = 0, 0.25, 0.50, 0.75, 1). The graph is magnified a 1000 times. a) $La(OH)_3$, b) $La_{0.75}Gd_{0.25}(OH)_3$, c) $La_{0.50}Gd_{0.50}(OH)_3$, d) $La_{0.25}Gd_{0.75}(OH)_3$, e) $Gd(OH)_3$.

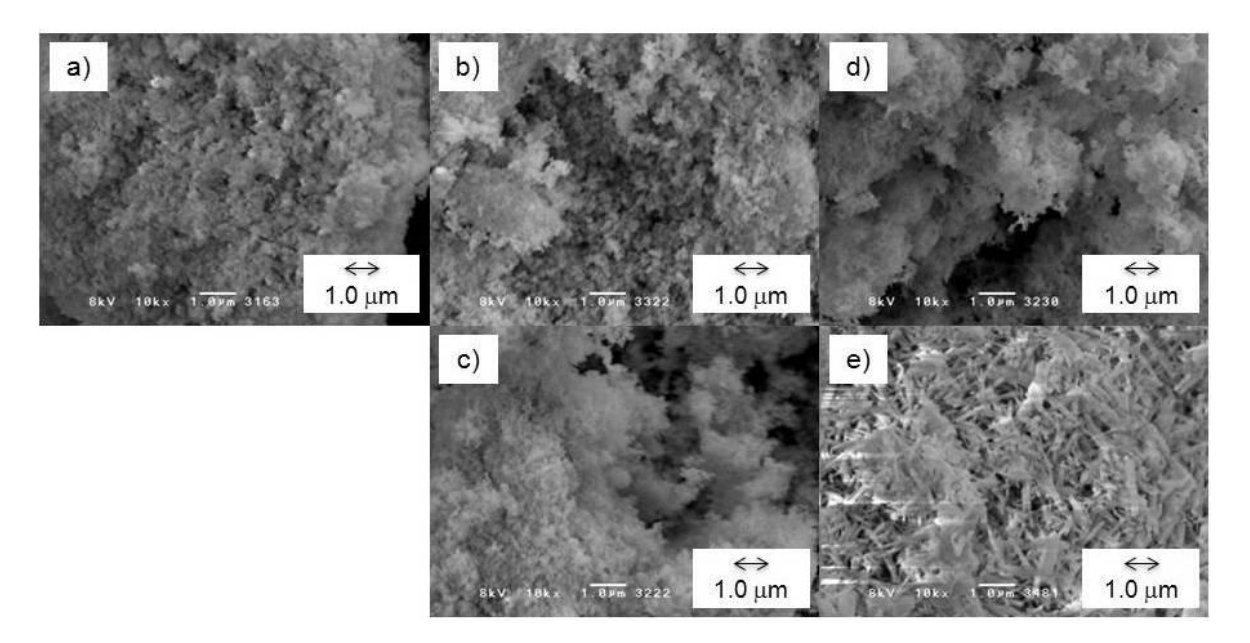


Figure 6.3-4 SEM micrographs of authentic $La_xGd_{1-x}(OH)_3$ (x = 0, 0.25, 0.50, 0.75, 1). The graph is magnified a 10000 times. a) $La(OH)_3$, b) $La_{0.75}Gd_{0.25}(OH)_3$, c) $La_{0.50}Gd_{0.50}(OH)_3$, d) $La_{0.25}Gd_{0.75}(OH)_3$, e) $Gd(OH)_3$.

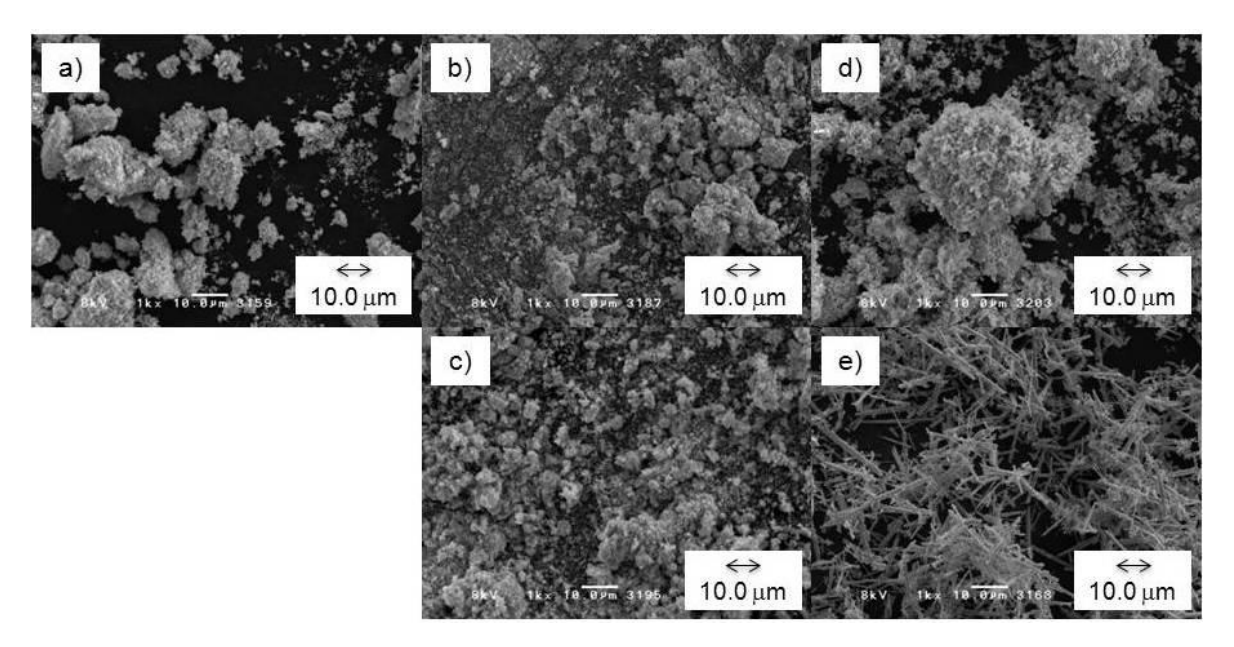


Figure 6.3-5 SEM micrographs of authentic $La_xY_{1-x}(OH)_3$ (x = 0, 0.25, 0.50, 0.75, 1). The graph is magnified a 1000 times. a) $La(OH)_3$, b) $La_{0.75}Y_{0.25}(OH)_3$, c) $La_{0.50}Y_{0.50}(OH)_3$, d) $La_{0.25}Y_{0.75}(OH)_3$, e) $Y(OH)_3$.

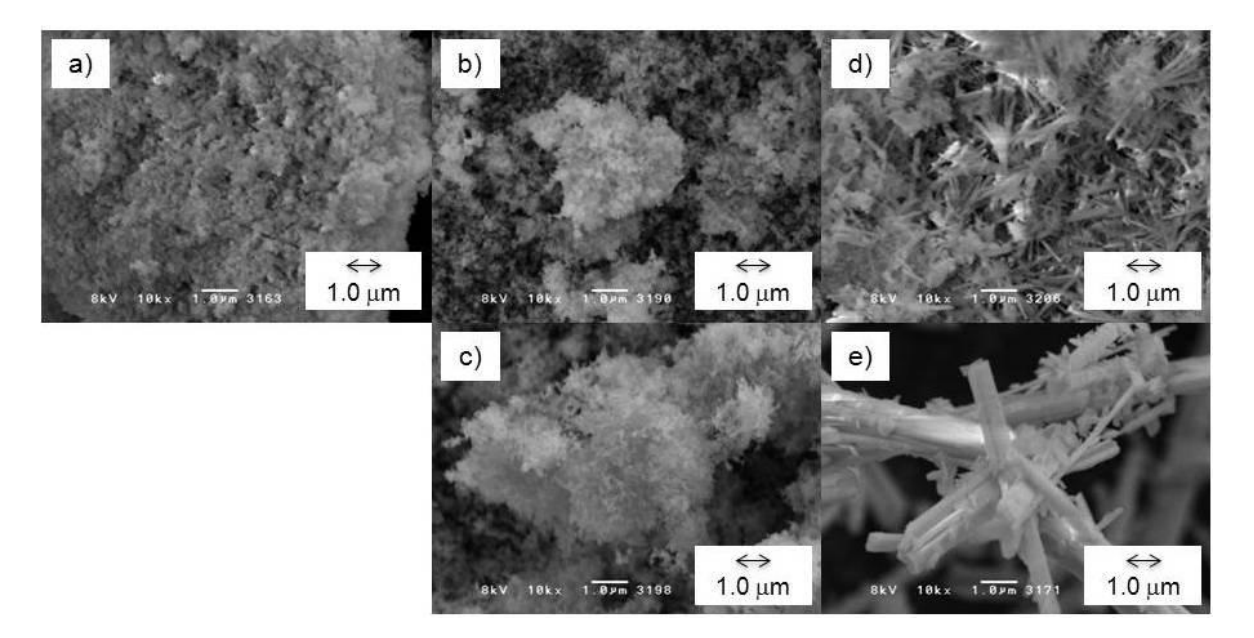


Figure 6.3-6 SEM micrographs of authentic $La_xY_{1-x}(OH)_3$ (x = 0, 0.25, 0.50, 0.75, 1). The graph is magnified a 10000 times. a) $La(OH)_3$, b) $La_{0.75}Y_{0.25}(OH)_3$, c) $La_{0.50}Y_{0.50}(OH)_3$, d) $La_{0.25}Y_{0.75}(OH)_3$, e) $Y(OH)_3$.

6.3.1.2 Crystal structure of rare earth mixed hydroxide

The XRD patterns for $La_xNd_{1-x}(OH)_3$ is shown in **Figure 6.3-7.** The reference XRD patterns indicate literature value of $La(OH)_3$ and $Nd(OH)_3$, and they are known to have an $Y(OH)_3$ structure $(P6_3/m)$. All of the samples showed the $Y(OH)_3$ -type structure. The peaks for the mixed hydroxides were not separated into individual $La(OH)_3$ and $Nd(OH)_3$ peaks. The peak positions shifted to the higher-angle side when the Nd ion composition was increased, indicating that the samples were $Y(OH)_3$ -type pure/mixed hydroxides.

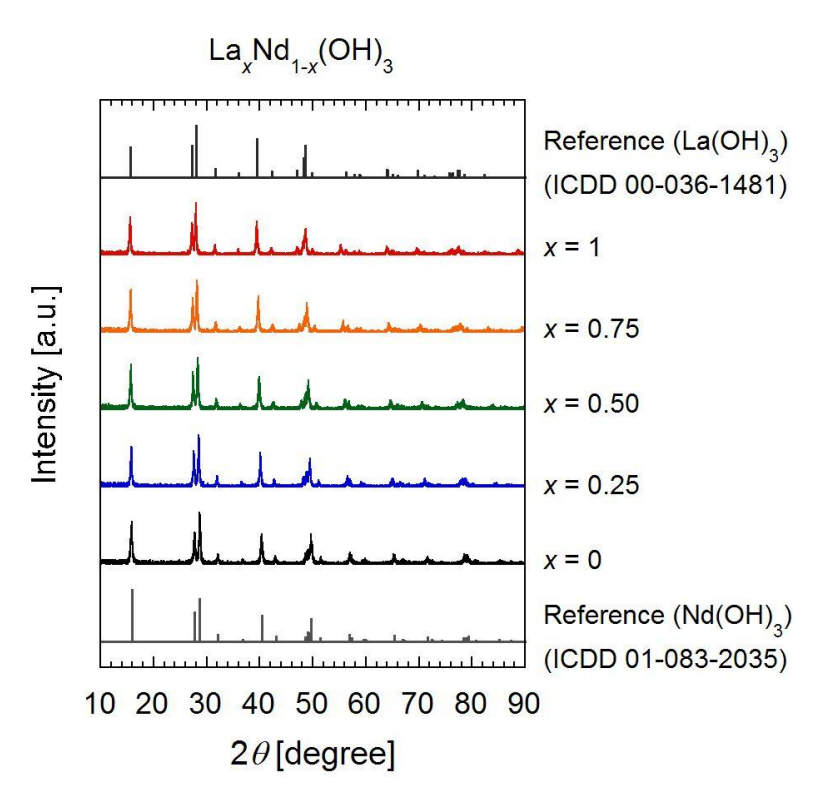


Figure 6.3-7 XRD patterns for $La_xNd_{1-x}(OH)_3$ and references ($La(OH)_3$ and $Nd(OH)_3$).

The XRD patterns for $La_xGd_{1-x}(OH)_3$ is shown in **Figure 6.3-8.** The reference XRD patterns indicate literature value of $La(OH)_3$ and $Gd(OH)_3$, and they are known to have an Y(OH)₃ structure. The peaks for the mixed hydroxides were not separated into individual $La(OH)_3$ and $Gd(OH)_3$ peaks. The peak positions shifted to the higher-angle side when the Gd ion composition was increased, indicating that the samples were Y(OH)₃-type pure/mixed hydroxides.

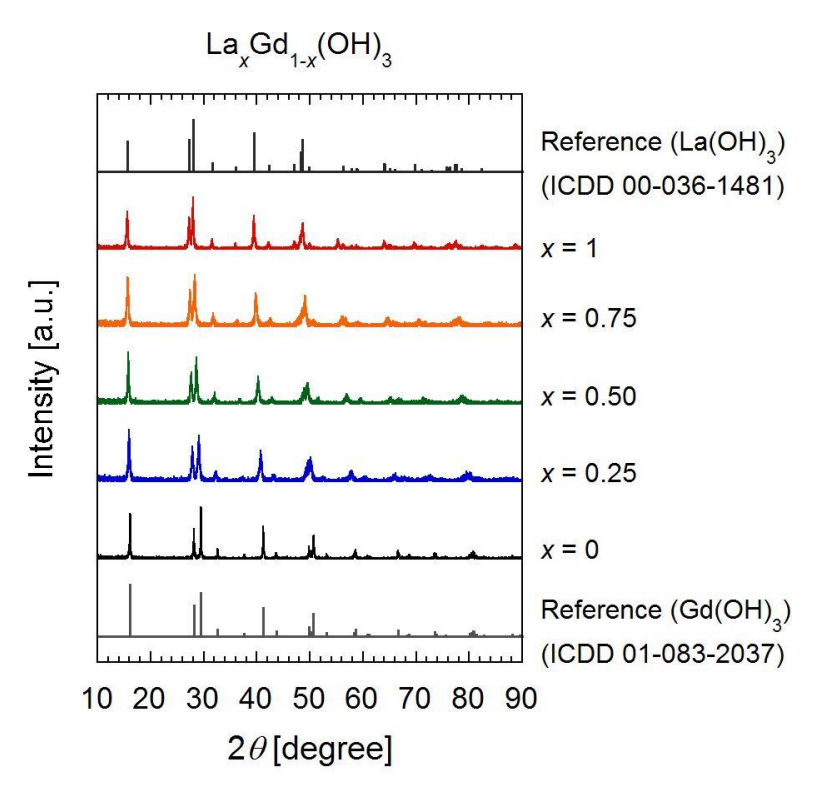


Figure 6.3-8 XRD patterns for $La_xGd_{1-x}(OH)_3$ and references ($La(OH)_3$ and $Gd(OH)_3$).

The XRD patterns for $La_xY_{1-x}(OH)_3$ is shown in **Figure 6.3-9.** The reference XRD patterns indicate literature value of $La(OH)_3$ and $Y(OH)_3$, and they are known to have an $Y(OH)_3$ structure. All the samples showed the $Y(OH)_3$ -type structure. The peaks for the mixed hydroxides were not separated into individual $La(OH)_3$ and $Y(OH)_3$ peaks. The peak positions shifted to the higher-angle side when the Y ion composition was increased, indicating that the samples were $Y(OH)_3$ -type pure/mixed hydroxides.

A shift of lattice constant for $La_xY_{1-x}(OH)_3$ is shown in **Figure 6.3-10**. The lattice constant of the hydroxide was decreased linearly with increase in Y content. This result suggests a formation of mixed hydroxides with homogeneous composition.

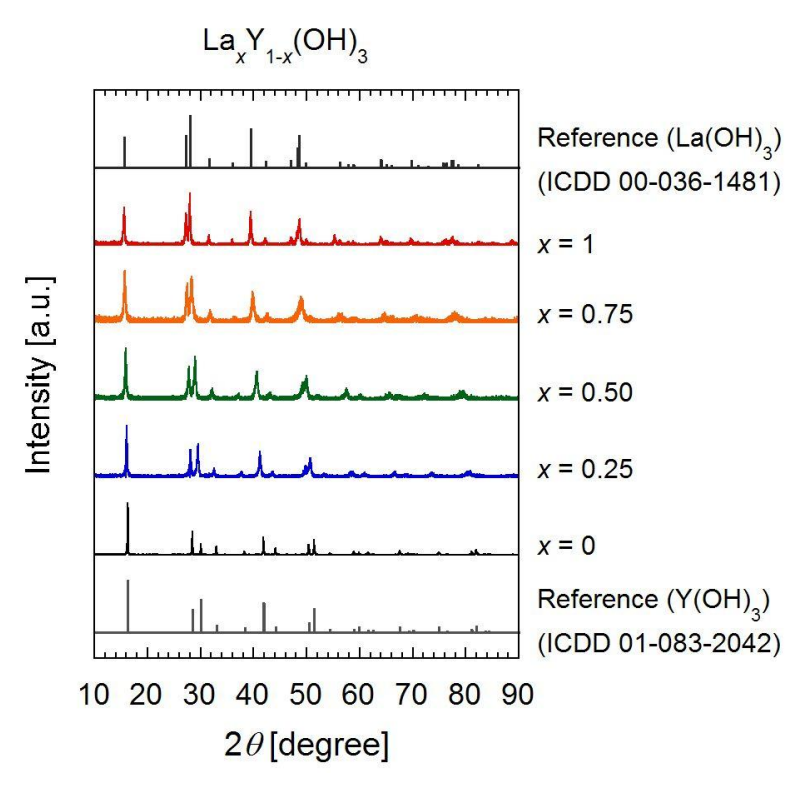


Figure 6.3-9 XRD patterns for $La_xY_{1-x}(OH)_3$ and references ($La(OH)_3$ and $Y(OH)_3$).

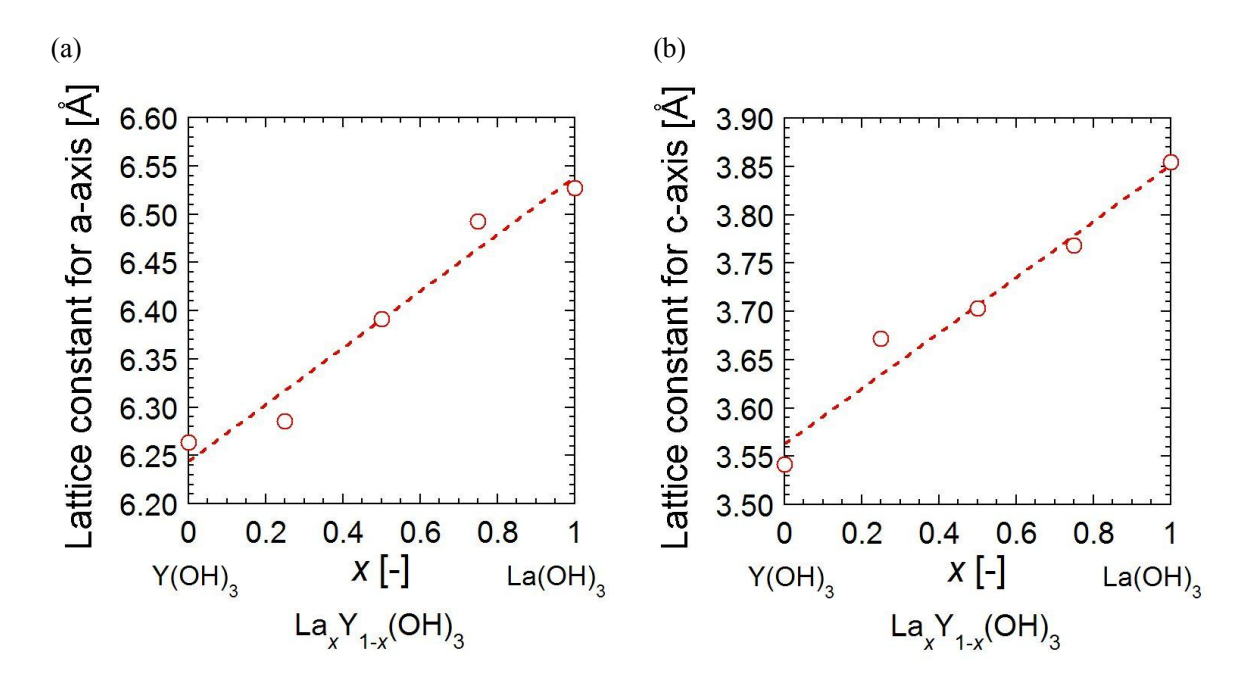


Figure 6.3-10 Shift of lattice constant for $La_xY_{1-x}(OH)_3$; (a) a-axis, (b) c-axis.

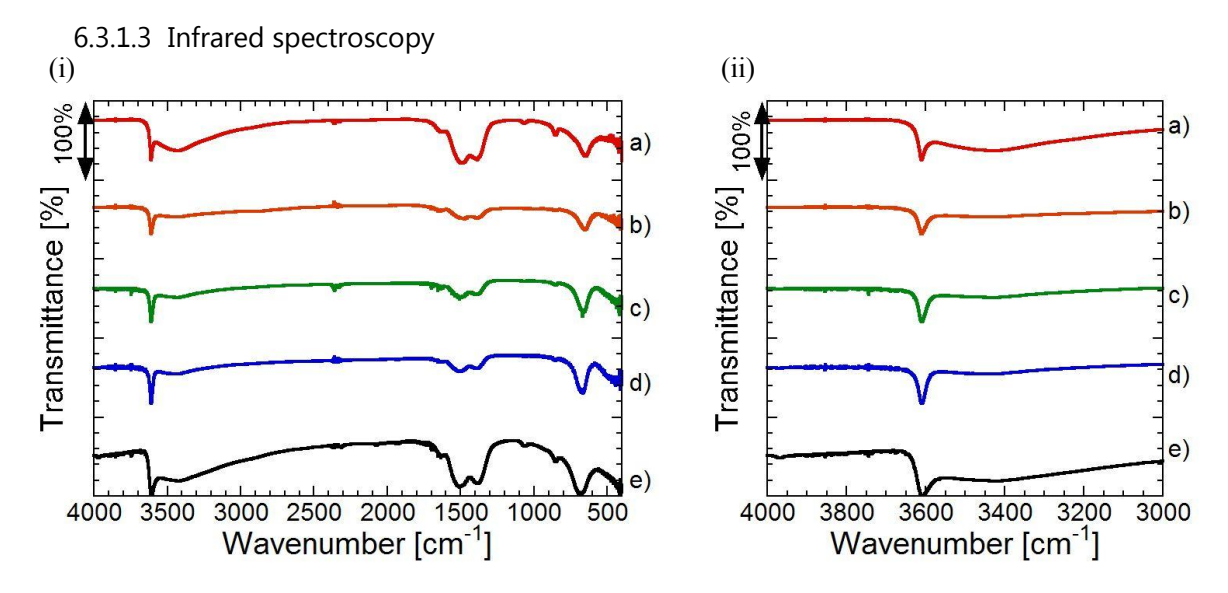


Figure 6.3-11 FT-IR spectra of $La_xNd_{1-x}(OH)_3$; (a) $La(OH)_3$, (b) $La_{0.75}Nd_{0.25}(OH)_3$, (c) $La_{0.50}Nd_{0.50}(OH)_3$, (d) $La_{0.25}Nd_{0.75}(OH)_3$, (e) $Nd(OH)_3$. (i) $4000-400 \text{ cm}^{-1}$, (ii) $4000-3000 \text{ cm}^{-1}$.

The FT-IR spectra of $La_xNd_{1-x}(OH)_3$ is shown in **Figure 6.3-11**. The peak positions of $La_xNd_{1-x}(OH)_3$ for fundamental of OH vibration were at around 3610 cm⁻¹. The absorption peaks for the mixed hydroxides were not separated into individual $La(OH)_3$ and $Nd(OH)_3$ peaks. These results agree with the results of XRD measurement. The mixed hydroxides with homogeneous composition were obtained.

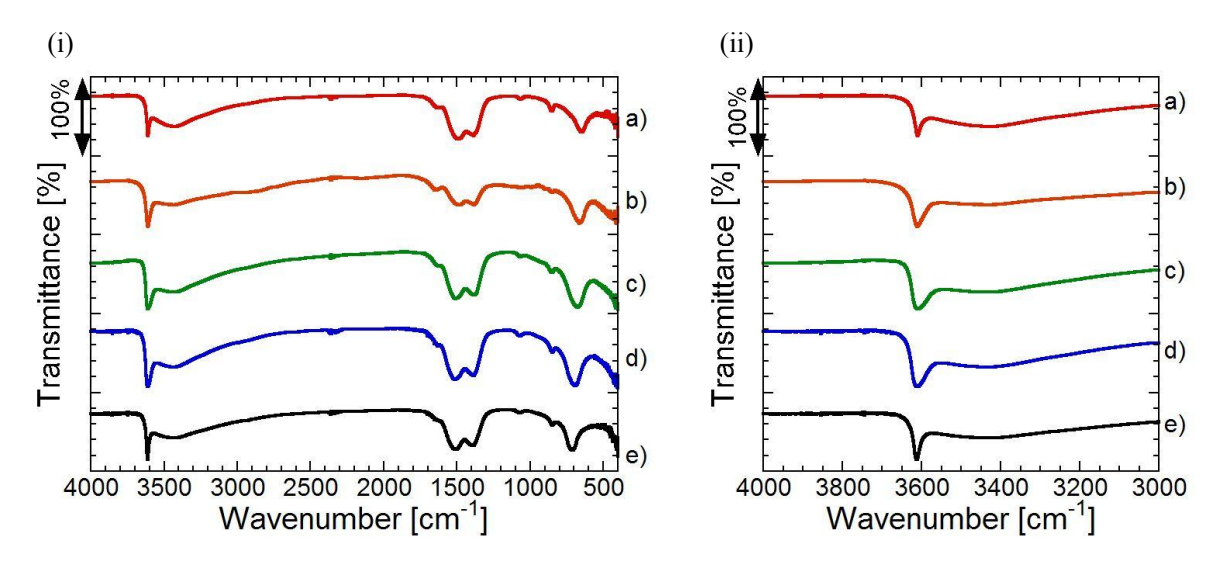


Figure 6.3-12 FT-IR spectra of $La_xGd_{1-x}(OH)_3$; (a) $La(OH)_3$, (b) $La_{0.75}Gd_{0.25}(OH)_3$, (c) $La_{0.50}Gd_{0.50}(OH)_3$, (d) $La_{0.25}Gd_{0.75}(OH)_3$, (e) $Gd(OH)_3$. (i) $4000-400 \text{ cm}^{-1}$, (ii) $4000-3000 \text{ cm}^{-1}$.

The FT-IR spectra of $La_xGd_{1-x}(OH)_3$ is shown in **Figure 6.3-12**. The peak positions of $La_xGd_{1-x}(OH)_3$ for fundamental of OH vibration were at around 3610 cm⁻¹. The absorption peaks for the mixed hydroxides were not separated into individual $La(OH)_3$ and $Gd(OH)_3$ peaks. These results

agree with the results of XRD measurement. The mixed hydroxides with homogeneous composition were obtained.

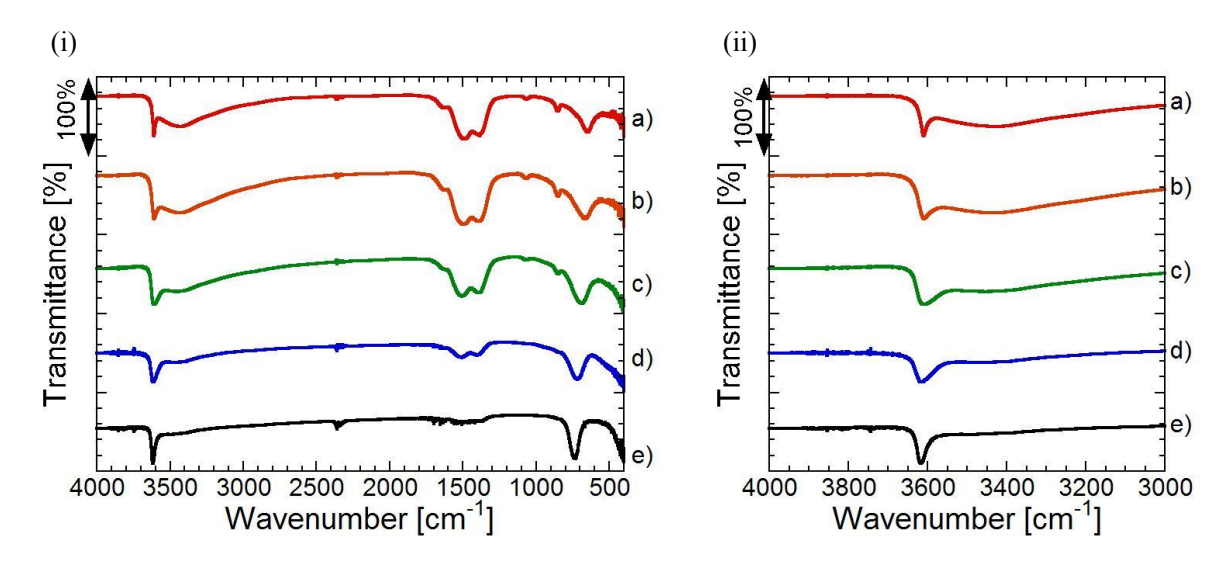


Figure 6.3-13 FT-IR spectra of $La_xY_{1-x}(OH)_3$; (a) $La(OH)_3$, (b) $La_{0.75}Y_{0.25}(OH)_3$, (c) $La_{0.50}Y_{0.50}(OH)_3$, (d) $La_{0.25}Y_{0.75}(OH)_3$, (e) $Y(OH)_3$. (i) $4000-400 \text{ cm}^{-1}$, (ii) $4000-3000 \text{ cm}^{-1}$.

The FT-IR spectra of $La_xY_{1-x}(OH)_3$ is shown in **Figure 6.3-13**. The peak positions of $La_xY_{1-x}(OH)_3$ for fundamental of OH vibration were at around 3610 cm⁻¹. The absorption peaks for the mixed hydroxides were not separated into individual $La(OH)_3$ and $Y(OH)_3$ peaks. These results agree with the results of XRD measurement. The mixed hydroxides with homogeneous composition were obtained.

6.3.2 Thermal decomposition measurement with thermogravimetry

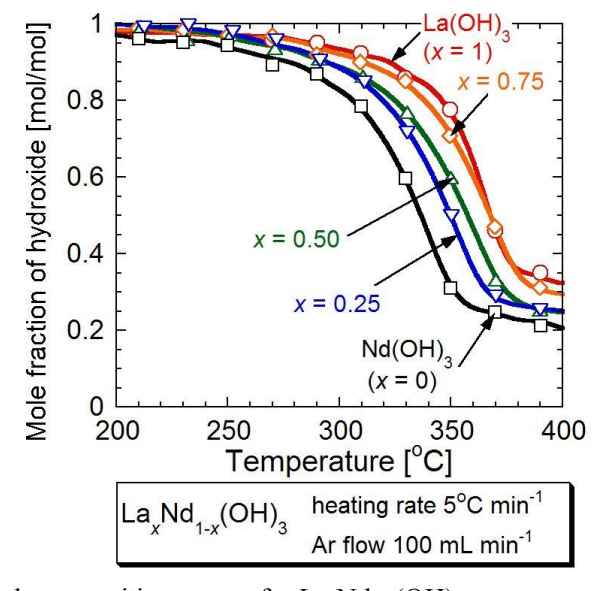


Figure 6.3-14 Thermal decomposition curves for $La_xNd_{1-x}(OH)_3$.

Thermal decomposition curves for $La_xNd_{1-x}(OH)_3$ are shown in **Figure 6.3-14**. The dehydration started at lower temperature when the Nd ion composition in $La_xNd_{1-x}(OH)_3$ was increased.

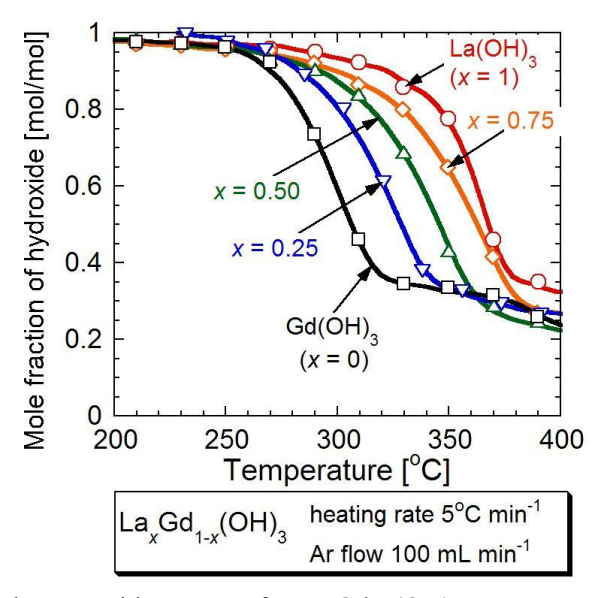


Figure 6.3-15 Thermal decomposition curves for $La_xGd_{1-x}(OH)_3$.

Thermal decomposition curves for $La_xGd_{1-x}(OH)_3$ are shown in **Figure 6.3-15**. The dehydration started at lower temperature when the Gd ion composition in $La_xGd_{1-x}(OH)_3$ was increased. The effect of the Gd ion composition on the temperature shift for dehydration was greater than that of the Nd ion composition.

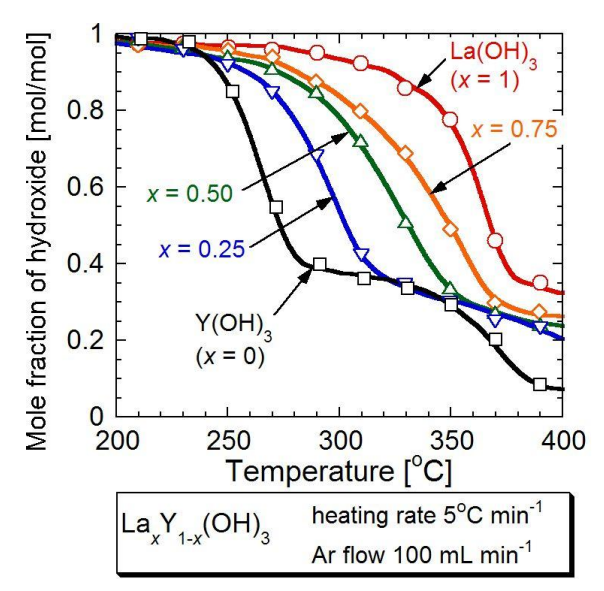


Figure 6.3-16 Thermal decomposition curves for $La_xY_{1-x}(OH)_3$.

Thermal decomposition curves for $La_xY_{1-x}(OH)_3$ are shown in **Figure 6.3-16**. The dehydration started at lower temperature when the Y ion composition in $La_xY_{1-x}(OH)_3$ was increased.

The effect of the Y ion composition on the temperature shift for dehydration was greater than that of the Nd ion and Gd ion composition.

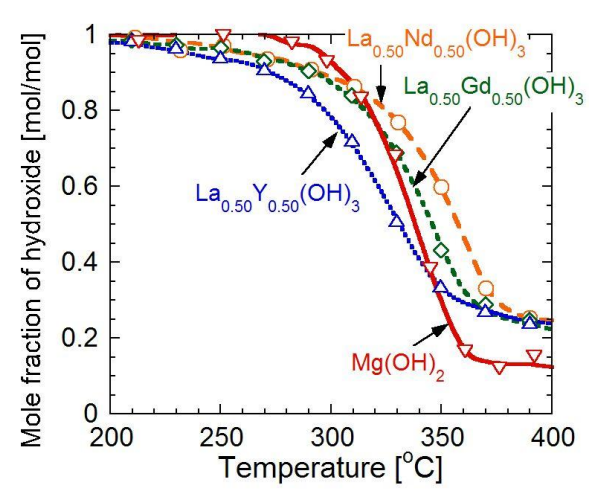


Figure 6.3-17 Thermal decomposition curves for $La_{0.50}Nd_{0.50}(OH)_3$, $La_{0.50}Gd_{0.50}(OH)_3$, $La_{0.50}Y_{0.50}(OH)_3$ and $Mg(OH)_2$.

The thermal decomposition curves for $La_{0.50}Nd_{0.50}(OH)_3$, $La_{0.50}Gd_{0.50}(OH)_3$, $La_{0.50}Y_{0.50}(OH)_3$ and $Mg(OH)_2$ are shown in **Figure 6.3-17**. $La_{0.50}Y_{0.50}(OH)_3$ started dehydration at lower temperature than $Mg(OH)_2$.

6.3.3 Dehydration-hydration measurement with thermogravimetry

Figure 6.3-18 shows the dehydration-hydration behavior of $La_xNd_{1-x}(OH)_3$. Dehydration of $La_xNd_{1-x}(OH)_3$ did not proceed to completion even upon heating at 300°C for 30 min. $La(OH)_3$ and $La_{0.75}Nd_{0.25}(OH)_3$ showed the value of X_c more than 0.9.

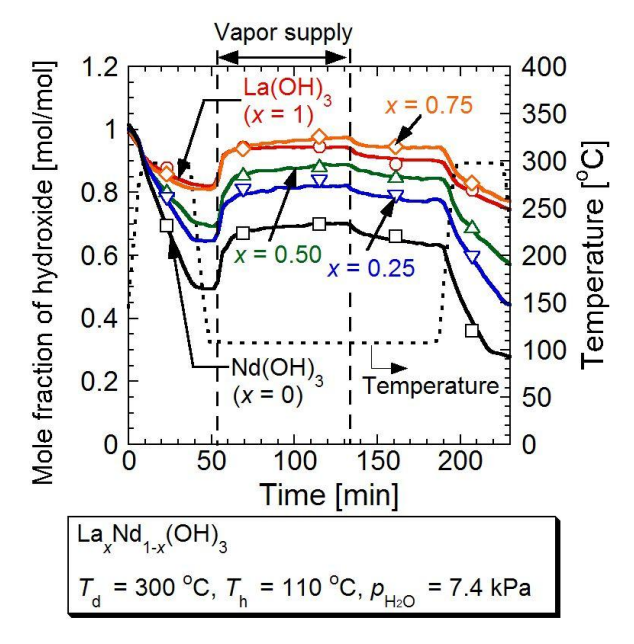


Figure 6.3-18 Dehydration and hydration behavior of $La_xNd_{1-x}(OH)_3$.

Figure 6.3-19 shows dehydration and hydration behavior of $La_xGd_{1-x}(OH)_3$. $La_{0.25}Gd_{0.75}(OH)_3$ and $Gd(OH)_3$ proceeded first dehydration well ($X_0 \approx 0.33$). However, $Gd(OH)_3$ did not hydrate enough.

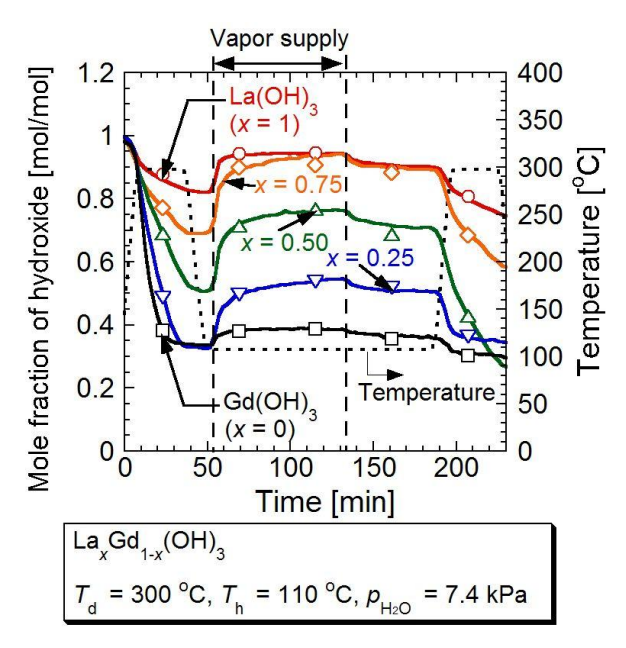


Figure 6.3-19 Dehydration and hydration behavior of $La_xGd_{1-x}(OH)_3$.

Figure 6.3-20 shows dehydration and hydration behavior of $La_xY_{1-x}(OH)_3$. $La_{0.50}Y_{0.50}(OH)_3$, $La_{0.25}Y_{0.75}(OH)_3$, and $Y(OH)_3$ proceeded first dehydration well ($X_0 \approx 0.33$). However, $La_{0.25}Y_{0.75}(OH)_3$ and Y(OH) did not hydrate enough.

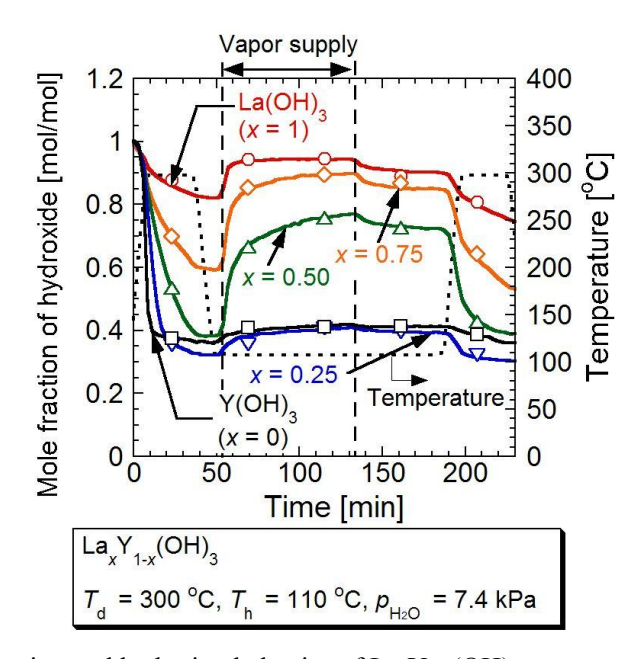


Figure 6.3-20 Dehydration and hydration behavior of $La_xY_{1-x}(OH)_3$.

Figure 6.3-21 shows dehydration and hydration behavior of $La_{0.50}Nd_{0.50}(OH)_3$, $La_{0.50}Gd_{0.50}(OH)_3$, $La_{0.50}Y_{0.50}(OH)_3$, and $Mg(OH)_2$. $Mg(OH)_2$ did not dehydrate enough at 300°C and did not hydrate enough at 110°C with water vapor pressure of 7.4 kPa.

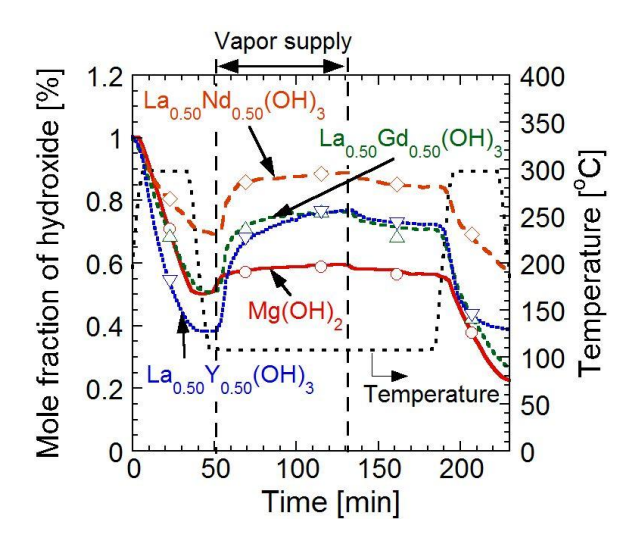


Figure 6.3-21 Dehydration and hydration behavior of $La_{0.50}Nd_{0.50}(OH)_3$, $La_{0.50}Gd_{0.50}(OH)_3$, $La_{0.50}Gd_{0.50}(OH)_3$, $La_{0.50}Y_{0.50}(OH)_3$, and $Mg(OH)_2$.

6.3.4 Measurement of reaction heat with differential scanning calorimetry

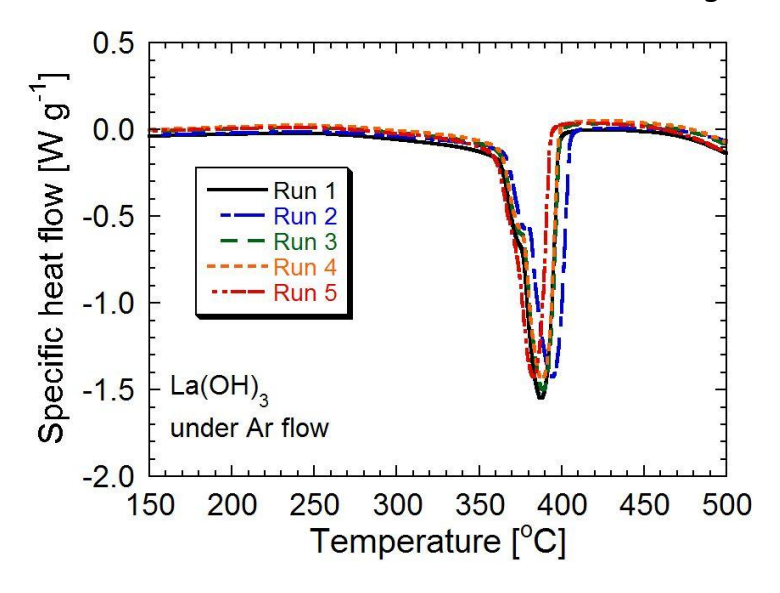


Figure 6.3-22 DSC profiles of La(OH)₃ under Ar flow.

DSC profiles of La(OH)₃ are shown in **Figure 6.3-22**. The negative value of specific heat flow indicates endothermic process. Endothermic peaks were found at 360–410°C.

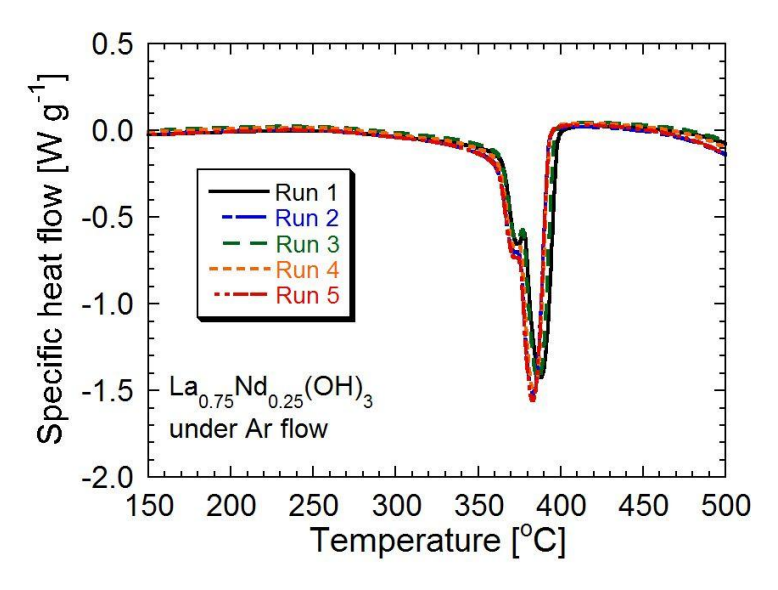


Figure 6.3-23 DSC profiles of La_{0.75}Nd_{0.25}(OH)₃ under Ar flow.

DSC profiles of $La_{0.75}Nd_{0.25}(OH)_3$ are shown in **Figure 6.3-23**. Endothermic peaks were found at 360–400°C. There were two peaks in the DSC curve of $La_{0.75}Nd_{0.25}(OH)_3$. From results of XRD measurement and FT-IR measurement, the composition of the sample was homogeneous. Thus, the two peaks would be consists of amorphous $La_{0.75}Nd_{0.25}(OH)_3$ and crystalline $La_{0.75}Nd_{0.25}(OH)_3$. Both amorphous $La_{0.75}Nd_{0.25}(OH)_3$ and crystalline $La_{0.75}Nd_{0.25}(OH)_3$ would be formed at the hydrothermal process.

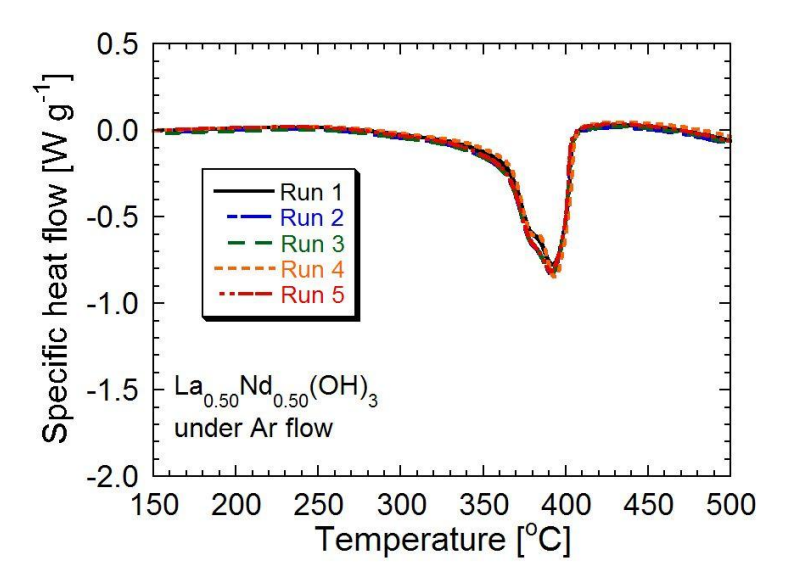


Figure 6.3-24 DSC profiles of La_{0.50}Nd_{0.50}(OH)₃ under Ar flow.

DSC profiles of $La_{0.50}Nd_{0.50}(OH)_3$ are shown in **Figure 6.3-24**. Endothermic peaks were found at 360–400°C.

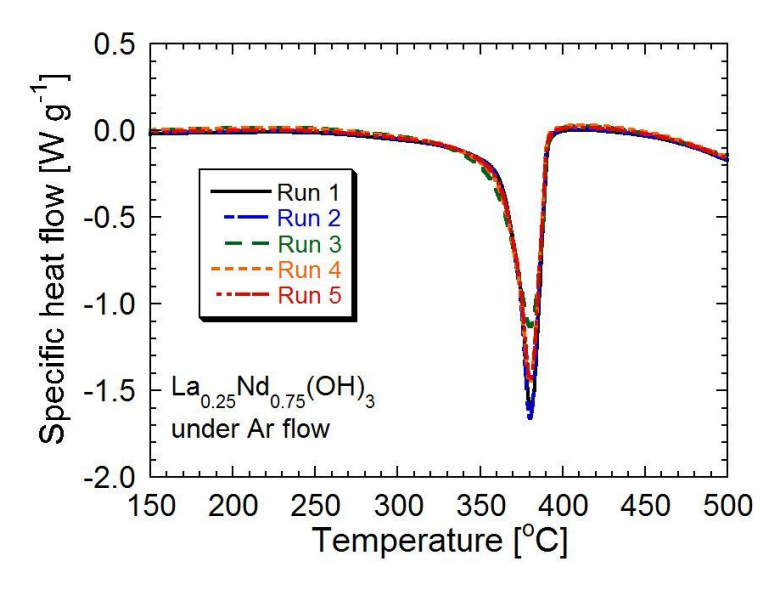


Figure 6.3-25 DSC profiles of La_{0.25}Nd_{0.75}(OH)₃ under Ar flow.

DSC profiles of $La_{0.25}Nd_{0.75}(OH)_3$ are shown in **Figure 6.3-25**. Endothermic peaks were found at 350–390°C.

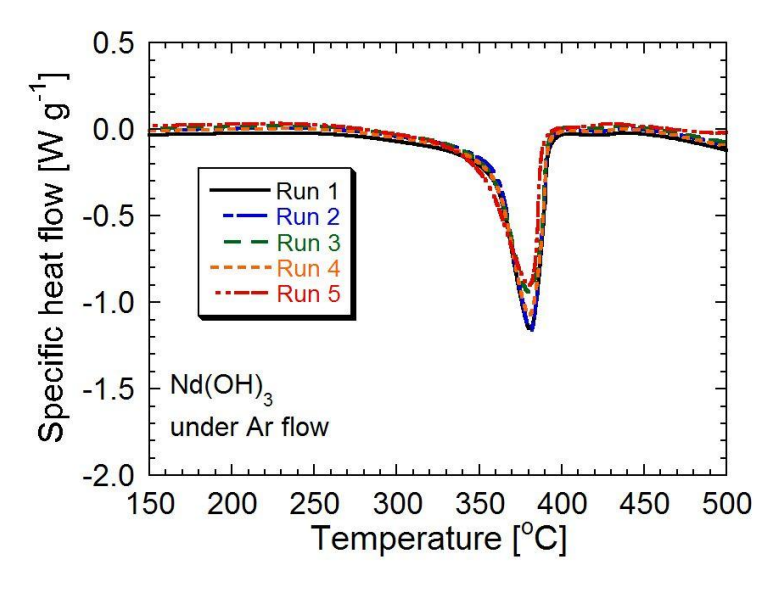


Figure 6.3-26 DSC profiles of Nd(OH)₃ under Ar flow.

DSC profiles of $Nd(OH)_3$ are shown in **Figure 6.3-26**. Endothermic peaks were found at 350-390°C.

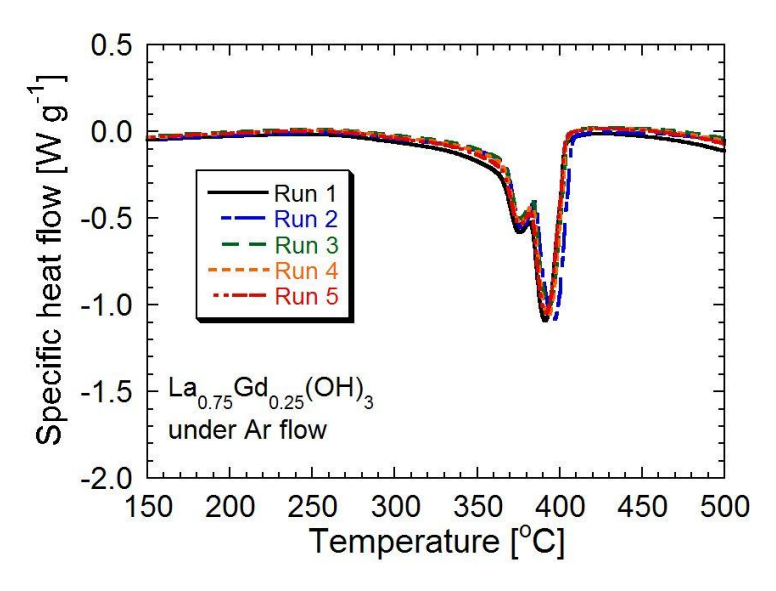


Figure 6.3-27 DSC profiles of La_{0.75}Gd_{0.25}(OH)₃ under Ar flow.

DSC profiles of $La_{0.75}Gd_{0.25}(OH)_3$ are shown in **Figure 6.3-27**. Endothermic peaks were found at 360–410°C. There were two peaks in the DSC curve of $La_{0.75}Gd_{0.25}(OH)_3$ as the DSC curve of $La_{0.75}Nd_{0.25}(OH)_3$. Same as $La_{0.75}Nd_{0.25}(OH)_3$, the two peaks would be consists of amorphous $La_{0.75}Gd_{0.25}(OH)_3$ and crystalline $La_{0.75}Gd_{0.25}(OH)_3$. Both amorphous $La_{0.75}Gd_{0.25}(OH)_3$ and crystalline $La_{0.75}Gd_{0.25}(OH)_3$ would be formed at the hydrothermal process.

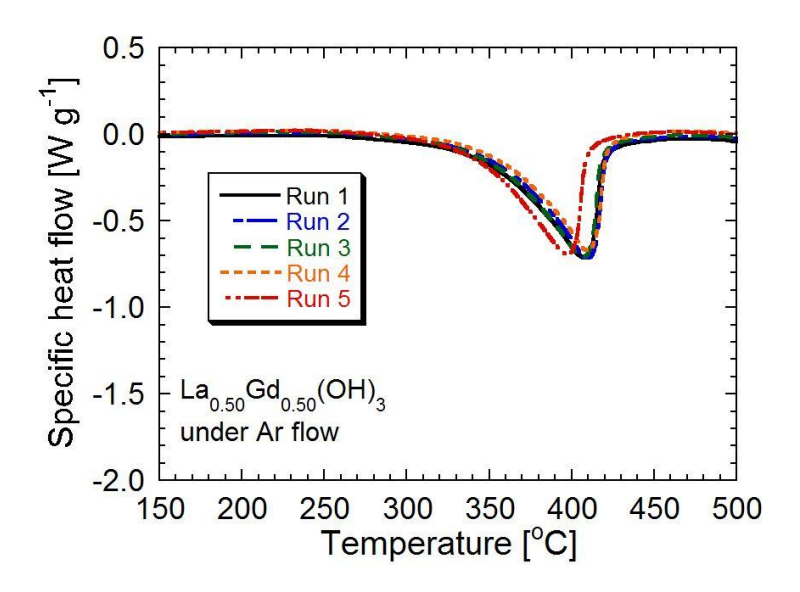


Figure 6.3-28 DSC profiles of La_{0.50}Gd_{0.50}(OH)₃ under Ar flow.

DSC profiles of $La_{0.50}Gd_{0.50}(OH)_3$ are shown in **Figure 6.3-28**. Endothermic peaks were found at 350–420°C.

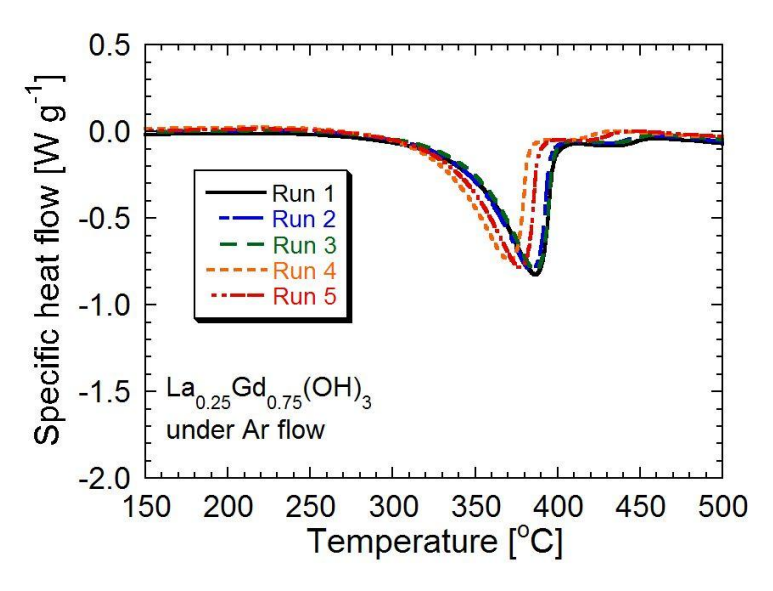


Figure 6.3-29 DSC profiles of La_{0.25}Gd_{0.75}(OH)₃ under Ar flow.

DSC profiles of $La_{0.25}Gd_{0.75}(OH)_3$ are shown in **Figure 6.3-29**. Endothermic peaks were found at 330–410°C.

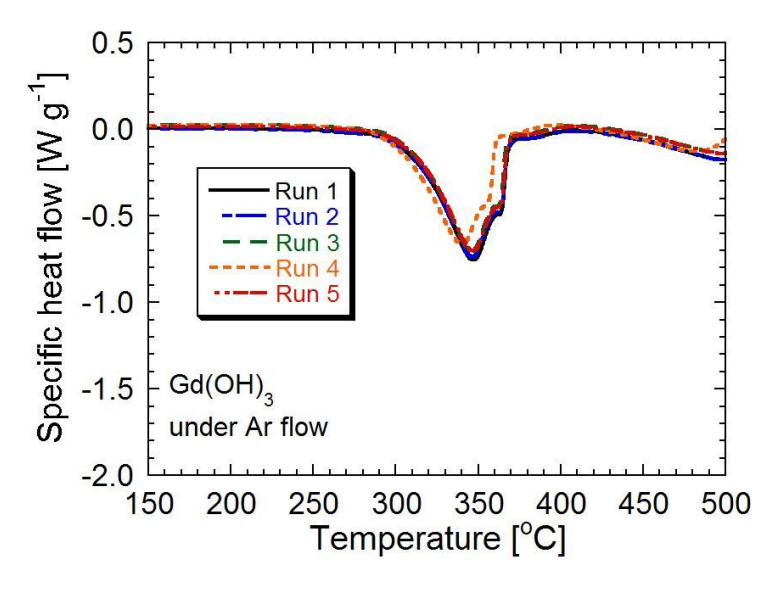


Figure 6.3-30 DSC profiles of Gd(OH)₃ under Ar flow.

DSC profiles of Gd(OH)₃ are shown in **Figure 6.3-30**. Endothermic peaks were found at 350–370°C. There were two peaks in the DSC curve of Gd(OH)₃. Same as La_{0.75}Nd_{0.25}(OH)₃, the two peaks would be consists of amorphous Gd (OH)₃ and crystalline Gd (OH)₃. Both amorphous Gd(OH)₃ and crystalline Gd(OH)₃ would be formed at the hydrothermal process.

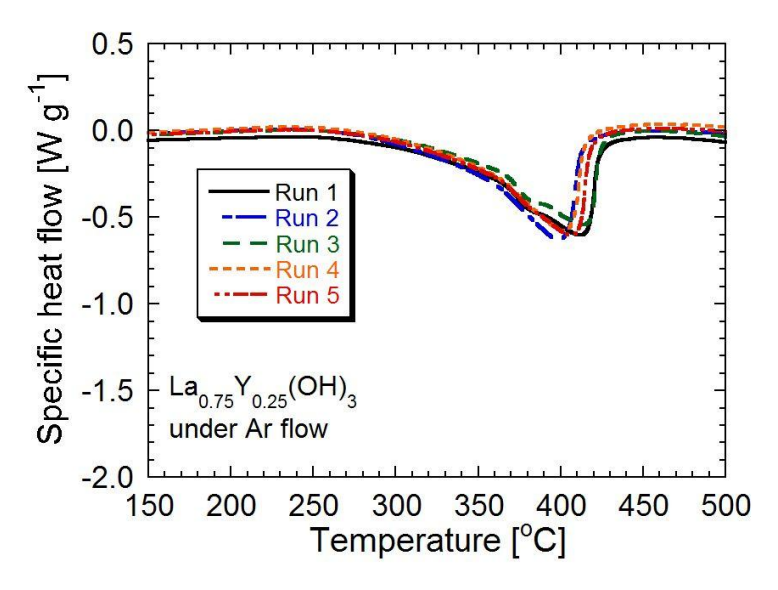


Figure 6.3-31 DSC profiles of La_{0.75}Y_{0.25}(OH)₃ under Ar flow.

DSC profiles of $La_{0.75}Y_{0.25}(OH)_3$ are shown in **Figure 6.3-31**. Endothermic peaks were found at 300–430°C.

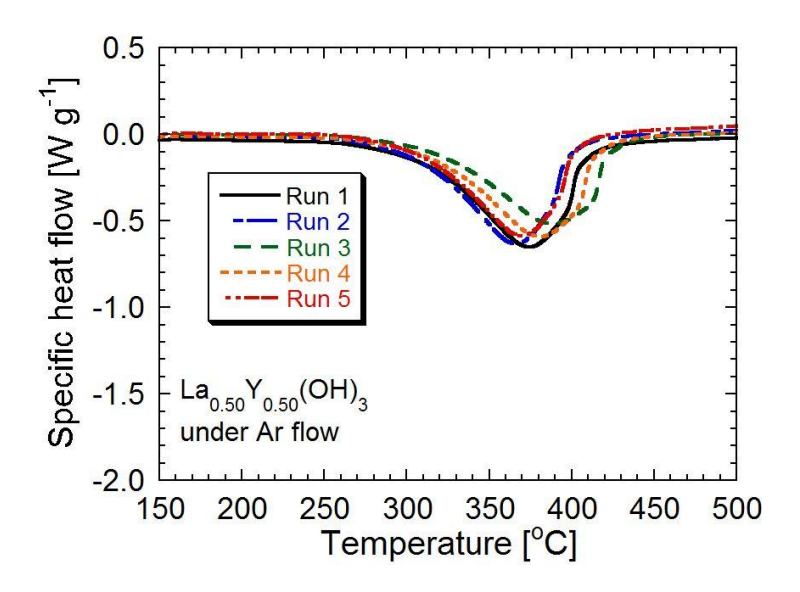


Figure 6.3-32 DSC profiles of $La_{0.50}Y_{0.50}(OH)_3$ under Ar flow.

DSC profiles of $La_{0.50}Y_{0.50}(OH)_3$ are shown in **Figure 6.3-32**. Endothermic peaks were found at 290–420°C.

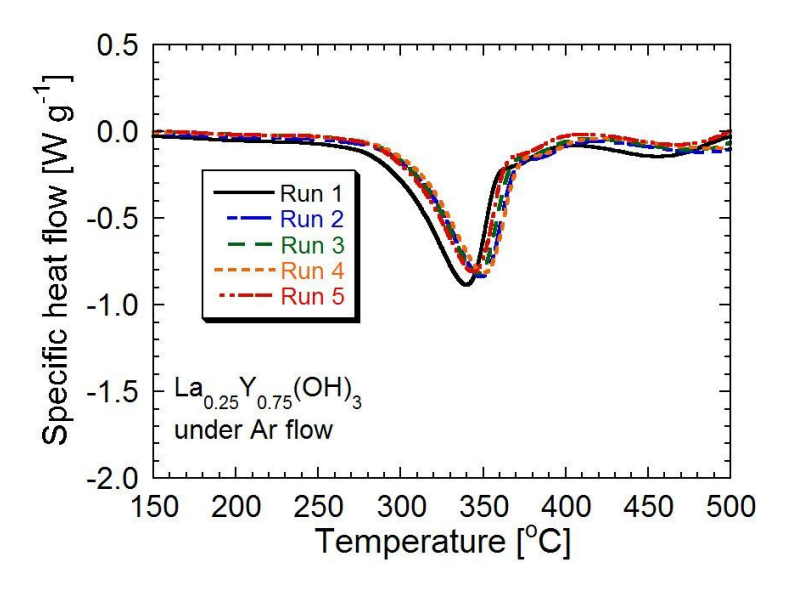


Figure 6.3-33 DSC profiles of $La_{0.25}Y_{0.75}(OH)_3$ under Ar flow.

DSC profiles of $La_{0.25}Y_{0.75}(OH)_3$ are shown in **Figure 6.3-33**. Endothermic peaks were found at 280–400°C.

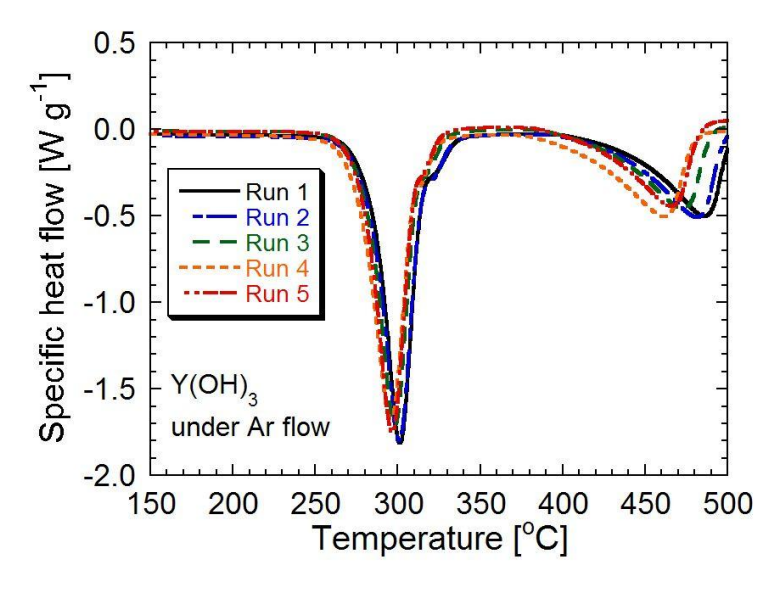


Figure 6.3-34 DSC profiles of Y(OH)₃ under Ar flow.

DSC profiles of Y(OH)₃ are shown in **Figure 6.3-34**. First endothermic peaks (Y(OH)₃ \rightarrow YOOH) were found at 260–340°C. Then, second endothermic peaks (YOOH \rightarrow 1/2Y₂O₃) were found at 400–500°C.

6.4 Discussion

6.4.1 Relationship between composition and thermal decomposition temperature

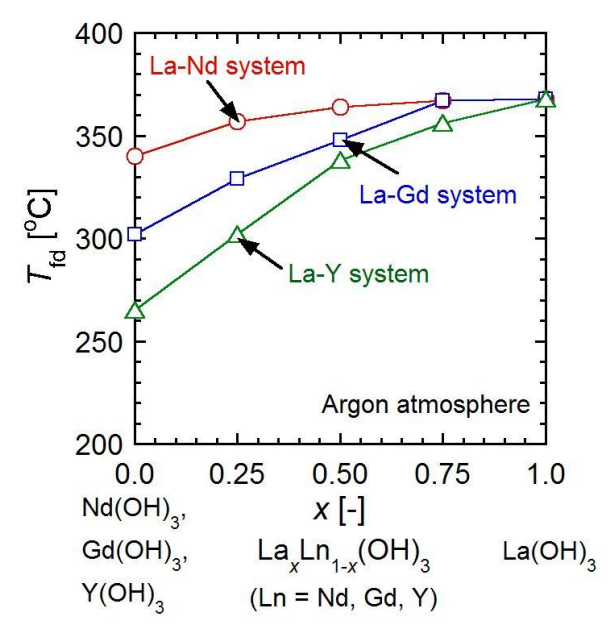


Figure 6.4-1 Relationship between composition of hydroxide and first dehydration temperature.

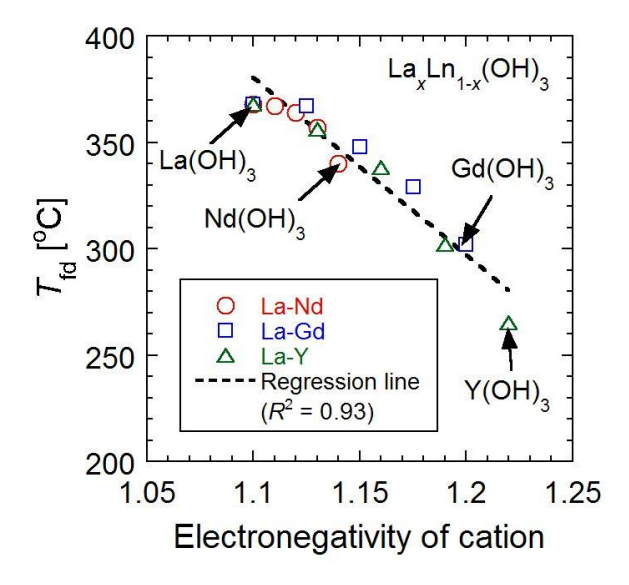


Figure 6.4-2 Relationship between electronegativity of cation and first dehydration temperature for rare earth pure/mixed hydroxides.

A relationship between composition of hydroxide and first dehydration temperature is shown in **Figure 6.4-1**. First dehydration temperature decreased with increase of Nd, Gd, or Y ion concentration. The effect on reduction of first dehydration temperature for each metal ion was found as follows: Y ion > Gd ion > Nd ion. The dehydration reactivity of materials would be enhanced by

adjusting the metal ion composition in the mixed hydroxide. This phenomenon is analyzed by a viewpoint of electronegativity of cation. **Figure 6.4-2** shows a relationship between electronegativity of cation and first dehydration temperature for rare earth pure/mixed hydroxides. Electronegativity of metal (La: 1.10, Nd: 1.14, Gd: 1.20, Y: 1.22) was obtained from a literature [6]. The electronegativity of mixed metal can be calculated weighted average value of electronegativity of each cation [14]. For example, electronegativity of cation for $La_{0.75}Y_{0.25}(OH)_3$ was calculated as follows;

$$\chi_{\text{mixed}} = x \times \chi_{\text{La}} + (1 - x) \times \chi_{\text{Y}}$$

$$= 0.75 \times 1.10 + 0.25 \times 1.22$$

$$= 1.13$$
(6-7)

here, χ_{mixed} is a electronegativity of mixed metal, χ_{La} is a electronegativity of lanthanum, χ_{Y} is a electronegativity of yttrium, respectively.

From **Figure 6.4-2**, first dehydration temperature for rare earth pure/mixed hydroxide was decreased with higher value of electronegativity of cation. A regression line was obtained as below.

$$T_{\rm fd} \, [^{\circ} \text{C}] = -830.8 \, \chi_{\rm cat} + 1294$$
 (6-8)

here, χ_{cat} is a electronegativity of cation (χ_{La} , χ_{Nd} , χ_{Gd} , χ_{Y} , or χ_{mixed}). This trend is explained as follows. A model of dehydration of rare rare earth pure/mixed hydroxide is shown in **Figure 6.4-3**. Electron pair of oxygen in the hydroxide is attracted by "Relatively electronegative cation". Thereby, an electron density in a bond of O–H is relatively low, which means easy to cut the bond. The dehydration would occur by electronic attack from oxygen to hydrogen (**Figure 6.4-3**). The higher electronegative cation attracts electron pair of oxygen more, and it results the dehydration process proceeds easily. Hence, first dehydration temperature for rare earth pure/mixed hydroxide was decreased with higher value of electronegativity of cation.

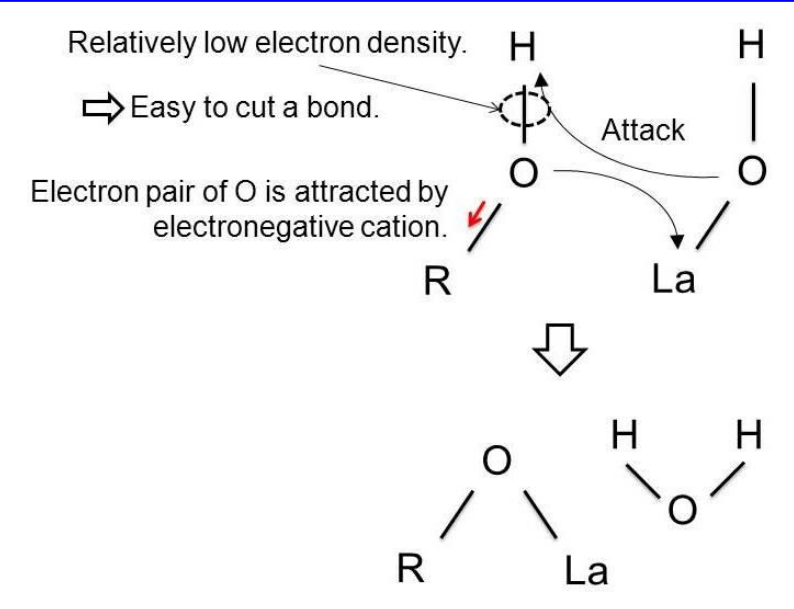


Figure 6.4-3 Model of dehydration of rare rare earth pure/mixed hydroxide.

6.4.2 Relationship between composition and conversion of hydration

A relationship between composition of $La_xNd_{1-x}(OH)_3$ and conversion of hydration is shown in **Figure 6.4-4**. These compounds did not proceed first dehydration enough. Especially, the values of ΔX_d were smaller than 0.20 mol/mol for $La(OH)_3$ and $La_{0.75}Nd_{0.25}(OH)_3$, thereby these compounds showed little value of ΔX_1 . The values of ΔX_1 for $La_xNd_{1-x}(OH)_3$ were around 0.15 mol/mol, which indicates their potentials for heat output are low.

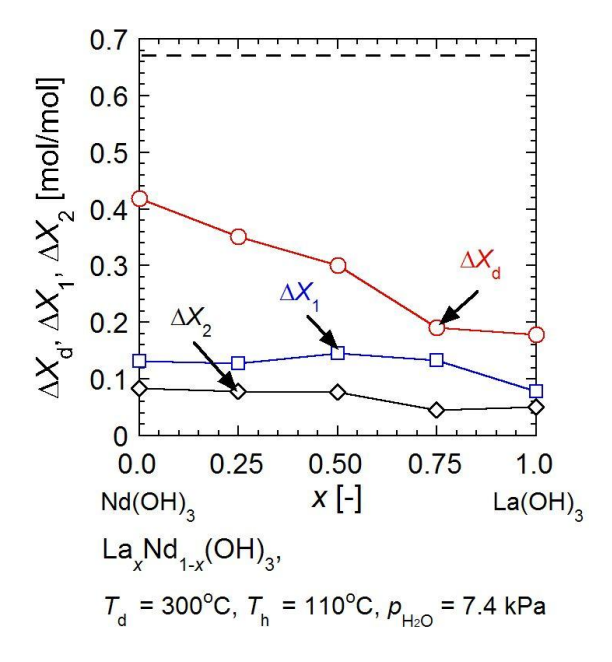


Figure 6.4-4 Relationship between composition of $La_xNd_{1-x}(OH)_3$ and conversion of hydration.

A relationship between composition of La_xGd_{1-x}(OH)₃ and conversion of hydration is shown

in **Figure 6.4-5**. La_{0.25}Gd_{0.75}(OH)₃ and Gd(OH)₃ proceeded first dehydration ($\Delta X_d > 0.60$ mol/mol). On the other hand, Gd(OH)₃ did not proceed hydration reaction well. La_{0.75}Gd_{0.25}(OH)₃ showed maximum value of ΔX_1 (0.20 mol/mol) for La_xGd_{1-x}(OH)₃. This result indicates La-rich compounds have potentials for hydration.

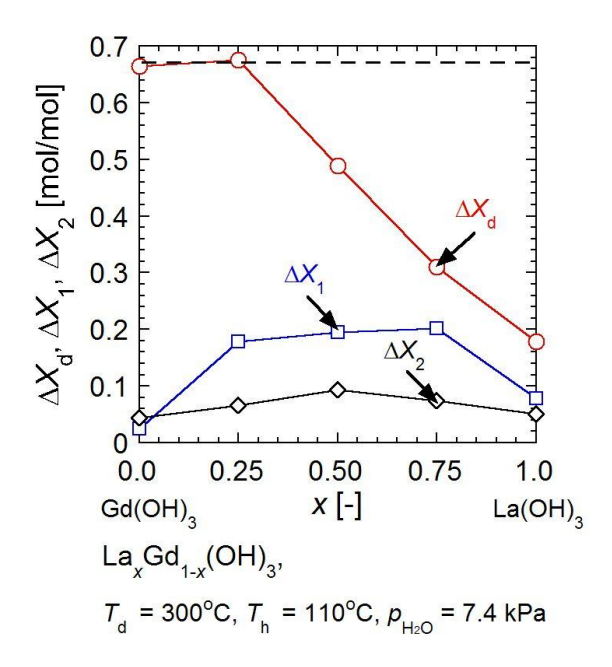


Figure 6.4-5 Relationship between composition of $La_xGd_{1-x}(OH)_3$ and conversion of hydration.

A relationship between composition of $La_xY_{1-x}(OH)_3$ and conversion of hydration is shown in **Figure 6.4-6**. $La_{0.50}Y_{0.50}(OH)_3$, $La_{0.25}Y_{0.75}(OH)_3$ and $Y(OH)_3$ proceeded first dehydration ($\Delta X_d > 0.60$ mol/mol). $La_{0.50}Y_{0.50}(OH)_3$ showed maximum value of ΔX_1 (0.34 mol/mol) for rare earth pure/mixed hydroxide.

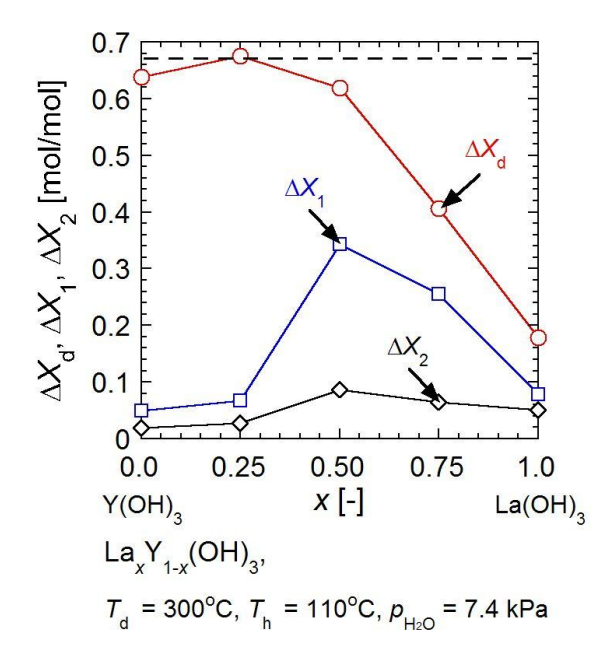


Figure 6.4-6 Relationship between composition of $La_xY_{1-x}(OH)_3$ and conversion of hydration.

6.4.3 Relationship between composition and reaction heat

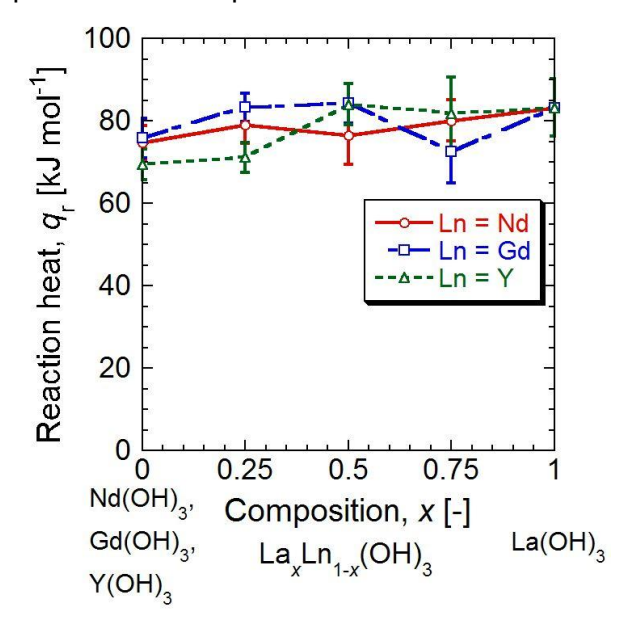


Figure 6.4-7 Relationship between composition of rare earth pure/mixed hydroxide and reaction heat.

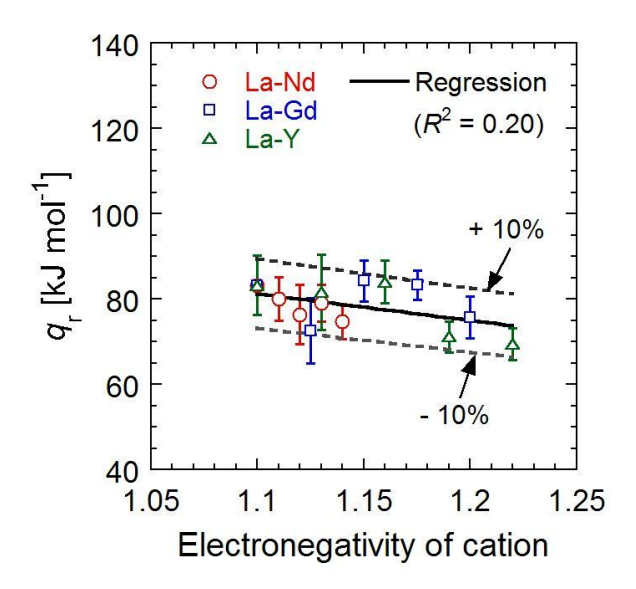


Figure 6.4-8 Relationship between electronegativity of cation and reaction heat.

A relationship between composition of rare earth pure/mixed hydroxide and reaction heat is shown in **Figure 6.4-7**. The reaction heat was around 78 kJ mol^{-1} for rare earth pure/mixed hydroxide. From a discussion at **Section 6.4.1**, higher electronegative cation attracts electron pair of oxygen more, and it results the dehydration process proceeds easily. Thus, it is expected that the reaction heat decreases with higher value of electronegativity of cation. A relationship between electronegativity of cation and reaction heat is shown in **Figure 6.4-8**. The measured reaction heats are within \pm 10% value of a regression formula as below.

$$q_{\rm r} [kJ \text{ mol}^{-1}] = -62.30 \chi_{\rm cat} + 149.8$$
 (6-9)

Reaction heats showed downward trend by increase of electronegativity of cation. This tendency supports the discussion at **Section 6.4.1**.

6.4.4 Heat output capacity

Heat output capacities of $La_xNd_{1-x}(OH)_3$ and $Mg(OH)_2$ are shown in **Figure 6.4-9**. The heat output capacities of $La_xNd_{1-x}(OH)_3$ were smaller than that of $Mg(OH)_2$. Hence, $La_xNd_{1-x}(OH)_3$ are not suitable for TCMs.

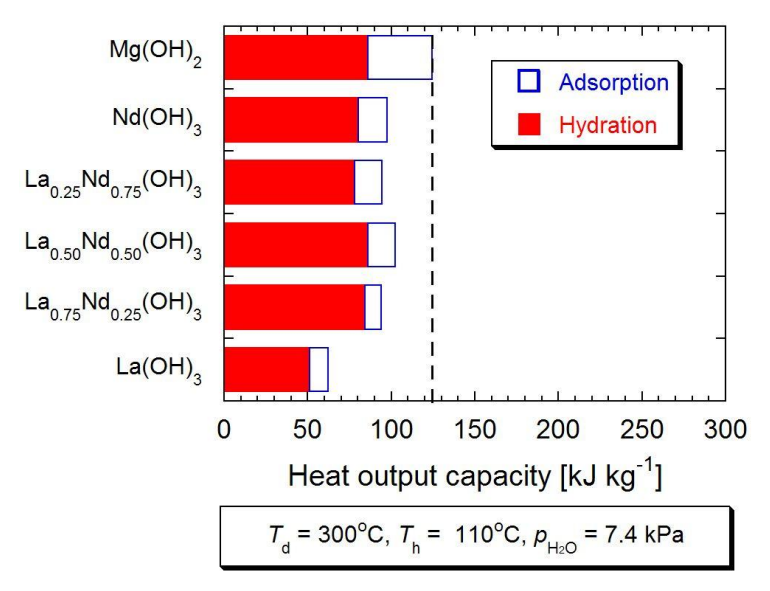


Figure 6.4-9 Heat output capacities of $La_xNd_{1-x}(OH)_3$ and $Mg(OH)_2$.

Heat output capacities of $La_xGd_{1-x}(OH)_3$ and $Mg(OH)_2$ are shown in **Figure 6.4-10**. The heat output capacities of $Gd(OH)_3$, $La_{0.25}Gd_{0.75}(OH)_3$, and $La(OH)_3$ were smaller than that of $Mg(OH)_2$. Hence, these compounds are not suitable for TCMs. On the other hand, The heat output capacities of $La_{0.50}Gd_{0.50}(OH)_3$, and $La_{0.75}Gd_{0.25}$ (OH)₃ were higher than that of $Mg(OH)_2$. Thus, these compounds are expected as candidates of TCMs.

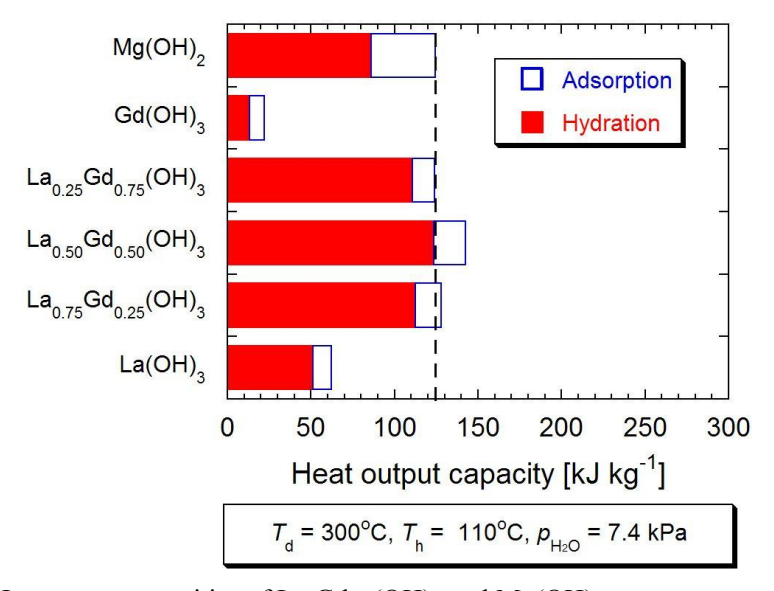


Figure 6.4-10 Heat output capacities of $La_xGd_{1-x}(OH)_3$ and $Mg(OH)_2$.

Heat output capacities of $La_xY_{1-x}(OH)_3$ and $Mg(OH)_2$ are shown in **Figure 6.4-11**. The heat output capacities of $Y(OH)_3$, $La_{0.25}Y_{0.75}(OH)_3$, and $La(OH)_3$ were smaller than that of $Mg(OH)_2$. Hence, these compounds are not suitable for TCMs. On the other hand, The heat output capacities of $La_{0.50}Y_{0.50}(OH)_3$, and $La_{0.75}Y_{0.25}(OH)_3$ were higher than that of $Mg(OH)_2$. Thus, these compounds are

expected as candidates of TCMs. Especially, $La_{0.50}Y_{0.50}(OH)_3$ shows highest heat capacity (282 kJ kg⁻¹) in the rare earth pure/mixed hydroxide because of its highest value on conversion of hydration (0.34 mol/mol).

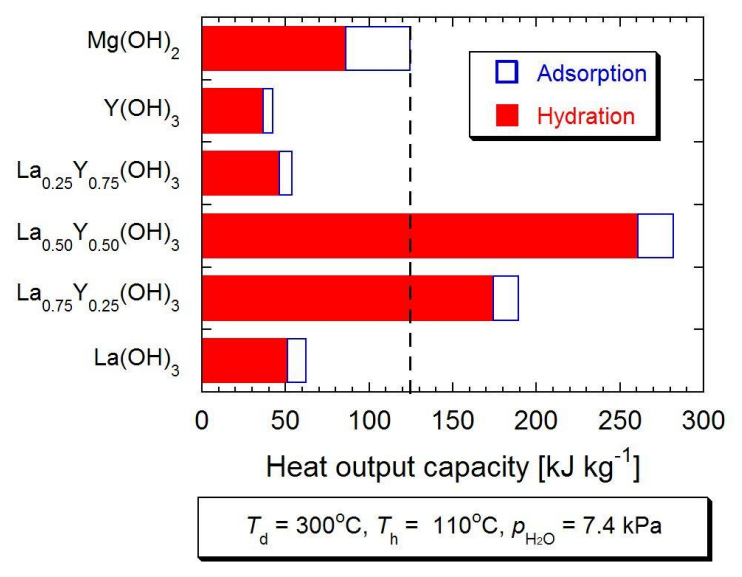


Figure 6.4-11 Heat output capacities of $La_xY_{1-x}(OH)_3$ and $Mg(OH)_2$.

6.4.5 Rare earth elements from spent nuclear fuels

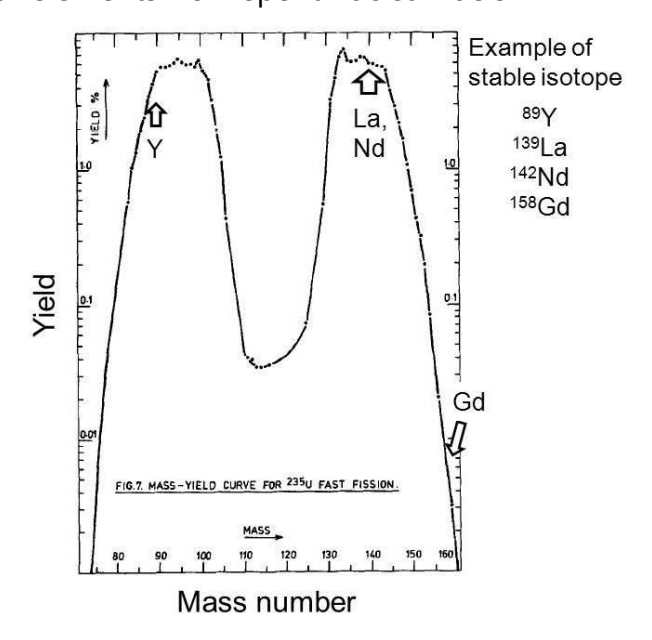


Figure 6.4-12 Yield of each fission product from ²³⁵U [15].

Yield of each fission product from 235 U [15] is shown in **Figure 6.4-12**. The rare earth elements (Y, La, Nd, and Gd) can be obtained from spent nuclear fuels. It is known that radioactivities of La and Nd will be lower than 0.1 Bq g⁻¹, which is lower than radioisotope regulation in Japan, after two years cooling [16]. The separation from rare earth mixture into each element is not easy because

of their similar properties. Separation processes by chromatography [17,18] or solvent extraction [19,20] were studied. The separation process requires a mixture of high concentration of nitric acid and methanol. Here, rare earth mixed hydroxides such as La_{0.50}Gd_{0.50}(OH)₃, La_{0.75}Y_{0.25}(OH)₃, or La_{0.50}Y_{0.50}(OH)₃ have potentials as TCMs, which indicates high-purity rare earth element is not essential for TCMs. Thus, rare earth mixed hydroxide can be obtained from spent nuclear fuels relatively easily.

6.5 Summary

Rare earth hydroxides are proposed as new candidates for TCMs. Rare earth elements can be obtained from natural resources or spent nuclear fuels. The dehydration reactivity of the hydroxides was enhanced by adjusting the metal ion composition, which indicated that the first dehydration temperature depends on electronegativity of cation. TCMs based on La_{0.50}Y_{0.50}(OH)₃ dehydrated at 300°C, and hydrated at 110°C with water vapor pressure of 7.4 kPa which corresponds to saturated vapor pressure at 40°C, and at which authentic MgO has small reactivity. Reactivity of conventional material (Mg(OH)₂) was lower than La_{0.50}Y_{0.50}(OH)₃ under these conditions. Reaction heats of rare earth pure/mixed hydroxides showed downward trend by increase of electronegativity of cation. The heat output capacities of La_{0.50}Gd_{0.50}(OH)₃, La_{0.75}Gd_{0.25}(OH)₃, La_{0.50}Y_{0.50}(OH)₃, and La_{0.75}Y_{0.25}(OH)₃ were higher than that of conventional material (Mg(OH)₂) at 110°C with water vapor pressure of 7.4 kPa. Thus, these compounds are expected as candidates of TCMs. Especially, La_{0.50}Y_{0.50}(OH)₃ shows highest heat output capacity (282 kJ kg⁻¹) in the rare earth pure/mixed hydroxide, then, is the best TCM in this study.

6.6 References

- [1] S. S. Batsanov, A. A. Deribas, G. N. Kustovq; Reaction of rare-earth metal oxides with water, *Russ. J. Inorg. Chem.*, **12**, 1206–1207 (1967)
- [2] O. Yamamoto, Y. Takeda, R. Kanno, M. Fushimi; Thermal decomposition and electrical conductivity of M(OH)₃ and MOOH (M = Y, Lamthanide), *Solid State Ionics*, **17**, 107–114 (1985)
- [3] M. Nagao, H. Hamano, K. Hirata, R. Kumashiro, Y. Kuroda; Hydration process of rare-earth sesquioxides having different crystal structures, *Langmuir*, **19**, 9201–9209 (2003)
- [4] A. Neumann, D. Walter; The thermal transformation from lanthanum hydroxide to lanthanum hydroxide oxide, *Thermochimica Acta*, **445**, 200–204 (2006)
- [5] J. Ryu, R. Takahashi, N. Hirao, Y. Kato; Effect of transition metal mixing on reactivities of magnesium oxide for chemical heat pump, *J. Chem. Eng. Jpn.*, **40**, 1281–1286 (2007)
- [6] A. L. Allred; Electronegativity values from thermochemical data, *J. Inorg. Nucl. Chem.*, **17**, 215–221 (1961)
- [7] F. S. Galasso; Structure and properties of inorganic solids, third ed., trans. in Japanese M. Kato, K. Uematsu, AGNE Gijutsu Center, Tokyo, Japan (2002)
- [8] W. O. Milligan, D. F. Mullica, J. D. Oliver; Rare-earth trihydroxide parameters, *J. Appl. Cryst.*, **12**, 411–412 (1979)

- [9] The Chemical Society of Japan ed., Handbook of chemistry (in Japanese), fifth ed., Maruzen Publishing, Tokyo, Japan (2004)
- [10] S. I. Smyshlyaev, B.P. Burylev; Thermodynamics of hydroxide of group III metals, *Russ. J. Phys. Chem.*, **50**, 528–529 (1976)
- [11] E. H. P. Cordfunke, R. J. M. Konings, W. Ouweltjes; The standard enthalpies of formation of hydroxides IV. La(OH)₃ and LaOOH, *J. Chem. Thermodyn.*, **22**, 449–452 (1990)
- [12] R. Alvero, A. Bernal, I. Carrizosa, J. A. Odriozola, J. M. Trillo; Lanthanide oxides: thermochemical approach to hydration, *J. Mater. Sci.*, **22**, 1517–1520 (1987)
- [13] L. R. Morss, C. M. Haar; Standard molar enthalpy of formation of neodymium hydroxide, *J. Chem. Thermodyn.*, **21**, 1079–1083 (1989)
- [14] K. Shibata, T. Kiyoura, J. Kitagawa, T. Sumiyoshi, K. Tanabe; Acidic properties of binary metal oxides, *Bull. Chem. Soc. Jpn.*, **46**, 2985–2988 (1973)
- [15] E. A. C. Crouch; Fission-product yields from newtron induced fission, *At. Data Nucl. Data Table*, **19**, 417–532 (1977)
- [16] M. Ozawa; Research strategy on advanced ORIENT cycle, *Genshiryoku-eye* (in Japanese), **56**, 7–11 (2010)
- [17] T. Suzuki, K. Itoh, A. Ikeda, M. Aida, M. Ozawa, Y. Fujii; Separation of rare earth elements by tertiary pyridine type resin, *J. Alloys Compd.*, **408–412**, 1013–1016 (2006)
- [18] T. Suzuki; Progress in research on separation, Genshiryoku-eye (in Japanese), 56, 12–15 (2010)
- [19] M. Ozawa, S. Suzuki, K. Takeshita; Advanced hydrometallurgical separation of actinides and rare metals in nuclear fuel cycle, *Solvent Extr. Res. Dev., Jpn.*, **17**, 19–34 (2010)
- [20] Y. Sasaki, S. Suzuki, M. Ozawa; Research review on novel ligands in nuclear back-end cycle, *Fine chemical (in Japanese)*, **38**, 47–62 (2009)

Chapter 7 Combination of thermochemical energy storage based on lithium chloride-modified magnesium hydroxide and small nuclear reactors

7.1 Introduction

In past decades, water cooled reactors [1–3] and a gas cooled reactor [4] with small capacity (5–330 MWt) were studied for district heating. Generally, nuclear plants are operated steady. On the other hand, heat load is not steady. Load leveling by using thermochemical energy storages (TcES) is considered as a method to overcome the problem [5,6]. However, required amount of thermochemical energy storage material (TCM) for load leveling of small nuclear reactors has not been studied. The required amount is needed to be studied to evaluate a potential of TCM for load leveling. In this chapter, LiCl/Mg(OH)₂ (α = 0.10) was considered as a TCM for load leveling because of its high heat output capacity (1.40 × 10³ kJ kg⁻¹ at $T_{\rm d}$ = 300°C, $T_{\rm h}$ = 110°C, $p_{\rm H2O}$ = 57.8 kPa, and 80 min for vapor supply) compared with rare-earth mixed hydroxides (282 kJ kg⁻¹ at $T_{\rm d}$ = 300°C, $T_{\rm h}$ = 110°C, $p_{\rm H2O}$ = 7.4 kPa, and 80 min for vapor supply).

At the accident at nuclear power plant, it is needed to remove decay heat from the reactor. Hydrogen was formed at the accident of Fukushima Dai-ichi nuclear power station because decay heat couldn't be removed by blackout. Thus, emergency core cooling system (ECCS) which can work without power is needed. LiCl/Mg(OH)₂ ($\alpha = 0.10$) is a candidate as a heat absorber because it dehydrate (endothermic reaction) at around 300°C, which is suitable for temperature of light water reactor (LWR), and its high heat storage capacity. Kim evaluated the required amount of a TCM (authentic Mg(OH)₂) [7]. For nuclear reactor of 1000 MWt capacity, 72 ton of authentic Mg(OH)₂ is needed to absorb heat after 10 h shutdown [7]. The required amount of LiCl/Mg(OH)₂ ($\alpha = 0.10$) for ECCS of small nuclear reactor is important to evaluate a possibility of LiCl/Mg(OH)₂ ($\alpha = 0.10$) as a material for ECCS.

In this chapter, the heat load of a town was assumed by sin curve modeling, and then the required amount of $LiCl/Mg(OH)_2$ for load leveling was estimated. The decay heat from a small nuclear reactor is calculated, and then required amount of $LiCl/Mg(OH)_2$ for ECCS was evaluated.

7.2 Small nuclear reactor for district heating

7.2.1 District heating system with thermochemical energy storage

Small nuclear reactors for district heating or cogeneration were studied in the last decades. Usually, the network of district heating is designed temperature range of 80–150°C [1–4]. Heat load is approximately 600–1200 MWt for large cities and 10–50 MWt for towns [8]. Usually, required

temperature of heat for space heating is 80°C, and that of heat for hot water production is 60°C [1]. In this chapter, a small pressurized water reactor (PWR) for combined heat and power generation is considered. A nuclear reactor at Bilibino, Russian federation was designed for cogeneration [9]. 25 MWt of heat output and 11 MWe of electric output are obtained from the reactor. In this work, a small reactor which outputs 10 MWt of heat and 4.4 MWe of electricity, is considered (reactor power: 23.3 MWt). Temperatures at primary and secondary system are shown in **Table 7.2-1**. The core output temperature is estimated at 350°C and supply temperature for district heating is estimated at 95°C. A generating efficiency of the nuclear power plant is assumed as 0.33. It is assumed that the load of electricity is constant. LiCl/Mg(OH)₂ (α = 0.10) is used as a TCM in this district heating system. Pressurized water is used as a heat medium. Schematic diagram of district heating system with TcES (operated for heat storage) is shown in **Figure 7.2-1**. The base load for district heating (10 MWt) is supplied from PWR, and surplus heat is stored by dehydration of LiCl/Mg(OH)₂ (α = 0.10) at low-heat demand period. The other heat is supplied for space heating, supply of hot water, and snow melting. The temperatures at inlet and outlet of heat exchangers and flow rate of water at a peak of heat storage are calculated from a following relationship. It is assumed that all pipes are insulated.

$$W_{\rm ex} = F \cdot C_{\rm p} \cdot \Delta T \tag{7-1}$$

Here, $W_{\rm ex}$ [kW] is a rate of heat exchange, F [kg s⁻¹] is a flow rate of water, $C_{\rm p}$ [kJ kg⁻¹ K⁻¹] is a isobaric specific heat capacity, and ΔT [°C] is a temperature drop at a heat exchanger, respectively. Schematic diagram of district heating system with TcES (operated for heat output) is shown in **Figure 7.2-2**. The base load for district heating (10 MWt) is supplied from PWR, and additional heat is supplied from hydration of LiCl/MgO ($\alpha = 0.10$) at high-heat demand period. The obtained heat is supplied for space heating, supply of hot water, and road heating. It is assumed that LiCl/Mg(OH)₂ ($\alpha = 0.10$) is dehydrated at around 300°C in the reactor, and LiCl/MgO ($\alpha = 0.10$) is hydrated at around 140°C with water vapor pressure of 57.8 kPa. The temperatures at inlet and outlet of heat exchangers and flow rate of water at a peak of heat storage are calculated (Eq. (7-1)). The set value of temperature for power generation loop of the small reactor is shown in **Figure 7.2-3**.

Table 7.2-1 Thermal parameters of a pressurized water reactor for district heating.

	Primary system		Secondary system	
Heat output	Core inlet	Core outlet	Supply temperature R	Return temperature
	temperature	temperature		
[MWt]	[°C]	[°C]	[°C]	[°C]
10	300	350	95	65

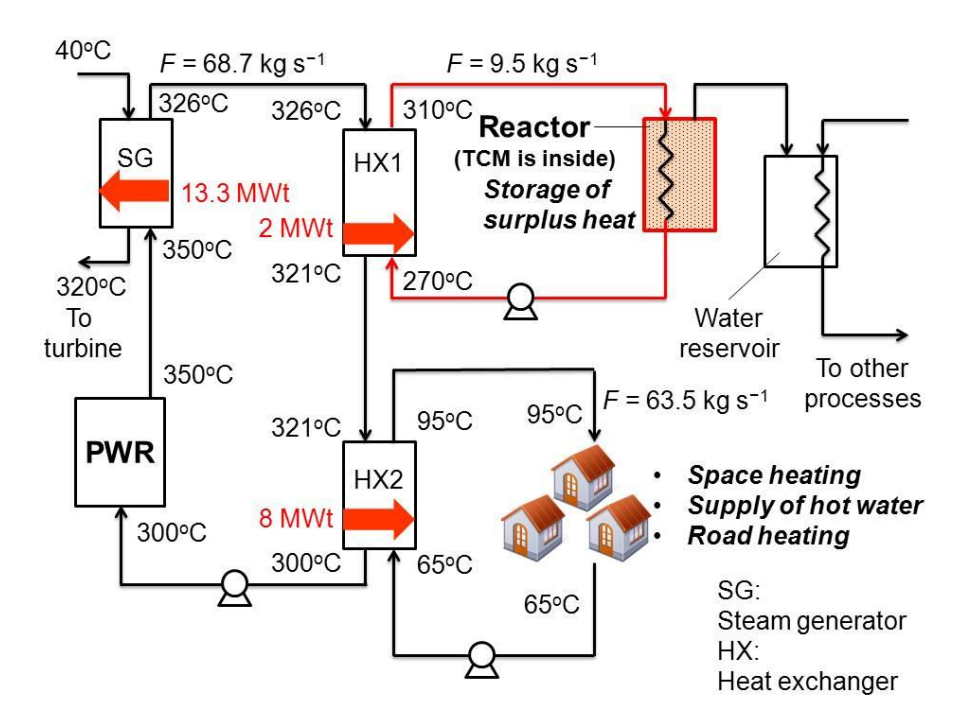


Figure 7.2-1 Schematic diagram of district heating system with thermochemical energy storage (at a peak of heat storage operation) at low-heat demand period.

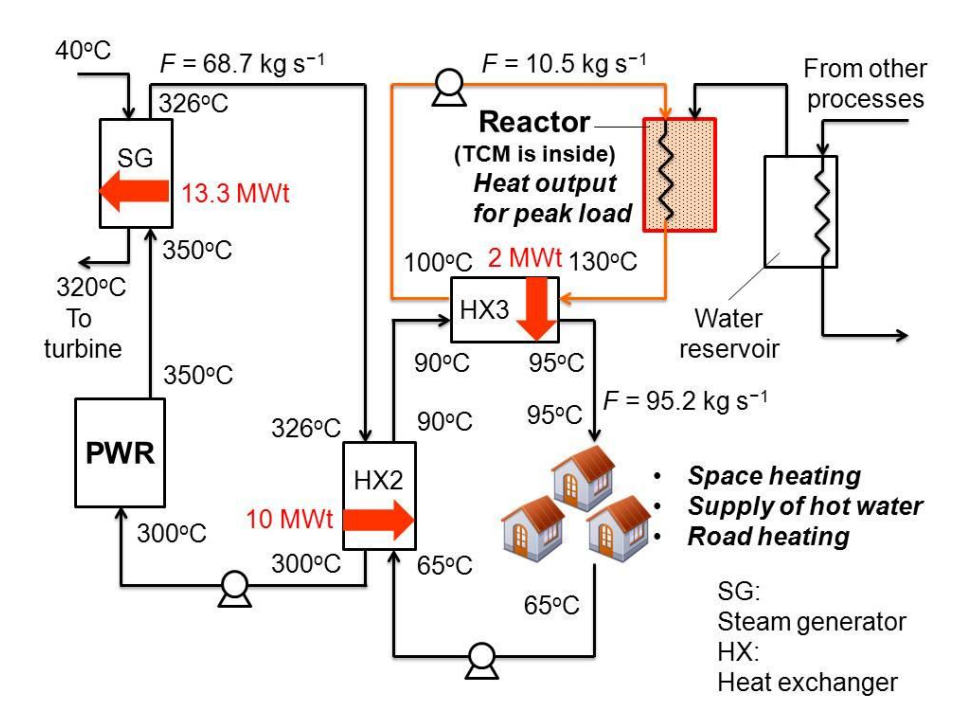


Figure 7.2-2 Schematic diagram of district heating system with thermochemical energy storage (at a peak of heat output operation) at high-heat demand period.

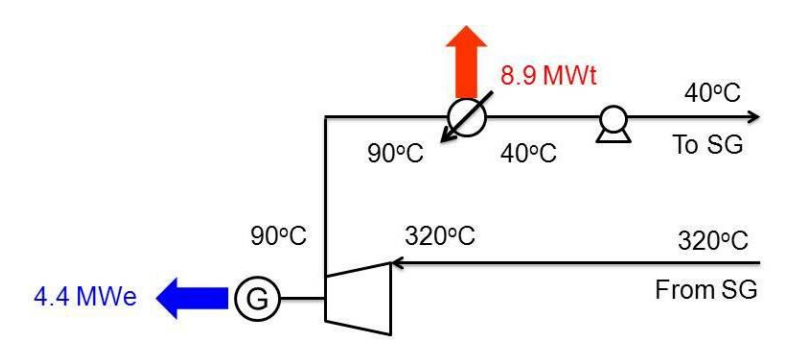


Figure 7.2-3 Set value of temperature for power generation loop of the small reactor

Heat load for district heating was studied by Dotzauer [11], and an example of heat load for district heating is shown in **Figure 7.2-4**. The heat load was approximately 300 ± 60 MWt for first 240 hours. The heat load of district heating was changed $\pm 20\%$ relative to a base load. The heat load for a town was modeled by using sin curve.

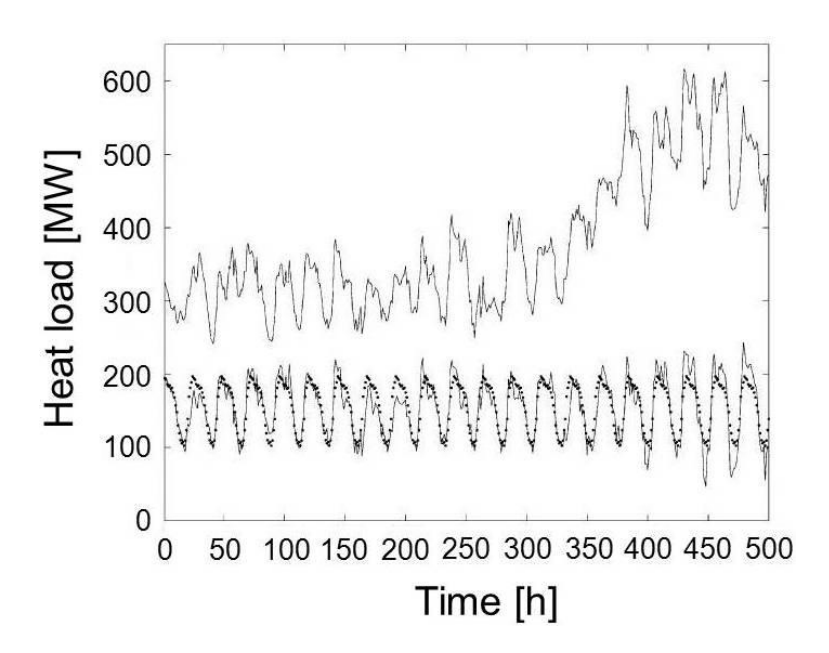


Figure 7.2-4 Example of heat load for district heating. Upper solid line indicates measured load [11].

It is assumed that base load is 10 MWt, and heat load can be changed \pm 20% relative to the base load within a day. The relationship between heat load (W_{heat} [MWt]) and time (t [s]) was calculated by a following equation.

$$W_{\text{heat}} = 10 + 2\sin\left(\frac{2\pi}{t_0}t\right) \tag{7-2}$$

Here, t_0 indicates the period of one cycle of heat load (= 24 h = 8.64 × 10⁴ s). The first term of Eq. (7-2), 10 MW, is heat output from the small nuclear reactor (base load). A model of heat load with

time in the town is shown in Figure 7.2-5.

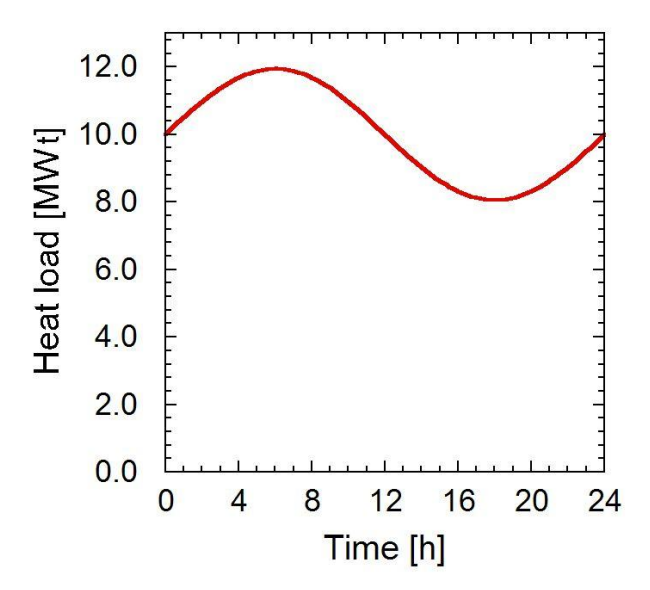


Figure 7.2-5 Model of heat load with time in the town.

The heat output from the TcES and heat storage to the TcES is expressed as below.

$$W_{\text{TcES}} = 2\sin\left(\frac{2\pi}{t_0}t\right) \tag{7-3}$$

The amount of surplus heat for recovery and storage was obtained by integration of Eq. (7-3) from the start of heat output ($t = t_1 = 0$ h = 0 s) to the end of heat output ($t = t_2 = 12$ h = 4.32×10^4 s).

$$Q = 2 \int_{t_1}^{t_2} \sin\left(\frac{2\pi}{t_0}t\right) dt$$

= 55 [GJ] (7-4)

55.0 GJ of heat is needed to output for the district heating system for load leveling, and same amount of heat is required to store from the start of heat storage ($t = t_2 = 12 \text{ h} = 4.32 \times 10^4 \text{ s}$) to the end of heat storage ($t = t_3 = 24 \text{ h} = 8.64 \times 10^4 \text{ s}$).

Then, the required amount of LiCl/Mg(OH)₂ ($\alpha = 0.10$) was estimated. The heat output capacity of LiCl/Mg(OH)₂ ($\alpha = 0.10$) at $T_d = 300^{\circ}$ C, $T_h = 140^{\circ}$ C, $p_{H2O} = 57.8$ kPa, and $t_v = 80$ min was 872 kJ kg⁻¹ (**Section 3.4.1.2**). Here, 55.0 GJ of heat is needed to store and output, 63.1 ton of LiCl/Mg(OH)₂ ($\alpha = 0.10$) is required for a thermal energy storage. It is assumed from former experimental study that the bulk density of LiCl/Mg(OH)₂ ($\alpha = 0.10$) is 0.716 ton m⁻³. The volume of the TCM is estimated as 88.1 m³. Adamov et al. studied nuclear reactor of 10 MWt capacity [1]. The nuclear reactor tank was designed as 3 m of diameter and 7 m of height at lower part, and 7 m of diameter and 10 m of height at upper part [1]. The volume of nuclear reactor tank (20 MWt capacity)

is estimated as 434 m³. The total volume of the TcES will be larger than 88.1 m³ because it needs heat exchanger, water reservoir and other components. However, the amount of LiCl/Mg(OH)₂ (α = 0.10) is acceptable to install TcES in the site of the nuclear plant compared with the volume of nuclear reactor tank.

Here, a flow rate of water at secondary system (F_s [kg s⁻¹]) is expressed as below.

$$F_{\rm s} = \frac{W_{\rm heat}}{C_{\rm p} \, \Delta T} \tag{7-5}$$

Here, W_{heat} [kW] is given by Eq. (7-2). A calculated profile of F_s is shown in **Figure 7.2-6**. The flow rate at one hour before from a switching from heat storage operation of TcES to heat output operation of TcES is calculated as 75.3 kg s⁻¹. The flow rate at one hour after from the switching is calculated as 84.5 kg s⁻¹. The flow rate increased 11% in two hours at the switching period. The change of flow rate is thought to be enough small to carry out the switching without unstable situation.

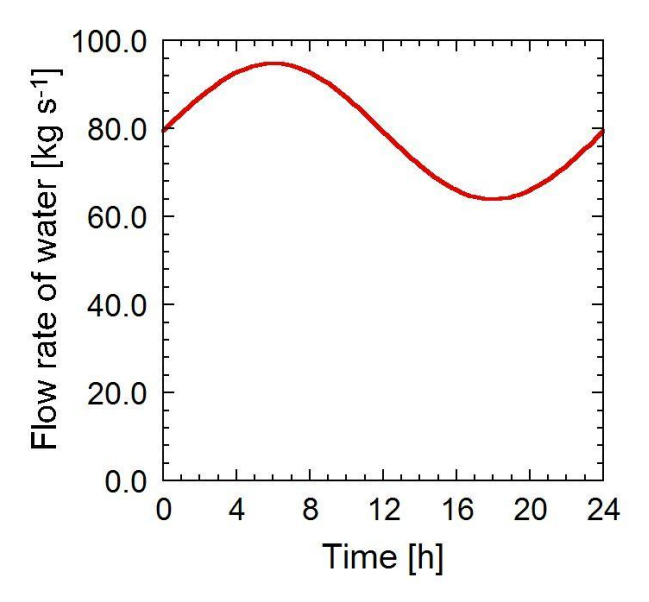


Figure 7.2-6 Calculated profile of flow rate of water at secondary system.

7.2.2 Emergency core cooling system with thermochemical energy storage The decay power of fission product from LWRs can be expressed following empirical formula [12].

$$\frac{W_{\text{dcy}}}{W_0} = 0.066 \left[t_s^{-0.2} - \left(t_s - \tau_s \right)^{-0.2} \right]$$
 (7-6)

Here, W_{dcy} [MWt]: decay thermal power, W_0 [MWt]: thermal power at constant operation, t_s [s]: time from shutdown, τ_s [s]: time for constant operation of nuclear reactor, respectively. For short time after

shut down compared with time for constant operation ($t_s \ll \tau_s$), Eq. (7-6) can be simplified as below [12].

$$W_{\text{dcy}} \cong W_0 \ 0.066 \left[t_s^{-0.2} - \tau_s^{-0.2} \right] \cong W_0 \ 0.066 \ t_s^{-0.2}$$
 (7-7)

The calculated decay thermal power (W_{dcy}) with time for 10 MWt capacity of small nuclear reactor is shown in **Figure 7.2-7**. Decay power was calculated by Eq. (7-7) with $W_0 = 10$ MWt.

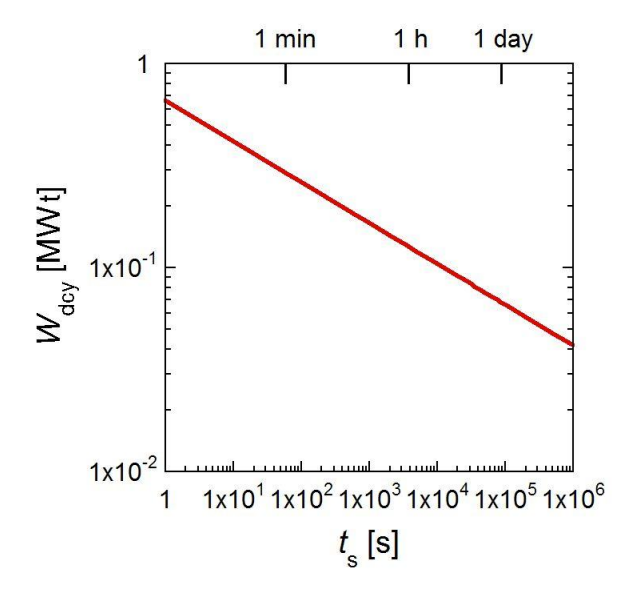


Figure 7.2-7 Calculated decay thermal power (W_{dcy}) with elapsed time from shutdown for 10 MWt capacity of small nuclear reactor.

Eq. (7-7) can be integrated, and Eq. (7-8) is obtained. Total decay heat amount (Q_{dcy} [MJ]) which was released from fission product can be calculated by Eq. (7-8).

$$Q_{\text{dey}} \cong W_0 \int_0^{t_s} 0.066 t_s^{-0.2} dt_s$$

$$= 8.25 \times 10^{-2} W_0 t_s^{0.8}$$
(7-8)

The calculated decay thermal power (W_{dcy}) with elapsed time from shutdown for 10 MWt capacity of a small nuclear reactor is shown in **Figure 7.2-8**.

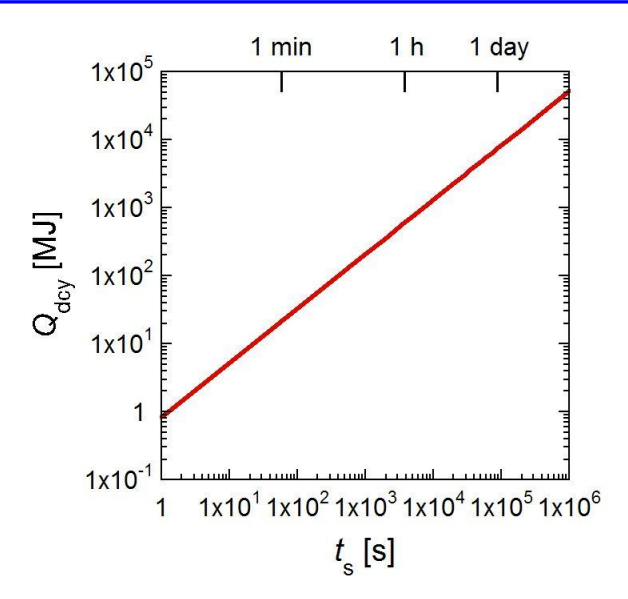


Figure 7.2-8 Calculated total decay heat amount (Q_{dcy}) with elapsed time from shutdown for 10 MWt capacity of a small nuclear reactor.

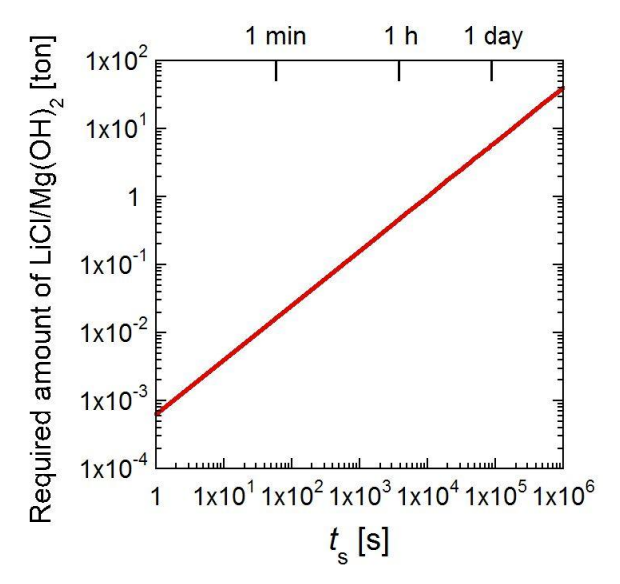


Figure 7.2-9 Required amount of LiCl/Mg(OH)₂ ($\alpha = 0.10$) with elapsed time from shutdown for 10 MWt capacity of a small nuclear reactor.

The required amount of LiCl/Mg(OH)₂ (α = 0.10) for ECCS is estimated from heat storage capacity of the material and calculated decay heat. The mole fraction of Mg(OH)₂ after the dehydration at 300°C for 30 min was 0.03 mol/mol for LiCl/Mg(OH)₂ (α = 0.10) (**Chapter 3**). Hence, heat storage capacity of the material at 300°C is 1.3 MJ kg⁻¹. It is assumed a blackout occurs together with the accident. **Figure 7.2-9** shows required amount of LiCl/Mg(OH)₂ (α = 0.10) with elapsed time from shutdown for 10 MWt capacity of small nuclear reactor. 0.44 ton of LiCl/Mg(OH)₂ (α = 0.10) is required when blackout continued one hour, and 5.6 ton of LiCl/Mg(OH)₂ (α = 0.10) is required when blackout continued one day. **Figure 7.2-10** shows Required volume of LiCl/Mg(OH)₂ (α = 0.10) with time from shutdown for 10 MWt capacity of small nuclear reactor. The volume of the TCM is

estimated as 0.62 m^3 for one hour blackout and 7.9 m^3 for one day blackout. As mentioned at **Section 7.2.1**, the volume of nuclear reactor tank (10 MWt capacity) is estimated as 434 m³. These amount of LiCl/Mg(OH)₂ ($\alpha = 0.10$) is acceptable for ECCS in the site of the nuclear plant.

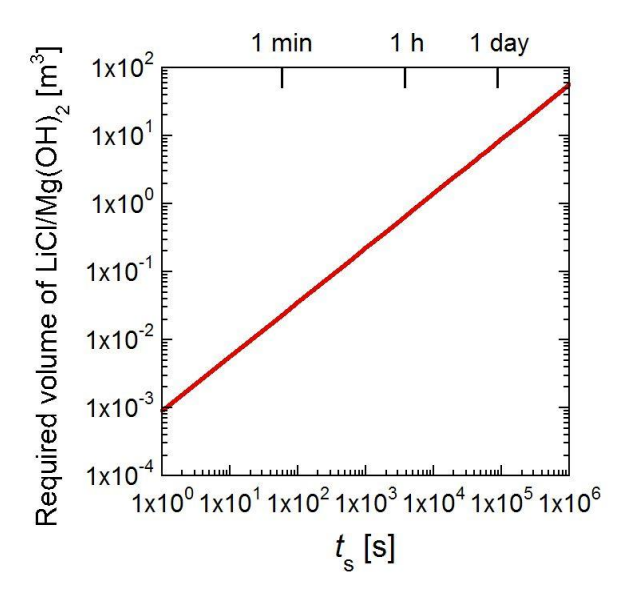


Figure 7.2-10 Required volume of LiCl/Mg(OH)₂ ($\alpha = 0.10$) with elapsed time from shutdown for 10 MWt capacity of small nuclear reactor.

7.2.3 Future prospects of thermochemical energy storage

The heat output capacity of LiCl/Mg(OH)₂ (α = 0.10) decreased by 21.1%, from 1.25 × 10³ kJ kg⁻¹ to 986 kJ kg⁻¹, in the 105 runs of the cyclic operation (**Chapter 5**). A price of Mg(OH)₂ is around 100 JPY kg⁻¹ [13], and that of LiCl is 1350–1450 JPY kg⁻¹ [14]. A price of LiCl/Mg(OH)₂ (α = 0.10) is around 250 JPY kg⁻¹ without preparation cost. This price is thought to be relatively law, thereby LiCl/Mg(OH)₂ (α = 0.10) which is used 100 days can be replaced by new LiCl/Mg(OH)₂ (α = 0.10).

A number of cells in the reactor of TcES are required for a load leveling of small nuclear reactors. To obtain desired heat storage/output rate, a control system for the cells in the reactors of TcES is required. Research and developments of the control system which can follow an actual heat load is needed to be studied.

An optimization of the reactors for TcES is needed to study. Especially, enhancements of heat transfer in the reactors are important. Thus, designs of heat exchangers in the reactors are upcoming significant technical issue.

7.3 Summary

A cogeneration system by using a small nuclear reactor was considered. The heat load of a town was assumed by sin curve modeling. Required amount of LiCl/Mg(OH)₂ ($\alpha = 0.10$) for load leveling of a 23.3 MWt reactor was 63.1 ton (88.1 m³). The decay heat from fission products after

shutdown by the accident was calculated. Required amount of LiCl/Mg(OH)₂ (α = 0.10) for ECCS was 0.44 ton (0.62 m³) for one hour blackout, and 5.6 ton (7.9 m³) for one day blackout. These amounts of LiCl/Mg(OH)₂ (α = 0.10) was acceptable to install the thermochemical energy storage combined with the nuclear plant.

7.4 References

- [1] E. O. Adamov, Yu. M. Cherkashov, A. A. Romenkov, V.I. Mikhan, V.I. Semenikhin; Inherently safe pool-type reactor as a generator of low-grade heat for district heating, air conditioning and salt water desalination, *Nucl. Eng. Des.*, **173**, 167–174 (1997)
- [2] R. W. Schleicher; TRIGA power system for power, water and heat in remote communities, *Potential of small nuclear reactor for future clean and safe energy sources*, H. Sekimoto ed., Elsevier, Amsterdam, the Netherlands, 157–165 (1992)
- [3] W. Zheng, D. Wang, J. Lin, D. dong, C. Ma, Y. Wu; Nuclear heating reactor, a safe, clean and economic energy source, *Potential of small nuclear reactor for future clean and safe energy sources*, H. Sekimoto ed., Elsevier, Amsterdam, the Netherlands, 359–366 (1992)
- [4] O. Sambuu, T. Obara; Conceptual design for a small modular district heating reactor for Mongolia, *Ann. Nucl. Energy*, 47, 210–215 (2012)
- [5] Y. Kato, N. Harada, Y. Yoshizawa; Kinetic feasibility of a chemical heat pump for heat utilization of high-temperature processes, *Appl. Therm. Eng.*, **19**, 239–254 (1999)
- [6] Y. Kato, M. Yamada, T. Kanie, Y. Yoshizawa; Calcium oxide/carbon dioxide reactivity in a packed bed reactor of a chemical heat pump for high-temperature gas reactors, *Nucl. Eng. Des.*, **210**, 1–8 (2001)
- [7] S. T. Kim; Reactivity enhancement of chemical materials for packed bed reactor of chemical heat pump, Tokyo Institute of Technology, Doctoral thesis (2012)
- [8] International atomic energy agency ed.; Advanced applications of water cooled nuclear power plants, International atomic energy agency, Vienna, Austria, 46–57 (2007)
- [9] International atomic energy agency ed.; Market potential for non-electric applications of nuclear energy, International atomic energy agency, Vienna, Austria, 42–43 (2002)
- [10] H. Sato; A study on a safety and a controllability of cogeneration system by using high temperature gas reactor as a heat source (*in Japanese*), Tokyo Institute of Technology, Doctoral thesis (2012)
- [11] E. Dotzauer; Simple model for prediction of loads in district-heating systems, *Appl. Energy*, **73**, 277–284 (2002)
- [12] N. E. Todreas, M. S. Kazimi; Nuclear systems Volume 1: Thermal hydraulic fundamentals, second ed., CRC press, Boca Raton, U.S. (2012)
- [13] Y. Kato, T. Saito, T. Soga, J. Ryu, Y. Yoshizawa; Durable reaction material development for magnesium oxide/water chemical heat pump, *J. Chem. Eng. Jpn.*, **40**, 1264–1269 (2007)
- [14] Ministry of Economy, Trade and Industry, Japan ed.; Supply and demand, recycles, applications of each metal in Japan, Ref.2-141–Ref.2-145 (2006)

(http://www.tohoku.meti.go.jp/2008/kankyo/recycle/date/27.pdf)

Chapter 8 Conclusion

The depletion of primary energy sources and the mismatch between the supply and demand of energy are becoming big social issues. Thus, researches and developments of recovery, storage and conversion of surplus heat or exhaust heat from nuclear reactors, cogeneration systems, and industrial plants are required. The surplus/exhaust heat from above mentioned sources at 200-300°C is released to environment without recovery. In this work, thermochemical energy storage (TcES) is studied to recover, store and convert the surplus/exhaust heat because of its higher heat output capacity than sensible heat storages and latent heat storages. A technical problem of conventional thermochemical energy storage materials (TCMs) based on metal hydroxides and metal carbonates is that their low dehydration or decarbonation (endothermic reaction) reactivity at 200-300°C. Thus, surface of Mg(OH)₂ was modified by LiCl, and the bulk composition of rare earth mixed hydroxide was modified to enhance dehydration reactivity. However, some technical issues of these materials were remained. The dehydration/hydration kinetic equations and parameters, relation between reaction conditions and heat output capacity, and durability properties of LiCl/Mg(OH)₂ had been unclear. Rare earth mixed hydroxides are candidate of TCMs. However, their dehydration and hydration reactivity had not been studied. Combination of TcES and small nuclear reactors can be used for load leveling and emergency core cooling systems (ECCS). Then, it was needed to estimate required amount of LiCl/Mg(OH)₂ for load leveling or ECCS to evaluate possibility and potential of the combination. These technical problems were studied in the thesis.

In **Chapter 1**, "General introduction", the research background of the thesis was reviewed, and importance of thermal energy storage was mentioned. The previous researches of thermal energy storages were reviewed and the technical issues of thermal energy storages were discussed. Then, the motivation of development of TCMs was explained. The objectives of the research were shown.

In **Chapter 2**, "Dehydration of lithium chloride-modified magnesium hydroxide", LiCl/Mg(OH)₂ at various LiCl mixing ratio (α) was prepared as candidates for TCMs. The dehydration of authentic Mg(OH)₂ and LiCl/Mg(OH)₂ were examined, and kinetic analysis were performed. α of 0.10 was optimum value for thermal energy storage at 250–300°C. The dehydration of LiCl/Mg(OH)₂ (α = 0.10) was understood by a two-step reaction model. The dehydration rate did not depend on the mole fraction of Mg(OH)₂ in the first step (zero-order reaction), but depended on the mole fraction of Mg(OH)₂ as a first-order reaction in the second step. On the other hand dehydration of authentic Mg(OH)₂ was understood by a single reaction model (first-order reaction only). The kinetic equations and parameters for dehydration were submitted.

In Chapter 3, "Hydration reactivity of lithium chloride-modified magnesium oxide",

hydration of LiCl/MgO was studied in detail. The effects of LiCl mixing ratio, hydration temperature, and water vapor pressure on the hydration behavior of LiCl/MgO were examined, and the heat output capacities at each condition were calculated. The kinetic analysis of hydration was performed by using shrinking core model. The heat output capacities of the material ($\alpha = 0.10$) at $p_{\rm H2O} = 57.8$ kPa were 724 kJ kg⁻¹ at hydration temperature of 180°C and 1.40 × 10³ kJ kg⁻¹ at 110°C. These were higher than the heat output capacity of the authentic material. The rate controlling process of overall hydration was changed by temperature. H₂O diffusion in Mg(OH)₂ layer is assumed to be the rate controlling process at 110–150°C, $p_{\rm H2O} = 57.8$ kPa. Water absorption into LiCl·nH₂O is assumed to be the rate controlling process of overall hydration rate at 180–200°C, $p_{\rm H2O} = 57.8$ kPa, at early period, and interface reaction is assumed to be the rate controlling process at latter period. Hydration kinetic equations and parameters of LiCl/MgO ($\alpha = 0.10$) are submitted, and heat output rate is evaluated.

In Chapter 4, "Near infrared spectroscopy for hydration observation of lithium chloride-modified magnesium oxide", hydration of authentic MgO and LiCl/MgO ($\alpha = 0.10$) was examined by near infrared (NIR) spectroscopy. The obtained spectra were decrivoluted into components (Mg(OH)₂, free water, and bound water or hydrated species). The hydration mechanism was discussed by profile of peak area for each component with time. For authentic MgO, supplied water vapor was consumed by hydration of MgO at surface until first 16 min, and water adsorption on the surface was started at 20 min. Hydration of MgO at inner side was proceeded by adsorbed water after 28 min. For LiCl/MgO ($\alpha = 0.10$) at 110°C, supplied water vapor was consumed for formation of free water and hydrated species for first 8 min, and then hydration of MgO was proceeded. For LiCl/MgO ($\alpha = 0.10$) at 180°C, hydration of MgO and water sorption was occurred almost simultaneously, and water sorption was reached equilibrium state at around 24 min. There are two possibilities of reaction paths for hydration of LiCl/MgO ($\alpha = 0.10$). One of them is a cascaded relationship between water absorption of LiCl and solid-solid reaction of LiCl·H₂O and MgO (Reaction path A). The other possibility is parallel relationship between water absorption of LiCl and hydration of MgO (Reaction path B). The hydration was enhanced by LiCl-modification (Chapter 3), the hydration mechanism of LiCl/MgO ($\alpha = 0.10$) can be explained by cascaded path (reaction path A).

In **Chapter 5**, "Durability of lithium chloride-modified magnesium hydroxide on repetitive reactions", 105 runs of dehydration/hydration cycles of LiCl/Mg(OH)₂ ($\alpha = 0.10$) were performed. The heat output capacity of the material decreased by 21.1%, from 1.25×10^3 kJ kg⁻¹ to 986 kJ kg⁻¹, in the 105 runs of the cyclic operation. A SEM micrograph revealed that LiCl was highly dispersed on the Mg(OH)₂ grains before the cyclic operation. In contrast, needle-like crystals of LiCl were observed on the Mg(OH)₂ grains after 105 runs of the cyclic operation. The XRD pattern showed no characteristic peak for LiCl in the sample prior to the cyclic operation. However, the peak did appear in the sample after 105 runs of the cyclic operation. These results indicate that highly dispersed LiCl on the surface of Mg(OH)₂ was aggregated and needle-like LiCl crystal was formed on the surface of

Mg(OH)₂. The change of surface state was thought to be decreased the reactivity of the material.

In **Chapter 6**, "Rare earth mixed hydroxide for thermochemical energy storages", rare earth hydroxides are proposed as new candidates for TCMs. The dehydration reactivity of the hydroxides was enhanced by adjusting the metal ion composition. A TCM based on $La_{0.50}Y_{0.50}(OH)_3$ dehydrated at 300°C, and hydrated at 110°C, water vapor pressure of 7.4 kPa. Reactivity of conventional material $(Mg(OH)_2)$ was lower than $La_{0.50}Y_{0.50}(OH)_3$ under these conditions. Reaction heats of rare earth pure/mixed hydroxides showed downward trend by increase of electronegativity of cation. The heat output capacities of $La_{0.50}Y_{0.50}(OH)_3$ was 282 kJ kg⁻¹ at 110°C with water vapor pressure of 7.4 kPa which is higher than that of conventional material $(Mg(OH)_2)$ at these conditions. Thus, these $La_{0.50}Y_{0.50}(OH)_3$ is expected as a candidate of TCM.

In **Chapter 7**, "Combination of thermochemical energy storages based on lithium chloride-modified magnesium hydroxide and small nuclear reactors", combination of a small nuclear reactor for district heating and a TcES based on LiCl/Mg(OH)₂ (α = 0.10) was studied. A cogeneration system by using a small nuclear reactor was considered. The thermochemical energy storage by using LiCl/Mg(OH)₂ (α = 0.10) is expected to use load leveling and expected as a heat absorber for emergency core cooling system (ECCS). Required amount of LiCl/Mg(OH)₂ (α = 0.10) for load leveling was estimated as 63.1 ton (88.1 m³). Required amount of LiCl/Mg(OH)₂ (α = 0.10) for ECCS was 0.44 ton (0.62 m³) for one hour blackout, and 5.6 ton (7.9 m³) for one day blackout. These amounts of LiCl/Mg(OH)₂ (α = 0.10) was acceptable to install the TcES in the site of the nuclear plant. Hence, combination of TcES and small nuclear reactors is possible by using LiCl/Mg(OH)₂ (α = 0.10).

LiCl/Mg(OH)₂ (α = 0.10) are expected to use as a TCM which can dehydrate at 250–300°C and hydrate at 110–180°C with water vapor pressure of 57.8 kPa. TcES based on LiCl/Mg(OH)₂ (α = 0.10) can use with small nuclear reactors for load leveling or ECCS. La_{0.50}Y_{0.50}(OH)₃ is expected to use as a TCM which can dehydrate at 300°C hydrate at 110°C with water vapor pressure of 7.4 kPa. These TCMs can be recover, store and convert the surplus/exhaust heat at 250–300°C from nuclear reactors, cogeneration systems, and industrial plants. These TCMs have potentials to overcome problems like depletion of primary energy sources and the mismatch between the supply and demand of energy.

Nomenclature

Roman		Subscripts			
$C_{ m p}$: specific heat capacity [kJ K^{-1} kg ⁻¹]	0	: initial value or pre-exponential factor		
$E_{\rm a}$: activation energy [kJ mol ⁻¹]	abs	: absorption		
G	: Gibbs free energy [kJ mol ⁻¹]		: adsorption		
H	: enthalpy [kJ mol ⁻¹]		: Boltzmann's constant		
M	: molecular weight [g mol ⁻¹]	c	: cyclic dehydration-hydraion-drying		
P	: pressure [kPa]	operation	n		
Q	: heat output capacity [kJ kg ⁻¹]	cnd	: condensation		
R	: gas constant [J mol ⁻¹ K ⁻¹]	dcy	: decay		
S	: entropy [J $K^{-1} \text{ mol}^{-1}$]	des	: desorption		
T	: temperature [°C] or [K]	e	: evaporation		
V	: potential [eV]	eq	: equilibrium		
W	: heat output rate $[W kg^{-1}]$	d	: dehydration		
X	: mole fraction of hydroxide [mol/mol]	f	: first-order		
h	: Planck's constant [J s]	fd	: first dehydration		
k	: rate constant $[s^{-1}]$ or $[m s^{-1}]$	fsn	: fusion		
p	: partial pressure [kPa]	h	: hydration		
t	: time [s]	r	: reaction		
w	: weight [g]	S	: shutdown		
x	: mole fraction of $Mg(OH)_2$ [mol/mol]	srp	: sorption		
		turn	: turnover		
Greek		v	: vapor		
α	: LiCl mixing ratio [mol/mol]	Z	: zero-order		
ν_1	: symmetric stretching vibration of water				
molecules					
ν_2	: bending vibration of water molecules				
ν_3	: asymmetric stretching vibration of				
water molecules					

Research achievements

Publications

- 1. <u>Hirokazu Ishitobi</u>, Keirei Uruma, Masato Takeuchi, Junichi Ryu, and Yukitaka Kato; "Dehydration and hydration behavior of metal-salt-modified materials for chemical heat pumps", *Applied Thermal Engineering*, **50**, 1639–1644 (2013) (**Chapter 2**)
- 2. <u>Hirokazu Ishitobi</u>, Keirei Uruma, Junichi Ryu, and Yukitaka Kato; "Durability of lithium chloride-modified magnesium hydroxide on cyclic operation for chemical heat pump", *Journal of Chemical Engineering of Japan*, **45**, 58–63 (2012) (**Chapter 5**)
- 3. <u>Hirokazu Ishitobi</u>, Junichi Ryu, and Yukitaka Kato; "Dehydration and hydration behavior of rare-earth hydroxides for chemical heat pumps", *Chemistry Letters*, **41**, 583–584 (2012) (**Chapter 6**)
- 4. <u>Hirokazu Ishitobi</u>, Naoya Hirao, Junichi Ryu, and Yukitaka Kato; "Evaluation of heat output capacities of lithium chloride-modified magnesium hydroxide at various mixing ratios, temperatures, and vapor pressures for thermochemical energy storages", *Industrial & Engineering Chemistry Research*, Submitted (**Chapter 3**)

Proceedings

- 1. <u>H. Ishitobi</u>, K. Uruma, J. Ryu and Y. Kato, "The reactivity of metal salt-modified materials for chemical heat pump in a repetitive reaction", *International Sorption Heat Pump Conference*, IIR/AICARR, Padua, Italy, 833–840 (2011)
- 2. <u>H. Ishitobi</u>, Y. Sato, K. Uruma, J. Ryu and Y. Kato, "Dehydration and hydration behavior of LiCl-modified Mg(OH)₂ as a material for chemical heat pumps", *International Symposium on Innovative Materials for processes in Energy Systems*, Research Publishing, Singapore, 255–262 (2010)

International conferences

- 1. <u>H. Ishitobi</u>, M. Takafumi, U. Keirei, J. Ryu, and Y. Kato, "Application of Lanthanum-Gadolinium Mixed Hydroxides into Chemical Heat Pumps", *The Fourth International Forum on Multidisciplinary Education and Research for Energy Science*, C123, Honolulu, United States, (Dec., 2011)
- 2. <u>H. Ishitobi</u>, K. Uruma, J. Ryu, and Y. Kato, "The reactivity of metal salt-modified materials for chemical heat pump in a repetitive reaction", *International Sorption Heat Pump Conference*, I61, Padua, Italy (Apr., 2011)
- 3. <u>H. Ishitobi</u>, Y. Sato, M. Takafumi, K. Uruma, J. Ryu and Y. Kato, "The reactivity under repetitive reaction of LiCl-modified Mg(OH)₂ as a material for chemical heat pumps", *Third International Forum on Multidisciplinary Education and Research for Energy Science*, A422, Ishigaki, Japan (Dec., 2010)
- 4. <u>H. Ishitobi</u>, Y. Sato, K. Uruma, J. Ryu and Y. Kato, "Dehydration and hydration behavior of LiCl-modified Mg(OH)₂ as a material for chemical heat pumps", *International Symposium on Innovative Materials for Processes in Energy Systems* (IMPRES2010), IMPRES017, Singapore (Dec., 2010)

博士論文に関係した国内学会発表

- 1. <u>石飛宏和</u>, 劉醇一, 加藤之貴, 「希土類複合水酸化物の脱水反応熱の測定」, 化学工学会第44回秋季大会, M105, 仙台 (2012年9月)
- 2. <u>石飛宏和</u>, 水野 峻史, 宇留間慶麗, 劉醇一, 加藤之貴, 「希土類複合水酸化物の化学蓄熱材料への適用」, 化学工学会第 77 回年会, J121, 東京 (2012 年 3 月)
- 3. <u>石飛宏和</u>, 佐藤義智, 宇留間慶麗, 劉醇一, 加藤之貴, 「塩化リチウム修飾水酸化マグネシウムの繰り返し反応に対する耐久性」, 化学工学会第 42 回秋季大会, C119, 京都 (2010 年 9 月)
- 4. <u>石飛宏和</u>, 佐藤義智, 宇留間慶麗, 劉醇一, 加藤之貴, 「金属塩修飾型ケミカルヒートポンプ材料における金属水酸化物純度の影響」, 化学工学会宇都宮大会 2010, SB202, 宇都宮 (2010年8月)
- 5. <u>石飛宏和</u>, 劉醇一, 加藤之貴,「金属塩添加水酸化マグネシウムの脱水反応特性」, 化学工学会第75年会, P104, 鹿児島(2010年3月)
- 6. <u>石飛宏和</u>, 平尾直也, 劉醇一, 加藤之貴, 「金属塩添加水酸化マグネシウムの水和反応特性 と化学蓄熱への適用」, 化学工学会第 41 回秋季大会, V206, 広島(2009 年 9 月)

Internship projects

1. Global COE Energy: Off-Campus Project, Institute of Advanced Technologies for Energy "Nicola Giordano" (CNR-ITAE), Messina, Italy, From September 11, 2011 to November 28, 2011.

Awards

- 1. 最優秀修士論文発表賞, 東京工業大学大学院理工学研究科原子核工学専攻 (2010)
- 2. 日本原子力学会フェロー賞, 日本原子力学会 (2010)
- 3. Best presentation award, *The Fourth International Forum on Multidisciplinary Education and Research for Energy Science* (2011)

Others

1. JSPS Research fellow (DC2), Japan Society of the Promotion of Science, From April, 2012 to the present.

Acknowledgements/謝辞

本研究は平成二十年四月から平成二十五年二月にわたって,東京工業大学大学院理工学研究 科原子核工学専攻において大学院修士課程および博士後期課程の研究として行ったものです. 本研究を遂行するにあたり,終始適切なご指導を賜った加藤之貴准教授に衷心より御礼申し上げます.また,私が研究を進めるにあたり,非常に多くの方々からのご支援をいただき,本論文の提出に至りました.心より感謝いたします.

指導教員の加藤之貴准教授からは、研究を進めるにあたって有益なご示唆およびご助言をいただきました。また、研究に関連しない事柄も含めて非常に多くの知識や行動原理をご教示くださりました。実り多き大学院生活は加藤先生のご指導によるものであります。深く御礼申し上げます。また、劉醇一助教には実験技術や材料設計の考え方、研究の進め方など、本研究を進めるにあたって非常に有意義なご指導をいただきました。日頃より頻繁にディスカッションをしていただき、かつ論文原稿の添削などを丁寧に行っていただきました。研究室の庶務一般に関しても、ご助言・ご助力をいただくこと大でありました。ここに謹んで謝意を表します。吉澤善男名誉教授には、修士課程において的確にご指導をいただきました。熱力学や伝熱工学に関して、精到な知識をもとに有益なご助言をいただきました。深く感謝いたします。

本論文を作成するにあたり,原子核工学専攻の矢野豊彦教授,池田泰久教授,竹下健二教授, 小原徹准教授には論文の内容について数々の有益なご助言・ご示唆をいただきました.ここに 謹んで謝意を表します.

本研究で利用した窒素吸着装置(Autosorb 1MP, Quantachrome instruments)は東京工業大学ものつくりセンターのご厚意により,使用いたしたものです。装置の使用方法および研究者としてのあり方を懇切丁寧にご指導いただいた河村一朗博士に厚く御礼申し上げます。また,本学原子炉工学研究所の矢野研究室に所属するダイヤモンドカッターをご厚意により使用いたしました。今井雅三氏にはダイヤモンドカッターの使用に関して直接のご支援をいただきました。吉田克己助教には材料研究の手法に関してご教示いただき,さらに私を激励してくださりました。心より御礼申し上げます。本論文に結果を掲載できませんでしたが,矢野研究室の小林知裕氏には SEM-EDX の測定で直接的なご支援をいただきました。I would like to express my sincere appreciation to Ms. Areerak Rueanngoen and Mr. Jiraborvornpongsa Noppasint for their kindest supports for TEM measurements。また,本学原子炉工学研究所の塚原剛彦准教授には,本研究に関して示唆を与えてくださり,かつ私を鼓舞していただきました。厚く御礼申し上げます。

5年間の大学院生活を送るにあたり、日本学生支援機構からの奨学金および日本学術振興会の研究奨励金、文部科学省グローバル COE「エネルギー学理の多元的融合」の RA 雇用、東京工業大学の TRA 雇用により経済的なご支援をいただきました。心より御礼申し上げます。

本研究を遂行するにあたり、常日頃より研究室の方々には大変お世話になりました.事務補 佐員の内山梢氏、山崎綾子氏、大泉まどか氏には、各種の事務処理に関して直接のご支援をい ただきました. 技術補佐員の宇留間慶麗氏には、研究に関する専門的な技術を教えていただきました. また、財津裕康氏および井上観大氏には実験手法や研究発表の手法について多くの事柄を教えていただきました. 佐藤義智氏、櫻井あずさ氏、黒田健太郎氏、水野峻史氏、村田興一氏、小野光遥氏、苅谷潤氏、初田浩之氏、藤井元太郎氏、原祐樹氏とは研究を進めるにあたって、切磋琢磨して成果を得ました. 佐藤博之博士には含蓄に富むご示唆および広い視点にたった有益なご助言をいただきました. I would like to express my gratitude to Dr. SeonTae Kim, Mr. Massimiliano Zamengo, Mr. Arnoldus Lambertus Dipu, and Ms. Myagmarjav Odtsetseg for your kindest friendships and supports.

私が大学院に在学している間に多くの事務的なご支援をいただきました.原子核工学専攻事務の鎌田しげこ氏,藤原典子氏には教務面および専攻の行事について適切なご支援および懇切丁寧なご助言をいただきました.謹んで謝意を表します.グローバル COE「エネルギー学理の多元的融合」に関する事柄については,道岡彩氏,目代絵美氏,川井田奈緒美氏,鈴木恵美子氏,大久保富久氏,三宅美香氏,青木久美恵氏に適切なご支援をいただきました.特に,インターンシップの日程変更では,急な案件であるにも関わらず川井田氏に迅速かつ的確にご差配いただきました.心より感謝いたします.

本論文の内容とは直接関連いたしませんが、各インターンシップにおける経験が、私の視野を広げるのに大変役立ちました。日立製作所でのインターンシップでは、使用済み核燃料を乾式分離する研究に携わることができました。安全管理やスケジュール管理、企業における研究手法について、まことに多くの事柄を学びました。特に、藤村幸治博士、笹平朗博士、渡辺大輔氏、溝田裕久博士、村田新治氏には適切な実習指導をいただきました。深く感謝いたします。 I studied at University of Messina (UNIME) and CNR Istituto di Tecnologie Avanzate per l'Energia "Nicola Giordano" (ITAE)、Italy for three months。 I appreciate the supports and fruitful discussions from Dr. Angelo Freni (ITAE)、Prof. Lucio Bonaccorsi (UNIME)、Dr. Giovanni Restuccia (ITAE)、Prof. Edoardo Proverbio (UNIME)、Prof. Candida Milone (UNIME)、and Dr. Luigi Calabrese (UNIME). I thank Mr. Paolo Bruzzasniti、Ms. Angela Capri、Dr. Marianna Fazio、Mr. Rahim Abudul for their kindest friendships and supports for a daily life at laboratory and dormitory.

京都大学の加納学教授にはリーダーとしてのありかたや良書,教育,マネジメントに関して 貴重なご示唆をいただきました。非常にご多忙であるにも関わらず、常に的確かつ親身にご助 言をいただいた事に、謹んで謝意を表します。大阪大学の龍崎奏助教には留学や研究について、 ご助言をいただきました。厚く御礼申し上げます。I would like to express gratitude to Prof. Andrei G. Fedorov (Georgia Institute of Technology) for his kindest discussions and encouragement to me.

刎頸の友である根本峻瑠氏は、至らない私を叱咤激励してくださりました.また、深い教養と広い視野は私の目標であります.小学生以来の親友である長谷川靖法務博士、松元裕貴氏はお互いにどのような事でも相談できる仲で、大変心強く思っております.東京理科大学における友人である三井龍一氏、小波さおり氏、市村聡氏、太田和洋氏、田口雅旦氏、岡田文徳氏、小川智史氏、原山敦氏、小西和也氏は大学在学中の折より今に至るまで昵懇にしていただきました.東京工業大学大学院における友人である三浦弘道氏、芝知宙氏、今道祥二氏には、お互

いに苦楽を共にして、勉学・研究を競って参りました. I would like to express appreciation to Dr. Fabrizio Freni, Ms. Enza Brancato, Mr. Domenico Di Pietro, Mr. Antonio Pinta, Mr. Giuseppe Mavilia, Ms. Rania Sayed, Mr. Soundara Rajan, Mr. Sundar Manickam for their kindness, friendships and helps. 東京工業大学で実施された文部科学省グローバル COE「エネルギー学理の多元的融合」では, 加茂祐一氏(材料工学専攻), 李聡一氏(化学専攻), 孟慶龍氏(化学専攻), Ms. Trinuruk Piyatida (Department of Nuclear Engineering), 向井登志広氏(国際開発工学専攻), 笠嶋俊介氏(電子物理工学専攻), 鈴木崇弘氏(機械制御システム専攻), アミール偉氏(人間行動システム専攻), Dr. Buddha Ratna Shrestha (Department of Metallurgy and Ceramics Science), Dr. Navvab Hosseini (Department of Mechanical and Control Engineering), Dr. Bhushan Patil (Department of Electronic Chemistry) に大変お世話になりました。また、専攻分野や出身が多様であったため、非常に有意義なご指摘やご示唆をいただきました。諸氏の心暖まる友情に深く感謝いたします。

中学校・高等学校の恩師, 黒島文章先生, 小林明久先生, 中村和孝先生, 遠藤修市先生には, 至らない私を根気強くご指導をいただきました. 東京理科大学において卒業研究のご指導を賜った庄野厚教授および大竹勝人教授, 高橋智輝助教には研究作法のイロハを懇切丁寧に教えていただき, 私に研究の楽しさを教えてくださりました. 心より御礼申し上げます.

私の長い学園生活を支えていただいた家族に御礼申し上げます. 父純二には技術者としてのあり方を言葉ではなく行動で示していただきました. 母佳代は慈愛に満ちた心で私のことを見守ってくださりました. 次弟の俊和には,日々努力すべきこと,誠実であるべきことを示していただきました. 三弟の政和には,機に臨んで迅速かつ的確な行動を,沈着冷静にとるべきこと示していただきました. 私が研究に専心できたのは,このような素晴らしい家族が暖かく応援してくださったためであります.

最後に、私の研究生活とご支援いただいた全ての方々に御礼を申し上げます。 化学蓄熱が世界のエネルギー問題を解決な一助になることを新念し、本論文の結がといたします。